Herausgeber
Tom Lahmer Timon Rabczuk Carsten Könke

ISM-Bericht 5/2019 ISSN: 1610-7381
Institut für Strukturmechanik
Fakultät Bauingenieurwesen
Bauhaus-Universität Weimar
Marienstraße 15
99423 Weimar
Germany

Tel. +49 3643 584504
Fax. +49 3643 584514

http://www.uni-weimar.de/ism

Operational modal analysis

Theory and aspects of application in civil engineering

Habilitationsschrift

vorgelegt am 23. November 2018

der Fakultät Bauingenieurwesen

der Bauhaus-Universität Weimar

von

Dr.-Ing. Volkmar Zabel

geboren am 26. November 1968 in Potsdam

Gutachter:

1. Prof. Dr.-Ing. habil. Carsten Könke
2. Prof. Dr.-Ing. habil. Manfred Bischoff

Erteilung der Habilitation am 16. Oktober 2019

Für Susann, Johanna und Jonathan

Danksagung

Diese Arbeit entstand über mehrere Jahre während meiner Tätigkeit auf dem Gebiet der Baudynamik am Institut für Strukturmechanik der Bauhaus-Universität Weimar. In dieser Zeit hat Prof. Carsten Könke mich stets in angenehm kollegialer Weise begleitet und motiviert. Dafür gilt ihm mein ganz besonderer Dank. Als weiterem Wegbegleiter spreche ich Herrn Prof. Christian Bucher meinen herzlichsten Dank aus für vielzählige Gespräche sowie für die Möglichkeit, an der TU Wien konzentriert an der vorliegenden Schrift zu arbeiten. Während der intensiven Arbeitsphasen in seinem Forschungsbereich sind wesentliche Teile der Habilitationsschrift entstanden.

Herrn Prof. Manfred Bischoff danke ich für die Bereitschaft zur Begutachtung der Habilitationsschrift. Bei Prof. Klaus Gürlebeck bedanke ich mich für die Leitung der Habilitationskommission. Den weiteren Kommissionsmitgliedern, Prof. Torsten Wichtmann, Prof. Volker Rodehorst und Prof. Reinhard Illge danke ich ebenfalls für ihre Mitwirkung im Habilitationsverfahren.

Für die ausgesprochen angenehme Zusammenarbeit am Institut für Strukturmechanik danke ich dem gesamten Kollegium, insbesondere Frau Marlies Terber, die durch ihre selbverständliche Hilfe bei vielen Aufgaben des Arbeitsalltags in herzlicher und engagierter Weise große Erleichterung geschaffen hat. Herrn Simon Marwitz gilt mein Dank für seine Unterstützung bei den experimentellen Untersuchungen sowie der Implementierung der in der Arbeit verwendeten numerischen Werkzeuge.

Die Durchführung der experimentellen Arbeiten wäre ohne die unterstützende Zusammenarbeit mit den Kollegen der Versuchstechnischen Einrichtung der Fakultät Bauingenieurwesen kaum möglich gewesen. Aus diesem Grund sei Wolf-Dieter Vogler, Holger Dabbert, Marko Friedel, Christian Ahrend und Gerd Wolf für ihre langjährige Hilfe gedankt. Besonderer Dank gilt für seine Begleitung bei experimentellen Untersuchungen an Türmen und Masten Herrn Dr.-Ing. Frank Wolf.

Für Ihren Beistand und stetige Ermutigungen über die Jahre der Arbeit an der Habilitationsschrift danke ich ganz besonders meiner Frau Susann sowie unseren Kindern Johanna und Jonathan.

Weimar, Oktober 2019 Volkmar Zabel

Zusammenfassung

Seit einigen Jahren ist ein steigender Bedarf an dynamischen Analysen von Bestandsbauwerken unterschiedlichster Art zu verzeichnen. Dabei werden Vorhersagen im Bauingenieurwesen in der Regel mit Hilfe numerischer Modelle getroffen. Die auf diese Weise erzielten Ergebnisse hängen folglich in hohem Maße von der Qualität des verwendeten Modells ab. Daher ist es in diesem Zusammenhang besonders wichtig, dass die numerischen Modelle das tatsächliche Tragverhalten einer bestehenden Konstruktion möglichst realitätsnah abbilden. Da jedes Modell auf einer Vielzahl von Annahmen beruht, sind modellbasierte numerische Simulationsergebnisse stets zu einem gewissen Grad mit Unsicherheiten behaftet. Zur Minimierung dieser Unsicherheiten in der Vorhersage der Antwort einer Konstruktion auf eine bestimmte Belastung ist es heute üblich, numerische Modelle und ihre Parameter durch einen Abgleich mit dem am bestehenden Bauwerk beobachteten Verhalten zu verbessern bzw. zu kalibrieren.

Die dafür erforderliche Ermittlung des Trag- und Antwortverhaltens einer bestehenden Konstruktion erfordert stets experimentelle Untersuchungen. Im Fall der Betrachtung des Verhaltens eines Bauwerks unter einer dynamischen Einwirkung sollten die entsprechenden Versuche auch auf die Identifikation des dynamischen Strukturverhaltens, das durch die modalen Parameter des Systems bestimmt ist, gerichtet sein. Durch die eingangs erläuterten und verwandte Fragestellungen motiviert sind seit den 1980er Jahren verschiedene Methoden zur experimentellen Identifikation modaler Parameter entwickelt worden.

Im Unterschied zu den Disziplinen des Fahrzeugbaus, des allgemeinen Maschinenbaus sowie der Luft- und Raumfahrttechnik bestehen im Bauingenieurwesen erhebliche technische Einschränkungen sowohl bezüglich der Instrumentierbarkeit der zu untersuchenden Struktur als auch hinsichtlich der Möglichkeit einer kontrollierten und erfassbaren dynamischen Anregung. Vor diesem Hintergrund wurden in den letzten Jahren mehrere Algorithmen entwickelt, die eine Identifikation von modalen Parametern ausschließlich aus gemessenen Strukturantworten infolge einer ambienten Anregung erlauben. Diese Methoden zur Identifikation modaler Parameter aus Betriebsschwingungszuständen werden im Englischen als *output-only* oder *operational modal analysis* bezeichnet. Eine entsprechende deutsche Bezeichnung hat sich in Fachkreisen noch nicht etabliert, weshalb hier auch der englische Begriff der *operational modal analysis* (OMA) beibehalten wird.

Da die Disziplin der Modalanalyse und somit auch die OMA sehr häufig an der Schnittstelle zwischen der numerischen Modellierung und Simulation einerseits und dem dynamischen Strukturverhalten einer bestehenden Konstruktion andererseits steht, verbinden die Algorithmen der Modalanalyse auch die Modelle der Strukturdynamik mit mathematischen Werkzeugen, die vorwiegend in der Signalanalyse angewendet werden. Aus diesem Grund sind in der Arbeit nach einer Einführung in die Thematik zunächst einige theoretische Grundlagen zusammengestellt.

Seit den 1990er Jahren wurden verschiedene OMA-Methoden entwickelt. Die meisten dieser Methoden basieren auf Ansätzen, die schon vorher im Rahmen der experimentellen Modalanalyse, sowohl gemessene Antwort- als auch Anregungssignale voraussetzend, etabliert waren. Die am häufigsten angewendeten Algorithmen der OMA werden in dieser Arbeit beschrieben. Ihre Anwendung wird anhand eines übersichtlichen numerischen Beispiels und der in einem Laborversuch gewonnenen Messdaten veranschaulicht.

Experimentell erzielte Ergebnisse unterliegen stets zahlreichen Einflüssen, weshalb die Einschätzung der Ergebnisqualität eine sehr sorgfältige Datenanalyse erfordert. Für die Qualitätsbewertung werden nicht nur geeignete Indikatoren benötigt, die Analysen schließen auch die Quantifizierung von Unsicherheiten ein.

Eine Besonderheit von Versuchen zur modalen Identifikation besteht darin, dass man häufig die zu untersuchende Struktur in mehreren Sensorkonfigurationen instrumentiert. Diese Vorgehensweise erlaubt eine höhere räumliche Auflösung der identifizierten Eigenschwingformen bei begrenzter Verfügbarkeit von Sensoren bzw. Messkanälen. Die nur einzelne Freiheitsgrade umfassenden Komponenten der Eigenschwingformen, die sich für die jeweiligen Sensorkonfigurationen identifizieren lassen, müssen im Nachhinein zusammengeführt werden. Verschiedene Algorithmen für diese Aufgabe werden ebenfalls vorgestellt.

Da bei der Aufzeichnung von dynamischen Strukturantworten sehr schnell relativ große Datenmengen entstehen, kann eine interaktive Datenanalyse sehr aufwendig oder sogar unmöglich werden. Dies trifft vor allem auf eine kontinuierliche Langzeitüberwachung von Bauwerken zu. In solchen Situationen ist die Automatisierung der modalen Identifikation und der nachgelagerten Datenbearbeitung unerlässlich für eine praktische Anwendung. Aus diesem Grund ist ein Abschnitt der Arbeit dieser Thematik gewidmet.

Abgesehen von den bereits erwähnten Besonderheiten der im Bauingenieurwesen betrachteten Konstruktionen hinsichtlich ihrer Dimension, Ortsgebundenheit und begrenzten Zugänglichkeit einzelner Bereiche, unterscheiden sich Bauwerke von in anderen Industriezweigen hergestellten Serienprodukten durch ihre Einmaligkeit. Jedes Bauwerk ist ein Unikat, auch wenn es teilweise konstruktive Gemeinsamkeiten mit anderen Bauwerken geben kann. In einem Kapitel der Arbeit werden ausgewählte Aspekte besprochen, die bei bestimmten praktischen Anwendungen der OMA von Bedeutung sein können. So werden Fallstudien vorgestellt, in denen die Strukturen Eigenschwingungen mit sehr dicht beieinander liegenden Frequenzen aufweisen oder Einschränkungen hinsichtlich der Instrumentierbarkeit bestanden. Darüber hinaus werden mehrere Methoden zur modalen Identifikation in ihrer Anwendung auf ein baupraktisches Beispiel miteinander verglichen. In diesem Zusammenhang wurde besonderes Augenmerk auf verschiedenartige Unsicherheiten, die in den unterschiedlichen Schritten einer OMA auftreten können, gelegt. In der Literatur werden in der Regel nur ausgewählte Aspekte, die jeweils die Unsicherheiten in bestimmten Analyseschritten betreffen, angesprochen. Hier wurde die Thematik der Unsicherheiten in den einzelnen Analyseschritten in einem weiteren Sinne behandelt und Ansätze vorgestellt, wie mit entsprechenden Problemen umgegangen werden kann.

Abschließend kann festgestellt werden, dass sowohl die Algorithmen der OMA als auch die für die praktische Anwendung erforderliche Technik bereits sehr ausgereift sind. Wie in jeder Fachdisziplin, die mit experimentellem Arbeiten verbunden ist, verbleiben in den Ergebnissen einer OMA stets Unsicherheiten. Aus dieser Schlussfolgerung leitet sich der Bedarf für weiterführende Forschungs- und Entwicklungsarbeiten ab, die darauf gerichtet sind, diese Unsicherheiten zu minimieren und die Analyseschritte mit ihren zugehörigen Parametern dahingehend zu optimieren.

Summary

In recent years the demand on dynamic analyses of existing structures in civil engineering has remarkably increased. These analyses are mainly based on numerical models. Accordingly, the generated results depend on the quality of the used models. Therefore it is very important that the models describe the considered systems such that the behaviour of the physical structure is realistically represented. As any model is based on assumptions, there is always a certain degree of uncertainty present in the results of a simulation based on the respective numerical model. To minimise these uncertainties in the prediction of the response of a structure to a certain loading, it has become common practice to update or calibrate the parameters of a numerical model based on observations of the structural behaviour of the respective existing system.

The determination of the behaviour of an existing structure requires experimental investigations. If the numerical analyses concern the dynamic response of a structure it is sensible to direct the experimental investigations towards the identification of the dynamic structural behaviour which is determined by the modal parameters of the system. In consequence, several methods for the experimental identification of modal parameters have been developed since the 1980ies.

Due to various technical restraints in civil engineering which limit the possibilities to excitate a structure with economically reasonable effort, several methods have been developed that allow a modal identification form tests with an ambient excitation. The approach of identifying modal parameters only from measurements of the structural response without precise knowledge of the excitation is known as output-only or operational modal analysis.

Since operational modal analysis (OMA) can be considered as a link between numerical modelling and simulation on the one hand and the dynamic behaviour of an existing structure on the other hand, the respective algorithms connect both the concepts of structural dynamics and mathematical tools applied within the processing of experimental data. Accordingly, the related theoretical topics are revised after an introduction into the topic.

Several OMA methods have been developed over the last decades. The most established algorithms are presented here and their application is illustrated by means of both a small numerical and an experimental example. Since experimentally obtained results always underly manifold influences, an appropriate postprocessing of the results is necessary for a respective quality assessment. This quality assessment does not only require respective indicators but should also include the quantification of uncertainties.

One special feature in modal testing is that it is common to instrument the structure in different sensor setups to improve the spacial resolution of identified mode shapes. The modal information identified from tests in several setups needs to be merged a posteriori. Algorithms

to cope with this problem are also presented.

Due to the fact that the amount of data generated in modal tests can become very large, manual processing can become extremely expensive or even impossible, for example in the case of a long-term continuous structural monitoring. In these situations an automated analysis and postprocessing are essential. Descriptions of respective methodologies are therefore also included in this work.

Every structural system in civil engineering is unique and so also every identification of modal parameters has its specific challenges. Some aspects that can be faced in practical applications of operational modal analysis are presented and discussed in a chapter that is dedicated specific problems that an analyst may have to overcome. Case studies of systems with very close modes, with limited accessibility as well as the application of different OMA methods are described and discussed. In this context the focus is put on several types of uncertainty that may occur in the multiple stages of an operational modal analysis. In literature only very specific uncertainties at certain stages of the analysis are addressed. Here, the topic of uncertainties has been considered in a broader sense and approaches for treating respective problems are suggested.

Eventually, it is concluded that the methodologies of operatinal modal analysis and related technical solutions have been well-engineered already. However, as in any discipline that includes experiments, a certain degree of uncertainty always remains in the results. From these conclusions has been derived a demand for further research and development that should be directed towards the minimisation of these uncertainties and to a respective optimisation of the steps and corresponding parameters included in an operational modal analysis.

Contents

List of Figures

List of Tables

List of abbreviations

AR	auto-regressive
ARMA	auto-regressive moving average
ARMAV	auto-regressive moving average vector
CMIF	complex mode identification function
COV	coefficient of variation
DFT	discrete Fourier transformation, discrete Fourier transform
DOF	degree-of-freedom
EFDD	enhanced frequency domain decomposion
EMA	experimental modal analysis
FDD	frequency domain decomposion
FFT	fast Fourier transformation, fast Fourier transform
FRF	frequency response function
FSDD	frequency-spacial domain decomposition
IRF	impulse response function
ITD	Ibrahim time-domain
LMFD	left matrix fraction description
LSCE	least square complex exponential
LSCF	least-squares complex frequency
LSFD	least-squares frequency domain
MA	moving average
MAC	modal assurance criterion
MCF	modal complexity factor
MDOF	multi-degree-of-freedom
MEL	mode energy level
MFD	matrix fraction description
MP	mean phase
MPC	modal phase collinearity
MPD	mean phase deviation
MSI	modal similarity index
MTN	modal transfer norm
NExT	natural excitation technique
ODS	operational deflection shape
OMA	operational modal analysis

OMAX	operational modal analysis in presence of exogenous inputs
PEM	prediction-error identification method
p-LSCE	poly-reference least square complex exponential
p-LSCF	poly-reference least-squares complex frequency
PSD	power spectral density
PoGER	post global estimation re-scaling
PoSER	post separate estimation re-scaling
PreGER	pre global estimation re-scaling
RDT	random decrement technique
RMFD	right matrix fraction description
SDOF	single-degree-of-freedom
SR	sampling rate
SSI	stochastic subspace identification
SSI-cov	covariance-driven stochastic subspace identification
SSI-cov/ref	reference-based covariance-driven stochastic subspace identification
SSI-data	data-driven stochastic subspace identification
SSI-data/ref	reference-based data-driven stochastic subspace identification
SVD	singular value decomposition

Notation and symbols

Roman letters

A	cross-sectional area
C	number of clusters in fuzzy C-means clustering
C_{xx}, C_{yy}, C_{xy}	covariance functions
E	Young's modulus
$F(t)$	exciting force as function of time
$F(s)$	Laplace transform of the exciting force
$F(\omega)$	Fourier transform of the exciting force $f(t)$
$\mathcal{F}$	Fourier operator
$G(s)$	Laplace transform of a function $g(t)$
$G(\omega)$	Fourier transform of a function $g(t)$
$G_{XX}(\omega)$, $G_{YY}(\omega)$, $G_{XY}(\omega)$	one-sided spectral densities of $x_i(t)$ and $y_i(t)$
$H(s)$	transfer function
$H(\omega)$	Frequency response function
$H_1(\omega H_2(\omega)$, $H_3(\omega)$	FRF estimators
I	impulse, cross-sectional moment of inertia
K	number of clusters in K-means clustering
L	number of rows in a block row
$\mathcal{L}$	Laplace operator
N	number of degrees-of-freedom
Q	Fourier transform of $q(t)$
R_{xx}, R_{yy}, R_{xy}	correlation functions
Re[], Im[]	real, imaginary part of a complex quantity
$S_{FF}(\omega)$, $S_{YY}(\omega)$	power spectral densities of $f(t)$ and $y(t)$
$S_{FY}(\omega)$, $S_{YF}(\omega)$	cross-spectral densities of $f(t)$ and $y(t)$
$S^{+}_{XX}(\omega)$, $S^{+}_{YY}(\omega)$, $S^{+}_{XY}(\omega)$	half spectra or positive cross- or power spectra
T	maximal number of iterations in fuzzy C-means clustering
U	Fourier transform of $u(t)$
$Y(\omega)$	Fourier transform of $y(t)$
$\mathcal{Z}$	operator of the z-transform

c_i	discrete viscous damping parameter
$\tilde{d}$	threshold
d_{ik}, d_{ik}^2	distance function or measure
$d(f_0)$	modal coherence
$\mathrm{d}f$, $\mathrm{d}\zeta$	tolerance values
$d(s)$	denominator polynomial in Laplace domain
f	frequency
f_r	natural frequency of mode r
f_γ	scalar coefficient to form the correction vector $\{\epsilon\}$
$h(t)$	impulse response function
i	imaginary unit $\sqrt{-1}$
i, j, k	indices
j_b	length of a statistically independent block
k_i	discrete stiffness parameter
l	number of time lags
m_i	discrete mass parameter
m_r	modal mass corresponding with mode r
n	dimension of the state space model, model order
n_b	number of statistically independent blocks
n_d	number of data sets sorted by fuzzy C-means clustering
n_{exc}	uncorrelated noise in the Fourier transform of measured excitation
n_f	number of frequency samples
n_h	number of harmonic components
n_m	number of considered modes
n_o	number of measured output signals
n_{ob}	number of objects to be assigned to clusters
n_R	number of block rows
n_r	number of reference output signals
n_{ref}	number of reference sensors
n_{resp}	uncorrelated noise in the Fourier transform of measured response
n_{rov}	number of roving sensors
n_s	number of setups
n_u	number of (measured) input or excitation signals
p	polynomial order
p_D	denominator polynomial order
p_N	numerator polynomial order
r	index referring to mode r
s	Laplace variable, index referring to mode s
q_j, $\dot{q}_j$, $\ddot{q}_j$	displacement, velocity and acceleration of DOF j
$q_{m,r}$, $\dot{q}_{m,r}$, $\ddot{q}_{m,r}$	modal contributions of mode r to the displacements, velocities and accelerations, respectively

t	time
u_{ik}	value of a fuzzy clustering membership function
w_f, w_ζ, w_φ	weighting factors
$x_{m,r}(t)$	rth element of the modal state vector $\{x_m(t)\}$
y_i	response measured at DOF i
$\bar{y}_i$	time-shifted response measured at DOF i
z	transformation variable of the z transform

Greek letters

Δt	time increment
$\alpha(\omega)$	receptance function
α, β	coefficients used in the model of proportional damping
α_k	coefficient in the autocorrelation function of excitation $f_k(t)$
β_l	coefficient to be calculated within the p-LSCE algorithm
γ_2	kurtosis
$\gamma^2_{y_i y_j}(\omega)$	output coherence function
δ	Kronecker symbol
δ_e, δ_m	global contribution of the prediction errors and of the modal components to the total response
$\delta(\tau)$	Dirac delta function
ε	excess
ε_t	termination criterion in fuzzy C-means clustering
ζ_r	modal damping ratio of mode r
ζ_{Q_1}, ζ_{Q_3}	lower and upper quartile modal damping ratios
ζ_{IQR}	interquartile range of modal damping ratios
θ_r	phase angle of mode r
λ_r	rth eigenvalue of the MDOF system with viscous damping
μ_r	rth eigenvalue of the discrete-time state-space model
μ_x, μ_y	mena values of $\{x_i\}$ and $\{y_i\}$
ρ	density
ρ_{xy}	correlation coefficient
σ	standard deviation
σ^2	variance
τ	time variable, instant of time of excitation impact
ϕ_j	mass-normalised modal amplitude of DOF j
ψ_j	arbitrarily scaled modal amplitude of DOF j
ω	circular frequency
ω_r	natural circular frequency of mode r
ω_l, ω_u	lower and upper frequency bound

Mathematical notation and symbols

$\otimes$	Kronecker product
$\cdot^*$	complex conjugate
$[\cdot]$	matrix
$\{\cdot\}$	vector
$\langle\cdot\rangle$	row vector
$[\cdot]^{-1}$	inverse matrix
$[\cdot]^{\dagger}$	More-Penrose pseudoinverse matrix
$[\cdot]^H$, $\{\cdot\}^H$	Hermetian or complex conjugate transpose of a matrix / vector
$[\cdot]^T$, $\{\cdot\}^T$	transpose of a matrix / vector
$\mathrm{cov}(\cdot)$	covariance
$diag\,[\cdot]$	diagonal matrix
$\mathbf{E}\,[\cdot]$	expected value
$\Delta\,[\cdot]$	perturbation of matrix $[\cdot]$
$[A]\,/\,[\mathbf{B}]$	orthogonal projection of the row space of a matrix $[A]$ onto the row space of a matrix $[B]$

Matrices

$[A]$	dicrete-time state-feedback matrix
$[\mathcal{A}]$	companion matrix
$[A_c]$	continuous-time state-feedback matrix
$[A_i]$	auto-regressive (AR) matrix coefficients
$[A^i]$	norm matrix
$diag[a_r]$	modal a matrix containing the inverse of the modal participation factors $\frac{1}{a_r}$
$[B]$	discrete-time state-input matrix
$[B_c]$	continuous-time state-input matrix
$diag[b_r]$	modal b matrix
$[B_2]$	input selection matrix
$[C]$	discrete-time state-output matrix
$[C_a]$	acceleration selection matrix
$[C_c]$	continuous-time state-output matrix
$[C_d]$	displacement selection matrix
$[C_i]$	moving average (MA) matrix coefficients
$[C_v]$	velocity selection matrix
$[C_2]$	viscous damping matrix in physical coordinates
$[D]$	discrete-time transmission matrix
$[D_c]$	continuous-time transmission matrix

$[D_L]$	matrix containing the denominator matrix coefficients of an LMFD
$[D_R]$	matrix containing the denominator matrix coefficients of an RMFD
$\left[\mathcal{E}_{l,m}^{a,b}\right]$	extraction matrix of dimension $a \times b$ that is zero apart from element (l, m) which is 1
$[G]$	next-state output covariance matrix
$[G_m]$	next modal state – output covariance or stochastic modal participation matrix
$[H(s)]$	transfer function matrix
$[\mathcal{H}]$	subspace matrix
$[I]$	identity matrix
$[J]$	sensitivity matrix
$[K]$	stiffness matrix in physical coordinates
$[\mathcal{K}]$	steady-state Kalman gain
$[L]^T$	modal input matrix of the discrete-time state-space model
$[L_c]^T$	modal input matrix of the continuous-time state-space model
$[LR]$	lower residuals
$[M]$	mass or inertia matrix in physical coordinates
$[N(s)]$	numerator matrix in Laplace domain
$[N_L]$	matrix containing the numerator matrix coefficients of an LMFD
$[N_R]$	matrix containing the numerator matrix coefficients of an RMFD
$[O_i]$	extended observability matrix
$[O_n]$	observability matrix
$[\mathcal{O}_i]$	obligue projection of the row space of a matrix $[Y_f]$ onto the joint row space of matrices $[U_p]$ and $\left[Y_p^{ref}\right]$
$[\mathcal{P}_{a,b}]$	permutation matrix
$[P_s]$, $[Q_s]$	matrices of the state space formulation obtained by extending the system of equations of motion
$[\mathcal{P}_i]$	orthogonal projection of the row space of a matrix $[Y_f]$ onto the row space of a matrix $[Y_p]$
$[Q]$, $[R]$	result matrices of a QR matrix decomposition
$[Q]$	upper left sub-matrix of the noise covariance matrix
$[R]$	lower right sub-matrix of the noise covariance matrix
$[R_i]$	discrete-time output covariance matrix
$[S]$	upper right sub-matrix of the noise covariance matrix
$[S]^T$	lower left sub-matrix of the noise covariance matrix
$[S_1]$	diagonal matrix with non-zero singular values
$[\mathcal{S}]$	selection matrix
$[T]$	transformation matrix
$\left[T_{1\|i}\right]$	block Toeplitz matrix

$[U_1]$, $[V_1]$	atrices containing the left and right singular vectors corresponding to non-zero singular values
$[U_i]$	fuzzy partition matrix
$[UR]$	upper residuals
$[V]$	modal output matrix of the discrete-time state-space model
$[V_c]$	modal output matrix of the continuous-time state-space model
$[V_i]$	matrix with cluster prototypes in fuzzy C-means clustering
$[\mathcal{V}]$, $[\mathcal{W}]$, $[\mathcal{Y}]$	Vandermonde matrices
$[W_1]$, $[W_2]$	weighting matrices
$[X]$	matrix containing data sets to be assigned to clusters
$\left[\hat{X}_i\right]$	Kalman filter state sequence
$[y]$	matrix of measured response
$[\bar{y}]$	matrix of time-shifted measured response
$\left[Y_{0\|2i-1}\right]$	output block Hankel matrix
$[Y_f]$	lower (“future”) part of the block Hankel matrix $\left[Y_{0\|2i-1}\right]$
$[Y_p]$	upper (“past”) part of the block Hankel matrix $\left[Y_{0\|2i-1}\right]$
$\left[Y_{i\|i}\right]$	ith block row of the block Hankel matrix

$[\Gamma]$	lower triangular block Toeplitz matrix
$[\Gamma_i]$	reversed extended controllability matrix
$[\Theta]$	upper left sub-matrix of $[\Psi_c]$
$[\Theta^*]$	upper right sub-matrix of $[\Psi_c]$
$[\theta]$	matrix containing model parameters
$[\Lambda]$	upper left sub-matrix of $[\Lambda_c]$
$[\Lambda^*]$	lower right sub-matrix of $[\Lambda_c]$
$[\Lambda_c]$	diagonal matrix containing the eigenvalues of matrix $[A_c]$
$[\Lambda_d]$	diagonal matrix containing the eigenvalues of matrix $[A]$
$[\Pi_\bullet]$	projection matrix
$[\Sigma]$	stochastic state covariance matrix
$\left[\Sigma_{[A,B]}\right]$	covariance matrix between matrices $[A]$ and $[B]$
$[\Phi]$	mass-normalised modal matrix
$[\Psi]$	modal matrix
$[\Psi_c]$	matrix containing the eigenvectors of matrix $[A_c]$
$[\Psi_2]$	matrix containing the eigenvectors of the companion matrix $[\mathcal{A}]$
$[\rho_v]$, $[\rho_w]$	Kalman filter residuals

Vectors

$\{e(t_k)\}$	innovation
$\{F(t)\}$	vector of excitation in physical coordinates

$\{F_m(t)\}$	vector of excitation in modal coordinates
$\{g_r\}$	operational reference factors
$\{l_{c_r}\}^T$	rth row of matrix $[L_c]^T$
$\{l_r\}$	modal participation factors
$\{q(t)\}$, $\{\dot{q}(t)\}$, $\{\ddot{q}(t)\}$	vectors of displacements, velocities and accelerations in physical coordinates
$\{q_m(t)\}$, $\{\dot{q}_m(t)\}$, $\{\ddot{q}_m(t)\}$	vectors of displacements, velocities and accelerations in modal coordinates
$\{u(t)\}$	input vector
$\{v\}$	measurment or output noise vector
$\{v_i\}$	vector of cluster prototypes in fuzzy C-means clustering
$\{v_{c_r}\}$	rth column of matrix $[V_c]$
$\{V_k\}$, $\{W_k\}$	spectral vectors of the measurement and process noise at spectral line k
$\{w\}$	process noise vector
$\{x(t)\}$, $\{\dot{x}(t)\}$	state vector and its first derivative with respect to time
$\{x_m(t)\}$	modal state vector
$\{x_i\}$, $\{y_i\}$	random processes
$\{\hat{x}(t_k\|t_{k-1})\}$	optimal one-step-ahead predictor of the state vector
$\{X_k\}$, $\{Y_k\}$	spectral vectors of the state and output vectors at spectral line k
$\{y(t)\}$	observed response or output vector
$\{y_r(t)\}$	rth modal component of the output vector $\{y(t)\}$
$\{\hat{y}(t_k\|t_{k-1})\}$	one-step-ahead predictor of the measured response $\{y_k\}$
$\{z(t)\}$	arbitrary state vector vector

$\{\alpha_j\}$, $\langle\beta_{oj}\rangle$	polynomial coefficient vectors
$\{\beta\}$	vector of coefficients to be calculated within the p-LSCE algorithm
$\{\gamma\}$	arbitrary vector to form the correction vector $\{\epsilon\}$
$\{\varepsilon(t_k)\}$	state prediction error
$\{\epsilon\}$	correction vector
$\{\theta\}$	vector of model parameters
$\{\phi_r\}$	mass-normalised mode shape vector of mode r
$\{\psi_r\}$	arbitrarily scaled mode shape vector of mode r

Chapter 1

Introduction

1.1 General remarks

Structural analysis is one of the major steps not only in the design of new structures but also in context with maintenance and life cycle engineering. As computer technology and numerical algorithms for modelling and simulation are evolving rapidly, one could think that the need for experimental analyses should decrease. However, the contrary is to observe. Both the number and complexity of experiments in numerous fields are generally increasing. There are several reasons causing this development.

First of all, the technical progress leads to a steady improvement of experimental equipment that relies on powerful computer technology. This opens completely new possibilities both to control complex excitation and loading equipment and to measure physical quantities in an extent one could hardly imagine a few decades ago. At the same time, new technologies do not only facilitate experiments but reduce also the costs for experimental analyses.

Another aspect is that the quality of any result obtained from a numerical simulation strongly depends on the quality of the used models and the assumptions these models are based on. This means that there is still a certain degree of uncertainty in any numerical simulation. The reduction of such uncertainties opens a new field of tasks of experimental analyses, such as the determination of parameters required for numerical models as well as model verification and validation.

Accordingly, the development of numerical and experimental techniques techniques interact significantly nowadays. One example for such developments is also the field of structural dynamics. Computer technology enables engineers to perform complex numerical simulations, for example by means of finite element analyses, as well as to acquire measured data simultaneously from multiple sensors at high sampling rates and over almost arbitrarily long periods. Together with the continuous improvement of the hardware, also sophisticated algorithms for data processing have been developed and are constantly in advancement. In context with structural dynamics this applies to a large extent to methods that allow for the identification of modal parameters from data acquired during vibration tests.

Beside the classical forward engineering problems usually considered during a design process, the second group of engineering tasks comprising inverse problems has gained an increasing importance. This trend is not only fostered by the continuosly progressing technological and scientific developments but also by the growing demand on engineering achievement concerning existing structures.

In the field of structural dynamics, the forward problem usually starts with the creation of a numerical model that describes the considered system with its physical properties and load model representing an assumed time-variant excitation acting on the structure. As the dynamic behaviour of a structure is characterised by its modal parameters, i.e. its natural frequencies, mode shapes and modal damping ratios, it is common practice to compute the modal solutions for the numerical model. The results of this analysis provide a modal model of the structure which gives the engineer valuable information necessary to evaluate the strutural response predictions generated by a numerical simulation. Depending on the method applied to simulate the response of a structure to a given dynamic excitation, the modal model may also be required in these analyses. The coherences between the major steps of the solution of a typical forward problem in structural dynamics is illustrated in figure 1.1.

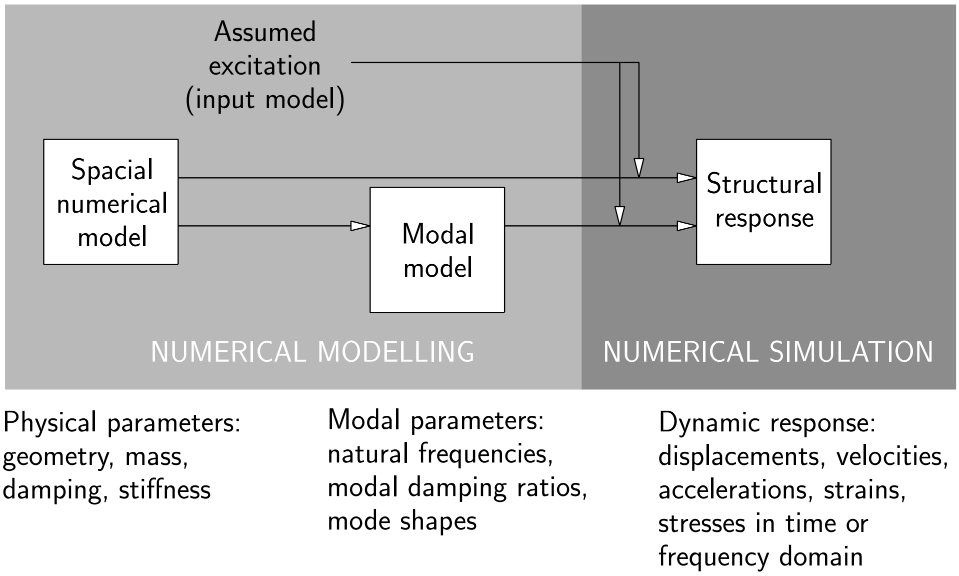

Figure 1.1: Schematic view of forward analyses in structural dynamics

As shown in figure 1.2, the starting point of a typical inverse analysis in structural dynamics are vibration tests. During the experiment the investigated structure, that can be either a physical model tested in the laboratory or an existing structure investigated by means of in-situ tests. Depending on the specific experimental procedure, the excitation may be known or unknown. In either case the structural response is measured by means of appropriate sensors. Typically, in vibration tests sensors for the measurement of either displacements, velocities, accelerations or strains are employed. Based on the measured time series, modal parameters of the structure can be identified. If an identification algorithm that works frequency domain is used, the time series needs to be transformed. This transformation is commonly performed by means of a fast Fourier transformation (FFT).

Several modal identification methods include the intermediate step of the identification of parameters of a system model that describes input-output relations as they are commonly used in control engineering. These methods are called *parametric modal identification methods*, while

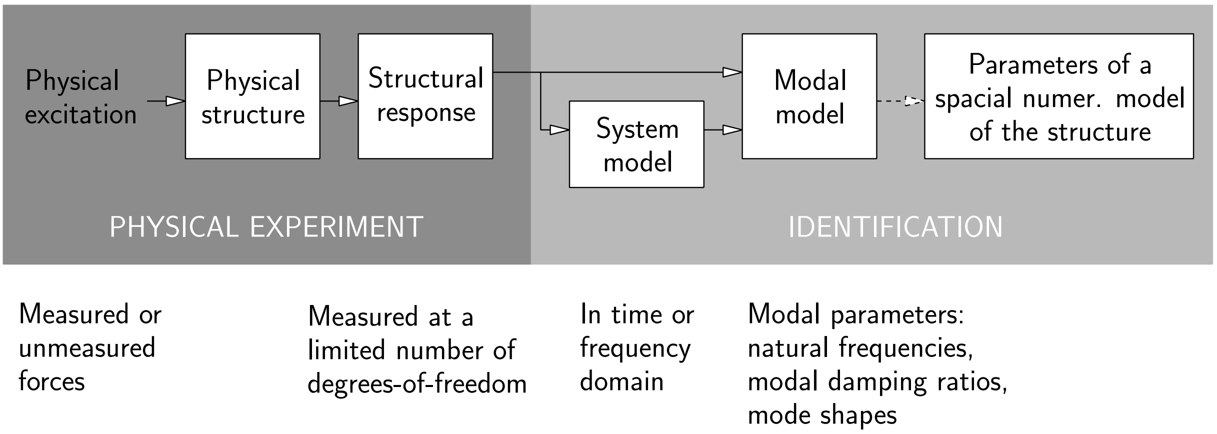

Figure 1.2: Schematic view of inverse analyses in structural dynamics

those algorithms which do not consider such a system model form the group of *non-parametric modal identification methods*. Depending on the specific objective of an engineering study, the identified modal parameters can be used, for example, to identify respective parameters for numerical models of the considered structure.

As becomes obvious from the diagrams in figures 1.1 and 1.2, the modal model occupies a central position between experimental and numerical analyses in structural dynamics. Paticularly, in the context with inverse problems, all activities from vibration tests to the identification of modal parameters form the engineering discipline which is called *modal analysis*. It combines all practical and scientific activities necessary to prepare and conduct the vibration tests, to acquire and process the experimental data and to interpret the results.

1.2 Experimental and operational modal analyses

1.2.1 Experimental modal analysis

In the classical approach of modal identification that is also called *experimental modal analysis* (EMA), both the excitation of the structure and the respective dynamic response of the system are measured. For this purpose, the structural system under investigation is subjected to a dynamic force that is commonly generated by means of shakers or impact hammers. During the test, the dynamic force that is transmitted onto the structure is measured by means of load cells.

This means that shakers need to be connected to the structure such that all force components generated by the shaker are travelling through load cells to the structure. Normally, a shaker can generate a unidirectional dynamic force in form of an inertia force originated by a mass that is driven either electro-dynamically or servo-hydraulically. Examples for shakers of different sizes that were designed for the investigation of different kinds of structures are shown in figure 1.3.

A second form of excitation frequently used for modal testing is an impulse excitation. The required technical effort is much lower than for the application of a controlled continuous force.

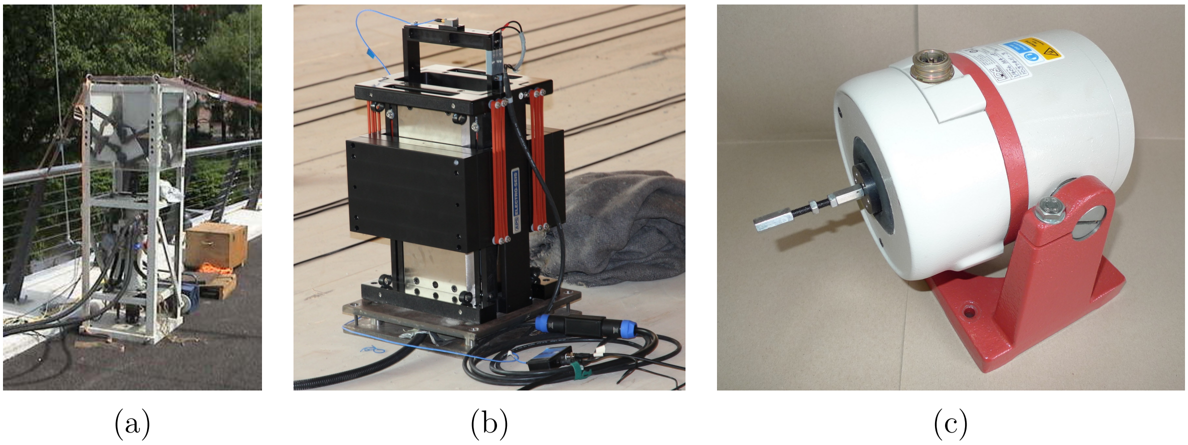
(a) (b) (c)

Figure 1.3: Examples for shaker types: (a) servo-hydraulic shaker for structures such as bridges, (b): electrodynamic shaker for structures such as floors, (c) electrodynamic shaker for laboratory models

Only a hammer and an appropriate load cell are needed. Most commonly, so-called *modal hammers* are used. These devices are special hammers with an integrated load cell built-in between the massive hammer head and an elastic hammer tip. One usually wants to identify only modes in a certain frequency range. Therefore, the energy of the excitation should also be concentrated in the respective frequency band. As the frequency content of an impulse force is related to its duration which depends on the stiffness of the hammer tip, modal hammers are usually provided with different hammer tips that can be exchanged. Figure 1.4 shows modal hammers of different size which should be selected depending on the dimension of the system to be analysed. For the excitation of larger structures such as, for example, bridge decks, a so-called *drop-weight system* as shown in figure 1.5 can be used.

Figure 1.4: Examples for modal hammers with integrated load cell and a variety of hammer tips that can be used for the modal analysis of structures of different kind and dimension

Figure 1.5: Drop-weight system to generate an impulsive excitation on structures such as bridge decks

Depending on the number of degrees-of-freedom at which the structure is excited and the response is measured simultaneously, one distiguises between tests with

- single input – single output (SISO),
- single input – multiple outputs (SIMO),
- multiple inputs – single output (MISO) and
- multiple inputs – multiple outputs (MIMO).

Related to the kind of test, respective algorithms have been developed for modal identification. Depending whether the data is analysed in time or frequency domain, these methods are based on the consideration of either impulse response functions (IRF) or frequency response functions (FRF), respectively.

Experimental modal analysis (EMA), this means modal testing with known excitation, has the following advantages:

- the system input is fully controlled and can be selected as required,
- the signal-to-noise ratio can be controlled to reduce the uncertainties in the identification and

- it is possible to identify mass-normalized mode shapes which is beneficial especially if the results are used for model calibration or validation.

On the other hand, EMA tests

- require a controlled environment and should preferably be performed in the laboratory, where the boundary conditions are not necessarily the same as under operational conditions which can be both beneficial or disadvantageous,
- require appropriate experimental equipment to excite the structure and
- do in many cases not allow for the analysis of a structure under operational conditions which may require the interruption of manufacturing processes or traffic in case that systems that cannot be tested in the laboratory are considered.

1.2.2 Operational modal analysis

In various cases it is hardly possible to perform an EMA test. For example, the excitation of structures such as buildings, bridges or other infrastructure structures requires devices that can generate sufficiently strong dynamic forces and their installation on site. Even if such equipment is available, the fundamental assumption that the structure is solely excited by the system used can also not be always satisfied due to other excitation forces such as wind or nearby traffic. Another group of tests where classical EMA tests can hardly be performed is in-flight testing of airplanes or spacecrafts.

The limitations associated with EMA testing gave reason for the development of modal identification algorithms that require only the measurement of the dynamic structural response. This group of methods is called *operational modal analysis* (OMA). Sometimes also the term *output-only modal analysis* is used, but over the last years, the term *operational modal analysis* has been more established.

Many of the OMA algorithms were derived based on previously developed EMA algorithms assuming certain properties of the unknown input. In the theoretical derivations of OMA algorithms an excitation by Gaussian white noise forces is assumed. However, even if this idealized assumption cannot be completely satisfied in practical applications, experience has shown that very good results can be achieved with an excitation from usually available ambient sources. Nevertheless, some limitations have to be made. For example, in case of the presence of forced vibration components in the measured signals that were caused by excitation sources such as rotating machinery that generates distinct harmonic components, caution needs to be taken.

Further limitations arising from the non-availability of the system input are that

- it is generally not possible to identify mass-normalised mode shapes and
- that frequency response or impulse response functions that are utilised in some model calibration and validation methods cannot be derived from the measured data.

However, in many practical cases the advantages of OMA do not only facilitate modal identification. There are also situations in which a modal identification without OMA techniques would be more or less almost impossible.

Apart from the afore mentioned classifications of modal identification methods with respect to the number of used input and output signals and whether the data is analysed in either frequency or time domain, one distiguishes between *parametric* and *non-parametric* methods. In parametric methods, in a first step the parameters of a mathematical model describing the observed process or system are identified. This step is also referred to *system identification*. From this identified mathematical model are then the modal parameters derived in a second step. Parametric methods are normally computational more demanding than non-parametric methods which do not require the intermediate step of identifying the parameters of a system model. Therefore, non-parametric methods are usually faster and very well suited for a quick assessment of measured data, for example on site [116].

1.3 Motivation and structure of this work

1.3.1 Motivation

Several doctoral theses such as [4], [106], [141], [104], [33], [120] and [91] have been published in recent years. They all contain, at least to some extent, a review of several operational modal analysis techniques and focus on specific aspects. Furthermore, two textbooks on operational modal analysis were recently published, [116] and [27]. Especially in these two textbooks, the authors describe the theoretical background of operational modal analysis, several algorithms and specific aspects of the authors' experience in practical applications.

With the availability of several software packages, operational modal analysis has been facilitated significantly such that it is applied by many users nowadays. However, as has also been mentioned in some publications, for example [29] and [116], there are several factors in the application of the complex algorithms that can influence the results of an operational modal analysis considerably. If a user of any modal analsysis software is not aware of this problem the results may have a higher degree of uncertainty or a large bias. As will be shown later, this strikes primarily the identified modal damping ratios rather than, for example, the natural frequencies. Especially if the identification of modal damping ratios may be a key objective of a study, this aspect deserves attention.

Therefore, these aspects are specifically addressed in the present work. It will be illustrated in several examples how the choice of some controlling parameters may affect the quality of the results.

In this context, also, several steps in postprocessing are described and discussed by means of practical examples. Further, the performance of different OMA methods is compared for case studies.

1.3.2 Organisation of this work

In chapter 2, the theoretical background of experimental and operational modal analyses are briefly described. Starting from the equations of motion which describe the equilibrium of a moving mechanical system at any time instant, the model of modes is explained. This leads to frequency response and impulse response functions that describe the dynamic behaviour of a structure in time and frequency domain, respectively. Since several modal identification methods are based on state space models, the corresponding theory is also described. As Signal processing is an important part in experimental and operational modal analyses, the most important methods in this context are also explained in brief for the sake of better understanding of following derivations.

Several OMA algorithms that can be considered as most established are explained in chapter 3. Both methods that use the measured data in time and frequency domain are considered. Several of the described algorithms that can also be considered as the most widely used methods were numerically implemented using the programming environment *python*. Both, parts of the theoretical background and the application of the implemented OMA algorithms are demonstrated in chapters 2 and 3 by means of numerical simulations for a two-degree-of-freedom system that is introduced at the beginning of chapter 2. Additionally, the application of the implemented OMA techniques is demonstrated at a practical example. Chapter 4 is dedicated to various issues related to postprocessing in modal identification. Without appropriate tools and algorithms which not only facilitate OMA but also provide essential prerequisits for the understanding and interpretation of the identification results, it would be impossible to relate the mathematical solutions with a physical meaning. Another aspect of postprocessing which is also of great importance is the assessment of the performed analysis with respect to confidence or uncertainty.

Even if effecient numerical tools for postprocessing of the identification results of a single test series are available, there are still situations in which, for example, the number of tests may make a manual inspection of the results simply impossible. A very typical example for such a situation is a continuous monitoring of a structure. Some methodologies for automated modal selection and automated mode tracking are therefore presented in chapter 5.

To illustrate how the techniques of OMA can be applied to practical engineering problems, some examples are given in chapter 6. For each of the case studies specific aspects related to situations that may occur in practical applications are discussed. All of the addressed issues have in common that they are related to some kind of uncertainty one may face performing an operational modal analysis.

Chapter 2

Theoretical models in structural dynamics

As pointed out in section 1.1, modal analysis can be considered as a core discipline within the field of structural dynamics. All modal identification algorithms have been derived from the theoretical descriptions used to describe the relations between an excitation applied to a structure and its response at certain degrees-of-freedom (DOF). The theoretical background of structural dynamics has been extensively described in numerous textbooks such as [36], [34], [85] and [111]. Some topics that are of great importance for modal analysis are briefly described in this chapter.

Another discipline that is essential in modal analysis is signal processing. In fact signal processing provides most of the tools needed to identify modal parameters from measured data. Therefore, also some theory that is applied within several modal identification algorithms is also provided in this chapter.

2.1 Equation of motion

In structural dynamics, the equilibrium between external, time varying loads and internal restoring, inertia and damping forces is considered. In many cases, and also throughout this book, it is assumed that the structural system to be analysed shows linear elastic material behaviour and does not change its parameters during the observation time. This means, the theory and algorithms presented in the following are based on the assumption that the considered system is *linear* and *time-invariant*.

Unless special damping devices such as friction dampers are part of the system to be analysed, it has become common practice to assume viscous damping behaviour for most structures. This applies especially to civil engineering, but also to many fields in mechanical engineering. Accordingly, one of the simplest multi-degree-of-freedom (MDOF) systems one can design based on these assumptions is sketched in figure 2.1. It will serve throughout this and the following chapter to illustrate exemplarily the presented theory and application of algorithms.

This system consists of two masses, m_1, m_2, which are coupled by two springs with stiffnesses k_1, k_2 and two viscous dampers with damping constants c_1, c_2. Furthermore, the system can be excited by dynamic forces, F_1, F_2, which act in the direction of the two degrees of freedom (DOF) q_1 and q_2.

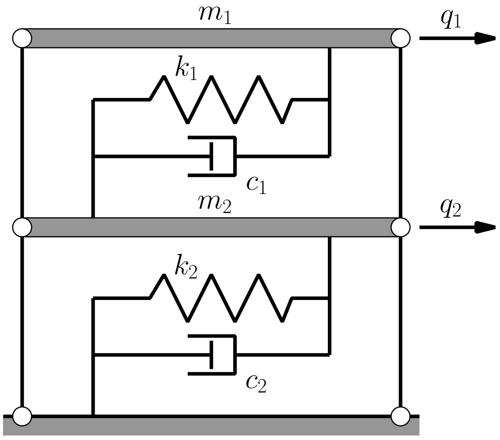

Figure 2.1: Two-degree-of-freedom system

Both, external and internal forces acting on the two masses have to form equlibrium at any state of motion. Accordingly, one can formulate a set of equilibrium equations for any such state based on d'Alambert's priciple and the force components illustrated in figure 2.2:

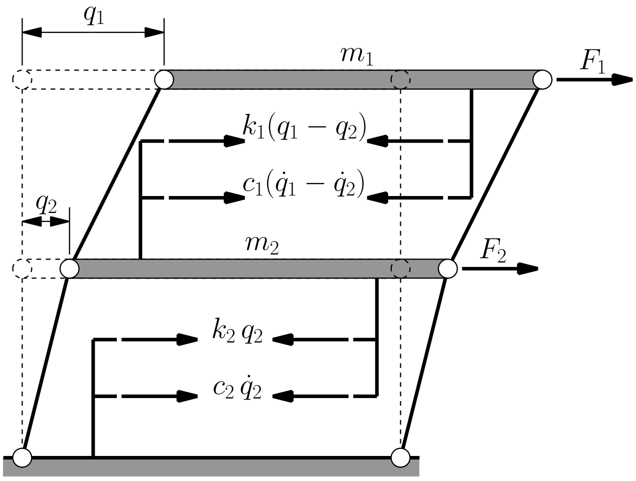

Figure 2.2: Forces acting on the moving two-degree-of-freedom system

$$\begin{bmatrix} m_1 & 0 \\ 0 & m_2 \end{bmatrix} \begin{Bmatrix} \ddot{q}_1 \\ \ddot{q}_2 \end{Bmatrix} + \begin{bmatrix} c_1 & -c_1 \\ -c_1 & c_1+c_2 \end{bmatrix} \begin{Bmatrix} \dot{q}_1 \\ \dot{q}_2 \end{Bmatrix} + \begin{bmatrix} k_1 & -k_1 \\ -k_1 & k_1+k_2 \end{bmatrix} \begin{Bmatrix} q_1 \\ q_2 \end{Bmatrix} = \begin{Bmatrix} F_1 \\ F_2 \end{Bmatrix} \tag{2.1}$$

or more generally

$$[M]_{N\times N}\,\{\ddot{q}(t)\}_N + [C_2]_{N\times N}\,\{\dot{q}(t)\}_N + [K]_{N\times N}\,\{q(t)\}_N = \{f(t)\}_N \tag{2.2}$$

where $[M]$, $[C_2]$ and $[K]$ refer to the mass or inertia, viscous damping and stiffness matrices, respectively. The subscript "2" is used here for the notation of the damping matrix to prevent confusion in later sections. The vectors $\{q(t)\}$, $\{\dot{q}(t)\}$ and $\{\ddot{q}(t)\}$ contain the displacements and their first and second derivatives with respect to time, meaning the velocities and accelerations at a certain instant of time t, while the vector $\{F(t)\}$ describes the external forces. These relations form a system of second order differential equations of dimension N, the number of degrees of freedom, which is, together with the initial conditions $\{q_0\}$, $\{\dot{q}_0\}$ and $\{\ddot{q}_0\}$, called *equation of motion*.

The structural systems considered in both mechanical and civil engineering are in general far more complex than the system shown in figure 2.1. Therefore, the system matrices are usually generated by means of advanced techniques such as the finite element method.

2.2 Classical analytical modal analysis

In the case of a free vibration, which means that all external forces are zero, and neglecting damping, equation (2.2) becomes

$$[M]\,\{\ddot{q}(t)\} + [K]\,\{q(t)\} = \{0\} \tag{2.3}$$

For the two-degree-of-freedom system in figure 2.1, the lines of the respective system of equations are then

$$\begin{aligned} m_1\,\ddot{q}_1 + k_{11}\,q_1 + k_{12}\,q_2 &= 0 \\ m_2\,\ddot{q}_2 + k_{21}\,q_1 + k_{22}\,q_2 &= 0 \end{aligned}$$

Using the ansatz

$$\begin{aligned} q_j &= \psi_j \sin\omega t \quad (j = 1,\,2,\,\ldots,\,N) \\ \ddot{q}_j &= -\omega^2\,\psi_j \sin\omega t \end{aligned}$$

one obtains

$$\begin{aligned} \Big[(-m_1\,\omega^2 + k_{11})\,\psi_1 + k_{12}\,\psi_2\Big] \sin\omega t &= 0 \\ \Big[k_{21}\,\psi_1 + (-m_2\,\omega^2 + k_{22})\,\psi_2\Big] \sin\omega t &= 0 \end{aligned}$$

Since these equations have to be satisfied at any instance t they can be reduced to

$$\begin{bmatrix} (k_{11} - m_1\,\omega^2) & k_{12} \\ k_{21} & (k_{22} - m_2\,\omega^2) \end{bmatrix} \begin{Bmatrix} \psi_1 \\ \psi_2 \end{Bmatrix} = \begin{Bmatrix} 0 \\ 0 \end{Bmatrix}$$

or

$$\Big([K] - \omega^2\,[M]\Big)\,\{\psi\} = \{0\} \tag{2.4}$$

which describes the eigenvalue problem of an undamped multi-degree-of-freedom system. The N solutions of equation (2.4), the *natural circular frequencies* ω_r and the eigenvectors $\{\psi_r\}$, are obtained by solving

$$\det\Big([K] - \omega^2\,[M]\Big) = 0 \tag{2.5}$$

This is an algebraic equation of Nth order in ω^2 which has N roots ω_r^2. The eigenvectors $\{\psi_r\}$ describe a set of unscaled deflection shapes of the mechanical system and are therefore also called *mode shapes*. It is common to collect all mode shapes in a matrix $[\Psi]_{N\times N}$, the *modal matrix*. Accordingly, equation (2.4) can be re-written as

$$\Big([K] - diag\big[\omega_r^2\big]\,[M]\Big)\,[\Psi] = [0] \tag{2.6}$$

Example 2.1. *For the 2-DOF system in figure 2.1 the following parameters are assumed:*

$$\begin{aligned} k_1 &= 2\cdot 10^5\,\tfrac{N}{m} \qquad & m_1 &= 1000\,kg \\ k_2 &= 5\cdot 10^5\,\tfrac{N}{m} \qquad & m_2 &= 2000\,kg \end{aligned}$$

Accordingly, the stiffness and mass matrices are then

$$[K] = \begin{bmatrix} 2 & -2 \\ -2 & 7 \end{bmatrix} \times 10^5\,\frac{N}{m} \qquad [M] = \begin{bmatrix} 1 & 0 \\ 0 & 2 \end{bmatrix} \times 10^3\,kg$$

The solution of the eigenvalue problem (2.6) gives

$$\omega_1^2 = 114.922\,\tfrac{rad^2}{s^2}, \qquad \omega_2^2 = 435.078\,\tfrac{rad^2}{s^2}, \qquad [\Psi] = \begin{bmatrix} 1 & -0.851 \\ 0.425 & 1 \end{bmatrix}$$

The eigenvectors were scaled here such that the maximal value of each vector is 1. *From the eigenvalues ω_r^2 the natural frequencies can be deduced as*

$$f_1 = 1.706\,Hz \qquad f_2 = 3.320\,Hz$$

A visualisation of the mode shapes is given in figure 2.3

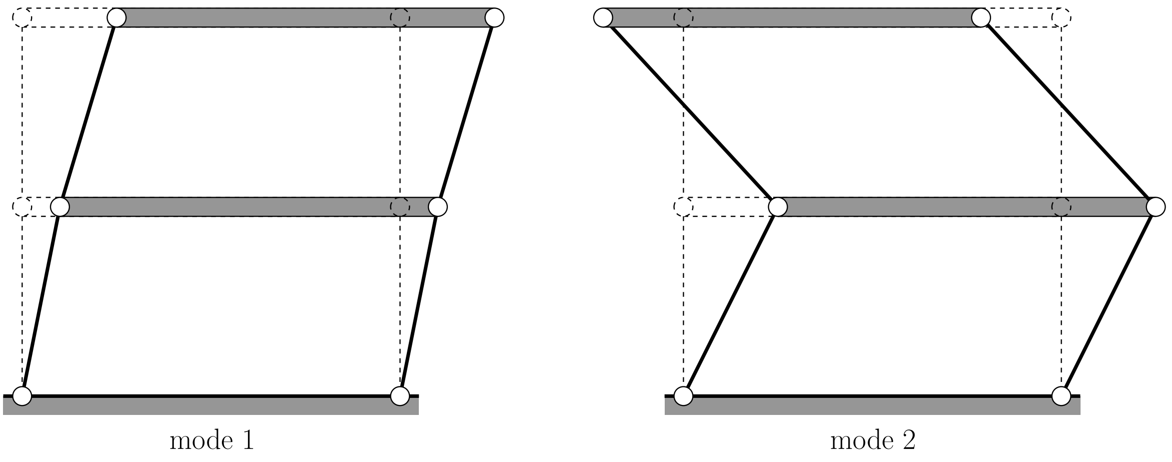

Figure 2.3: Calculated mode shapes of the two-degree-of-freedom system

2.3 Computation of dynamic response by modal superposition

2.3.1 Modal transformation

The displacements at any instant of time t can be described as a superposition of the mode shapes by introducing the transformation

$$\{q(t)\} = [\Psi]\{q_m(t)\}\ , \quad \{\dot{q}(t)\} = [\Psi]\{\dot{q}_m(t)\}\ , \quad \{\ddot{q}(t)\} = [\Psi]\{\ddot{q}_m(t)\} \tag{2.7}$$

Substituting the relations in equation (2.7) into equation (2.2) and negelcting damping results after pre-multiplication by $[\Psi]^T$ in

$$[\Psi]^T\ [M]\ [\Psi]\{\ddot{q}_m(t)\} + [\Psi]^T\ [K]\ [\Psi]\{q_m(t)\} = [\Psi]^T\ \{F(t)\} \tag{2.8}$$

As the mode shapes can be scaled arbitrarily, they can also be normalised such that

$$[\Phi]^T\ [M]\ [\Phi] = [I] \tag{2.9}$$

where $[I]$ is the identity matrix and $[\Phi]$ contains the mass-normalised mode shapes. From equation (2.4) it becomes then obvious that

$$[\Phi]^T\ [K]\ [\Phi] = diag\left[\omega_r^2\right] \tag{2.10}$$

Substituting relations (2.9) and (2.10) into equation (2.8) leads to a system of N decoupled equations

$$\ddot{q}_{m,r} + \omega_r^2\, q_{m,r} = F_r(t), \quad r = 1, \ldots, N \tag{2.11}$$

with the modal excitation component F_r corresponding to mode r. The initial conditions for the response in modal coordinates $q_{m,r}$ in $\{q_m\}$ can be obtained by inverting equations (2.7) at instant of time $t = 0$:

$$\begin{aligned} \{q_m(0)\} &= [\Phi]^{-1}\{q(0)\} &= [\Phi]^{-1}\{q_0\} \\ \{\dot{q}_m(0)\} &= [\Phi]^{-1}\{\dot{q}(0)\} &= [\Phi]^{-1}\{\dot{q}_0\} \end{aligned} \tag{2.12}$$

In many applications one can usually assume that only a small set of k modes contributes significantly to the structural response. Accordingly, not all modes need to be taken into account in a numerical simulation which reduces the dimension of the system of equations to be solved for each time step considerably.

2.3.2 Description of damping in MDOF systems

In the previous section damping has not been considered. Even though damping of civil engineering structures is in most cases rather weak it has an influence on the structural response and is therefore of importance in many applications.

However, the mechanisms which lead to energy dissipation in a vibrating system are manyfold. Apart from external damping that can be caused, for example, by the aerodynamics of the system, internal damping is responsible for the decay of free vibrations. If damping devices such as viscous or friction dampers are used, the parameters for a numerical description can be obtained from technical specifications. However, these applications are very limited in civil engineering. In most cases internal damping is caused by friction within the material or at connections and numerous interfaces between different structural components what makes the modelling very difficult.

Therefore, the concept of modal damping is usually used. Each line (2.11) of the system of decoupled equations of motion can be considered as a single-degree-of-freedom (SDOF) equation into which a damping coefficient, that describes a fraction of critical viscous damping, can be introduced:

$$\ddot{q}_{m,r}(t) \,+\, 2\,\zeta_r\,\omega_r\,\dot{q}_{m,r} \,+\, \omega_r^2\,q_{m,r}(t) \,=\, F_r(t) \tag{2.13}$$

ζ_r is called the *modal damping ratio* related to mode r.

Accordingly, the equation of motion in modal space becomes now

$$\{\ddot{q}_m(t)\} \,+\, diag[2\zeta_r\omega_r]\,\{\dot{q}_m(t)\} \,+\, diag\left[\omega_r^2\right]\{q_m(t)\} \,=\, [\Phi]^T\,\{F(t)\} \,=\, \{F_m(t)\} \tag{2.14}$$

Each of these decoupled SDOF equations of motion for mode r can be solved separately applying any available time step method. The resulting response components for all considered modes can be superimposed. Applying equations (2.7) gives then the total response vectors $\{q(t)\}$, $\{\dot{q}(t)\}$ and $\{\dot{q}(t)\}$ in physical coordinates.

From a comparison of equation (2.14) with equation (2.2) one can deduce that

$$[\Phi]^T\,[C_2]\,[\Phi] \,=\, diag[2\zeta_r\omega_r] \tag{2.15}$$

As stated earlier, it is difficult to create the complete viscous damping matrix $[C_2]$ based on models describing the physical phenomena causing energy dissipation in a vibrating structure. Regardless the possibility of transforming the equation into modal space as described above, there may arise the demand of providing acomplete viscous damping matrix $[C_2]$. In these situations certain assumptions for the distribution of damping within the structure are commonly applied. One of the most straighforward assumptions is to expect proportionality of the damping matrix to either the stiffness or the mass matrix:

$$[C_2] \,=\, \alpha\,[K]\,; \qquad [C_2] \,=\, \beta\,[M] \tag{2.16}$$

Pre-multiplication with $[\Psi]^T$ and post-multiplication with $[\Psi]$ yields with equations (2.9) and (2.10) for stiffness and mass proportional damping, respectively,

$$[\Psi]^T\,[C_2]\,[\Psi] \,=\, \alpha\,[\Psi]^T\,[K]\,[\Psi] \,=\, \alpha\left(diag\left[\omega_r^2\right]\right) \tag{2.17}$$

and

$$[\Psi]^T\,[C_2]\,[\Psi] \,=\, \beta\,[\Psi]^T\,[M]\,[\Psi] \,=\, \beta\,[I] \tag{2.18}$$

With equation (2.15), one obtains for stiffness proportional damping

$$\zeta_r = \frac{\alpha\,\omega_r}{2}\,; \qquad \alpha = \frac{2\,\zeta_r}{\omega_r} \tag{2.19}$$

and

$$\zeta_r = \frac{\beta}{2\,\omega_r}\,; \qquad \beta = 2\,\zeta_r\,\omega_r \tag{2.20}$$

for mass proportional damping.

While stiffness proportionality leads to damping ratios that increase linearly with frequency, mass proportional damping is inversely proportional to ω^2 which means a decrease of damping with increasing frequency. To overcome the limitations of either of the two models which do not necessarily agree with experimental observations, the idea of combining the concepts of mass and stiffness proportional damping was born:

$$[C_2] = \alpha\,[K] + \beta\,[M] \tag{2.21}$$

This model of proportional damping is also called Rayleigh damping. The modal damping ratio becomes then:

$$\zeta_r = \frac{1}{2}\left(\alpha\,\omega_r + \frac{\beta}{\omega_r}\right) \tag{2.22}$$

If two modal damping ratios with the corresponding circular frequencies are given, the two coefficients α and β can be obtained as solutions of the respective system of equations

$$\left\{\begin{array}{c}\zeta_1\\ \zeta_2\end{array}\right\} = \frac{1}{2}\left[\begin{array}{cc}\omega_1 & \frac{1}{\omega_1}\\ \omega_2 & \frac{1}{\omega_2}\end{array}\right]\left\{\begin{array}{c}\alpha\\ \beta\end{array}\right\}, \quad (\omega_1 < \omega_2) \longrightarrow \left\{\begin{array}{c}\alpha\\ \beta\end{array}\right\} = 2\,\frac{\omega_1\,\omega_2}{\omega_2^2-\omega_1^2}\left[\begin{array}{cc}-\frac{1}{\omega_2} & \frac{1}{\omega_1}\\ \omega_2 & -\omega_1\end{array}\right]\left\{\begin{array}{c}\zeta_1\\ \zeta_2\end{array}\right\} \tag{2.23}$$

The relations between frequencies and modal damping ratios for the discussed models of proportional damping are illustrated in figure 2.4.

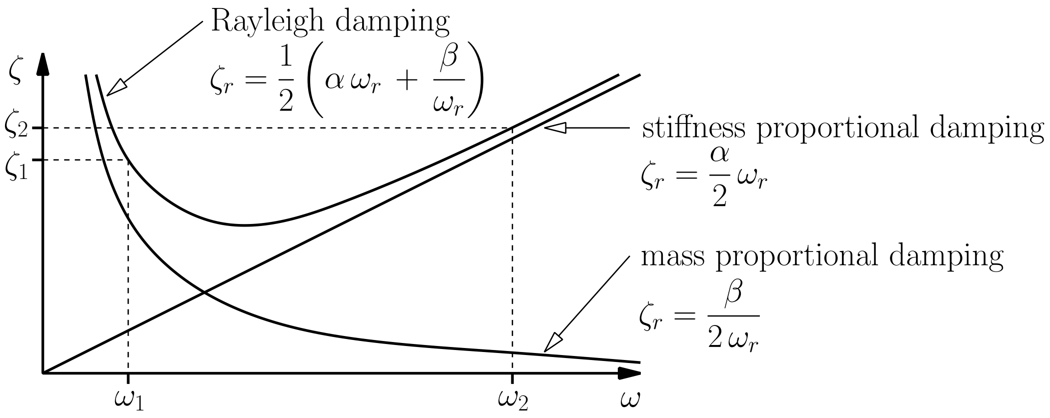

Figure 2.4: Relations between frequencies and modal damping ratios for models of proportional damping

Example 2.2. *Continuing example 2.1, assuming modal damping ratios of*

$$\zeta_1 = 0.02 \qquad \zeta_2 = 0.01$$

the coefficients α and β according to equations (2.19) and (2.20) become

$$\alpha = -3.63 \times 10^{-5} \qquad \beta = 4.33 \times 10^{-1}$$

With these results, the damping matrix $[C_2]$ can be composed from the stiffness and mass matrices as

$$[C_2] = \begin{bmatrix} 425.714 & 7.269 \\ 7.269 & 840.525 \end{bmatrix} \left[\frac{N\,s}{m}\right]$$

2.4 State-space formulation

Starting point for the following derivations is the system of equations of motion for a viscously damped system with N degrees of freedom:

$$[M]\{\ddot{q}(t)\} + [C_2]\{\dot{q}(t)\} + [K]\{q(t)\} = \{F(t)\} = [B_2]\{u(t)\}. \tag{2.24}$$

The external loads $\{F(t)\}_N$ are expressed by an input selection matrix $[B_2]_{N\times n_u}$, determining those degrees-of-freedom at which the $n_u \le N$ loads are acting, and an input vector $\{u(t)\}_{n_u}$ containing the external forces.

To obtain the eigenvectors and eigenvalues of a system with general viscous damping, the system of differential equations of second order has to be transformed into a system of first order differential equations. Therefore equation (2.24) is extended by the equality expression $[M]\{\dot{q}(t)\} = [M]\{\dot{q}(t)\}$:

$$\underbrace{\begin{bmatrix} [C_2] & [M] \\ [M] & [0] \end{bmatrix}}_{[P_s]} \underbrace{\begin{Bmatrix} \{\dot{q}(t)\} \\ \{\ddot{q}(t)\} \end{Bmatrix}}_{\{\dot{x}(t)\}} + \underbrace{\begin{bmatrix} [K] & [0] \\ [0] & [-M] \end{bmatrix}}_{[Q_s]} \underbrace{\begin{Bmatrix} \{q(t)\} \\ \{\dot{q}(t)\} \end{Bmatrix}}_{\{x(t)\}} = \begin{bmatrix} [B_2] \\ [0] \end{bmatrix} \{u(t)\}. \tag{2.25}$$

The vector $\{x(t)\}$ is called *state vector*. From the formulations for free vibrations the eigenvalue problem related to equation (2.25) is obtained:

$$[P_s][\Psi_c][\Lambda_c] + [Q_s][\Psi_c] = [0], \tag{2.26}$$

where matrix $[\Psi_c]_{n\times n}$ consists of $n = 2N$ complex column eigenvectors while the matrix $[\Lambda_c] = diag[\lambda_r]$ contains the n complex eigenvalues λ_r $\left[\frac{rad}{s}\right]$ on its diagonal.

The matrices $[\Lambda_c]$ and $[\Psi_c]$ have the following structure:

$$[\Lambda_c] = \begin{bmatrix} [\Lambda] & [0] \\ [0] & [\Lambda^*] \end{bmatrix}, \qquad [\Psi_c] = \begin{bmatrix} [\Theta] & [\Theta^*] \\ [\Theta][\Lambda] & [\Theta^*][\Lambda^*] \end{bmatrix}, \tag{2.27}$$

where the matrices $[\Lambda]$ and $[\Theta]$ contain the N complex eigenvalues and eigenvectors of the second order eigenvalue problem that can be generated from equation (2.24):

$$[M][\Theta][\Lambda]^2 + [C_2][\Theta][\Lambda] + [K][\Theta] = [0]. \tag{2.28}$$

The superscript * denotes the complex conjugate. Both the damping coefficiens and natural circular frequencies are included within the complex eigenvalues:

$$\lambda_r,\ \lambda_r^* \ = \ -\zeta_r\omega_r \pm \mathrm{i}\omega_r\sqrt{1-\zeta_r^2} \tag{2.29}$$

The imaginary part of the eigenvalue λ_r, $\omega_r\sqrt{1-\zeta_r^2}$, is the natural circular frequency of the damped system.

Similarly as shown in section 2.3, the eigenvectors $[\Psi_c]$ can be used for an orthogonality transformation of the matrices $[P_s]$ and $[Q_s]$:

$$[\Psi_c]^T\,[P_s]\,[\Psi_c] = diag[a_r] \tag{2.30}$$

and

$$[\Psi_c]^T\,[Q_s]\,[\Psi_c] = diag[b_r] \tag{2.31}$$

The matrices $diag[a_r]$ and $diag[b_r]$ are called the *modal a matrix* and *modal b matrix*, respectively. Pre-multiplying equations (2.30) and (2.31) by matrix $[\Psi_c]^{-T}$ and substituting the resulting expressions into the eigenvalue problem (2.26), one obtaines

$$[\Psi_c]^{-T}\,diag[a_r]\,[\Lambda_c] + [\Psi_c]^{-T}\,diag[b_r] = [0] \tag{2.32}$$

or

$$[\Lambda_c] = diag[\lambda_r] = -diag\left[\frac{1}{a_r}\right]diag[b_r] \tag{2.33}$$

Solving equation (2.25) for $\{\dot{x}\,(t)\}$ after pre-multiplication by

$$[P_s]^{-1} = \left[\begin{array}{cc} [0] & [M]^{-1} \\ [M]^{-1} & -\,[M]^{-1}\,[C_2]\,[M]^{-1} \end{array}\right] \tag{2.34}$$

gives

$$\{\dot{x}\,(t)\} = \underbrace{-\,[P_s]^{-1}\,[Q_s]}_{[A_c]}\{x\,(t)\} + \underbrace{[P_s]^{-1}\left[\begin{array}{c} [B_2] \\ [0] \end{array}\right]}_{[B_c]}\{u\,(t)\} \tag{2.35}$$

or

$$\begin{aligned} \{\dot{x}\,(t)\} \ &= \ -\left[\begin{array}{cc} [0] & [M]^{-1} \\ [M]^{-1} & -\,[M]^{-1}\,[C_2]\,[M]^{-1} \end{array}\right]\left[\begin{array}{cc} [K] & [0] \\ [0] & [-M] \end{array}\right]\{x\,(t)\} \\ &\quad + \left[\begin{array}{cc} [0] & [M]^{-1} \\ [M]^{-1} & -\,[M]^{-1}\,[C_2]\,[M]^{-1} \end{array}\right]\left[\begin{array}{c} [B_2] \\ [0] \end{array}\right]\{u\,(t)\} \end{aligned} \tag{2.36}$$

$$\{\dot{x}\,(t)\} = \underbrace{\left[\begin{array}{cc} [0] & [I] \\ -\,[M]^{-1}\,[K] & -\,[M]^{-1}\,[C_2] \end{array}\right]}_{[A_c]\in\mathbb{R}^{n\times n}}\{x\,(t)\} + \underbrace{\left[\begin{array}{c} [0] \\ [M]^{-1}\,[B_2] \end{array}\right]}_{[B_c]\in\mathbb{R}^{n\times n_u}}\{u\,(t)\} \tag{2.37}$$

where $[A_c]$ and $[B_c]$ are called the *continuous-time state-feedback* and *continuous-time state-input matrices*, respectively. Substituting equations (2.30), (2.31) and (2.33), matrix $[A_c] = -\,[P]^{-1}\,[Q]$ can also be written as:

$$[A_c] = -\,[\Psi_c]\,diag\left[\frac{1}{a_r}\right][\Psi_c]^T\,[\Psi_c]^{-T}\,diag\,[b_r]\,[\Psi_c]^{-1} = [\Psi_c]\,[\Lambda_c]\,[\Psi_c]^{-1}\,. \tag{2.38}$$

This formulation corresponds to the standard eigenvalue problem $[A_c]\,[\Psi_c] = [\Psi_c]\,[\Lambda_c]$. Accordingly, matrices $[\Psi_c]$ und $[\Lambda_c]$ contain the eigenvectors and eigenvalues of matrix $[A_c]$.

Example 2.3. *Solving the eigenvalue problem (2.26) for the 2-dof system already considered in examples 2.1 and 2.2, produces*

$$[\Lambda_c] = \left[\begin{array}{cc|cc} -0.2086+20.857\mathrm{i} & 0 & 0 & 0 \\ 0 & -0.2144+10.718\mathrm{i} & 0 & 0 \\ \hline 0 & 0 & -0.2086-20.857\mathrm{i} & 0 \\ 0 & 0 & 0 & -0.2144-10.718\mathrm{i} \end{array}\right]$$

and

$$[\Psi_c] = \left[\begin{array}{cc|cc} -0.851 & 1 & -0.851 & 1 \\ 1 & 0.425 & 1 & 0.425 \\ \hline 0.1775-17.745\mathrm{i} & -0.2144+10.718\mathrm{i} & 0.1775+17.745\mathrm{i} & -0.2144-10.718\mathrm{i} \\ -0.2086+20.857\mathrm{i} & -0.0912+4.559\mathrm{i} & -0.2086-20.857\mathrm{i} & -0.0912-4.559\mathrm{i} \end{array}\right]$$

Assuming that the 2-dof system is excited at both degerees-of-freedom, matrices $[A_c]$ and B_c become

$$[A_c] = \begin{bmatrix} 0 & 0 & 1 & 0 \\ 0 & 0 & 0 & 1 \\ -200 & 200 & -0.4257 & -7.2689\times10^{-3} \\ 100 & -350 & -3.6345\times10^{-3} & -0.4203 \end{bmatrix} \qquad [B_c] = \begin{bmatrix} 0 & 0 \\ 0 & 0 \\ 0.001 & 0 \\ 0 & 0.0005 \end{bmatrix}$$

The eigenvectors were normalized such that the maximal values are 1. This scaling facilitates the comparison with the eigenvectors of the undamped system. It is furthermore remarked that the matrices of the eigensolutions were composed here as in the theoretical derivations. In numerical routines it is common that the complex conjugate pairs are arranged at consecutive positions. This should be taken into account in respective implementations.

2.5 Impulse response function and Duhamel integral

Any row in equation (2.14) can be re-written as a single degree-of-freedom equation of motion for mode r:

$$m_r\,\ddot{q}_{m,r}(t) \;+\; 2\,m_r\zeta_r\omega_r\,\dot{q}_{m,r}(t) \;+\; m_r\omega_r^2 q_{m,r}(t) \;=\; \{\psi_r\}^T\;\{F(t)\} \tag{2.39}$$

allowing for arbitrary scaling of the mode shapes such that the modal mass $m_r \neq 1$.

The well known solution of the free vibration of a single degree-of-freedom system can therefore be directly applied to the modal contribution of a single mode to the total structural response:

$$q_{m,r}(t) \;=\; e^{-\zeta_r\omega_r t}\left[a\,\cos\left(\sqrt{1-\zeta_r^2}\,\omega_r t\right) + b\,\sin\left(\sqrt{1-\zeta_r^2}\,\omega_r t\right)\right] \tag{2.40}$$

$$\begin{aligned} \dot{q}_{m,r}(t) \;&=\; -\zeta_r\,\omega_r\,e^{-\zeta_r\omega_r t}\left[a\,\cos\left(\sqrt{1-\zeta_r^2}\,\omega_r t\right) + b\,\sin\left(\sqrt{1-\zeta_r^2}\,\omega_r t\right)\right] \\ &\quad + \sqrt{1-\zeta_r^2}\,\omega_r\,e^{-\zeta_r\omega_r t}\left[-a\,\sin\left(\sqrt{1-\zeta_r^2}\,\omega_r t\right) + b\,\cos\left(\sqrt{1-\zeta_r^2}\,\omega_r t\right)\right] \end{aligned} \tag{2.41}$$

Using the initial conditions

$$q_{m,r}(t=0) \;=\; 0\,; \quad \dot{q}_{m,r}(t=0) \;=\; \frac{I}{m_r}$$

where I denotes the exciting impulse, the coefficients a and b in equations (2.40) and (2.41) can be derived as

$$\begin{aligned}
q_{m,r}(t=0) \;=\; 0 \;&=\; 1\;(a \cdot 1 \;+\; b \cdot 0) \;\rightarrow\; a \;=\; 0 \\
\dot{q}_{m,r}(t=0) \;=\; \frac{I}{m_r} \;&=\; -\zeta_r\,\omega_r \cdot 1\;(0 \cdot 1 \;+\; b \cdot 0) \;+\; \sqrt{1-\zeta_r^2}\,\omega_r \cdot 1\;(0 \cdot 0 \;+\; b \cdot 1) \\
&=\; b\,\omega_r\,\sqrt{1-\zeta_r^2} \\
\rightarrow\; b \;&=\; \frac{I}{m_r\,\omega_r\,\sqrt{1-\zeta_r^2}} \;\rightarrow\; \text{for the unit impulse}\; I \;=\; 1\,\text{follows}\; b \;=\; \frac{1}{m_r\,\omega_r\,\sqrt{1-\zeta_r^2}}
\end{aligned}$$

This leads to the solution, the contribution of a single mode r to the *impulse response function* (IRF):

$$h_r(t) = e^{-\zeta_r \omega_r t}\,\frac{1}{m_r\,\omega_r\,\sqrt{1-\zeta_r^2}}\,\sin\left(\sqrt{1-\zeta_r^2}\,\omega_r t\right) \tag{2.42}$$

Accordingly, the contribution of mode r to the total response can be calculated by means of the well-known DUHAMEL integral that superimposes the impulse responses of an SDOF system at instant of time t to all excitation contributions $F(\tau)$ applied to the system in the past at instants of time τ.

$$\begin{aligned}
q_{m,r}(t) \;&=\; \int_{\tau=-\infty}^{t} h_r(t-\tau)\;\{\psi_r\}^T\;\{F(\tau)\}\;\mathrm{d}\tau \\
&=\; \frac{1}{m_r\omega_r}\frac{1}{\sqrt{1-\zeta_r^2}}\;\int_{\tau=-\infty}^{t} \{\psi_r\}^T\;\{F(\tau)\}\;e^{-\zeta_r\omega_r(t-\tau)}\;\sin\left[\sqrt{1-\zeta_r^2}\,\omega_r\,(t-\tau)\right]\mathrm{d}\tau
\end{aligned} \tag{2.43}$$

Substituting equation (2.43) into the modal transformation (2.7) results in the total response of the multi degree-of-freedom system

$$\{q(t)\} = \sum_{r=1}^{N}\{\psi_r\}\int_{\tau=-\infty}^{t}\{\psi_r\}^T\;\{F(\tau)\}\;e^{-\zeta_r\omega_r(t-\tau)}\;\sin\left[\sqrt{1-\zeta_r^2}\,\omega_r\,(t-\tau)\right]\mathrm{d}\tau \tag{2.44}$$

The more general IRF describing the response at degree-of-freedom i due to an initial excitation in form of a Dirac delta function at instant τ and degree-of-freedom j is then [81]

$$h_{ij}(t-\tau) = \sum_{r=1}^{N}\frac{\psi_{ir}\psi_{jr}}{m_r\omega_r\,\sqrt{1-\zeta_r^2}}\;e^{-\zeta_r\omega_r(t-\tau)}\;\sin\left(\sqrt{1-\zeta_r^2}\,\omega_r\,(t-\tau)\right) \tag{2.45}$$

From equation (2.45) one can conclude that the impulse response function completely describes the dynamic behaviour of a linear structural system in time domain. The IRF contains the modal parameters what gives reason to develop algorithms that allow the identification of modal parameters from impulse response functions derived from measured data.

2.6 Frequency response function

The frequency response function (FRF) of a single-degree-of-freedom system gives the structural response due to a harmonic unit excitation at frequency ω. Similarly, one can relate the response at one degree-of-freedom (DOF) i of a multi-degree-of-freedom system to an excitation at another degree-of-freedom j. Accordingly, for MDOF systems an FRF matrix that is related to all considered response degrees-of-freedom i and excitation degrees-of-freedom j can be formulated for any excitation frequency ω. If the considered response are displacements, the FRF matrix is called *receptance* matrix. For velocities and accelerations, the names *mobility* and *accelerance* or *inertance* are respectively used [49].

Assuming a harmonic excitation, the response can also be assumed as being harmonic. Therefore, both the excitation and the displacements can be represented by a single Fourier series component. The respective derivatives are then obtained, accordingly.

$$u_j(t) = U_j\, e^{\mathrm{i}\Omega t}\,; \qquad q_i(t) = Q_i\, e^{\mathrm{i}\Omega t}\,; \qquad \dot{q}_i(t) = \mathrm{i}\Omega\, Q_i\, e^{\mathrm{i}\Omega t}\,; \qquad \ddot{q}_i(t) = -\Omega^2\, Q_i\, e^{\mathrm{i}\Omega t} \tag{2.46}$$

The state-space formulation of the equation of motion (2.25) becomes then

$$[P_s]\left\{\begin{array}{c}\{\mathrm{i}\Omega\, Q\}\\ \{-\Omega^2\, Q\}\end{array}\right\} + [Q_s]\left\{\begin{array}{c}\{Q\}\\ \{\mathrm{i}\Omega\, Q\}\end{array}\right\} = \left[\begin{array}{c}[B_2]\\ [0]\end{array}\right]\{U\} \tag{2.47}$$

which can be modified to

$$(\mathrm{i}\Omega\ [P_s]\ +\ [Q_s])\left\{\begin{array}{c}Q\\ \mathrm{i}\Omega Q\end{array}\right\} = \left[\begin{array}{c}[B_2]\\ [0]\end{array}\right]\{U\} \tag{2.48}$$

or solved for the response:

$$\left\{\begin{array}{c}Q\\ \mathrm{i}\Omega Q\end{array}\right\} = \underbrace{(\mathrm{i}\,\Omega\ [P_s]\ +\ [Q_s])^{-1}}_{\text{receptance matrix } [\alpha(\omega)]}\ \left[\begin{array}{c}[B_2]\\ [0]\end{array}\right]\{U\} \tag{2.49}$$

From equations (2.30) and (2.31) one can deduce that

$$[P_s] = [\Psi_c]^{-T}\ diag\,[a_r]\ [\Psi_c]^{-1} \quad \text{and} \quad [Q_s] = [\Psi_c]^{-T}\ diag\,[b_r]\ [\Psi_c]^{-1} \tag{2.50}$$

Hence,

$$[\Psi_c]^T\ (\mathrm{i}\,\omega\ [P_s]\ +\ [Q_s])\ [\Psi_c]\ =\ \mathrm{i}\,\omega\, diag\,[a_r]\ +\ diag\,[b_r]\ =\ [\Psi_c]^T\ [\alpha(\omega)]^{-1}\ [\Psi_c] \tag{2.51}$$

After inverting and re-organising equation (2.51) one obtains

$$[\alpha(\omega)]\ =\ [\Psi_c]\ [\mathrm{i}\,\omega\ diag\,[a_r]\ +\ diag\,[b_r]]^{-1}\ [\Psi_c]^T \tag{2.52}$$

Substituting $b_r\ =\ -\lambda_r\, a_r$ from equation (2.33) yields

$$[\alpha(\omega)]\ =\ [\Psi_c]\ diag\,[a_r\,(\mathrm{i}\,\omega\ -\ \lambda_r)]^{-1}\ [\Psi_c]^T\ . \tag{2.53}$$

With $\lambda_r = \omega_r\left(-\zeta_r \pm \mathrm{i}\sqrt{1-\zeta_r^2}\right)$ from equation (2.29) the receptance matrix can be completely expressed in terms of the solutions of the eigenvalue problem derived from the state-space formulation for the structural system:

$$[\alpha(\omega)] = [\Psi_c]\; diag\left[a_r\left(\omega_r\,\zeta_r + \mathrm{i}\left(\omega \mp \omega_r\sqrt{1-\zeta_r^2}\right)\right)\right]^{-1}[\Psi_c]^T \tag{2.54}$$

Since both, eigenvalues and eigenvectors, occur in complex conjugate pairs any element of the receptance matrix α_{ij} is computed by:

$$\alpha_{ij}(\omega) = \sum_{r=1}^{m}\left(\frac{(\psi_{ir})\,(\psi_{jr})}{a_r\left(\omega_r\,\zeta_r + \mathrm{i}\left(\omega - \omega_r\sqrt{1-\zeta_r^2}\right)\right)} + \frac{(\psi_{ir})^*\,(\psi_{jr})^*}{a_r^*\left(\omega_r\,\zeta_r + \mathrm{i}\left(\omega + \omega_r\sqrt{1-\zeta_r^2}\right)\right)}\right) \tag{2.55}$$

or as can also be directly derived from equation (2.53)

$$\alpha_{ij}(\omega) = \sum_{r=1}^{m}\left(\frac{(\psi_{ir})\,(\psi_{jr})}{a_r\,(\mathrm{i}\omega - \lambda_r)} + \frac{(\psi_{ir})^*\,(\psi_{jr})^*}{a_r^*\,(\mathrm{i}\omega - \lambda_r^*)}\right) = \sum_{r=1}^{m}\left(\frac{A_{ij,r}}{\mathrm{i}\omega - \lambda_r} + \frac{A_{ij,r}^*}{\mathrm{i}\omega - \lambda_r^*}\right) \tag{2.56}$$

where the values $\dfrac{1}{a_r}$ are also known as *modal participation factors.*

Example 2.4. *The four frequency response functions of the 2-dof system described in the previous examples were calculated by means of equation (2.56). In figure 2.5 the diagrams for the absolute values of the four frequency response functions are shown. The peaks in the curves indicate an amplification of the response at the two resonance frequencies.*

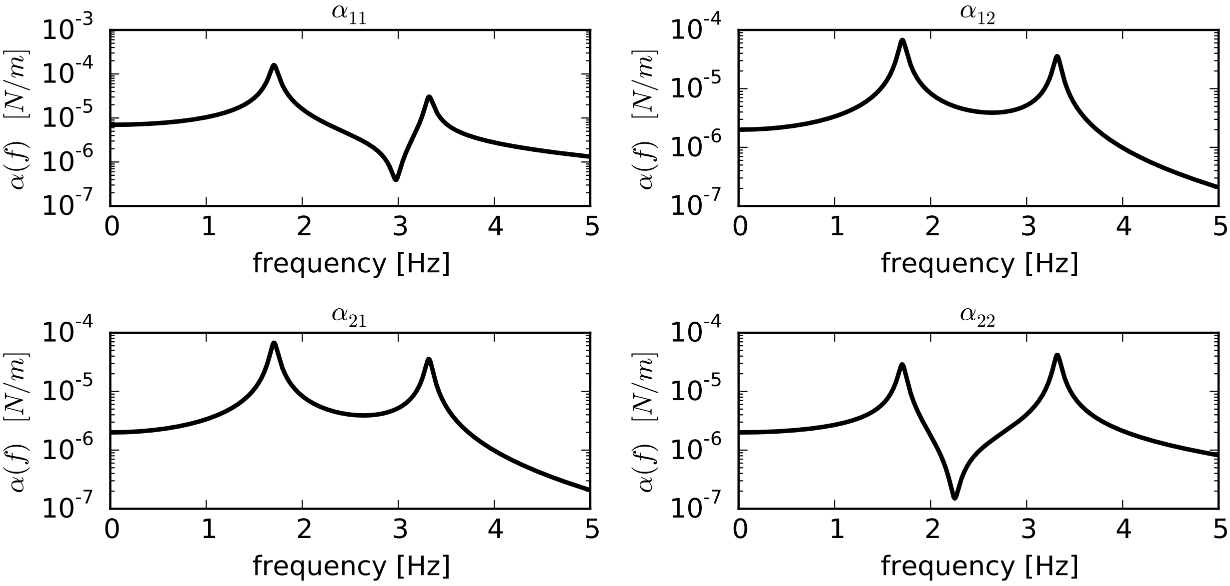

Figure 2.5: Absolute values of the frequency response functions for the 2-dof system

2.7 Relations between structural models and experimental data in time domain

2.7.1 Observation equation

The number of degrees-of-freedom of numerical models N is in almost all cases by far larger than the number of measurement points at which the structural response can be observed during an experimental investigation. Additionally, it is particularly difficult to measure rotational degrees-of-freedom. Accordingly, one can usually assume a great difference between the dimension of a finite element model and the *number of experimental output observations* n_o.

In many applications, the structural response is measured as accelerations. However, depending on the experimental setup, it is also possible to measure the response as velocities or displacements. Independent from the response quantities, the measured values at any instant of time t can be collected in a *response vector* $\{y\left(t\right)\}$:

$$\{y\left(t\right)\}_{n_o} = \left[C_a\right]_{n_o \times N} \{\ddot{q}\left(t\right)\}_N + \left[C_v\right]_{n_o \times N} \{\dot{q}\left(t\right)\}_N + \left[C_d\right]_{n_o \times N} \{q\left(t\right)\}_N \tag{2.57}$$

The matrices $\left[C_a\right], \left[C_v\right], \left[C_d\right]$ select those n_o degrees-of-freedom corresponding to the measurement points of accelerations, velocities and displacements, respectively, from the set of all N DOF's of a finite element model. These response selection matrices are sparse matrices with only few elements equal to one at those locations that link the respective line in the output vector $\{y(t)\}$ with the column corresonding to the associated DOF of a finite element model.

Solving the equation of motion (2.24) for $\{\ddot{q}\left(t\right)\}$:

$$\{\ddot{q}\left(t\right)\} = -\left[M\right]^{-1}\left[C_2\right]\{\dot{q}\left(t\right)\} - \left[M\right]^{-1}\left[K\right]\{q\left(t\right)\} + \left[M\right]^{-1}\left[B_2\right]\{u\left(t\right)\} \tag{2.58}$$

and substituting the result into equation (2.57) yields

$$\begin{aligned}\{y\left(t\right)\} &= \left[C_a\right]\left(-\left[M\right]^{-1}\left[C_2\right]\{\dot{q}\left(t\right)\} - \left[M\right]^{-1}\left[K\right]\{q\left(t\right)\} + \left[M\right]^{-1}\left[B_2\right]\{u\left(t\right)\}\right) \\ &\quad + \left[C_v\right]\{\dot{q}\left(t\right)\} + \left[C_d\right]\{q\left(t\right)\}\end{aligned} \tag{2.59}$$

Equation (2.59) can be summarised as:

$$\begin{aligned}\{y\left(t\right)\} &= \underbrace{\left[\left(\left[C_d\right] - \left[C_a\right]\left[M\right]^{-1}\left[K\right]\right) \quad \left(\left[C_v\right] - \left[C_a\right]\left[M\right]^{-1}\left[C_2\right]\right)\right]}_{\left[C_c\right]} \left\{\begin{array}{c}\{q\left(t\right)\} \\ \{\dot{q}\left(t\right)\}\end{array}\right\} \\ &\quad + \underbrace{\left[C_a\right]\left[M\right]^{-1}\left[B_2\right]}_{\left[D_c\right]}\{u\left(t\right)\}\end{aligned} \tag{2.60}$$

or

$$\{y\left(t\right)\} = \left[C_c\right]\{x\left(t\right)\} + \left[D_c\right]\{u\left(t\right)\} \tag{2.61}$$

Matrix $\left[C_c\right]$ is called *output matrix* while $\left[D_c\right]$ denotes the *transmission matrix*. One can deduce from equation (2.60) that matrix $\left[D_c\right]$ becomes zero, if $\left[C_a\right]$ is zero. This means that the transmission matrix only exists in the case of acceleration measurements. This is in many applications the case since accelerometers are the most widely used sensors in structural dynamics.

Example 2.5. *Based on the assumption that the response is exclusivly measured as accelerations, the matrices* $[C_c]$ *and* $[D_c]$ *become for the 2-dof system already discussed in the examples 2.1 to 2.4*

$$[C_c] = \begin{bmatrix} -200 & 200 & -0.426 & -7.269 \times 10^{-3} \\ 100 & -350 & -3.634 \times 10^{-3} & -0.420 \times 10^{6} \end{bmatrix}$$

and

$$[D_c] = \begin{bmatrix} 0.001 & 0 \\ 0 & 0.0005 \end{bmatrix}$$

2.7.2 Definition of the state-space model in continuos time domain

Combining equations (2.37) and (2.61) gives the classical *continuous-time-state-space model*

$$\begin{aligned} \{\dot{x}(t)\} &= [A_c]\{x(t)\} + [B_c]\{u(t)\} \\ \{y(t)\} &= [C_c]\{x(t)\} + [D_c]\{u(t)\} \end{aligned} \tag{2.62}$$

The state vector $\{x(t)\}$ contains all displacements and velocities corresponding to all N degrees of freedom of the FE-model, while the L excitations (system input) form the vector $\{u(t)\}$.

To prepare the following derivations a similarity transformation that leads to another state vector is introduced:

$$\{x(t)\} = [T]\{z(t)\}, \tag{2.63}$$

where $[T] \in \mathbb{C}^{n \times n}$ is a quadratic non-singular complex matrix. Applying this coordinate transformation to equation (2.62) one obtains

$$\begin{aligned} \{\dot{z}(t)\} &= [T]^{-1}[A_c][T]\{z(t)\} + [T]^{-1}[B_c]\{u(t)\} \\ \{y(t)\} &= [C_c][T]\{z(t)\} + [D_c]\{u(t)\} \end{aligned} \tag{2.64}$$

Even though the new vector $\{z(t)\}$ does not contain the response variables in physical coordinates, as present in the state vector $\{x(t)\}$, equations (2.64) still describe the same input-output relations as equations (2.62). Merely the reference system has been changed by the transformation.

One possibility to substitute $[T]$ is to use the eigenvectors $[\Psi_c]$ which were obtained from the state-space formulation of the structural system. This results in a transformation to the complex modal state vectors $\{x_m(t)\}_n$:

$$\{x(t)\} = [\Psi_c]\{x_m(t)\}. \tag{2.65}$$

Inserting equation (2.65) and the modal decomposition $[A_c] = [\Psi_c][\Lambda_c][\Psi_c]^{-1}$ (2.38) into equations (2.64) yields

$$\begin{aligned} \{\dot{x}_m(t)\} &= [\Psi_c]^{-1}[A_c][\Psi_c]\{x_m(t)\} + [\Psi_c]^{-1}[B_c]\{u(t)\} \\ &= [\Psi_c]^{-1}[\Psi_c][\Lambda_c][\Psi_c]^{-1}[\Psi_c]\{x_m(t)\} + [\Psi_c]^{-1}[B_c]\{u(t)\} \\ &= [\Lambda_c]\{x_m(t)\} + [\Psi_c]^{-1}[B_c]\{u(t)\} \\ \{y(t)\} &= [C_c][\Psi_c]\{x_m(t)\} + [D_c]\{u(t)\} \end{aligned} \tag{2.66}$$

or

$$\begin{aligned} \{\dot{x}_m(t)\} &= [\Lambda_c]\{x_m(t)\} + [L_c]^T\{u(t)\} \\ \{y(t)\} &= [V_c]\{x_m(t)\} + [D_c]\{u(t)\} \end{aligned} \tag{2.67}$$

with the *modal input matrix*

$$[L_c]^T = [\Psi_c]^{-1}[B_c] \tag{2.68}$$

and *the modal output matrix*

$$[V_c] = [C_c][\Psi_c] \tag{2.69}$$

To investigate the matrices $[L_c]^T$ and $[V_c]$, the definitions of matrices $[P_s]$ and $[B_c]$ (2.30), (2.35) are re-called

$$[P_s] = [\Psi_c]^{-T}\, diag\,[a_r]\,[\Psi_c]^{-1} \longrightarrow [\Psi_c]^{-1} = diag\left[\frac{1}{a_r}\right][\Psi_c]^T[P_s]$$

$$[B_c] = [P_s]^{-1}\begin{bmatrix} [B_2] \\ [0] \end{bmatrix}$$

and substituted into equation (2.68):

$$[L_c]^T = diag\left[\frac{1}{a_r}\right][\Psi_c]^T[P_s][P_s]^{-1}\begin{bmatrix} [B_2] \\ [0] \end{bmatrix} \tag{2.70}$$

From the structure of the eigenvector matrix $[\Psi_c]$ given in equation (2.27)

$$[\Psi_c] = \begin{bmatrix} [\Theta] & [\Theta^*] \\ [\Theta][\Lambda] & [\Theta^*][\Lambda^*] \end{bmatrix} \longrightarrow [\Psi_c]^T = \begin{bmatrix} [\Theta]^T & ([\Theta][\Lambda])^T \\ [\Theta]^H & ([\Theta^*][\Lambda^*])^T \end{bmatrix}$$

follows for the modal input matrix:

$$[L_c]^T = diag\left[\frac{1}{a_r}\right]\begin{bmatrix} [\Theta]^T \\ [\Theta]^H \end{bmatrix}[B_2] \tag{2.71}$$

The superscript H denotes the Hermetian or complex conjugate transpose.

Similarly, the definition of matrices $[C_c]$ and $[\Psi_c]$, (2.60) and (2.27), are substituted into equation (2.69) defining the modal output matrix $[V_c]$:

$$[V_c] = \begin{bmatrix} [C_d] - [C_a][M]^{-1}[K] & [C_v] - [C_a][M]^{-1}[C_2] \end{bmatrix}\begin{bmatrix} [\Theta] & [\Theta^*] \\ [\Theta][\Lambda] & [\Theta^*][\Lambda^*] \end{bmatrix} \tag{2.72}$$

If only one response quantity is measured, equation (2.72) reduces

- for displacement measurements to

$$[V_c] = [C_d]\begin{bmatrix} [\Theta] & [\Theta^*] \end{bmatrix} \tag{2.73}$$

- for velocity measurements to

$$[V_c] = [C_v]\begin{bmatrix} [\Theta][\Lambda] & [\Theta^*][\Lambda^*] \end{bmatrix} \tag{2.74}$$

- for acceleration measurements to:

$$[V_c] = \begin{bmatrix} \begin{pmatrix} -[C_a]\left([M]^{-1}[K][\Theta]\right. \\ \left.+[M]^{-1}[C_2][\Theta][\Lambda]\right) \end{pmatrix} & \begin{pmatrix} -[C_a]\left([M]^{-1}[K][\Theta^*]\right. \\ \left.+[M]^{-1}[C_2][\Theta^*][\Lambda^*]\right) \end{pmatrix} \end{bmatrix} \tag{2.75}$$

It is known from the eigenvalue problem (2.28) that

$$[M]^{-1}[C_2][\Theta][\Lambda] + [M]^{-1}[K][\Theta] = -[\Theta]\left[\Lambda^2\right] \tag{2.76}$$

and

$$[M]^{-1}[C_2][\Theta^*][\Lambda^*] + [M]^{-1}[K][\Theta^*] = -[\Theta^*]\left[\Lambda^{*2}\right] \tag{2.77}$$

Accordingly, equation (2.75) can be simplified to

$$[V_c] = [C_a]\begin{bmatrix} [\Theta][\Lambda^2] & [\Theta^*][\Lambda^{*2}] \end{bmatrix} \tag{2.78}$$

From equations (2.73), (2.74) and (2.78) becomes obvious, that matrix $[V_c]$ determines that part of the mode shapes which can be identified from the measured data. Furthermore it can be noticed that the modal parameters of the system are given by the matrices $[\Lambda_c]$ (2.27), (2.29), $[L_c]^T$ and $[V_c]$.

The last derivations showed the modal decomposition of the equations of the state-space formulation (2.67) apart from the transmission component $[D_c]\{u(t)\}$ in the second equation. Therefore the modal decomposition of the transmission matrix $[D_c]$ is considered next. For this purpose it is assumed that only accelerations and velocities are measured, matrix $[C_d]$ is assumed to be zero, which reduces equation (2.57) to

$$\{y(t)\} = [C_a]\{\ddot{q}(t)\} + [C_v]\{\dot{q}(t)\} = \begin{bmatrix} [C_v] & [C_a] \end{bmatrix}\{\dot{x}(t)\} \tag{2.79}$$

Substituting the first equation of the state-space model (2.62)

$$\{\dot{x}(t)\} = [A_c]\{x(t)\} + [B_c]\{u(t)\}$$

yields with equations (2.79) and (2.61)

$$\begin{aligned}
\{y(t)\} &= \begin{bmatrix} [C_v] & [C_a] \end{bmatrix}\left([A_c]\{x(t)\} + [B_c]\{u(t)\}\right) && (2.80)\\
&\downarrow \\
&\downarrow \longleftarrow [A_c] = \begin{bmatrix} [0] & [I] \\ -[M]^{-1}[K] & -[M]^{-1}[C_2] \end{bmatrix} \quad (2.37) \\
&\downarrow \\
&= \underbrace{\begin{bmatrix} -[C_a][M]^{-1}[K] & -[C_v]-[C_a][M]^{-1}[C_2] \end{bmatrix}}_{=[C_c]\text{ for }[C_d]=[0]}\{x(t)\} \\
&\quad + \begin{bmatrix} [C_v] & [C_a] \end{bmatrix}[B_c]\{u(t)\} \\
&\downarrow \\
&\downarrow \longleftarrow [B_c] = \begin{bmatrix} [0] \\ [M]^{-1}[B_2] \end{bmatrix} \quad (2.35) \\
&\downarrow \\
&= [C_c]\{x(t)\} + \underbrace{[C_a][M]^{-1}[B_2]}_{=[D_c]}\{u(t)\} && (2.81)
\end{aligned}$$

From these relations one can recognize that post-multiplying $[C_c]$ by $[A_c]^{-1}[B_c]$ yields the following expression:

$$[C_c][A_c]^{-1}[B_c] = \left[\begin{array}{cc} [C_v] & [C_a] \end{array}\right][A_c][A_c]^{-1}[B_c] = [C_a][M]^{-1}[B_2] = [D_c] \tag{2.82}$$

Substituting the modal decomposition of matrix $[A_c]$

$$[A_c] = [\Psi_c][\Lambda_c][\Psi_c]^{-1} \quad (2.38) \quad \longrightarrow [A_c]^{-1} = [\Psi_c][\Lambda_c]^{-1}[\Psi_c]^{-1}$$

into equation (2.82) results with equations (2.68) and (2.69) in

$$[D_c] = [C_c][\Psi_c][\Lambda_c]^{-1}[\Psi_c]^{-1}[B_c] = [V_c][\Lambda_c]^{-1}[L_c]^T \tag{2.83}$$

or

$$[D_c] = \sum_{r=1}^{n} \frac{1}{\lambda_r}\{v_{c_r}\}\{l_{c_r}\}^T \tag{2.84}$$

where

- λ_r = the rth diagonal element of the eigenvalue matrix $[\Lambda_c]$,
- $\{v_{c_r}\}$ = the rth column of matrix $[V_c]$ and
- $\{l_{c_r}\}^T$ = the rth row of matrix $[L_c]^T$.

Hence, the state-space model in equation (2.67) can be transformed to

$$\begin{aligned} \{\dot{x}_m(t)\} &= [\Lambda_c]\{x_m(t)\} + [L_c]^T\{u(t)\} \\ \{y(t)\} &= [V_c]\{x_m(t)\} + [V_c][\Lambda_c]^{-1}[L_c]^T\{u(t)\} \end{aligned} \tag{2.85}$$

or

$$\begin{aligned} \dot{x}_{m,r}(t) &= \lambda_r\, x_{m,r}(t) + \{l_{c_r}\}^T\{u(t)\} \\ \{y_r(t)\} &= \{v_{c_r}\}\, x_{m,r}(t) + \frac{1}{\lambda_r}\{v_{c_r}\}\{l_{c_r}\}^T\{u(t)\} \end{aligned} \tag{2.86}$$

The vector $\{y_r(t)\}$ contains the rth modal component of the output vector $\{y(t)\}$. The complex scalar $x_{m,r}(t)$ refers to the rth element of the modal state vector.

Equations (2.85) and (2.86) imply that the total response $\{y(t)\}$ can be composed by superimposing the modal components $\{y_r(t)\}$, similarly as derived in the context with numerical analyses in section 2.3. As in numerical analyses one usually assumes that only a limited number of modes contributes to the structural response, measured response data contains as well only significant contributions related to a limited number of modes that were excited sufficiently strong to be identified form the signals. Accordingly, it is also sensible to reduce the modal state-space model.

First the entries in the matrices and vectors of the modal state-space model are sorted such that the modes to be retained or held (subscript h) appear before the elements to be eliminated (subscript e):

$$\begin{aligned}
\left\{\begin{array}{c} \{\dot{x}_{m_h}(t)\}_{h\times 1} \\ \{\dot{x}_{m_e}(t)\}_{(n-h)\times 1} \end{array}\right\} &= \left[\begin{array}{cc} [\Lambda_{c_h}] & [0] \\ [0] & [\Lambda_{c_e}] \end{array}\right] \left\{\begin{array}{c} \{x_{m_h}(t)\}_{h\times 1} \\ \{x_{m_e}(t)\}_{(n-h)\times 1} \end{array}\right\} \\
&\quad + \left[\begin{array}{c} \left[L_{c_h}^T\right]_{h\times n_u} \\ \left[L_{c_e}^T\right]_{(n-h)\times n_u} \end{array}\right] \{u(t)\}_{n_u\times 1} \\
\{y(t)\}_{n_o\times 1} &= \left[\begin{array}{cc} [V_{c_h}]_{n_o\times h} & [V_{c_e}]_{n_o\times (n-h)} \end{array}\right] \left\{\begin{array}{c} \{x_{m_h}(t)\}_{h\times 1} \\ \{x_{m_e}(t)\}_{(n-h)\times 1} \end{array}\right\} \\
&\quad + [D_c]_{n_o\times m} \{u(t)\}_{n_u\times 1}
\end{aligned} \tag{2.87}$$

Setting the part to be eliminated from the derivative of the state vector with respect to time $\{\dot{x}_e(t)\}$ to zero, gives

$$\begin{aligned}
\{0\} &= [\Lambda_{c_e}] \{x_{m_e}(t)\} + \left[L_{c_e}^T\right] \{u(t)\} \\
\longrightarrow \{x_{m_e}(t)\} &= -[\Lambda_{c_e}]^{-1} \left[L_{c_e}^T\right] \{u(t)\}
\end{aligned} \tag{2.88}$$

Substituting equation (2.88) into the observation equation of the state-space model (2.87), one has

$$\begin{aligned}
\{y(t)\} &= \left[\begin{array}{cc} [V_{c_h}] & [V_{c_e}] \end{array}\right] \left\{\begin{array}{c} \{x_{m_h}(t)\} \\ -[\Lambda_{c_e}]^{-1} \left[L_{c_e}^T\right] \{u(t)\} \end{array}\right\} + [D_c] \{u(t)\} \\
&= [V_{c_h}] \{x_{m_h}(t)\} - [V_{c_e}] [\Lambda_{c_e}]^{-1} \left[L_{c_e}^T\right] \{u(t)\} + [D_c] \{u(t)\}
\end{aligned} \tag{2.89}$$

Inserting equation (2.83)

$$[D_c] = [V_c] [\Lambda_c]^{-1} [L_c]^T = [V_{c_h}] [\Lambda_{c_h}]^{-1} [L_{c_h}]^T + [V_{c_e}] [\Lambda_{c_e}]^{-1} [L_{c_e}]^T \tag{2.90}$$

into equation (2.89) yields

$$\{y(t)\} = [V_{c_h}] \{x_{m_h}(t)\} + [D_{c_h}] \{u(t)\}, \tag{2.91}$$

where

$$[D_{c_h}] = [V_c] [\Lambda_c]^{-1} [L_c]^T - [V_{c_e}] [\Lambda_{c_e}]^{-1} [L_{c_e}]^T = [V_{c_h}] [\Lambda_{c_h}]^{-1} [L_{c_r}]^T \tag{2.92}$$

Hence, the reduced modal state-space model has the following form:

$$\begin{aligned}
\{\dot{x}_{m_h}(t)\} &= [\Lambda_{c_h}] \{x_{m_h}(t)\} + [L_{c_h}]^T \{u(t)\} \\
\{y(t)\} &= [V_{c_h}] \{x_{m_h}(t)\} + [D_{c_h}] \{u(t)\}
\end{aligned} \tag{2.93}$$

2.7.3 Definition of the state-space model in discrete time domain

Both from numerical simulations and vibration measurements the available time series of excitation and response are always discretized at instants of time t. This discretization has an influence on the state-space model as is described in this section.

Usually the data is sampled with a constant time interval Δt. In numerical time step analyses the response of a system at instant of time $t = (k+1)\Delta t$ is computed by solving an initial value problem using the response from the previous time step $t_0 = k\,\Delta t$. Simlarly, the first equation of the continuos-time state-space model (2.62)

$$\{\dot{x}\,(t)\} = [A_c]\,\{x\,(t)\} + [B_c]\,\{u\,(t)\} \quad \text{or} \quad \{\dot{x}\,(t)\} - [A_c]\,\{x\,(t)\} = [B_c]\,\{u\,(t)\}$$

is now considered over an interval Δt. The solution of this linear differential equation for a given initial value $\{x\,(t_0)\}$ at an instant of time $t = t_0$ is: [83]:

$$\{x\,(t)\} = e^{[A_c](t-t_0)}\,\{x\,(t_0)\} \;+\; \int_{t_0}^{t} e^{[A_c](t-\tau)}\,[B_c]\,\{u\,(\tau)\}\,\mathrm{d}\tau \tag{2.94}$$

This equation describes the variation of the state variable $\{x\}$ depending on the initial condition $\{x\,(t_0)\}$ and excitation $u\,(t)$. As stated earlier, the sampling interval Δt of the time series is usually constant. Therefore, equation (2.94) can be re-written for $t = (k+1)\,\Delta t$ and $t_0 = k\Delta t$ as

$$\{x\,((k+1)\,\Delta t)\} = e^{[A_c]\Delta t}\,\{x\,(k\Delta t)\} \;+\; \int_{k\Delta t}^{(k+1)\Delta t} e^{[A_c]((k+1)\Delta t-\tau)}\,[B_c]\,\{u\,(\tau)\}\,\mathrm{d}\tau \tag{2.95}$$

Furthermore, one can assume that the excitation $\{u\,(\tau)\}$ is constant between two sampling instants:

$$\{u\,(\tau)\} = \{u\,(k\Delta t)\} \tag{2.96}$$

As long as both mass distribution and loading locations do not change within a time step, matrix $[B_c]$ is also constant. Hence, equation (2.95) can be re-written in the following form:

$$\{x\,((k+1)\,\Delta t)\} = e^{[A_c]\Delta t}\,\{x\,(k\Delta t)\} \;+\; \left[\int_{0}^{\Delta t} e^{[A_c]\tau'}\mathrm{d}\tau'\,[B_c]\right]\{u\,(k\Delta t)\} \tag{2.97}$$

where the variable τ in equation (2.95) has been replaced by $\tau' = (k+1)\,\Delta t - \tau$. With the notations

$$\begin{aligned}
[A] &= e^{[A_c]\Delta t} && (2.98)\\
[B] &= \int_0^{\Delta t} e^{[A_c]\tau'}\mathrm{d}\tau'\,[B_c] \;=\; ([A]-[I])\,[A_c]^{-1}\,[B_c] && (2.99)\\
[C] &= [C_c] && (2.100)\\
[D] &= [D_c] && (2.101)\\
\{x_{k+1}\} &= \{x\,((k+1)\,\Delta t)\} && (2.102)\\
\{u_k\} &= \{u\,(k\Delta t)\} && (2.103)
\end{aligned}$$

the *discrete-time state-space model* is obtained:

$$\begin{aligned}
\{x_{k+1}\} &= [A]\,\{x_k\} + [B]\,\{u_k\}\\
\{y_k\} &= [C]\,\{x_k\} + [D]\,\{u_k\}
\end{aligned} \tag{2.104}$$

It should be noticed that the left side of the first equation does not contain the derivative of the state vector $\{x_k\}$, as in the continuos-time state-space model, but the state vector at the next instant $(k+1)\Delta t$. As will be shown in more detail, the discrete-time state-space model is fundamental for several parametric modal analysis algorithms.

The discrete-time state-space model can also be transformed into modal domain. By substituting the modal decomposition of matrix $[A_c]$ (2.38) into equation (2.98) and describing the exponential function by its Taylor series one can derive the modal decomposition of the dicrete-time state-feedback matrix $[A]$:

$$\begin{aligned}
[A] &= e^{[A_c]\Delta t} \\
&= e^{[\Psi_c][\Lambda_c][\Psi_c]^{-1}\Delta t} \\
&= [I] + \Delta t\,[\Psi_c]\,[\Lambda_c]\,[\Psi_c]^{-1} + \frac{\Delta t^2}{2!}\,[\Psi_c]\,[\Lambda_c]\,[\Psi_c]^{-1}\,[\Psi_c]\,[\Lambda_c]\,[\Psi_c]^{-1} \\
&\quad + \frac{\Delta t^3}{3!}\,[\Psi_c]\,[\Lambda_c]\,[\Psi_c]^{-1}\,[\Psi_c]\,[\Lambda_c]\,[\Psi_c]^{-1}\,[\Psi_c]\,[\Lambda_c]\,[\Psi_c]^{-1}\ldots \\
&= [I] + \Delta t\,[\Psi_c]\,[\Lambda_c]\,[\Psi_c]^{-1} + \frac{\Delta t^2}{2!}\,[\Psi_c]\,[\Lambda_c]^2\,[\Psi_c]^{-1} + \frac{\Delta t^3}{3!}\,[\Psi_c]\,[\Lambda_c]^3\,[\Psi_c]^{-1}\ldots \\
&= [\Psi_c]\left([I] + \Delta t\,[\Lambda_c] + \frac{\Delta t^2}{2!}\,[\Lambda_c]^2 + \frac{\Delta t^3}{3!}\,[\Lambda_c]^3\ldots\right)[\Psi_c]^{-1} \\
&= [\Psi_c]\,e^{[\Lambda_c]\Delta t}\,[\Psi_c]^{-1} \qquad (2.105) \\
&= [\Psi_c]\,[\Lambda_d]\,[\Psi_c]^{-1} = [\Psi_c]\,diag\,[\mu_r]\,[\Psi_c]^{-1} \qquad (2.106)
\end{aligned}$$

where the diagonal matrix $[\Lambda_d]$ contains the eigenvalues of the discrete-time state-space model, μ_r, that are related to the eigenvalues of the continuous-time state-space model in the following way:

$$\mu_r = e^{\lambda_r \Delta t} \quad \Longleftrightarrow \quad \lambda_r = \frac{\ln(\mu_r)}{\Delta t} \qquad (2.107)$$

One has to notice that the eigenvectors are the same as for the contiuous-time system while the eigenvalues are different.

Example 2.6. *Matrix $[A]$ of the discrete-time state-space model becomes for the 2-dof system for which matrix $[A_c]$ is given in 2.3*

$$[A] = \begin{bmatrix} 0.990 & 9.940\times10^{-3} & 9.945\times10^{-3} & 3.281\times10^{-5} \\ 4.970\times10^{-3} & 0.983 & 1.640\times10^{-5} & 9.921\times10^{-3} \\ -1.986 & 1.978 & 0.986 & 9.854\times10^{-3} \\ 0.989 & -3.469 & 4.927\times10^{-3} & 0.978 \end{bmatrix}$$

assumung that a time step $\Delta t = 0.01\,s$ has been chosen. The eigenvalues $[\Lambda_d]$ of matrix $[A]$ are obtained as

$$[\Lambda_d] = \begin{bmatrix} 0.9763+0.2066\mathrm{i} & 0 & 0 & 0 \\ 0 & 0.9921+0.1067\mathrm{i} & 0 & 0 \\ 0 & 0 & 0.9763-0.2066\mathrm{i} & 0 \\ 0 & 0 & 0 & 0.9921-0.1067\mathrm{i} \end{bmatrix}$$

which are related by equation (2.107) to the eigenvalues $[\Lambda_c]$ given in example 2.3.

With equations (2.69):

$$[V_c] = [C_c]\,[\Psi_c]$$

and (2.100):

$$[C] = [C_c]$$

one can define the *modal output matrix of the discrete-time state-space model*:

$$[V_c] = [C_c]\,[\Psi_c] = [C]\,[\Psi_c] = [V] \tag{2.108}$$

Analogously, the *modal input matrix of the discrete-time state-space model* is defined as

$$[L]^T = [\Psi_c]^{-1}\,[B] \quad \Longleftrightarrow \quad [B] = [\Psi_c]\,[L]^T \tag{2.109}$$

Substituting the modal decompositions of the matrices $[A_c]$ and $[A]$

$$\begin{aligned} [A_c] &= [\Psi_c]\,[\Lambda_c]\,[\Psi_c]^{-1} \\ [A] &= [\Psi_c]\,[\Lambda_d]\,[\Psi_c]^{-1} \end{aligned}$$

into equation (2.99)

$$[B_c] = [A_c]\,([A] - [I])^{-1}\,[B]$$

gives

$$[B_c] = [\Psi_c]\,[\Lambda_c]\,[\Psi_c]^{-1}\left([\Psi_c]\,[\Lambda_d]\,[\Psi_c]^{-1} - [I]\right)^{-1}[B] \tag{2.110}$$

Since matrix $[\Lambda_d]$ is a diagonal matrix, equation (2.110) simplifies to

$$[B_c] = [\Psi_c]\,[\Lambda_c]\,([\Lambda_d] - [I])^{-1}\,[\Psi_c]^{-1}\,[B] \tag{2.111}$$

With equation (2.68) and (2.109) the following relation between the modal input matrices of the continuous-time and discrete-time state-space models, respectively, becomes

$$\begin{aligned} [L_c]^T &= [\Psi_c]^{-1}\,[\Psi_c]\,[\Lambda_c]\,([\Lambda_d] - [I])^{-1}\,[\Psi_c]^{-1}\,[\Psi_c]\,[L]^T \\ [L_c]^T &= [\Lambda_c]\,([\Lambda_d] - [I])^{-1}\,[L]^T \end{aligned} \tag{2.112}$$

It can be deduced from equations (2.83) and (2.101) that

$$[D] = [D_c] = [V_c]\,[\Lambda_c]^{-1}\,[L_c]^T \tag{2.113}$$

According to equation (2.108) $[V_c]$ can be replaced by $[V]$ which leads with equation (2.112) to

$$[D] = [V]\,([\Lambda_d] - [I])^{-1}\,[L]^T \tag{2.114}$$

Applying the same transformation as in equation (2.65), the discrete-time state vector can be formulated also in modal coordinates:

$$\{x_k\} = [\Psi_c]\,\{x_{m,k}\} \tag{2.115}$$

Substituting the relations derived above, the discrete-time state-space model can be transferred into modal domain:

$$\begin{aligned} \{x_{m,k+1}\} &= [\Psi_c]\,[\Lambda_d]\,\{x_{m,k}\} + [\Psi_c]\,[L]^T\,\{u_k\} \\ \{y_k\} &= [V]\,\{x_{m,k}\} + [V]\,([\Lambda_d] - [I])^{-1}\,[L]^T\,\{u_k\} \end{aligned} \tag{2.116}$$

which has a very similar structure as the modal discrete-time state-space model in equation (2.85)

2.7.4 Response to an impulse excitation

Assuming that the initial condition of the system is given by $\{x_0\} = \{0\}$, one can compute the structural response of the discrete-time state-space model with the respective system matrices in the following way:

$$\begin{aligned}
\{x_0\} &= \{0\} \\
\{y_0\} &= [D]\{u_0\} \qquad (2.117)\\
\{x_1\} &= [B]\{u_0\} \\
\{y_1\} &= [C][B]\{u_0\} + [D]\{u_1\} \\
\{x_2\} &= [A][B]\{u_0\} + [B]\{u_1\} \\
\{y_2\} &= [C][A][B]\{u_0\} + [C][B]\{u_1\} + [D]\{u_2\} \\
\{x_3\} &= [A]^2[B]\{u_0\} + [A][B]\{u_1\} + [B]\{u_2\} \\
\{y_3\} &= [C][A]^2[B]\{u_0\} + [C][A][B]\{u_1\} + [C][B]\{u_2\} + [D]\{u_3\} \\
&\vdots \\
\{x_k\} &= \sum_{i=1}^{k} [A]^{i-1}[B]\{u_{k-i}\} \qquad (2.118)\\
\{y_k\} &= \sum_{i=1}^{k} [C][A]^{i-1}[B]\{u_{k-1}\} + [D]\{u_k\} \qquad (2.119)
\end{aligned}$$

The dynamic behaviour of a linear elastic system can be described by its impulse response function (IRF) which describes the system response to a unit impulse at instant $t = 0$ ($u_i(0) = 1;\ u_i(k) = 0;\ k > 0$). As the frequency response function (FRF) can relate the input at one degree-of-freedom to the output at any other degree-of-freedom in frequency domain, one can describe the same input-output relation between two degrees-of-freedom in time domain by a respective IRF.

Since the excitation $\{u_i(k)\}$ is zero for all instants of time except for $k = 0$, the IRF matrices can be computed for any time lag between excitation and response instant from the system matrices of the discrete-time state-space model based on equations (2.117) and (2.119):

$$[h_0] = [D] \qquad (2.120)$$

$$[h_k] = [C][A]^{k-1}[B], \quad (k > 0) \qquad (2.121)$$

Inserting the modal decompositions of matrices $[A]$, $[B]$, $[C]$ und $[D]$, given by equations (2.97), (2.109), (2.108) and (2.114), the relations (2.120) and (2.121) become

$$[h_0] = [V]([\Lambda_d] - [I])^{-1}[L]^T \qquad (2.122)$$

$$[h_k] = [V][\Lambda_d]^{k-1}[L]^T, \quad (k > 0) \qquad (2.123)$$

Example 2.7. *If the same system matrices $[A]$, $[B]$, $[C]$ and $[D]$ as computed in the previous examples are used, the acceleration impulse response functions at the two degrees-of-freedom of the system shown in figure 2.1 can be computed based on equations (2.120) and (2.121). To obtain all impulse response functions, it is necessary to assume excitations at all degrees-of-freedom in matrix $[B_2]$ which is included in matrix $[D]$. The resulting functions with respect of time are shown in figure 2.6.*

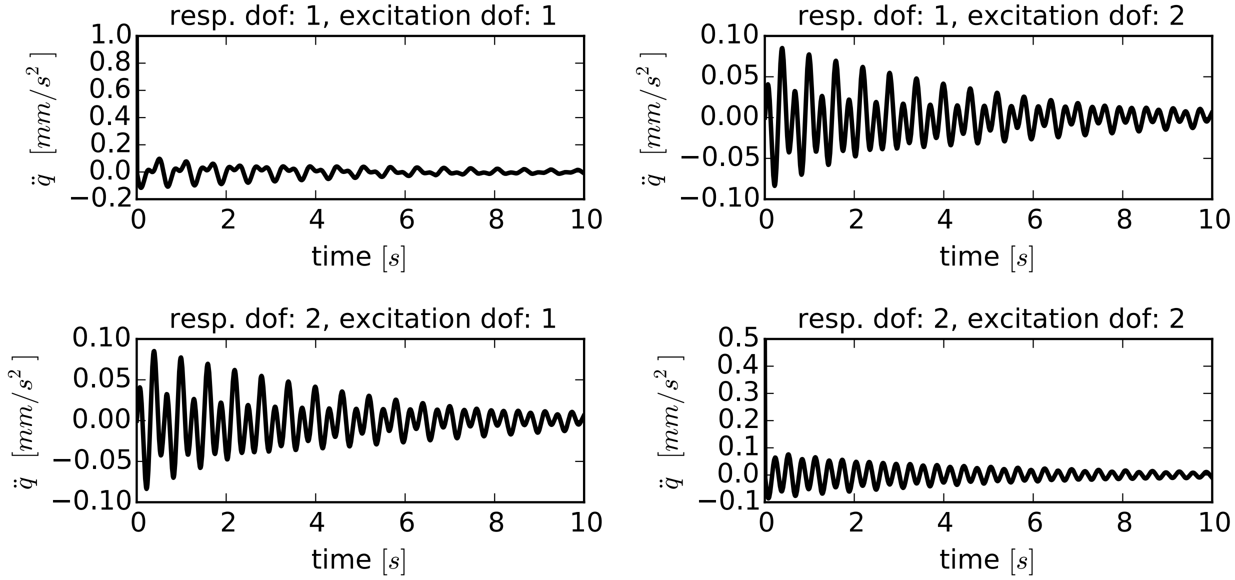

Figure 2.6: Impulse response functions for the 2-dof system

From the diagrams in figure 2.6 one can see how the accelerations at the location of excitation follow the impulse during the loading period and change to a free decay afterwards as it is also the case for single degree-of-freedom systems. If the impulse excitation is applied to another degree-of-freedom, the impulse response function shows only the shape of a freely decaying vibration.

2.7.5 The stochastic forward model

So far all derived models considered exclusively deterministic excitations. To overcome this limitation, uncertainties due to random influences, for example in modelling of dynamic loads, are taken into account by means of a stochastic *process noise vector* $\{w_k\}$ while *measurement or output noise* is represented by the random process $\{v_k\}$. By introducing these two components into the deterministic discrete-time state-space model one obtains:

$$\begin{aligned} \{x_{k+1}\} &= [A]\{x_k\} + [B]\{u_k\} + \{w_k\} \\ \{y_k\} &= [C]\{x_k\} + [D]\{u_k\} + \{v_k\} \end{aligned} \tag{2.124}$$

Assuming that both random processes have zero mean and a constant spectrum (white noise), the covariance matrices for two arbitrary instants of time k_1 and k_2 are

$$\left[\mathbf{E}\left[\left\{\begin{array}{c} \{w_{k_1}\} \\ \{v_{k_1}\} \end{array}\right\}\left[\begin{array}{cc} \{w_{k_2}\}^T & \{v_{k_2}\}^T \end{array}\right]\right]\right] = \left[\begin{array}{cc} [Q] & [S] \\ [S]^T & [R] \end{array}\right] \delta_{k_1 k_2} \tag{2.125}$$

where $\mathbf{E}[\cdot]$ denotes the expected value and $\delta_{k_1 k_2}$ is the Kronecker symbol

$$\delta_{k_1 k_2} = \left\{\begin{array}{ll} 1 & \text{for} \quad k_1 = k_2 \\ 0 & \text{for} \quad k_1 \neq k_2 \end{array}\right. \tag{2.126}$$

The models described here shall be applied to output-only modal identification which means that only the system response to a stochastic excitation is measured. Consequently, it is not possible to distinguish between the stochastic excitations $\{u_k\}$ and the noise signals $\{w_k\}$ or $\{v_k\}$ in equation (2.124). Therefore it is convenient to combine the stochastic excitation with the noise components in the state-space model. The same statistical properties as for the noise components (zero mean, white noise) are assumed for the excitations. Accordingly, the *discrete-time stochastic state-space model* is obtained as:

$$\begin{aligned} \{x_{k+1}\} &= [A]\{x_k\} + \{w_k\} \\ \{y_k\} &= [C]\{x_k\} + \{v_k\} \end{aligned} \tag{2.127}$$

After having discussed some properties of the stochastic input processes $\{w_k\}$ and $\{v_k\}$, the properties of the stochastic processes $\{x_k\}$ and $\{y_k\}$ representing the system output need to be considered. As for the input zero mean stationarity was assumed, it is reasonable to apply this assumption as well to the system output:

$$\left[\mathbf{E}\left[\{x_k\}\{x_k\}^T\right]\right] = [\Sigma] \;, \qquad \{\mathbf{E}\left[\{x_k\}\right]\} = \{0\} \tag{2.128}$$

where the *stochastic state covariance matrix* $[\Sigma]$ is independent from instant k. Since $\{w_k\}$ and $\{v_k\}$ have zero mean and are independent from the respective time instant,

$$\left[\mathbf{E}\left[\{x_k\}\{w_k\}^T\right]\right] = \left[\mathbf{E}\left[\{w_k\}\{x_k\}^T\right]\right] = [0] \;, \qquad \left[\mathbf{E}\left[\{x_k\}\{v_k\}^T\right]\right] = \left[\mathbf{E}\left[\{v_k\}\{x_k\}^T\right]\right] = [0] \tag{2.129}$$

is also valid.

Furthermore, the *output covariance matrix* $[R_i]$

$$[R_i] = \left[\mathbf{E}\left[\{y_{k+i}\}\{y_k\}^T\right]\right] \tag{2.130}$$

and the *next state output covariance matrix*

$$[G] = \left[\mathbf{E}\left[\{x_{k+1}\}\{y_k\}^T\right]\right] \tag{2.131}$$

are defined for any arbitrary time lag i.

From the assumptions for the process $\{x_k\}$ can be concluded for the first equation of the stochastic state-space model (2.127)

$$\{\mathbf{E}\left[\{x_k\}\right]\} = \{\mathbf{E}\left[\{x_{k+1}\}\right]\} = \{\mathbf{E}\left[[A]\{x_k\} + \{w_k\}\right]\} \tag{2.132}$$

Consequently, the state covariance matrix $[\Sigma]$ can be re-written in the following way:

$$\begin{aligned} [\Sigma] &= \left[\mathbf{E}\left[\{x_k\}\{x_k\}^T\right]\right] = \left[\mathbf{E}\left[\left([A]\{x_k\} + \{w_k\}\right)\left(\{x_k\}^T[A]^T + \{w_k\}^T\right)\right]\right] \qquad (2.133) \\ &= [A]\underbrace{\left[\mathbf{E}\left[\{x_k\}\{x_k\}^T\right]\right]}_{=[\Sigma]}[A]^T + [A]\underbrace{\left[\mathbf{E}\left[\{x_k\}\{w_k\}^T\right]\right]}_{=[0]} + \underbrace{\left[\mathbf{E}\left[\{w_k\}\{x_k\}^T\right]\right]}_{=[0]}[A]^T \\ &\quad + \underbrace{\left[\mathbf{E}\left[\{w_k\}\{w_k\}^T\right]\right]}_{=[Q]} \\ [\Sigma] &= [A][\Sigma][A]^T + [Q] \qquad (2.134) \end{aligned}$$

Similarly, one has for the discrete-time output covariance matrix with a time lag $i = 0$

$$\begin{aligned}
[R_0] &= \left[\mathbf{E}\left[\{y_k\}\{y_k\}^T\right]\right] = \left[\mathbf{E}\left[\left([C]\{x_k\} + \{v_k\}\right)\left(\{x_k\}^T[C]^T + \{v_k\}^T\right)\right]\right] \\
&= [C]\underbrace{\left[\mathbf{E}\left[\{x_k\}\{x_k\}^T\right]\right]}_{=[\Sigma]}[C]^T + [C]\underbrace{\left[\mathbf{E}\left[\{x_k\}\{v_k\}^T\right]\right]}_{=[0]} + \underbrace{\left[\mathbf{E}\left[\{v_k\}\{x_k\}^T\right]\right]}_{=[0]}[C]^T \\
&\quad + \underbrace{\left[\mathbf{E}\left[\{v_k\}\{v_k\}^T\right]\right]}_{=[R]}
\end{aligned} \tag{2.135}$$

$$[R_0] = [C][\Sigma][C]^T + [R] \tag{2.136}$$

and for the next-state output covariance matrix

$$\begin{aligned}
[G] &= \left[\mathbf{E}\left[\{x_{k+1}\}\{y_k\}^T\right]\right] = \left[\mathbf{E}\left[\left([A]\{x_k\} + \{w_k\}\right)\left(\{x_k\}^T[C]^T + \{v_k\}^T\right)\right]\right] \\
&= [A]\underbrace{\left[\mathbf{E}\left[\{x_k\}\{x_k\}^T\right]\right]}_{=[\Sigma]}[C]^T + [A]\underbrace{\left[\mathbf{E}\left[\{x_k\}\{v_k\}^T\right]\right]}_{=[0]} + \underbrace{\left[\mathbf{E}\left[\{w_k\}\{x_k\}^T\right]\right]}_{=[0]}[C]^T \\
&\quad + \underbrace{\left[\mathbf{E}\left[\{w_k\}\{v_k\}^T\right]\right]}_{=[S]}
\end{aligned} \tag{2.137}$$

$$[G] = [A][\Sigma][C]^T + [S] \tag{2.138}$$

From the equations of the discrete-time stochastic state-space model (2.127) one can deduce that

$$\{y_{k+i}\} = [C]\{x_{k+i}\} + \{v_{k+i}\} \tag{2.139}$$

and

$$\{x_{k+i}\} = [A]^i\{x_k\} + \sum_{j=1}^{i}[A]^{j-1}\{w_{k+j-1}\} \tag{2.140}$$

Substituting equations (2.139) and (2.140) into equation (2.130) yields

$$\begin{aligned}
[R_i] &= \left[\mathbf{E}\left[\left([C][A]^i\{x_k\} + \sum_{j=1}^{i}[A]^{j-1}\{w_{k+j-1}\} + \{v_{k+i}\}\right)\{y_k\}^T\right]\right] \\
&= [C][A]^i\left[\mathbf{E}\left[\{x_k\}\{y_k\}^T\right]\right] + \sum_{j=1}^{i}[A]^{j-1}\underbrace{\left[\mathbf{E}\left[\{w_{k+j-1}\}\{y_k\}^T\right]\right]}_{=[0]} + \underbrace{\left[\mathbf{E}\left[\{v_{k+i}\}\{y_k\}^T\right]\right]}_{=[0]} \\
&\downarrow \longleftarrow \{x_k\} = [A]^{-1}\{x_{k+1}\} - [A]^{-1}\{w_k\} \\
&= [C][A]^{i-1}\left[\underbrace{\mathbf{E}\left[\{x_{k+1}\}\{y_k\}^T\right]}_{=[G]} - \underbrace{\mathbf{E}\left[\{w_k\}\{y_k\}^T\right]}_{=[0]}\right]
\end{aligned}$$

$$[R_i] = [C][A]^{i-1}[G]; \qquad i = 1, 2, \dots \tag{2.141}$$

Similarly one can derive [138]

$$[R_{-i}] = [G]^T\left([A]^{i-1}\right)^T[C]^T; \qquad i = 1, 2, \dots \tag{2.142}$$

Equation (2.141) looks very similar to equation (2.121) that was derived for the representation of the impulse response function. As in equation (2.123), it is obvious to substitute the modal decomposition of matrix $[A]$ (2.106) into equation (2.141), what delivers a representation of the output covariance in modal domain:

$$\begin{aligned}[R_i] &= [C]\,[A]^{i-1}\,[G] \\ &= [C]\,[\Psi_c]\,[\Lambda_d]^{i-1}\,[\Psi_c]^{-1}\,[G] \\ &= [V]\,[\Lambda_d]^{i-1}\,[G_m]\,,\end{aligned} \tag{2.143}$$

where $[G_m]$ denotes the *next modal state – output covariance* or *stochastic modal participation matrix*. A comparison with equation (2.123) shows that matrix $[G_m]$ has in output-only modal analysis apparently the same meaning as matrix $[L]^T$ in classical modal analysis with measured input and output. Furthermore, it can be concluded that an appropriate decomposition of the output covariance matrix $[R_i]$, which is entirely based on measured response data, can be used to identify the modal parameters of a considered structure that are included in the matrices $[V]$ and $[\Lambda_d]$.

2.8 State-space models in frequency domain

2.8.1 Transformation of the continuos-time state-space model into frequency domain

In section 2.7.3 has been mentioned that state-space models form the base of several parametric modal identification algorithms. Some of these algorithms were developed to consider the measured signals not in time but in frequency domain. For these methods, a respective transformation of the models explained in the preceding sections is required. This gives reason for a corresponding presentation of some theoretical background of such transformations and its application to models used in structural dynamics.

2.8.1.1 Laplace transform

As has already been shown in section 2.6, it is possible to transfer the differential equation of motion in its state-space formulation into a system of algebraic equations (2.47). In this section this concept is introduced in a more general way as it has been proposed, for example, by [83] and [67]. Starting point for the derivations is the *Laplace transform* $G(s)$ of a function $g(t)$ which is defined as [102]

$$G(s) = \mathcal{L}\left\{g(t)\right\}(s) = \int_{-\infty}^{\infty} g(t)\,e^{-st}\mathrm{d}t \tag{2.144}$$

The Laplace transform is also called s-transform referring to the complex variable s. In the special case that the transformation variable $s = \mathrm{i}\omega$, the Laplace transform becomes the *Fourier transform*:

$$G(\omega) = \mathcal{F}\left\{g(t)\right\}(\omega) = \mathcal{L}\left\{g(t)\right\}(\mathrm{i}\omega) = \int_{-\infty}^{\infty} g(t)\,e^{-\mathrm{i}\omega t}\mathrm{d}t \tag{2.145}$$

Due to the fact that the time series to be analized in practical applications start usually at instant of time $t = 0$, which means that all values of the function to be transformed are zero for $-\infty \leq t < 0$, in the literature often only the one-sided Laplace transform is considered [59], [83] [128].

2.8.1.2 Application of the Laplace transform to the equation of motion

Assuming zero initial conditions, the one-sided Laplace transform of the equation of motion (2.2) can be written as [83]:

$$\Big([M]\,s^2 + [C_2]\,s + [K]\Big)\;\{Q(s)\} \;=\; \{F(s)\} \tag{2.146}$$

or solved for the response vector:

$$\{Q(s)\} \;=\; \Big[[M]\,s^2 + [C_2]\,s + [K]\Big]^{-1}\;\{F(s)\} \tag{2.147}$$

The inverse matrix on the right handside of equation (2.147) relates the excitation $\{F(s)\}$ to the response $\{Q(s)\}$ in the Laplace domain and is therefore also called *transfer function matrix* $[H(s)]$:

$$[H(s)] \;=\; \Big[[M]\,s^2 + [C_2]\,s + [K]\Big]^{-1} \tag{2.148}$$

Since the inverse of a matrix $[\cdot]$ is calculated by dividing the adjoint of the matrix by its determinant $[\cdot]^{-1} = \dfrac{1}{\det[\cdot]}\,\mathrm{adj}\,[\cdot]$, the transfer function matrix can be formulated as a matrix fractional polynomial [83]:

$$\Big[[M]\,s^2 + [C_2]\,s + [K]\Big]^{-1}_{N\times N} \;=\; \sum_{i=0}^{N-2}\,[N_i]\,\frac{s^{2N-2-i}}{d(s)} \tag{2.149}$$

with the numerator matrix

$$[N(s)]_{N\times N} \;=\; [N_0]\,s^{2N-2} \;+\; [N_1]\,s^{2N-2-1} \;+\; [N_2]\,s^{2N-2-2} \;+\; \ldots \;+\; [N_{2N-2}] \tag{2.150}$$

and the common denominator polynomial

$$d(s) \;=\; d_0\,s^{2N} \;+\; d_1\,s^{2N-1} \;+\; d_2\,s^{2N-2} \;+\; \ldots \;+\; d_{2N} \tag{2.151}$$

While it is clear from equation (2.149) that the matrices $[N_i]$ can be derived from matrices $[M]$, $[C_2]$ and $[K]$ it is in the inverse direction also possible to obtain matrices $[M]$, $[C_2]$ and $[K]$ provided that matrices $[N_0]$, $[N_1]$ and $[N_2]$ are known. Pre-multiplication of equation (2.149) by $d(s)\;[[M]\,s^2 + [C_2]\,s + [K]]$ results in

$$\begin{aligned} &(d_0\,s^{2N} \;+\; d_1\,s^{2N-1} \;+\; d_2\,s^{2N-2} \;+\; \ldots \;+\; d_{2N})\;[I] \\ &= [[M]\,s^2 + [C_2]\,s + [K]]\;\Big[[N_0]\,s^{2N-2} \;+\; [N_1]\,s^{2N-2-1} \;+\; [N_2]\,s^{2N-2-2} \;+\; \ldots \;+\; [N_{2N-2}]\Big] \end{aligned} \tag{2.152}$$

The first three components of this matrix polynomial are

$$\begin{array}{lrcl} \text{for } s^{2N}: & d_0\;[I] & = & [M]\,[N_0] \\ \text{for } s^{2N-1}: & d_1\;[I] & = & [C_2]\,[N_0] \;+\; [M]\,[N_1] \\ \text{for } s^{2N-2}: & d_2\;[I] & = & [K]\,[N_0] \;+\; [C_2]\,[N_1] \;+\; [M]\,[N_2] \end{array} \tag{2.153}$$

$$\begin{aligned} \therefore \qquad [M] &= d_0\,[N_0]^{-1} \qquad \longrightarrow [N_0]^{-1} = \frac{1}{d_0}\,[M] \\ [C_2] &= \left(d_1\,[I] - [M]\,[N_1]\right)\frac{1}{d_0}\,[M] \\ [K] &= \left(d_2\,[I] - [C_2]\,[N_1] - [M]\,[N_2]\right)\frac{1}{d_0}\,[M] \end{aligned} \tag{2.154}$$

Example 2.8. *From equation (2.1) the following mass, damping and stiffness matrices of the two-degree-of-freedom system are given:*

$$[M] = \begin{bmatrix} m_1 & 0 \\ 0 & m_2 \end{bmatrix} \qquad [C_2] = \begin{bmatrix} c_1 & -c_1 \\ -c_1 & c_1 + c_2 \end{bmatrix} \qquad [K] = \begin{bmatrix} k_1 & -k_1 \\ -k_1 & k_1 + k_2 \end{bmatrix}$$

The dynamic stiffness matrix is then

$$[H]^{-1} = \Big[[M]\,s^2 + [C_2]\,s + [K]\Big] = \begin{bmatrix} m_1\,s^2 + c_1\,s + k_1 & -c_1\,s - k_1 \\ -c_1\,s - k_1 & m_2\,s^2 + (c_1 + c_2)s + k_1 + k_2 \end{bmatrix}$$

Accordingly, its adjoint and determinant are

$$\begin{aligned} \operatorname{adj}\Big[[M]\,s^2 + [C_2]\,s + [K]\Big] &= \begin{bmatrix} m_2\,s^2 + (c_1 + c_2)s + k_1 + k_2 & c_1\,s + k_1 \\ c_1\,s + k_1 & m_1\,s^2 + c_1\,s + k_1 \end{bmatrix} \\ \det\Big[[M]\,s^2 + [C_2]\,s + [K]\Big] &= m_1 m_2\,s^4 \\ &\quad + \left(m_1\,(c_1 + c_2) + m_2 c_1\right)\,s^3 \\ &\quad + \left(m_1\,(k_1 + k_2) + m_2 k_1 + c_1 c_2\right)\,s^2 \\ &\quad + \left(k_1 c_2 + k_2 c_1\right)\,s \\ &\quad + k_1 k_2 \end{aligned}$$

from which the numerator matrix polynomial coefficients and the denominator polynomial coefficients are obtained as

$$[N_0] = \begin{bmatrix} m_2 & 0 \\ 0 & m_1 \end{bmatrix} \qquad [N_1] = \begin{bmatrix} c_1 + c_2 & c_1 \\ c_1 & c_1 \end{bmatrix} \qquad [N_2] = \begin{bmatrix} k_1 + k_2 & k_1 \\ k_1 & k_1 \end{bmatrix}$$

$$\begin{aligned} d_0 &= m_1\,m_2 \\ d_1 &= \left(m_1\,(c_1 + c_2) + m_2 c_1\right) \\ d_2 &= \left(m_1\,(k_1 + k_2) + m_2 k_1 + c_1 c_2\right) \\ d_3 &= \left(k_1 c_2 + k_2 c_1\right) \\ d_4 &= k_1\,k_2 \end{aligned}$$

This yields with reference to equations (2.153) and (2.154)

- *for* s^2*:*

$$\begin{aligned}
d_0\,[I] &= \begin{bmatrix} m_1m_2 & 0 \\ 0 & m_1m_2 \end{bmatrix} \\
[M]\,[N_0] &= \begin{bmatrix} m_1 & 0 \\ 0 & m_2 \end{bmatrix} \begin{bmatrix} m_2 & 0 \\ 0 & m_1 \end{bmatrix} = \begin{bmatrix} m_1m_2 & 0 \\ 0 & m_1m_2 \end{bmatrix} = d_0\,[I] \\
&\textit{and} \\
\tfrac{1}{d_0}\,[M] &= \begin{bmatrix} \dfrac{1}{m_2} & 0 \\ 0 & \dfrac{1}{m_1} \end{bmatrix}
\end{aligned}$$

- *for* s^1*:*

$$\begin{aligned}
d_1\,[I] &= \begin{bmatrix} m_1\,(c_1+c_2)+m_2c_1 & 0 \\ 0 & m_1\,(c_1+c_2)+m_2c_1 \end{bmatrix} \\
[C_2]\,[N_0] &= \begin{bmatrix} m_2c_1 & -m_1c_1 \\ -m_2c_1 & m_1\,(c_1+c_2) \end{bmatrix} \\
[M]\,[N_1] &= \begin{bmatrix} m_1\,(c_1+c_2) & m_1c_1 \\ m_2c_1 & m_2c_1 \end{bmatrix} \\
[C_2]\,[N_0]+[M]\,[N_1] &= \begin{bmatrix} m_1\,(c_1+c_2)+m_2c_1 & 0 \\ 0 & m_1\,(c_1+c_2)+m_2c_1 \end{bmatrix} = d_1\,[I]
\end{aligned}$$

and

$$[d_1\,[I]\;-\;[M]\,[N_1]]\cdot\frac{1}{d_0}\,[M] \;=\; \begin{bmatrix} c_1 & -c_1 \\ -c_1 & c_1+c_2 \end{bmatrix} = [C_2]$$

- *for* s^0*:*

$$\begin{aligned}
d_2\,[I] &= \begin{bmatrix} m_1\,(k_1+k_2)+m_2k_1+c_1c_2 & 0 \\ 0 & m_1\,(k_1+k_2)+m_2k_1+c_1c_2 \end{bmatrix} \\
[K]\,[N_0] &= \begin{bmatrix} m_2k_1 & -m_1k_1 \\ -m_2k_1 & m_1\,(k_1+k_2) \end{bmatrix} \\
[C_2]\,[N_1] &= \begin{bmatrix} c_1c_2 & 0 \\ 0 & c_1c_2 \end{bmatrix} \\
[M]\,[N_2] &= \begin{bmatrix} m_1\,(k_1+k_2) & m_1k_1 \\ m_2k_1 & m_2k_1 \end{bmatrix} \\
[K]\,[N_0]+[C_2]\,[N_1]+[M]\,[N_2] &= \begin{bmatrix} m_1\,(k_1+k_2)+m_2k_1+c_1c_2 & 0 \\ 0 & m_1\,(k_1+k_2)+m_2k_1+c_1c_2 \end{bmatrix} \\
&= d_2\,[I]
\end{aligned}$$

and

$$[d_2\,[I]\;-\;[C_2]\,[N_1]\;-\;[M]\,[N_2]]\cdot\frac{1}{d_0}\,[M] \;=\; \begin{bmatrix} k_1 & -k_1 \\ -k_1 & k_1+k_2 \end{bmatrix} = [K]$$

2.8.1.3 Application of the Laplace transform to the continuous-time state-space model

Similarly as for the equation of motion, the continuous-time state-space model (2.62) is transformed into Laplace domain as

$$\begin{aligned} s\,\{X\,(s)\} &= [A_c]\,\{X\,(s)\} + [B_c]\,\{U\,(s)\} \\ \{Y\,(s)\} &= [C_c]\,\{X\,(s)\} + [D_c]\,\{U\,(s)\} \end{aligned} \tag{2.155}$$

Solving the first of equations (2.155) for $\{X\,(s)\}$

$$\{X(s)\} = \left[\left[s\,[I] - [A_c]\right]^{-1}\,[B_c]\right]\{U(s)\} \tag{2.156}$$

and substing into the second equation produces

$$\{Y(s)\} = \left[[C_c]\left[s\,[I] - [A_c]\right]^{-1}\,[B_c] + [D_c]\right]\{U(s)\} \tag{2.157}$$

Equations (2.156) and (2.157) relate the input vector $\{U(s)\}$ with the state vector $X(s)$ and the output vector $\{Y(s)\}$, respectively. Accordingly, the matrices $\left[\left[s\,[I] - [A_c]\right]^{-1}\,[B_c]\right]$ and $\left[[C_c]\left[s\,[I] - [A_c]\right]^{-1}\,[B_c] + [D_c]\right]$ are the respective transfer functions. Similar to equation (2.149), the *transfer function* or *impulse response s-Transform* ([83]) becomes

$$[H(s)] = \left[[C_c]\left[s\,[I] - [A_c]\right]^{-1}\,[B_c] + [D_c]\right] \tag{2.158}$$

which links the excitation $\{U(s)\}$ to the output $\{Y(s)\}$. This can also be expressed by a common denominator model, as for instance described in [91]:

$$[H(s)] = \frac{1}{\det\left[s\,[I] - [A_c]\right]}\left[[C_c]\ \mathrm{adj}\left[s\,[I] - [A_c]\right]\,[B_c] + \det\left[s\,[I] - [A_c]\right][D_c]\right] \tag{2.159}$$

2.8.2 Transformation of the discrete-time state-space model into frequency domain

2.8.2.1 z-transform

In section 2.8.1 was shown that the Laplace transform $G(s)$ represents a continuous-time function $g(t)$ in frequency domain. Due to the fact that signals recorded during dynamic tests are digitized, an equivalent transformation for the application to discrete-time signals was developed, the *z-transform.* Provided that a digital signal has been sampled at constant intervals Δt,

$$y_k = y(k\,\Delta t), \qquad k = 0, 1, 2, \ldots$$

the z-transform is defined as

$$Y(z) \;=\; \mathcal{Z}\left[y(k\,\Delta t)\right] \;=\; \sum_{k=-\infty}^{\infty} y(k\,\Delta t)\,z^{-k} \tag{2.160}$$

Similarly to variable s in the Laplace transform, z is also a complex variable. As already mentioned in context with the Laplace transform, one assumes in many practical applications zero inital conditions. Therefore, as for the Laplace transform, in many cases also only the one-sided z-transform is discussed in literature [59], [83], [129], [55] while other authors' derivations refer to the two-sided z-transform [101]. As for the one-sided Laplace transform, it is assumed that the values of the discrete series to be transformed are zero for negative time instants. Accordingly, the lower limit of the summation changes for the one-sided z-transform from $-\infty$ to 0.

As, for example, described in [83], the Laplace transform of a sampled time series is equal to its z-transform if

$$z = e^{s\,\Delta t}$$

Then the one-sided z-transform becomes

$$Y(z) \;=\; Y(e^{s\,\Delta t}) \;=\; \sum_{k=0}^{\infty} y(k\,\Delta t)\,\left(e^{s\,\Delta t}\right)^{-k} \;=\; \sum_{k=0}^{\infty} y(k\,\Delta t)\,e^{-sk\,\Delta t} \tag{2.161}$$

As was shown in section 2.8.1, the Fourier transform is a special case of the Laplace transform. Similarly, the z-transform becomes the *Discrete Fourier transform*(DFT) if $s = i\omega \;\rightarrow\; z = e^{-\mathrm{i}\omega k\,\Delta t}$ is choosen.

$$Y(\omega) \;=\; Y(z = e^{\mathrm{i}\omega\,\Delta t}) \;=\; \sum_{k=-\infty}^{\infty} y(k\,\Delta t)\,\left(e^{\mathrm{i}\omega\,\Delta t}\right)^{-k} \;=\; \sum_{k=-\infty}^{\infty} y(k\,\Delta t)\,e^{-\mathrm{i}\omega k\,\Delta t} \tag{2.162}$$

2.8.2.2 Application of the z-transform to the discrete-time state-space model

In section 2.8.1 the Laplace transform of the continuous-time state-space model has been discussed. Similarly, the z-transform of the discrete-time state-space model (2.104)

$$\begin{aligned} \{x_{k+1}\} &= [A]\,\{x_k\} + [B]\,\{u_k\} \\ \{y_k\} &= [C]\,\{x_k\} + [D]\,\{u_k\} \end{aligned}$$

is derived in the following.

Assuming zero initial conditions, ($\{x(k \le 0)\} = \{0\}$), the z-transform of $\{x(k)\}\,,\; k = 0, 1, 2, \ldots$ is according to equation (2.160)

$$\{X(z)\} \;=\; \mathcal{Z}\,[\{x(k)\}] \;=\; \sum_{k=0}^{\infty} \{x(k)\}\;z^{-k} \tag{2.163}$$

It follows for $\{x(k+1)\}$:

$$\begin{aligned} \mathcal{Z}\,[\{x(k+1)\}] \;&=\; \sum_{k=0}^{\infty} \{x(k+1)\}\;z^{-k} \;=\; z\sum_{k=0}^{\infty} \{x(k+1)\}\;z^{-(k+1)} \\ &=\; z\left(\sum_{k=-1}^{\infty} \{x(k+1)\}\;z^{-(k+1)} \;-\; x(0)\right) \\ \downarrow \;&\longleftarrow\; k' = k+1 \\ &=\; z\left(\sum_{k'=0}^{\infty} \{x(k')\}\;z^{k'} \;-\; \{x(0)\}\right) \;=\; z\,(\{X(z)\} \;-\; \{x(0)\}) \end{aligned}$$

Recalling the assumption of zero initial condition, ($\{x(0)\} = \{0\}$), the z-transform of the first equation of the discrete-time state-space model is therefore

$$\begin{aligned} z\,\{X(z)\} &= [A]\,\{X(z)\} + [B]\,\{U(z)\} \\ [z\,[I] - [A]]\,\{X(z)\} &= [B]\,\{U(z)\} \\ \{X(z)\} &= [z\,[I] - [A]]^{-1}\,[B]\,\{U(z)\} \end{aligned} \tag{2.164}$$

The z-transform of the second equation of the discrete-time state-space model becomes then

$$\begin{aligned} \{Y(z)\} &= [C]\,\{X(z)\} + [D]\,\{U(z)\} \\ &= \Big[[C]\,[z\,[I] - [A]]^{-1}\,[B] \,+\, [D]\Big]\,\{U(z)\} \end{aligned} \tag{2.165}$$

It can be concluded from equations (2.164) and (2.165) that the z-transform of the discrete-time state-space model has a very similar structure as the Laplace transform of the continuous-time state-space model.

2.9 Matrix fraction descriptions

Regardless which of the models described in the preceding sections is considered, they have all in common that they describe an input-output relation. One of the major steps in an inverse analysis is the link between input-output relations observed in an experiment with respective theoretical models. One very common way to describe input-output relations in structural dynamics from data measured during a test is given by frequency response functions (FRF). How an FRF can be obtained from input-output measurements will be shown in section 2.10. In this section it is assumed, that FRF's are available from tests. To derive modal parameters from FRF data, a suitable decomposition is necessary.

One possibility for such a decomposition is the identification of a common denominator model, where the components of the system matrices occur in a numerator polynomial matrix and a common denominator polynomial, as derived in equations (2.148) to (2.151). A second common denominator model for the transfer function matrix was obtained from the state-space model in equation (2.159). Using the more general formulation of the Laplace domain, the two mentioned models are re-called:

$$[H(s)]_{N\times N} = \Big[[M]\,s^2 + [C_2]\,s + [K]\Big]^{-1} = \frac{\operatorname{adj}\,[[M]\,s^2 + [C_2]\,s + [K]]}{\det\,[[M]\,s^2 + [C_2]\,s + [K]]} = \frac{[N(s)]}{d(s)} \tag{2.166}$$

$$[H(s)]_{n_o\times n_u} = \frac{[[C_c]\;\operatorname{adj}\,[s\,[I] - [A_c]]\;[B_c] + \det\,[s\,[I] - [A_c]]\,[D_c]]}{\det\,[s\,[I] - [A_c]]} \tag{2.167}$$

It should be noticed that equation (2.167) is generally not equal to equation (2.166). The FRF in equation (2.167) contains only relations between the n_o observed response quantities in the observation equation and the respective n_u excitations, while equation (2.166) refers to all displacements at the N degrees-of-freedom of the equation of motion. The common denominator model can be considered as a special case of *matrix fraction description* (MFD) [141]. There are two kinds of MFD, the left matrix fraction description (LMFD) and the right matrix fraction description (RMFD). The LMFD of the transfer function matrix relating n_u

loads or inputs to n_o (measured) outputs, is given by

$$[H(s)] = [D_L]^{-1}\,[N_L] = \left[\sum_{p=0}^{p_D}\left[D_{L_p}\right]\,s^p\right]^{-1}\left[\sum_{p=0}^{p_N}\left[N_{L_p}\right]\,s^p\right] \tag{2.168}$$

where the denominator matrix coefficients $\left[D_{L_p}\right]$ are of dimension $(n_o \times n_o)$ while the numerator coefficients are collected in $(n_o \times n_u)$ matrices $\left[N_{L_p}\right]$. The orders of denominator and numerator polynomials are denoted by p_D and p_N, respectively.

Similarly, the right matrix fraction description of the transfer function is then

$$[H(s)] = [N_R]\,[D_R]^{-1} = \left[\sum_{p=0}^{p_N}\left[N_{R_p}\right]\,s^p\right]\left[\sum_{p=0}^{p_D}\left[D_{R_p}\right]\,s^p\right]^{-1} \tag{2.169}$$

While the numerator matrix coefficients of the RMFD $[N_R]$ are of the same dimension as those for the LFMD in matrix $[N_L]$, the denominator matrix coefficients $[D_R]$ are collected in an $(n_u \times n_u)$ matrix [141].

Example 2.9. *The common denominator model of equation (2.166) has already been derived for the two-degree-of-freedom system in figure 2.1 in example 2.8:*

$$[H(s)] = \frac{[N(s)]}{d(s)}$$

with

$$[N(s)] = \mathrm{adj}\left[[M]\,s^2 + [C_2]\,s + [K]\right] = \begin{bmatrix} m_2\,s^2 + (c_1+c_2)s + k_1 + k_2 & c_1\,s + k_1 \\ c_1\,s + k_1 & m_1\,s^2 + c_1\,s + k_1 \end{bmatrix}$$

and

$$\begin{aligned} d(s) = \det\left[[M]\,s^2 + [C_2]\,s + [K]\right] &= m_1 m_2\,s^4 \\ &\quad + \left(m_1\,(c_1+c_2) + m_2 c_1\right)\,s^3 \\ &\quad + \left(m_1\,(k_1+k_2) + m_2 k_1 + c_1 c_2\right)\,s^2 \\ &\quad + \left(k_1 c_2 + k_2 c_1\right)\,s \\ &\quad + k_1 k_2 \end{aligned}$$

In general, there is no unique matrix fraction description [16]. However, from the common denominator model above, the following possible LFMD and RMFD can be easily derived:

$$\begin{aligned} [N_R] = [N_L] = [N(s)] &= \begin{bmatrix} m_2\,s^2 + (c_1+c_2)s + k_1 + k_2 & c_1\,s + k_1 \\ c_1\,s + k_1 & m_1\,s^2 + c_1\,s + k_1 \end{bmatrix} \\ &= \left[\sum_{r=0}^{2}[N_r]\,s^r\right] \end{aligned}$$

and

$$\begin{aligned} [D_R]^{-1} = [D_L]^{-1} &= [d(s)\,[I]]^{-1} \\ &= \left[\sum_{r=0}^{4}[d_r\,[I]]\,s^r\right]^{-1} \end{aligned}$$

where $[N_r]$ *and* d_r *are the numerator matrix polynomial coefficients and the denominator polynomial coefficients as given in example 2.8:*

$$[N_0] = \begin{bmatrix} m_2 & 0 \\ 0 & m_1 \end{bmatrix} \qquad [N_1] = \begin{bmatrix} c_1 + c_2 & c_1 \\ c_1 & c_1 \end{bmatrix} \qquad [N_2] = \begin{bmatrix} k_1 + k_2 & k_1 \\ k_1 & k_1 \end{bmatrix}$$

$$\begin{aligned} d_0 &= m_1\, m_2 \\ d_1 &= (m_1\,(c_1 + c_2) + m_2 c_1) \\ d_2 &= (m_1\,(k_1 + k_2) + m_2 k_1 + c_1 c_2) \\ d_3 &= (k_1 c_2 + k_2 c_1) \\ d_4 &= k_1\, k_2 \end{aligned}$$

It should be noticed that the polynomial orders for the numerator and for the denominator, p_N *and* p_R *respectively, are in the chosen matrix fraction description not the same.*

2.10 FRF estimation from measured input and output

As described in section 2.6, the frequency response function (FRF) describes the relation between excitation and response in frequency domain. Since the frequency response function can be formulated for any circular frequeny ω, the response component at any frequency $Y(\omega)$ can be obtained by spectral multiplication of the FRF by the Fourier transform of the excitation $F(\omega)$ that can be considered as a special case of the more general Laplace transform $F(s)$:

$$Y(\omega) \;=\; H(\omega)\, F(\omega) \tag{2.170}$$

Solving equation (2.170) for $H(\omega)$ enables one to calculate an FRF directly from the Fourier transforms of measured input and output signals:

$$H(\omega) \;=\; \frac{Y(\omega)}{F(\omega)} \tag{2.171}$$

In case that $F(\omega)$ becomes zero, equation (2.171) will cause numerical problems. Therefore, frequency response functions are in practice usually estimated from measured input and output signals using *power spectral densities* (PSD) $S_{FF}(\omega)$, $S_{YY}(\omega)$ and cross-spectral densities $S_{YF}(\omega)$, $S_{FY}(\omega)$ of the measured signals [49], [67]:

$$H(\omega) \;=\; \frac{Y(\omega)}{F(\omega)}\frac{F^*(\omega)}{F^*(\omega)} \;=\; \frac{S_{YF}(\omega)}{S_{FF}(\omega)} \;=\; H_1(\omega) \tag{2.172}$$

$$H(\omega) \;=\; \frac{Y(\omega)}{F(\omega)}\frac{Y^*(\omega)}{Y^*(\omega)} \;=\; \frac{S_{YY}(\omega)}{S_{FY}(\omega)} \;=\; H_2(\omega) \tag{2.173}$$

One great advantage of the application of equations (2.172) and (2.173) is that averaged cross- and power spectral densities can be used which reduces the influence of uncorrelated noise within the measured signals [67]. In fact, the first estimator $H_1(\omega)$ assumes no noise on the excitation but allows for uncorrelated noise n_{resp} on the response:

$$Y(\omega) - n_{resp} \;=\; H(\omega)\, F(\omega) \tag{2.174}$$

Multiplication of equation (2.174) by $F^*(\omega)$ gives

$$Y(\omega)F^*(\omega) - n_{resp}F^*(\omega) \;=\; H(\omega)\,F(\omega)F^*(\omega) \tag{2.175}$$

Since the noise on the response signal is supposed to be uncorrelated, equation (2.175) can be simplified to

$$S_{YF}(\omega) \;=\; H(\omega)\,S_{FF} \;\longrightarrow\; H_1(\omega) \;=\; \frac{S_{YF}(\omega)}{S_{FF}(\omega)} \tag{2.176}$$

Similarly, it can be shown that the estimator $H_2(\omega)$ allows for noise-free response and uncorrelated noise n_{exc} on the excitation. To overcome the described drawbacks of the two estimators, the Fourier transform of a third signal $V(\omega)$, for example the voltage that is used to drive a shaker during the test, can be used to extend equation (2.171) such that one obtains a third FRF estimator

$$H_3(\omega) \;=\; \frac{Y(\omega)}{F(\omega)}\frac{V^*(\omega)}{V^*(\omega)} \;=\; \frac{S_{YV}(\omega)}{S_{FV}(\omega)} \tag{2.177}$$

This estimator is less sensitive to noise contamination on either the input or output signals since the cross-spectral densities are less affected than the power spectral densities.

In the derivations above, only a single input and a single output were considered. For the more general case of multiple inputs and multiple outputs equations (2.172), (2.173) and (2.177) become matrix equations for each frequency [67].

$$[H_1(\omega)] \;=\; [S_{YF}(\omega)]\,[S_{FF}(\omega)]^{-1} \tag{2.178}$$

$$[H_2(\omega)] \;=\; [S_{YY}(\omega)]\,[S_{FY}(\omega)]^{-1} \tag{2.179}$$

$$[H_3(\omega)] \;=\; [S_{YV}(\omega)]\,[S_{FV}(\omega)]^{-1} \tag{2.180}$$

A more thorough discussion about the estimation of frequency response functions from measured response and excitations is, for example, given in [141].

2.11 Output spectra estimation from response measurements

In context with the estimation of frequency response functions from measured excitation and response signals, usually power and cross-spectral densities are computed as discussed in section 2.10. In frequency domain output-only modal identification techniques, spectral density estimates form the foundation of the algorithms as explained in chapter 3. Therefore some relations and concepts of spectral estimation are discussed in this section.

2.11.1 Some remarks on correlations and covariance

Though a complete survey of the theory of time series and random variable analysis is outside the scope of this work, some definitions and relations are repeated here for the sake of clarity.

Provided that two random processes $\{x_i\}$ and $\{y_i\}$ with the mean values

$$\mu_x(t) = \mathbf{E}\left[x_i(t)\right] \qquad \mu_y(t) = \mathbf{E}\left[y_i(t)\right] \tag{2.181}$$

are given, the *covariance fuctions* of two signals that are time-shifted by an interval τ are defined by

$$\begin{aligned} C_{xx}(t,t+\tau) &= \mathbf{E}\left[(x_i(t)-\mu_x(t))\,(x_i(t+\tau)-\mu_x(t+\tau))\right] \\ C_{yy}(t,t+\tau) &= \mathbf{E}\left[(y_i(t)-\mu_y(t))\,(y_i(t+\tau)-\mu_y(t+\tau))\right] \\ C_{xy}(t,t+\tau) &= \mathbf{E}\left[(x_i(t)-\mu_x(t))\,(y_i(t+\tau)-\mu_y(t+\tau))\right] \end{aligned} \tag{2.182}$$

If the statistical parameters $\mu_x(t)$, $\mu_x(t)$, $C_{xx}(t,t+\tau)$, $C_{yy}(t,t+\tau)$ and $C_{xy}(t,t+\tau)$ are independent of time, which means they are constant for any time t, the random processes $\{x_k\}$ and $\{y_k\}$ satisfy the conditions of weak stationarity. Furthermore, the functions

$$\begin{aligned} R_{xx}(\tau) &= \mathbf{E}\left[x_i(t)\,x_i(t+\tau)\right] \\ R_{yy}(\tau) &= \mathbf{E}\left[y_i(t)\,y_i(t+\tau)\right] \\ R_{xy}(\tau) &= \mathbf{E}\left[x_i(t)\,y_i(t+\tau)\right] \end{aligned} \tag{2.183}$$

are defined as *autocorrelation functions* $R_{xx}(\tau)$, $R_{yy}(\tau)$ and *cross-correlation function* $R_{xy}(\tau)$. Covariance functions and correlation functions are related to each other by

$$\begin{aligned} C_{xx}(\tau) &= R_{xx}(\tau)-\mu_x^2 \\ C_{yy}(\tau) &= R_{yy}(\tau)-\mu_y^2 \\ C_{xy}(\tau) &= R_{xy}(\tau)-\mu_x\mu_y \end{aligned} \tag{2.184}$$

As can be deduced from equations (2.185), the correlation functions are identical to the covariance functions if $\mu_x = \mu_y = 0$. For zero time shift $\tau = 0$, the variances σ_x^2 and σ_y^2 are defined as

$$\begin{aligned} \sigma_x^2(t) &= C_{xx}(t,t) = \mathbf{E}\left[(x_k(t)-\mu_x(t))^2\right] \\ \sigma_y^2(t) &= C_{yy}(t,t) = \mathbf{E}\left[(y_k(t)-\mu_y(t))^2\right] \end{aligned} \tag{2.185}$$

The square root of the variance $\sigma_x = \sqrt{\sigma_x^2}$ is known as the *standard deviation* of the random process $\{x_k\}$. If the covariance $C_{xy}(\tau)$ is normalized by the product of the two respective standard deviations, one obtains the *correlation coefficient function*:

$$\rho_{xy}(\tau) = \frac{C_{xy}(\tau)}{\sqrt{\sigma_x^2\,\sigma_y^2}} = \frac{C_{xy}(\tau)}{\sigma_x\,\sigma_y} \tag{2.186}$$

Due to the scaling of the covariance, the correlation coefficient is always within the range $-1 \leq \rho_{xy}(\tau) \leq 1$. Therefore the correlation coefficient is a very convenient measure to assess the cross-correlation between two signals or the autocorrelation of a single signal without the need of knowledge about the actual range of the time series' values.

The definitions given in this section follow those in the standard text books [17] and [101] which comply with much earlier works in the field of signal analysis such as [146] and [58]. However, it should be mentioned that, for example in [58] many of the relations are formulated for covariance functions assuming zero means without calling these functions correlation functions. Furthermore, there is some literature such as, for example [82], where the value defined in equation (2.186) is called correlation function rather than correlation coefficient function. So, the use of these definitions is not always completely consistent and requires attention especially in context with respective implementations.

2.11.2 Estimation of spectral density functions

In section 2.10 spectral density functions have already been used in the context with the estimates of frequency response functions without investigation of different ways of computing spectral density functions from measured data.

Spectral density functions are defined as the Fourier transforms of the correlation functions of the random processes $\{x_i\}$ and $\{y_i\}$, provided that these Fourier transforms exist [17]:

$$\begin{aligned} S_{XX}(\omega) &= \int_{-\infty}^{\infty} R_{xx}(\tau)\, e^{-\mathrm{i}\omega\tau} \mathrm{d}\tau \\ S_{YY}(\omega) &= \int_{-\infty}^{\infty} R_{yy}(\tau)\, e^{-\mathrm{i}\omega\tau} \mathrm{d}\tau \\ S_{XY}(\omega) &= \int_{-\infty}^{\infty} R_{xy}(\tau)\, e^{-\mathrm{i}\omega\tau} \mathrm{d}\tau \end{aligned} \tag{2.187}$$

where $S_{XX}(\omega)$ and $S_{YY}(\omega)$ are the *autospectral density functions* or *autospectra* and $S_{XY}(\omega)$ denotes the *cross-spectral density function* or *cross-spectrum* of $\{x_i\}$ and $\{y_i\}$. According to equations (2.188), which are also called the Wiener-Khinchin relations, correlation functions and spectral density functions form Fourier transform pairs. Therefore, the correlation functions can also be obtained as inverse Fourier transforms of the respective spectral density functions.

$$\begin{aligned} R_{xx}(\tau) &= \frac{1}{2\pi} \int_{-\infty}^{\infty} S_{xx}(\omega)\, e^{\mathrm{i}\omega\tau} \mathrm{d}\omega \\ R_{yy}(\tau) &= \frac{1}{2\pi} \int_{-\infty}^{\infty} S_{yy}(\omega)\, e^{\mathrm{i}\omega\tau} \mathrm{d}\omega \\ R_{xy}(\tau) &= \frac{1}{2\pi} \int_{-\infty}^{\infty} S_{xy}(\omega)\, e^{\mathrm{i}\omega\tau} \mathrm{d}\omega \end{aligned} \tag{2.188}$$

While the autospectral density functions are real-valued, the cross-spectral density functions are complex-valued functions of frequency. Hence, the autospectral density functions can be considered as a special case of the cross-spectral density functions. Therefore only the cross-spectral density functions will be considered in the following.

The spectral density functions as given in equations (2.188) are defined in the frequency range from $-\infty$ to ∞ with the properties

$$S_{XY}(-\omega) = S^*_{XY}(\omega) = S_{YX}(\omega) \tag{2.189}$$

and are therefore also called *two-sided spectral density functions*. However, the physical meaning of negative frequencies is less obvious. Consequently, in practical applications usually the *one-sided spectral density functions* $G_{XY}(\omega)$ are used:

$$G_{XY}(\omega) = \begin{cases} 0 & \text{for } \omega < 0 \\ S_{XY}(\omega) & \text{for } \omega = 0 \\ 2\, S_{XY}(\omega) & \text{for } \omega > 0 \end{cases} \tag{2.190}$$

The one-sided spectral density function should not be confused with the one-sided discrete Fourier transform of the correlation function which is also called *positive cross- or power spectrum* [116] or *half spectrum* [108], [91]

$$S^{+}_{XY}(\omega) = DFT\,(R_{xy}(\tau \geq 0)) \tag{2.191}$$

Equation (2.191) means that the positive power spectrum is obtained as discrete Fourier transform of the correlation function's part for non-negative time lags which is also called *causal* part. The respective counterpart, the discrete Fourier transform of the correlation function's *non-causal* or *anti-causal* part, is then

$$S^{-}_{XY}(\omega) = DFT\,(R_{xy}(\tau < 0)) \tag{2.192}$$

Consequently, the two sided power spectral density can be represented by the sum of $S^{+}_{XY}(\omega)$ and $S^{-}_{XY}(\omega)$:

$$S_{XY}(\omega) = S^{+}_{XY}(\omega) + S^{-}_{XY}(\omega) \tag{2.193}$$

In the special case of the autospectral density function, the positive power spectrum is related to the discrete versions of the two-sided and one-sided power spectral densities by

$$\begin{aligned} S^{+}_{XX}(\omega < 0) &= \frac{1}{2} S_{XX}(\omega < 0) \\ S^{+}_{XX}(\omega = 0) &= \frac{1}{2} S_{XX}(\omega = 0) = \frac{1}{2} G_{XX}(\omega = 0) \\ S^{+}_{XX}(\omega > 0) &= \frac{1}{2} S_{XX}(\omega > 0) = \frac{1}{4} G_{XX}(\omega > 0) \end{aligned} \tag{2.194}$$

since $\mathrm{Re}\left[S^{+}_{xy}(\omega)\right] = \mathrm{Re}\left[S^{-}_{xy}(\omega)\right]$.

In practice, spectral density functions are usually estimated directly from the discrete Fourier transforms $X(\omega)$ and $Y(\omega)$ of the respective signals $\{x(t)\}$, $\{y(t)\}$ as, for example described in [118]:

$$S_{xy}(\omega) = X(\omega)^{*}\, Y(\omega)^{*} \tag{2.195}$$

Sometimes, as for example in [17], a scaling by $\frac{1}{T}$, with T being the record duration, is introduced in the definition of spectral density functions. However, this scaling is often neglected due to its minor importance in practical applications [118] and therefore also omitted in equation (2.195). If positive cross-power spectral densities are needed for further analyses, they should be computed from estimates of respective correlation functions, as for example suggested in [108], [116] and [120]. However, it should be noticed that the quality of the resulting spectra depends then also on the quality of the correlation functions' estimate.

Spectral estimates are in practice often computed as averaged spectra. This procedure was first proposed by Peter D. Welch [145] and is therefore sometimes also referred to as Welch's method. The advantage of spectral averaging is that the random noise contributions are reduced such that smoother spectra are obtained. However, averaging also affects the phase information what should be taken into account if cross-spectral densities are considered.

Example 2.10. *To illustrate the relations between the representations of the correlation function in frequency domain, the two-degree-of-freedom system in figure 2.1 is considered. The dynamic response to an excitation of the structure by two independent, uniformly distributed, band-limited noise excitations at both degrees-of-freedom was calculated by means of the Newmark-*$\beta = \frac{1}{6}$ *method. It is deduced from the time series of the excitations and the respective one-sided auto- and cross-spectral density functions in figure 2.7 that the two random processes can be considered as uniformly distributed and uncorrelated.*

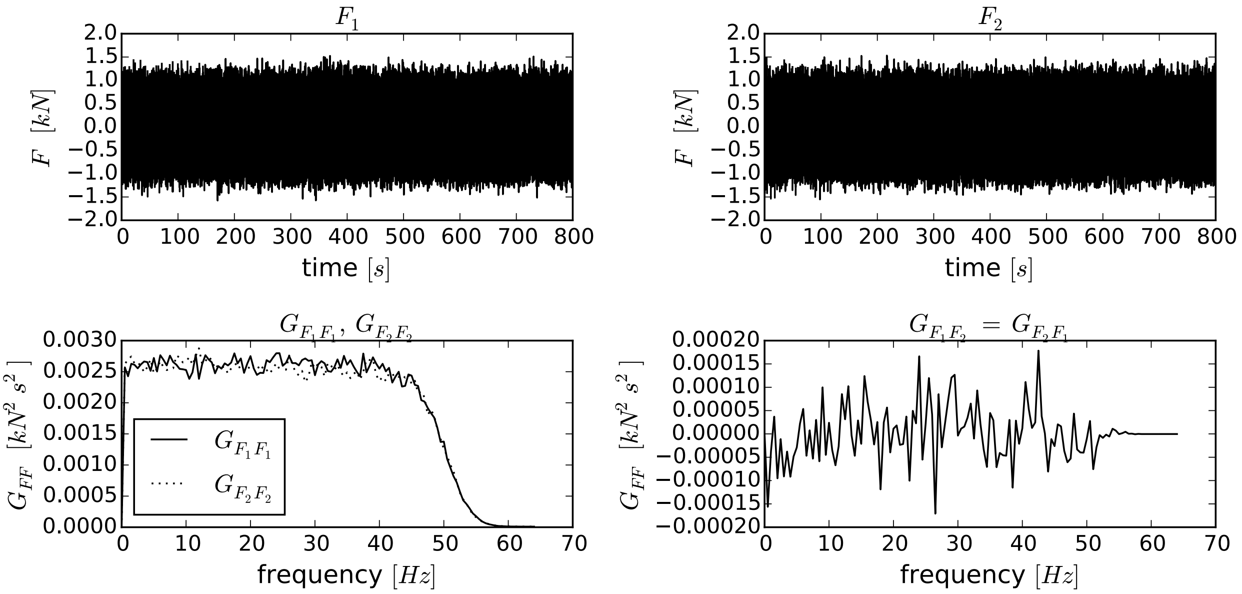

Figure 2.7: Two-degree-of-freedom system: simulated excitation signals – time series and one-sided autospectral density functions

The simulated displacement time series and their one-sided autospectral desities are given in figure 2.8. These diagrams indicate that the structural response consists mainly of spectral contributions close to the two resonance frequencies as expected from modal theory.

Figure 2.9 contains the one-sided autospectral density function, the two-sided autospectral density function and the two-sided DFT of the autocorrelation function of the displacements at the second degree-of-freedom. This diagram illustrates the relations between the three types of spectra given in equations (2.195). The spectral density functions illustrated in figure 2.9 were computed as averaged spectra using a rectangular weighting function.

While the different representations of autospectral desity functions are presented in figure 2.9, the respective forms of cross-spectral density functions' real and imaginary parts are shown in figures 2.11 and 2.12, respectively. These diagrams clearly indicate especially the differences

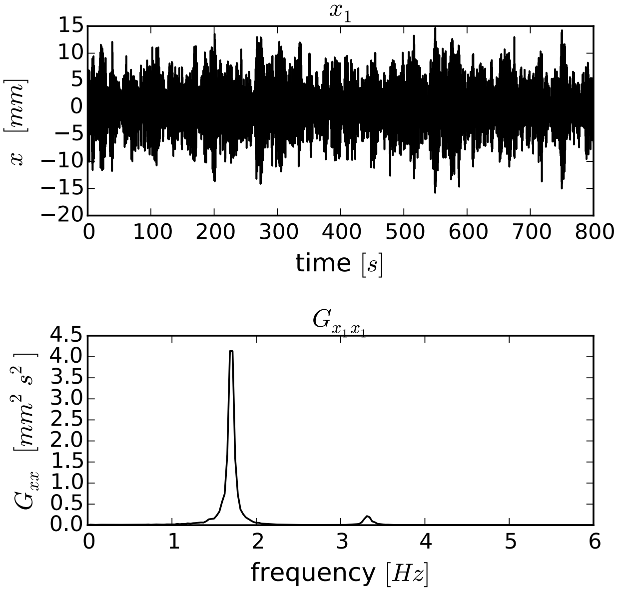

Figure 2.8: Two-degree-of-freedom system: simulated displacement signals – time series and one-sided autospectral density functions

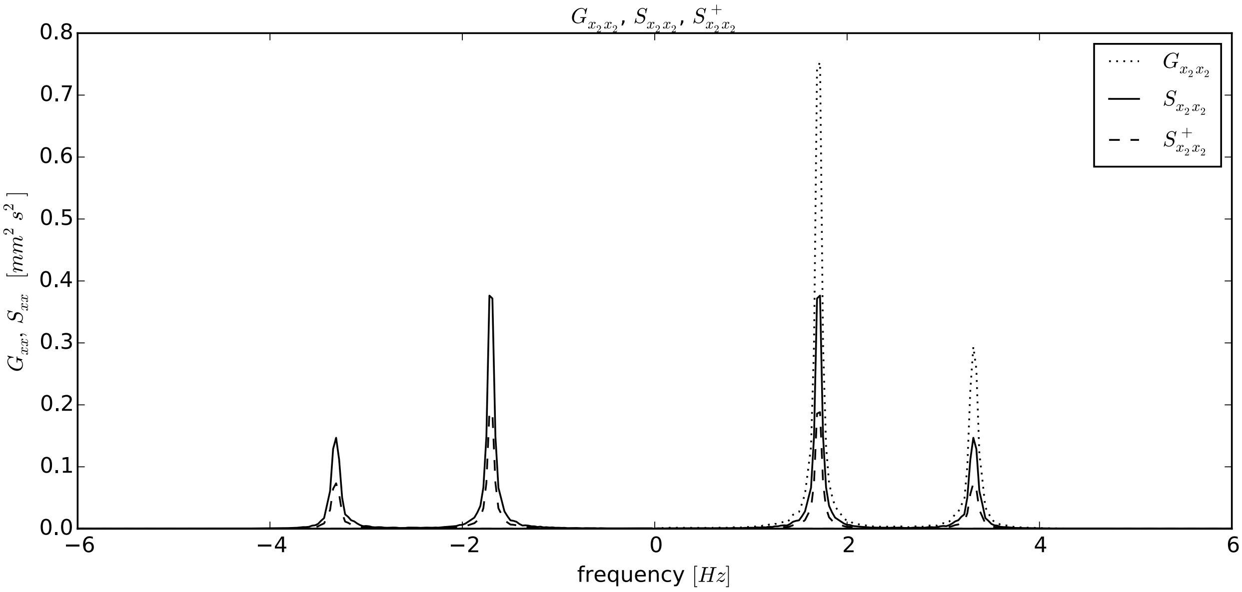

Figure 2.9: Two-degree-of-freedom system: one-sided and two-sided autospectral density functions, one-sided Fourier transform of the autocorrelation function at degree-of-freedom 2

between the imaginary parts of $S_{x_1x_2}(\omega)$, $S^+_{x_1x_2}(\omega)$ *and* $S^-_{x_1x_2}(\omega)$. *The cross correlation function with its causal and anti-causal parts is given in figure 2.10.*

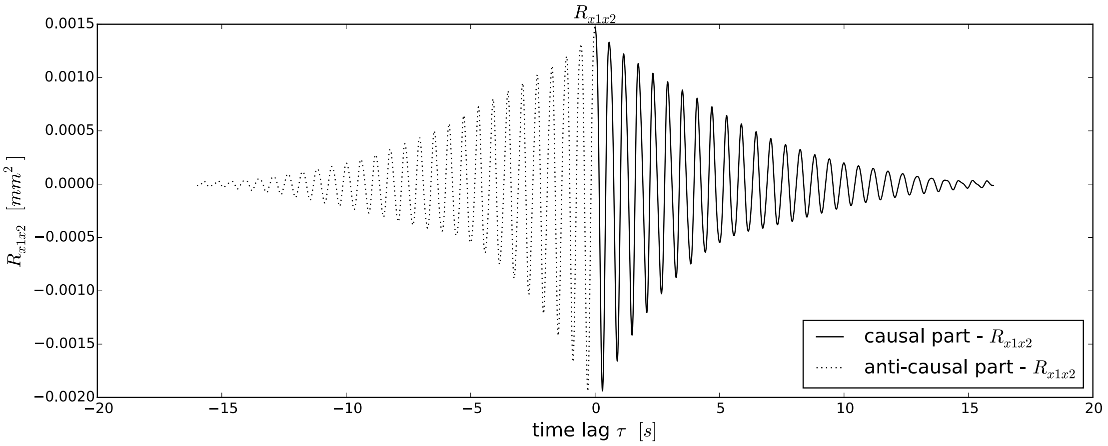

Figure 2.10: Two-degree-of-freedom system: cross-correlation function between the two response signals

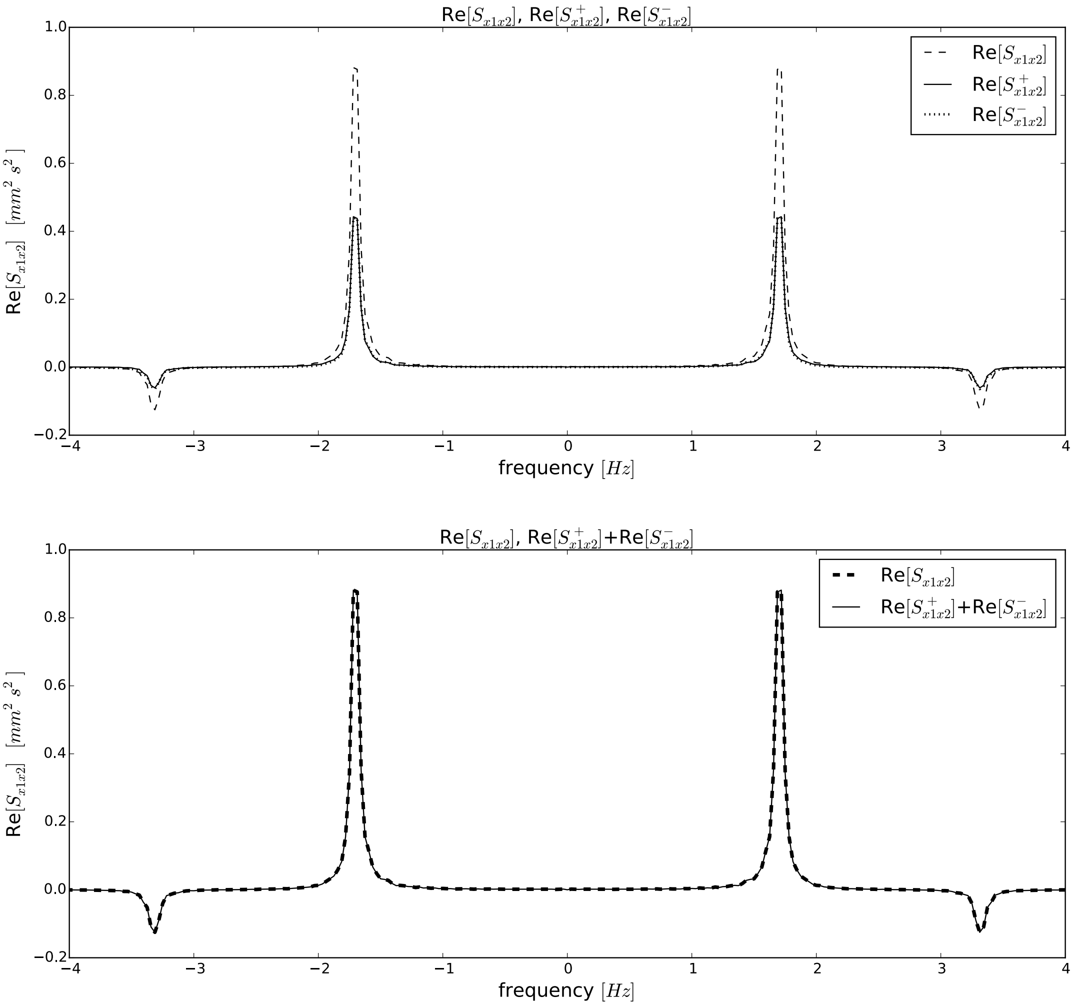

Figure 2.11: Two-degree-of-freedom system: real parts of the cross-spectral estimates $S_{x_1x_2}(\omega)$, $S^+_{x_1x_2}(\omega)$ and $S^-_{x_1x_2}(\omega)$ – separate (top) and superimposed (bottom)

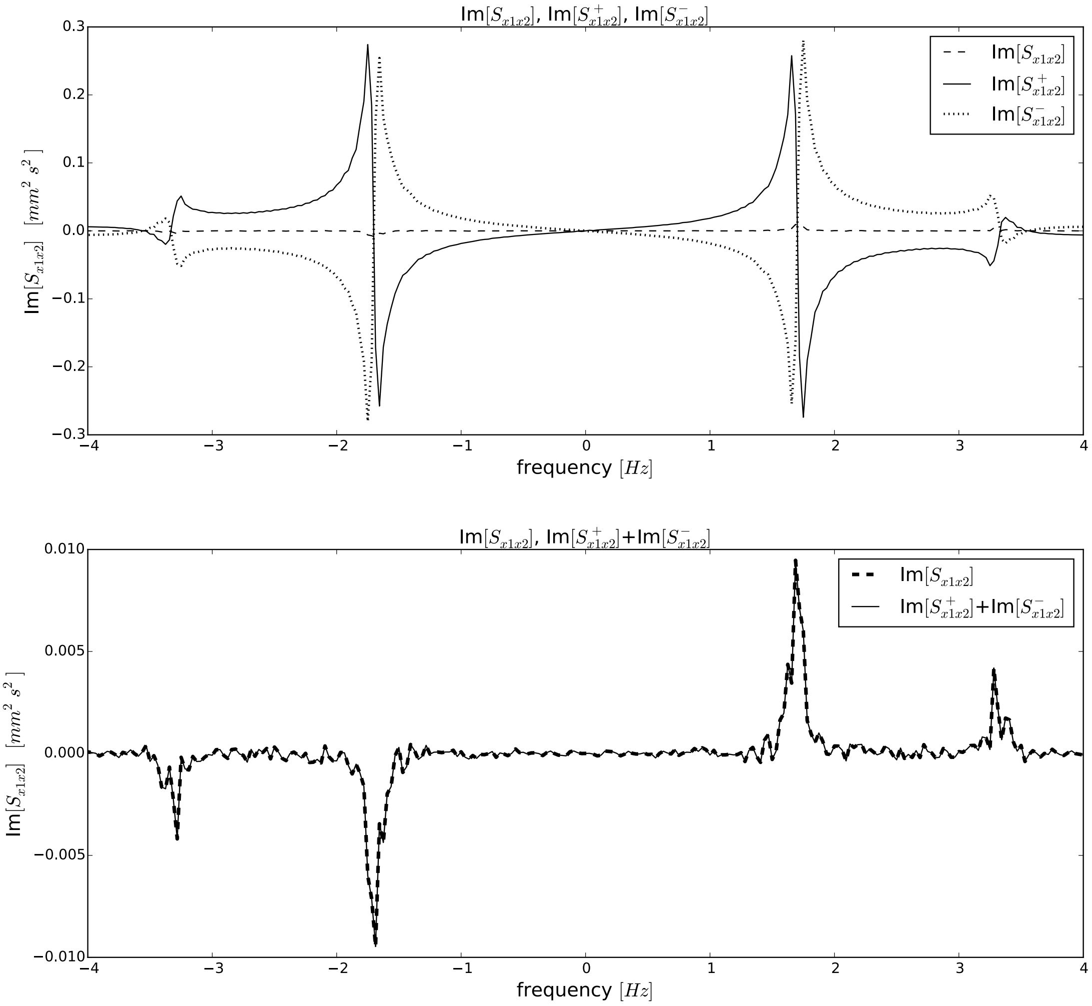

Figure 2.12: Two-degree-of-freedom system: imaginary parts of the cross-spectral estimates $S_{x_1x_2}(\omega)$, $S^+_{x_1x_2}(\omega)$ and $S^-_{x_1x_2}(\omega)$ – separate (top) and superimposed (bottom)

Chapter 3

Algorithms for operational modal analysis

3.1 General remarks

Operational modal analysis techniques were mainly derived from "classical" experimental modal identification algorithms. While the measurement of the excitation is a fundamental prerequisite in *experimental modal analysis* (EMA), this information is not available in *operational modal analysis* (OMA). Therefore some assumptions with respect to the excitation need to be taken. Commonly it is assumed that the excitation of the structure can be described by a white noise random process. Even though this theoretical assumption is usually not strictly satisfied, the methods deliver also very good estimates of modal parameters for band-limited excitations.

As in experimental modal analysis, the identification algorithms in operational modal analysis can also be classified into *single degree-of-freedom* (SDOF) and *multi-degree-of-freedom* (MDOF) methods. In this context, single degree-degree-of-freedom does not refer to structural systems which are modelled to have only one degree-of-freedom. SDOF modal analysis methods are rather based on a separation of the modes in the analysis. This means that only one mode is considered in a single analysis which estimates the respective parameters for a single mode. These analyses can be applied to different modes, but sequentially.

In the second group, the MDOF methods, the analysis of the measured data yields the modal parameters for several modes at the same time. Many of these methods are based on the identification of parameters of mathematical models, such as state space or fraction polynomial models which are described in chapter 2, from which the modal parameters are then derived in a second step. These methods are also called *parametric methods*.

Both for experimental modal analysis and operational modal analysis several algorithms were developed to identify modal parameters from measured data either in *time domain* or in *frequency domain*. Some of these algorithms for operational modal analysis have become well established and are nowadays applied in engineering practice. In the following sections some of the most widely used methods are described while other algorithms which are less frequently applied in practice, are only mentioned.

Several well established algorithms have been numerically implemented in context with this work. Their performance is discussed in section 3.6 by means of the two degree-of-freedom system introduced in chapter 2 and a practical example using experimental data.

3.2 Time domain methods

3.2.1 Natural excitation technique (NExT)

As mentioned before, operational modal analysis was developed mainly on the base of traditional experimental modal analysis techniques by which modal parameters were extracted from impulse response functions or frequency response functions in case of frequency domain methods. Therefore, the starting point for several operational modal analysis algorithms was to show that it is possible to find functions that can be estimated on output-only data assuming random excitation.

For the time domain was shown in [81, 79, 80] that cross-correlation functions can be represented by a series of decaying harmonic functions, which have a similar structure as the modal components of the impulse response function in equation (2.42). It was derived in the afore mentioned references that the cross-correlation function between two response signals at degrees-of-freedom i and j of a structure that is excited by a random force at degree-of-freedom k can be superimposed by n_m contributions of modes r, s in the form

$$R_{y_i y_j,k}(\tau) = \sum_{r=1}^{n_m} \left(G_{ijk,r}\, e^{\zeta_r \omega_r \tau} \cos\left(\sqrt{1-\zeta_r^2}\, \omega_r\, \tau \right) + H_{ijk,r}\, e^{\zeta_r \omega_r \tau} \sin\left(\sqrt{1-\zeta_r^2}\, \omega_r\, \tau \right) \right) \tag{3.1}$$

where τ denotes the time lag between the analysed signals y_i and y_j and

$$G_{ijk,r} = \sum_{s=1}^{n_m} \frac{\alpha_k\, \psi_{ir}\psi_{kr}\, \psi_{js}\psi_{ks}}{m_r\, m_s\, \sqrt{1-\zeta_r^2}\, \omega_r} \left(\frac{I_{rs}}{J_{rs}^2 + I_{rs}^2} \right) \tag{3.2}$$

$$H_{ijk,r} = \sum_{s=1}^{n_m} \frac{\alpha_k\, \psi_{ir}\psi_{kr}\, \psi_{js}\psi_{ks}}{m_r\, m_s\, \sqrt{1-\zeta_r^2}\, \omega_r} \left(\frac{J_{rs}}{J_{rs}^2 + I_{rs}^2} \right) \tag{3.3}$$

with

$$I_{rs} = 2\sqrt{1-\zeta_r^2}\, \omega_r\, \left(\zeta_r\, \omega_r + \zeta_s\, \omega_s \right)$$

and

$$J_{rs} = \left(1-\zeta_s^2\right) \omega_s^2 - \left(1-\zeta_r^2\right) \omega_r^2 + \left(\zeta_r\, \omega_r + \zeta_s\, \omega_s \right)^2$$

The constant α_k originates from the autocorrelation function of the excitation $f_k(t)$ that is assumed to have the properties of white noise [79]:

$$R_{f_k f_k}(\tau) = \alpha_k\, \delta(\tau) \tag{3.4}$$

where $\delta(\tau)$ is the Dirac delta function.

It becomes obvious from equations (3.2) and (3.3) that the variables $G_{ijk,r}$ and $H_{ijk,r}$ depend only on the mode shapes, natural frequencies, damping ratios and modal masses of modes r and s but not on time. Therefore, it is possible to summarize equation (3.1) such that it obtains a very similar structure as equation (2.45) which shows that the response at one degree-of-freedom due to an excitation at a second degree-of-freedom can be represented by a sum of decaying sinusoids [79]:

$$R_{y_i y_j,k}(\tau) = \sum_{r=1}^{n_m} \frac{\psi_{ir} A_{jr}}{m_r \omega_r \sqrt{1-\zeta_r^2}}\, e^{-\zeta_r\, \omega_r\, \tau} \sin\left(\sqrt{1-\zeta_r^2}\, \omega_r\, \tau + \theta_r \right) \tag{3.5}$$

With this result the foundation stone was layed for the application of modal identification methods, that were originally developed for the use with impulse response functions (IRF). Now cross-correlation functions, rather than IRF's, could be used to estimate modal parameters.

3.2.1.1 Poly-reference least square complex exponential (p-LSCE) method

The least-square complex exponential (LSCE) method was initially developed for the derivation of modal parameters from impulse response functions and was according to [151] first suggested in [28]. After the publication of the NExT procedures, the LSCE method has been also applied to correlation functions as, for example, described in [98] and [52].

Introducing the phase angle $\theta'_r = \theta_r - \frac{\pi}{2}$ equation (3.5) can be re-written as

$$R_{y_i y_j,k}(\tau) = \sum_{r=1}^{n_m} \frac{\psi_{ir} A_{jr}}{m_r \omega_r \sqrt{1-\zeta_r^2}} \; e^{-\zeta_r \, \omega_r \, \tau} \; \cos\left(\sqrt{1-\zeta_r^2}\, \omega_r \, \tau + \theta'_r\right) \tag{3.6}$$

According to Euler's formula, the cosine can be replaced by a sum of exponential functions:

$$\begin{aligned} \cos\left(\sqrt{1-\zeta_r^2}\, \omega_r \, \tau + \theta'_r\right) &= \frac{1}{2}\left(e^{\mathrm{i}\left(\sqrt{1-\zeta_r^2}\, \omega_r\, \tau + \theta'_r\right)} + e^{-\mathrm{i}\left(\sqrt{1-\zeta_r^2}\, \omega_r\, \tau + \theta'_r\right)}\right) \\ &= \frac{1}{2}\left(e^{\mathrm{i}\left(\sqrt{1-\zeta_r^2}\, \omega_r\, \tau\right)} \; e^{\mathrm{i}\theta'_r} + e^{-\mathrm{i}\left(\sqrt{1-\zeta_r^2}\, \omega_r\, \tau\right)} \; e^{-\mathrm{i}\theta'_r}\right) \end{aligned} \tag{3.7}$$

Substituting equation (3.7) into equation (3.6) yields for discrete time lags $\tau = l\,\Delta t$

$$R_{y_i y_j,k}(l\,\Delta t) = \sum_{r=1}^{2n_m} C_{ij,r}\; \mu_r^l \tag{3.8}$$

where

$$C_{ij,r} = \frac{\psi_{ir}\, A_{jr}}{2\, m_r\, \omega_r \sqrt{1-\zeta_r^2}} \; e^{\mathrm{i}\theta_r} \tag{3.9}$$

and

$$\mu_r = e^{(\lambda_r\, \Delta t)} \qquad \lambda_r = -\zeta_r\, \omega_r \; + \mathrm{i}\, \omega_r \sqrt{1-\zeta_r^2} \tag{3.10}$$

Since the exponential terms now occur in complex conjugate pairs, the upper limit of the summation changed to $2n_m$.

Equation (3.8) is also called *Prony* series named after Gaspard Clair François Marie Riche de Prony who suggested a method to solve this polynomial for μ_r [114] which will be illustrated in the following [49]. For the sake of simplicity, the subscript k referring to the location of excitation is dropped.

The summation formular (3.8) can be formulated for any time shift as

$$\begin{array}{ccccccccc} R_{y_i y_j}(0) & = & C_{ij,1} & + & C_{ij,2} & + & \dots & + & C_{ij,2n_m} \\ R_{y_i y_j}(\Delta t) & = & C_{ij,1}\, \mu_1 & + & C_{ij,2}\, \mu_2 & + & \dots & + & C_{ij,2n_m}\, \mu_{2n_m} \\ R_{y_i y_j}(2\Delta t) & = & C_{ij,1}\, \mu_1^2 & + & C_{ij,2}\, \mu_2^2 & + & \dots & + & C_{ij,2n_m}\, \mu_{2n_m}^2 \\ \vdots & = & & & \vdots & & & & \\ R_{y_i y_j}(p\Delta t) & = & C_{ij,1}\, \mu_1^p & + & C_{ij,2}\, \mu_2^p & + & \dots & + & C_{ij,2n_m}\, \mu_{2n_m}^p \end{array} \tag{3.11}$$

In the next step both sides of each row l in equations (3.11) is multiplied by a coefficient β_l:

$$\begin{array}{ccccccccc} \beta_0\, R_{y_iy_j}(0) & = & \beta_0\, C_{ij,1} & + & \beta_0\, C_{ij,2} & + & \ldots & + & \beta_0\, C_{ij,2n_m} \\ \beta_1\, R_{y_iy_j}(\Delta t) & = & \beta_1\, C_{ij,1}\, \mu_1 & + & \beta_1\, C_{ij,2}\, \mu_2 & + & \ldots & + & \beta_1\, C_{ij,2n_m}\, \mu_{2n_m} \\ \beta_2\, R_{y_iy_j}(2\Delta t) & = & \beta_2\, C_{ij,1}\, \mu_1^2 & + & \beta_2\, C_{ij,2}\, \mu_2^2 & + & \ldots & + & \beta_2\, C_{ij,2n_m}\, \mu_{2n_m}^2 \\ \vdots & = & & & \vdots & & & & \\ \beta_p\, R_{y_iy_j}(p\Delta t) & = & \beta_p\, C_{ij,1}\, \mu_1^p & + & \beta_p\, C_{ij,2}\, \mu_2^p & + & \ldots & + & \beta_p\, C_{ij,2n_m}\, \mu_{2n_m}^p \end{array} \tag{3.12}$$

The sum of all p equations produces

$$\sum_{l=0}^{p} \beta_l\, R_{y_iy_j}(l\Delta t) \;=\; \sum_{r=1}^{2n_m} \left(C_{ij,r} \sum_{l=0}^{p} \beta_l\, \mu_r^l \right) \tag{3.13}$$

For convenience it is common to set the upper limits of the summations in equation (3.13) to the same value: $p = 2n_m$. If the inner sum on the right hand side in equation (3.13) becomes zero:

$$\sum_{l=0}^{2n_m} \beta_l\, \mu_r^l \;=\; 0 \qquad r = 1 \ldots 2n_m \tag{3.14}$$

follows that the whole right hand side of equation (3.13) becomes zero and therefore

$$\sum_{l=0}^{2n_m} \beta_l\, R_{y_iy_j}(l\Delta t) \;=\; 0 \tag{3.15}$$

Accordingly, the coefficients β_l can be scaled arbitrarily, also such that $\beta_{2n_m} = 1$. Hence, equation (3.15) can be rearranged in the form

$$\sum_{l=0}^{2n_m-1} \beta_l\, R_{y_iy_j}(l\Delta t) \;=\; -R_{y_iy_j}(2n_m\, \Delta t) \tag{3.16}$$

which can be written in vector notation as

$$\left\{ \; R_{y_iy_j}(0) \quad R_{y_iy_j}(\Delta t) \quad R_{y_iy_j}(2\,\Delta t) \quad \ldots \quad R_{y_iy_j}((2n_m - 1)\,\Delta t) \; \right\} \left\{ \begin{array}{c} \beta_0 \\ \beta_1 \\ \vdots \\ \beta_{(2n_m-1)} \end{array} \right\} = -R_{y_iy_j}(2n_m\, \Delta t) \tag{3.17}$$

By repeating the procedure described in equations (3.11) to (3.17) with $2n_m$ data sets of the cross-correlation functions which are separated by Δt, a system of equations can be assembled

$$\left[R_{y_iy_j} \right]\, \{\beta\} \;=\; \left\{ \tilde{R}_{y_iy_j} \right\} \tag{3.18}$$

with the *Hankel* matrix

$$\left[R_{y_iy_j} \right] = \left[\begin{array}{cccc} R_{y_iy_j}(0) & R_{y_iy_j}(\Delta t) & \ldots & R_{y_iy_j}((2n_m - 1)\Delta t) \\ R_{y_iy_j}(\Delta t) & R_{y_iy_j}(2\Delta t) & \ldots & R_{y_iy_j}((2n_m)\Delta t) \\ \vdots & \vdots & \ldots & \vdots \\ R_{y_iy_j}((2n_m - 1)\Delta t) & R_{y_iy_j}((2n_m)\Delta t) & \ldots & R_{y_iy_j}((4n_m - 2)\Delta t) \end{array} \right] \tag{3.19}$$

the vector of unknown coefficients

$$\{\beta\} = \left\{ \begin{array}{c} \beta_0 \\ \beta_1 \\ \vdots \\ \beta_{(2n_m-1)} \end{array} \right\} \tag{3.20}$$

and the vector of the last $2n_m$ samples of the correlation function

$$\left\{\tilde{R}_{y_iy_j}\right\} = -\left\{ \begin{array}{c} R_{y_iy_j}((2n_m)\Delta t) \\ R_{y_iy_j}((2n_m+1)\Delta t) \\ \vdots \\ R_{y_iy_j}((4n_m-1)\Delta t) \end{array} \right\} \tag{3.21}$$

Solving equation (3.18) delivers the coefficients β_l

$$\{\beta\} = \left[R_{y_iy_j}\right]^{-1} \left\{\tilde{R}_{y_iy_j}\right\} \tag{3.22}$$

from which the values μ_r can be derived as the roots of equation (3.14). The natural frequencies and damping ratios are then derived from equation (3.10):

$$\mu_r = e^{(\lambda_r\,\Delta t)} \qquad \lambda_r = -\zeta_r\,\omega_r + \mathrm{i}\,\omega_r\sqrt{1-\zeta_r^2}$$

If not only one correlation function is taken into account equation (3.18) can be extended to an overdetermined system of equations

$$\left[\begin{array}{c} [R_{y_1y_1}] \\ [R_{y_1y_2}] \\ \vdots \end{array} \right] \{\beta\} = -\left\{ \begin{array}{c} \left\{\tilde{R}_{y_1y_1}\right\} \\ \left\{\tilde{R}_{y_1y_2}\right\} \\ \vdots \end{array} \right\} \tag{3.23}$$

which can be solved in the least-squares sense. The modal constants that contain also the mode shapes are obtained from equations (3.11) which can be written in matrix -vector form as

$$\left[\begin{array}{cccc} 1 & 1 & \dots & 1 \\ \mu_1 & \mu_2 & \dots & \mu_{2n_m} \\ \mu_1^2 & \mu_2^2 & \dots & \mu_{2n_m}^2 \\ \vdots & \vdots & \dots & \vdots \\ \mu_1^{2n_m-1} & \mu_2^{2n_m-1} & \dots & \mu_{2n_m}^{2n_m-1} \end{array} \right] \left\{ \begin{array}{c} C_{ij,1} \\ C_{ij,2} \\ C_{ij,3} \\ \vdots \\ C_{ij,2n_m} \end{array} \right\} = \left\{ \begin{array}{c} R_{y_iy_j}(0) \\ R_{y_iy_j}(\Delta t) \\ R_{y_iy_j}(2\Delta t) \\ \vdots \\ R_{y_iy_j}((2n_m-1)\Delta t) \end{array} \right\} \tag{3.24}$$

3.2.1.2 Ibrahim time-domain method (ITD)

Originally the *Ibrahim time-domain method* (ITD) was developed for the modal identification from free vibration response time series [70]. This means, it can be considered as an early output-only modal analysis method. It was then used to analyse estimated impulse response functions which had the advantage that also mass-normalized mode shapes could be identified. Since the introduction of the principle of NExT, to analyse estimated correlation functions rather than impulse response functions, the ITD method has also been applied to correlation functions. Compared to the use of measured free response data, this has the advantage that the analysed data is less noise-contaminated.

However, for the explanation of the procedure it will be, as in [49] started from the original idea, the consideration of a free vibration response of one degree-of-freedom i of a multi degree-of-freedom system:

$$y_i(k\Delta t) \;=\; \sum_{r=1}^{2n_m} \psi_{ir}\, e^{\lambda_r\, k\Delta t} \tag{3.25}$$

with the complex variable $\lambda_r = -\omega_r\,\zeta_r \pm \mathrm{i}\,\omega_r\sqrt{1-\zeta_r^2}$ It is noted that ϕ_{ir} denotes the element i of an unscaled mode r. The number of modes n_m to be taken into account does not necessarily equal the number of degrees-of-freedom N as usually only a limited number of modes contribute to or can be identified from measured output signals.

After collecting the response data measured at n_o degrees-of-freedom over the period $0\ldots p\,\Delta t$ a system of equations can be established:

$$\begin{bmatrix} y_1(\Delta t) & y_1(2\Delta t) & \ldots & y_1(p\,\Delta t) \\ y_2(\Delta t) & y_2(2\Delta t) & \ldots & y_2(p\,\Delta t) \\ \vdots & \vdots & \ldots & \vdots \\ y_{n_o}(\Delta t) & y_{n_o}(2\Delta t) & \ldots & y_{n_o}(p\,\Delta t) \end{bmatrix} = \begin{bmatrix} \psi_{11} & \psi_{12} & \ldots & \psi_{1\,2n_m} \\ \psi_{21} & \psi_{22} & \ldots & \psi_{2\,2n_m} \\ \vdots & \vdots & \ldots & \vdots \\ \psi_{n_o1} & \psi_{n_o2} & \ldots & \psi_{n_o\,2n_m} \end{bmatrix} \begin{bmatrix} e^0 & e^{\lambda_1\,\Delta t} & & e^{\lambda_1\,p\Delta t} \\ e^0 & e^{\lambda_2\,\Delta t} & & e^{\lambda_2\,p\Delta t} \\ \vdots & \vdots & \ldots & \vdots \\ e^0 & e^{s\lambda_{2n_m}\,\Delta t} & & e^{\lambda_{2n_m}\,p\Delta t} \end{bmatrix} \tag{3.26}$$

or in compact form:

$$[y] \;=\; [\Psi]\;[\Lambda] \tag{3.27}$$

Taking a second set of data that is shifted by Δt, equation (3.25) becomes

$$\bar{y}_i(\Delta t) \;=\; y_i((k+1)\Delta t) \;=\; \sum_{r=1}^{2n_m} \psi_{ir}\, e^{\lambda_r\,(k+1)\Delta t} \;=\; \sum_{r=1}^{2n_m} \bar{\psi}_{ir}\, e^{\lambda_r\, k\Delta t} \tag{3.28}$$

with the relation

$$\bar{\psi}_{ir} \;=\; \psi_{ir}\, e^{\lambda_r\,\Delta t} \tag{3.29}$$

Similar to equation (3.27) one can also arrange a system of equations gathering all measured signals

$$[\bar{y}] \;=\; \left[\bar{\Psi}\right]\;[\Lambda] \tag{3.30}$$

Matrices $[\Psi]$ and $\left[\bar{\Psi}\right]$ can be related by a transformation matrix $[T]$ which is also called *system matrix* [49], [116]:

$$[T]\;[\Psi] \;=\; \left[\bar{\Psi}\right] \tag{3.31}$$

Substituting into equation (3.30) yields

$$[\bar{y}] \;=\; [T]\;[\Psi]\;[\Lambda] \tag{3.32}$$

which becomes with relation (3.27)

$$[\bar{y}] \;=\; [T]\;[y] \tag{3.33}$$

consequently, it is possible to obtain matrix $[T]$ directly from the two sets af measured response series.

$$[T] \;=\; [\bar{y}]\;[y]^T\,\left([y]\,[y]^T\right)^{-1} \tag{3.34}$$

From equation (3.29) can be directly concluded that the respective columns of matrices $\left[\bar{\Psi}\right]$ and $[\Psi]$ are related by

$$\left\{\bar{\psi}_r\right\} = \{\psi_r\}\, e^{\lambda_r \Delta t} \tag{3.35}$$

With equation (3.31) one obtains

$$[T]\,\{\psi_r\} = e^{\lambda_r \Delta t}\,\{\psi_r\} \tag{3.36}$$

which is a standard eigenvalue problem. While the eigenvectors of matrix $[T]$ are unscaled eigenvectors of the considered system, the natural frequencies and damping values can be derived from the eigenvalues [49]:

$$\mu_r = e^{\lambda_r \Delta t} = e^{-\omega_r \zeta_r + \mathrm{i}\,\omega_r \sqrt{1-\zeta_r^2}\,\Delta t} \tag{3.37}$$

$$\longrightarrow\ \lambda_r = \frac{\ln(\mu_r)}{\Delta t} \tag{3.38}$$

$$\omega_r = |\lambda_r| \tag{3.39}$$

$$\zeta_r = -\frac{\mathrm{Re}\,[\lambda_r]}{|\lambda_r|} \tag{3.40}$$

As mentioned earlier, it is possible to apply the described algorithm also to correlation functions rather than measured free vibration response series. In [116] is suggested, not to use only two but p sets of time shifted correlation functions. By arranging them in a block Hankel matrix with p block rows, one obtains a system of equations of which every pair of consecutive block rows forms a set of equations as in equations (3.26) and (3.30). An improvement of the ITD, especially with respect to the identification of close modes, was suggested in [93].

3.2.2 Random Decrement Technique (RDT)

The *random decrement technique* (RDT) was proposed in [37] and [38] to derive a free vibration response estimate from random vibration measurements by averaging sequences of the acquired time series starting from a point that satisfies a common trigger condition. Later it was shown, that the random decrement signature is proportional to the autocorrelation function of a zero-mean, stationary Gaussian random process [139].

So, the RDT is not a modal identification technique by itself. However, it can be applied to estimate correlation functions which are, in a second step, be used as base for modal identification. In [25] was show by some studies, that the RDT can be faster than the traditional FFT-based approach. It can also deliver more accurate results for short correlation function estimates and in case of low damping [25], [26]. However, for the estimation of cross-correlation functions between signals with small correlation, the RDT produces larger errors than the FFT-based technique [26].

In case that both excitation and response measurements are available, Frequency response functions can be estimated from Fourier transforms of the random decrement signatures as suggested in [9], [24] and [87]. However, in context with operational modal analysis, the random decrement technechnique has been mainly proposed as an estimator of correlation functions which are analyzed subsequently by means of the Ibrahim time domain method or another algorithm that requires correlation functions or free vibration response data [11], [69], [25].

Since the random decrement technique was originally developed for the application to single time series, further studies were focused on trigger conditions that improve the accuracy of correlation function estimates in multi-signal analyses. As a result the vector triggering random decrement technique was proposed [68], [12]. Alternative to the application of time domain identification techniques, in [126] and [125] was suggested to derive power spectral densities from the random decrement sequences which are then used as base for a modal identification by means of a frequency domain method.

The quality of the correlation function estimates depends on the choice of parameters such as the trigger level and the length of the extracted sequences. Two approaches to assess the quality of the random decrement signatures have been presented in [13]. A strategy that can be applied to vector triggered random decrement signatures was developed in [10]. An overview about different triggering conditions is given in [8]. Further investigations on the quality of random decrement signatures and the choice of trigger parameters are still the subject of ongoing research [153]

3.2.3 ARMA methods

As derived in section 2.7.5, a dynamic system subjected to a random excitation can be represented by the discrete-time stochastic state-space model (2.127)

$$\begin{aligned} \{x_{k+1}\} &= [A]\,\{x_k\} + \{w_k\} \\ \{y_k\} &= [C]\,\{x_k\} + \{v_k\} \end{aligned} \tag{3.41}$$

One problem in output-only system identification is that the random inputs $\{v_k\}$ and $\{w_k\}$ are unknown. Therefore, the system state vector $\{x_{k+1}\}$ can only be estimated even if one assumes that the system matrices are known. Suppose that there is a method to estimate $\{x(t_k)\} = \{x_k\}$ from the state vectors at previous instants up to t_{k-1}, one can define $\{\hat{x}(t_k|t_{k-1})\}$ as the *optimal one-step-ahead predictor of the state vector*. Similarly, $\{\hat{y}(t_k|t_{k-1})\}$ is the *one-step-ahead predictor of the measured response* $\{y_k\}$ [4]. The deviations of these predictions from the respective true values are according to [4] defined as the *state prediction error*

$$\{\varepsilon(t_k)\} = \{\hat{x}(t_k|t_{k-1})\} - \{x(t_k)\} \tag{3.42}$$

and the so-called *innovation*

$$\begin{aligned} \{e(t_k)\} &= \{y(t_k)\} - \{\hat{y}(t_k|t_{k-1})\} \\ &= \{y(t_k)\} - [C]\,\{\hat{x}(t_k|t_{k-1})\} \end{aligned} \tag{3.43}$$

which represents the part of the response $\{y(t_k)\}$ that cannot be predicted from the response until instant t_{k-1}.

To predict the state vector $\{\hat{x}(t_k|t_{k-1})\}$ such that the state prediction error $\{\varepsilon(t_k)\}$ is minimized, the so-called *Kalman filtering* was developed. Assuming steady-state response of the system due to Gaussian white noise excitation, the state predictor can be be formulated as [4]

$$\{\hat{x}(t_{k+1}|t_k)\} = \{\hat{x}(t_{k+1}|t_{k-1})\} + [\mathcal{K}]\;\{e(t_k)\} \tag{3.44}$$

where $[\mathcal{K}]$ is the *steady-state Kalman gain.*

Since $\{\hat{x}(t_{k+1}|t_{k-1})\}$ can be estimated based on the state-space model by means of the system matrix $[A]$ and the steady-state prediction at time step t_k, the steady-state optimal state predictor can be described in terms of the Kalman filter of the state-space system with Gaussian white noise excitation. This description forms together with equation (3.43) the *innovation state-space model*:

$$\begin{aligned}\{\hat{x}(t_{k+1}|t_k)\} &= [A]\,\{\hat{x}(t_k|t_{k-1})\} + [\mathcal{K}]\,\{e(t_k)\} && (3.45)\\ \{y(t_k)\} &= [C]\,\{\hat{x}(t_k|t_{k-1})\} + \{e(t_k)\} && (3.46)\end{aligned}$$

By recursively substituting the innovation state-space model into equation (3.46), one obtains for instant t_{k+l} [4]

$$\{y(t_{k+l})\} = [C]\,[A]^l\,\{\hat{x}(t_k|t_{k-1})\} + \sum_{j=1}^{l}[C]\,[A]^{l-j}\,[\mathcal{K}]\,\{e(t_{k+j-1})\} + \{e(t_{k+l})\} \tag{3.47}$$

The observation equation of the innovation state space model (3.46) can also be represented by an *Auto-Regressive Moving Average Vector* (ARMAV) model of order n [4], [20]:

$$\begin{aligned}\{y(t_k)\} &+ [A_1]\,\{x(k-1)\} + [A_2]\,\{x(k-2)\} + \ldots + [A_n]\,\{x(k-n)\}\\ &= \{e(t_k)\} + [C_1]\,\{e(t_{k-l})\} + \ldots + [C_n]\,\{e(t_{k-n})\} && (3.48)\end{aligned}$$

Each of the n *auto-regressive* (AR) matrix coefficients $[A_i]$ as well as the *moving average* (MA) matrix coefficients $[C_i]$ are of dimension $n_o \times n_o$, where n_o is the number of measured response signals. The AR and MA matrix coefficients are related to the system matrices by [4]

$$\begin{bmatrix}[A_n] & [A_{n-1}] & \ldots & [A_2] & [A_1]\end{bmatrix} = -[C]\,[A]^n \underbrace{\begin{bmatrix}[C]\\ [C]\,[A]\\ \vdots\\ [C]\,[A]^{n-1}\end{bmatrix}^{-1}}_{[O_n]^{-1}} \tag{3.49}$$

and

$$\begin{bmatrix}[C_n] & [C_{n-1}] & \ldots & [C_1] & [I]\end{bmatrix} = \begin{bmatrix}[A_n] & [A_{n-1}] & \ldots & [A_1] & [I]\end{bmatrix}\,[T(n-1)] \tag{3.50}$$

where $[O_n]$ is called the *observability matrix* and

$$[T(n-1)] = \begin{bmatrix}[I] & [0] & \ldots & [0] & [0]\\ [C]\,[\mathcal{K}] & [I] & \ldots & [0] & [0]\\ [C]\,[A]\,[\mathcal{K}] & [C]\,[\mathcal{K}] & \ldots & [0] & [0]\\ \vdots & \vdots & \ldots & \vdots & \vdots\\ [C]\,[A]^{n-2}\,[\mathcal{K}] & [C]\,[A]^{n-3}\,[\mathcal{K}] & \ldots & [I] & [0]\end{bmatrix} \tag{3.51}$$

According to [4], the ARMAV model can be represented in state-space form as

$$\begin{aligned}\{\hat{x}(t_{k+1}|t_k)\} &= \left[\tilde{A}\right]\,\{\hat{x}(t_k|t_{k-1})\} + \left[\tilde{\mathcal{K}}\right]\,\{e(t_k)\} && (3.52)\\ \{y(t_k)\} &= \left[\tilde{C}\right]\,\{\hat{x}(t_k|t_{k-1})\} + \{e(t_k)\} && (3.53)\end{aligned}$$

with matrices $\left[\tilde{A}\right]$, $\left[\tilde{\mathcal{K}}\right]$ and $\left[\tilde{C}\right]$ and the state vector $\{\hat{x}(t_k|t_{k-1})\}$ being defined as

$$\left[\tilde{A}\right] = \begin{bmatrix} [0] & [I] & \dots & [0] & [0] \\ [0] & [0] & \dots & [0] & [0] \\ \vdots & \vdots & \dots & \vdots & \vdots \\ [0] & [0] & \dots & [0] & [I] \\ -[A_n] & -[A_{n-1}] & \dots & -[A_2] & -[A_1] \end{bmatrix} \tag{3.54}$$

$$\left[\tilde{\mathcal{K}}\right] = \begin{bmatrix} [I] & [0] & \dots & [0] & [0] \\ [A_1] & [I] & \dots & [0] & [0] \\ [A_2] & [A_1] & \dots & [0] & [0] \\ \vdots & \vdots & \dots & \vdots & \vdots \\ [A_{n-1}] & [A_{n-2}] & \dots & [A_1] & [I] \end{bmatrix}^{-1} \begin{bmatrix} [C_1]-[A_1] \\ [C_2]-[A_2] \\ [C_3]-[A_3] \\ \vdots \\ [C_n]-[A_n] \end{bmatrix} \tag{3.55}$$

$$\left[\tilde{C}\right] = \begin{bmatrix} [I] & [0] & \dots & [0] & [0] \end{bmatrix} \tag{3.56}$$

and

$$\{\hat{x}(t_k|t_{k-1})\} = \begin{Bmatrix} \{\hat{y}(t_k|t_{k-1})\} \\ \{\hat{y}(t_{k+1}|t_{k-1})\} \\ \vdots \\ \{\hat{y}(t_{k+n-2}|t_{k-1})\} \\ \{\hat{y}(t_{k+n-1}|t_{k-1})\} \end{Bmatrix} \tag{3.57}$$

The AR and MA matrix coefficients can be identified by application of a *prediction-error identification method* (PEM) [90] with the objective to minimize the *prediction error*

$$\{\varepsilon(t_k,\{\theta\})\} = \{y(t_k)\} - \{\hat{y}(t_k|t_{k-1};\{\theta\})\} \tag{3.58}$$

which depends on the *model parameters* $\{\theta\}$.

It has been derived in [4] that the solution of the eigenvalue problem

$$\left[\tilde{A}\right]\{v_r\} = \mu_r\{\psi_r\} \tag{3.59}$$

yields the eigenvectors

$$\{v_r\} = \begin{Bmatrix} \{\psi_r\} \\ \mu_r\{\psi_r\} \\ \mu_r^2\{\psi_r\} \\ \vdots \\ \mu_r^{n-1}\{\psi_r\} \end{Bmatrix} \tag{3.60}$$

The mode shapes $\{\psi_r\}$ are related to the eigenvectors of matrix $\left[\tilde{A}\right]$ by

$$\{\psi_r\} = \left[\tilde{C}\right]\{v_r\} \tag{3.61}$$

Eventually, the natural frequencies and modal damping ratios can be extracted from the eigenvalues $\mu_r = e^{\lambda_r\,\Delta t} = e^{-\omega_r\,\zeta_r + \mathrm{i}\,\omega_r\sqrt{1-\zeta_r^2}\,\Delta t}$ by applying equations (3.38) to (3.40).

The identification of the AR and MA parameters involves a nonlinear optimization with $n\cdot n_o$ variables. The model order n is not known in advance. Furthermore, the quality of the solution of the optimization problems depends on several factors such as the

- choice of the objective function
- choice of the optimization method
- choice of an initial parameter set
- choice of number of signals n_o and
- choice of model order n.

Consequently, the identification of modal parameters by means of ARMAV models is less robust than other methods. Therefore, the ARMA methods are less frequently used.

3.2.4 Stochastic Subspace Identification (SSI)

The application of *stochastic subspace identification* (SSI) techniques has become very popular within the last two decades. The objective of the algorithms is the identification of system matrices of the stochastic state-space model (2.127) from which the modal parameters can be derived. One distinguishes two major methods, the *covariance-driven* and the *data-driven stochastic subspace identification*. Both procedures are explained in the following subsections.

3.2.4.1 Covariance-driven stochastic subspace identification (SSI-cov)

It has been derived in section 2.7.5 that the covariance matrix of n_o measured response signals for a certain time shift t_i can be represented by means of the system matrices of the state-space model as (2.141)

$$[R_i] = [C]\,[A]^{i-1}\,[G]\,; \qquad i = 1, 2, \ldots \tag{3.62}$$

As described, for example, in [107] and [106], which are the major references for the following explanations, the covariance matrices estimated from the measured response signals can be arranged in a *block Toeplitz matrix* in the form

$$\left[T_{1|i}\right] = \begin{bmatrix} [R_i] & [R_{i-1}] & \ldots & [R_1] \\ [R_{i+1}] & [R_i] & \ldots & [R_2] \\ \vdots & \vdots & \ldots & \vdots \\ [R_{2i-1}] & [R_{2i-2}] & \ldots & [R_i] \end{bmatrix} \tag{3.63}$$

From equation (3.62) follows that this block Toeplitz matrix can be related to the matrices of the state-space model by

$$\left[T_{1|i}\right] = \underbrace{\begin{bmatrix} [C] \\ [C]\,[A] \\ \vdots \\ [C]\,[A]^{i-1} \end{bmatrix}}_{[O_i]} \underbrace{\left[\; [A]^{i-1}\,[G] \quad \ldots \quad [A]\,[G] \quad [G] \;\right]}_{[\Gamma_i]} \tag{3.64}$$

$$= [O_i]_{(n_o i \times n)} [\Gamma_i]_{(n \times n_o i)} \tag{3.65}$$

where $[O_i]$ denotes the *extended observability matrix* while $[\Gamma_i]$ is the *reversed extended controllability matrix* [138], [106], [116]. The term *extended* refers to the assumption that $i > n$. Since $\left[T_{1|i}\right]$ can be obtained from the multiplication of a matrix with n columns by a matrix with n rows, its rank is n, the order of the model to be identified. A common method to determine the rank of the matrix is to count the number of non-zero singular values of a respective *singular value decomposition* (SVD). For the block Toeplitz matrix one obtains

$$\left[T_{1|i}\right] = [U]\,[S]\,[V]^T = \begin{bmatrix} [U_1] & [U_2] \end{bmatrix} \begin{bmatrix} [S_1] & [0] \\ [0] & [0] \end{bmatrix} \begin{bmatrix} [V_1]^T \\ [V_2]^T \end{bmatrix} = [U_1]\,[S_1]\,[V_1]^T \tag{3.66}$$

with the real, orthonormal matrices singular $[U]$ and $[V]$.

$$\left([U]^T\,[U] = [U]\,[U]^T = [I]_{(n_o i \times n_o i)}\right)$$

$$\left([V]^T\,[V] = [V]\,[V]^T = [I]_{(n_o i \times n_o i)}\right)$$

Matrix $[S_1]$ is a diagonal matrix containing the non-zero singular values.

From equations (3.65) and (3.66) can be derived that one set of matrices $[O_i]$ and $[\Gamma_i]$ can be obtained from seperating the results of the singular value decomposition of the block Toeplitz matrix:

$$[O_i] = [U_1]\,[S_1]^{\frac{1}{2}} \tag{3.67}$$

$$[\Gamma_i] = [S_1]^{\frac{1}{2}}\,[V_1]^T \tag{3.68}$$

This means that the observability matrix $[O_i]$ and the controllability matrix $[\Gamma_i]$ can be directly computed from the covariances of all measured output signals. Accordingly, matrix $[C]$ equals to the first n_o rows of matrix $[O_i]$ while matrix $[G]$ can be obtained by extracting the last n_o columns of matrix $[\Gamma_i]$.

For the determination of matrix $[A]$ one can follow several approaches. It can be computed, for example, by means of sub-matrices of the observability matrix $[O_i]$ as:

$$[A] = \begin{bmatrix} [C] \\ [C]\,[A] \\ \vdots \\ [C]\,[A]^{i-2} \end{bmatrix}^{\dagger} \begin{bmatrix} [C]\,[A] \\ [C]\,[A]^2 \\ \vdots \\ [C]\,[A]^{i-1} \end{bmatrix} \tag{3.69}$$

where the superscript † denotes the More-Penrose pseudoinverse.

Another option is the calculation by means of a block Toeplitz matrix $\left[T_{2|i+1}\right]$, which differs from matrix $\left[T_{1|i}\right]$ by the composition of correlation matrices for time lags from 2 to $2i$ rather than from 1 to $2i-1$:

$$\left[T_{2|i+1}\right] = \begin{bmatrix} [R_{i+1}] & [R_i] & \dots & [R_2] \\ [R_{i+2}] & [R_{i+1}] & \dots & [R_3] \\ \vdots & \vdots & \dots & \vdots \\ [R_{2i}] & [R_{2i-1}] & \dots & [R_{i+1}] \end{bmatrix} \tag{3.70}$$

$$\begin{aligned} &= \begin{bmatrix} [C]\,[A] \\ [C]\,[A]^2 \\ \vdots \\ [C]\,[A]^i \end{bmatrix} \begin{bmatrix} [A]^{i-1}\,[G] & \dots & [A]\,[G] & [G] \end{bmatrix} \\ &= \begin{bmatrix} [C] \\ [C]\,[A] \\ \vdots \\ [C]\,[A]^{i-1} \end{bmatrix} [A] \begin{bmatrix} [A]^{i-1}\,[G] & \dots & [A]\,[G] & [G] \end{bmatrix} \\ &= [O_i]\,[A]\,[\Gamma_i] \end{aligned} \tag{3.71}$$

Solving equation (3.71) for matrix $[A]$ and substituting equations (3.67) and (3.68) yields

$$[A] = [O_i]^{\dagger} \left[T^{ref}_{2|i+1}\right] [\Gamma_i]^{\dagger} = [S_1]^{-\frac{1}{2}} [U_1]^T \left[T_{2|i+1}\right] [V_1]\,[S_1]^{-\frac{1}{2}} . \tag{3.72}$$

As derived in section 2.7.3 in equations (2.106) and (2.107), the modal parameters can be computed from the eigenvalue decomposition of matrix $[A]$:

$$[A]\,[\Psi] = [\Psi]\,[\Lambda_d] = [\Psi]\,[diag(\mu_r)] \tag{3.73}$$

$$\lambda_r = \frac{\ln(\mu_r)}{\Delta t} \tag{3.74}$$

$$\omega_r = |\lambda_r| \tag{3.75}$$

$$\zeta_r = -\frac{\mathrm{Re}\,[\lambda_r]}{|\lambda_r|} \tag{3.76}$$

The observed mode shapes are eventually computed by means of equation (2.108):

$$[V] = [C]\,[\Psi]$$

In the descriptions above it was always assumed that the covariance matrices contain the complete set of covariances that can be derived from the measured signals. However, to reduce the computational effort, it is possible to compute only the covariances of all response signals to $n_r \le n_o$ selected reference signals [107], [106]. The covariance matrices have then n_o rows but only as many columns as reference signals were selected. The reversed controllability matrix $[\Gamma_i]$ has then also a respectively reduced number of columns.

3.2.4.2 Data-driven stochastic subspace identification (SSI-data)

By means of the data driven stochastic subspace identification technique (SSI-data), that was derived in [134] and described in further publications such as [135], [138], the matrices of the innovation state-space model (3.45) and (3.46) of model order n are derived by means of the Kalman filter state estimates $\{\hat{x}_k\} = \{\hat{x}(t_k|t_{k-1})\}$ and the extended $(i > n)$ observabilty matrix $[O_i]$. The Kalman filter state sequences

$$\left[\hat{X}_i\right] = \left[\begin{array}{cccc} \{\hat{x}_i\} & \{\hat{x}_{i+1}\} & \dots & \{\hat{x}_{i+j-1}\} \end{array}\right] \tag{3.77}$$

are derived directly from the measured response signals.

Since the identification is based on the geometrical concept of orthogonal projections of a row space of one matrix onto the row space of a second matrix, first the definition of an *orthogonal projection* of the row space of a matrix $[A]$ onto the row space of a matrix $[B]$ is introduced [138]:

$$\begin{aligned} [A] \,/\, [\mathbf{B}] &= [A]\,[B]^T \left[[B]\,[B]^T\right]^{\dagger} [B] \\ \downarrow &\leftarrow \left[\Sigma_{[A,B]}\right] = [A]\,[B]^T , \left[\Sigma_{[B,B]}\right] = [B]\,[B]^T \\ &= \left[\Sigma_{[A,B]}\right] \left[\Sigma_{[B,B]}\right]^{\dagger} [B] \\ &= [A]\,[\Pi_B] \end{aligned} \tag{3.78}$$

where $\left[\Sigma_{[A,B]}\right]$ is the *covariance matrix* between the two matrices indicated in the subscript. For the sake of enhanced clarity, the matrix on which's row space the result lies is printed bold face. The geometrical interpretation of such an orthogonal projection for the case of a two-dimensional row space is illustrated in figure 3.1.

The projection of the row space of a matrix $[A]$ onto the orthogonal complement of the row space of a matrix $[B]$ is defined as

$$[A] \,/\, [\mathbf{B}]^{\perp} = [A]\,[\Pi_{B^\perp}] \tag{3.79}$$

with

$$[\Pi_{B^\perp}] + [\Pi_B] = [I] \tag{3.80}$$

Accordingly, one obtains

$$[A] = [A]\,[\Pi_B] + [A]\,[\Pi_{B^\perp}] \tag{3.81}$$

As also indicated in figure 3.1 for the two-dimensional case, the application of the two projections $[\Pi_B]$ and $[\Pi_{B^\perp}]$ to the row space of matrix $[A]$ results in two matrices with orthogonal row spaces.

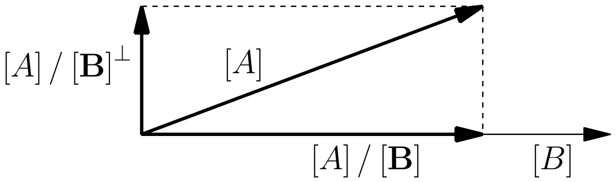

Figure 3.1: Illustration of the orthogonal projection of the two-dimensional space $[A]$ onto the two-dimensional space $[B]$

In [134], [135] and [138] has been derived how the orthogonal projection of the row space of a submatrix of an output block Hankel matrix onto the row space of a second submatrix of the same matrix can be used to identify the stochastic state-space system. The *output block Hankel matrix* $\left[Y_{0|2i-1}\right]$ is constructed from $(2i+j-1)$ sets of measured response samples $\{y_k\}$:

$$
\begin{aligned}
\left[Y_{0|2i-1}\right] &= \frac{1}{\sqrt{j}}
\begin{array}{c} \\ \\ i \\ \\ \\ \\ \\ i \\ \\ \end{array}
\overset{\xleftrightarrow{\qquad\qquad j \qquad\qquad}}{\left[\begin{array}{cccc}
\{y_0\} & \{y_1\} & \dots & \{y_{j-1}\} \\
\{y_1\} & \{y_2\} & \dots & \{y_j\} \\
\vdots & \vdots & \dots & \vdots \\
\{y_{i-2}\} & \{y_{i-1}\} & \dots & \{y_{i+j-3}\} \\
\{y_{i-1}\} & \{y_i\} & \dots & \{y_{i+j-2}\} \\ \hline
\{y_i\} & \{y_{i+1}\} & \dots & \{y_{i+j-1}\} \\
\{y_{i+1}\} & \{y_{i+2}\} & \dots & \{y_{i+j}\} \\
\vdots & \vdots & \dots & \vdots \\
\{y_{2i-1}\} & \{y_{2i}\} & \dots & \{y_{2i+j-2}\}
\end{array}\right]}
\begin{array}{c} \\ \\ \text{“past”} \\ \\ \\ \\ \\ \text{“future”} \\ \\ \end{array}
= \left[\frac{\left[Y_{0|i-1}\right]}{\left[Y_{i|2i-1}\right]}\right] = \left[\frac{[Y_p]}{[Y_f]}\right] \\
&= \frac{1}{\sqrt{j}}
\begin{array}{c} \\ \\ i+1 \\ \\ \\ \\ \\ i-1 \\ \\ \end{array}
\left[\begin{array}{cccc}
\{y_0\} & \{y_1\} & \dots & \{y_{j-1}\} \\
\{y_1\} & \{y_2\} & \dots & \{y_j\} \\
\vdots & \vdots & \dots & \vdots \\
\{y_{i-2}\} & \{y_{i-1}\} & \dots & \{y_{i+j-3}\} \\
\{y_{i-1}\} & \{y_i\} & \dots & \{y_{i+j-2}\} \\
\{y_i\} & \{y_{i+1}\} & \dots & \{y_{i+j-1}\} \\ \hline
\{y_{i+1}\} & \{y_{i+2}\} & \dots & \{y_{i+j}\} \\
\vdots & \vdots & \dots & \vdots \\
\{y_{2i-1}\} & \{y_{2i}\} & \dots & \{y_{2i+j-2}\}
\end{array}\right]
\begin{array}{c} \\ \\ \text{“past”} \\ \\ \\ \\ \\ \text{“future”} \\ \\ \end{array}
= \left[\frac{\left[Y_{0|i}\right]}{\left[Y_{i+1|2i-1}\right]}\right] = \left[\frac{\left[Y_p^+\right]}{\left[Y_f^-\right]}\right]
\end{aligned}
\tag{3.82}
$$

The extended observability matrix

$$
[O_i] = \left[\begin{array}{c} [C] \\ [C]\,[A] \\ \vdots \\ [C]\,[A]^{i-1} \end{array}\right] \tag{3.83}
$$

and the reversed extended controllability matrix

$$
[\Gamma_i] = \left[\begin{array}{cccc} [A]^{i-1}\,[G] & \dots & [A]\,[G] & [G] \end{array}\right] \tag{3.84}
$$

have already been defined in section 3.2.4.1 but are re-called here for the sake of completeness. According to the main theorem of the stochastic subspace identification problem formulated in [138], the following relations pertain:

- The projection

  $$
  \begin{aligned}
  [\mathcal{P}_i] &= [Y_f] \,/\, [\mathbf{Y_p}] = [Y_f]\,[Y_p]^T \left[[Y_p]\,[Y_p]^T\right]^{\dagger} [Y_p] \\
  &= \left[\Sigma_{[Y_f,Y_p]}\right] \left[\Sigma_{[Y_p,Y_p]}\right]^{\dagger} [Y_p]
  \end{aligned}
  \tag{3.85}
  $$

  equals the product of the extended observability matrix and the *Kalman filter state sequence*:

  $$
  [\mathcal{P}_i] = [O_i] \left[\hat{X}_i\right] \tag{3.86}
  $$

- From the singular value decomposition

$$[W_1]\,[\mathcal{P}_i]\,[W_2] = \begin{bmatrix} [U_1] & [U_2] \end{bmatrix} \begin{bmatrix} [S_1] & [0] \\ [0] & [0] \end{bmatrix} \begin{bmatrix} [V_1]^T \\ [V_2]^T \end{bmatrix} = [U_1]\,[S_1]\,[V_1]^T \tag{3.87}$$

  where $[W_1]_{n_oi\times n_oi}$ and $[W_2]_{j\times j}$ are two user-defined *weighting matrices*, one can obtain the order of the state-space model as the number of non-zero singular values and the extended observability matrix $[O_i]$ as well as the associated extended controllability matrix $[\Gamma_i]$

$$\begin{aligned} [O_i] &= [W_1]^{-1}\,[U_1]\,[S_1]^{\frac{1}{2}}\,[T] \\ [\Gamma_i] &= [O_i]^{\dagger}\left[\Sigma_{[Y_f,Y_p]}\right] \end{aligned} \tag{3.88}$$

  Matrix $[T]$ is a transformation matrix that is usually chosen to be an identity matrix $[T] = [I]$.

- One can derive the Kalman filter state sequence $\left[\hat{X}_i\right]$ from either

$$\left[\hat{X}_i\right] = [O_i]^{\dagger}\,[\mathcal{P}_i] \tag{3.89}$$

  or

$$\left[\hat{X}_i\right]\,[W_2] = [T]^{-1}\,[S_1]^{\frac{1}{2}}\,[V_1]^T \tag{3.90}$$

For the identification of the state matrices, three algorithms are suggested in [138] of which the first that solves the state-space equations, is explained here. Similar to $\left[\hat{X}_i\right]$, the Kalman filter state sequence $\left[\hat{X}_{i+1}\right]$ is computet from the orthogonal projection

$$[\mathcal{P}_{i-1}] = \left[Y_f^-\right] / \left[\mathbf{Y}_\mathbf{p}^+\right] = [O_{i-1}]\left[\hat{X}_{i+1}\right] \tag{3.91}$$

$$\longrightarrow \left[\hat{X}_{i+1}\right] = [O_{i-1}]^{\dagger}\,[\mathcal{P}_{i-1}] \tag{3.92}$$

To create matrix $[O_{i-1}]$ one has only to discard the last M rows of matrix $[O_i]$.

With the computed state sequences $\left[\hat{X}_i\right]$ and $\left[\hat{X}_{i+1}\right]$ the stochastic state-system can be desribed by

$$\begin{bmatrix} \left[\hat{X}_{i+1}\right] \\ \left[Y_{i|i}\right] \end{bmatrix} = \begin{bmatrix} [A] \\ [C] \end{bmatrix}\left[\hat{X}_i\right] + \begin{bmatrix} [\rho_w] \\ [\rho_v] \end{bmatrix} \tag{3.93}$$

where $\left[Y_{i|i}\right]$ denotes the ith block row of the block Hankel matrix. Since the *Kalman filter residuals* $[\rho_w]$ and $[\rho_v]$ are uncorrelated with the sequences $\left[\hat{X}_i\right]$ the system of equations (3.93) can be solved for $[A]$ and $[C]$ in a least squares sense [138]:

$$\begin{bmatrix} [A] \\ [C] \end{bmatrix} = \begin{bmatrix} \left[\hat{X}_{i+1}\right] \\ \left[Y_{i|i}\right] \end{bmatrix}\left[\hat{X}_i\right]^{\dagger} \tag{3.94}$$

The modal parameters can then be calculated by means of equations (3.73) to (3.76). Matrix $[G]$ is obtained by extracting the last M columns of matrix $[\Gamma_i]$.

Similarly as for the covariance-driven stochastic subspace identification, a referenced-based version was also suggested in [107], [106] for the data-driven stochastic subspace identification.

The difference is that the row space of the "future" parts of the block Hankel matrix are projected to that part of the "past" submatrices that contains only the response data of selected reference sensors:

$$[\mathcal{P}_{i,ref}] = [Y_f] \,/\, [\mathbf{Y_{p,ref}}] \tag{3.95}$$

$$[\mathcal{P}_{i-1,ref}] = \left[Y^-_{f,ref}\right] \,/\, \left[\mathbf{Y}^+_{\mathbf{p,ref}}\right] \tag{3.96}$$

Furthermore it is noted, that some special choices of the weighting matrices $[W_1]$ and $[W_2]$ can be related to principle component (PC), unweighted principle component (UPC) and canonical variate analysis (CVA). The unweighted principle component analysis corresponds to choosing identity matrices for both weighting matrices as also recommended in [106]. Equation (3.88) simplifies then, with $[T] = [I]$ to

$$[O_i] = [U_1]\,[S_1]^{\frac{1}{2}} \tag{3.97}$$

The block Hankel matrix $\left[Y_{0|2i-1}\right]$ consists of $2i$ block rows of which each has n_o rows, n_o being the number of measured output signals, and j columns, each column referring to one instant of time. Typically, the number of columns is considerably larger than the number of rows ($j \gg 2n_oi$). Consequently, the computation of the projections according to equation (3.85) is computationally very demanding. Therefore, a more efficient possibility to compute the projections $[\mathcal{P}_i]$ and $[\mathcal{P}_{i-1}]$ was suggested in [107] and [106].

Since it is possible to find a QR decomposition of any matrix which has not less rows than columns this is also possible for the transpose of the block Hankel matrix $\left[Y_{0|2i-1}\right]$ assuming that the condition $j \gg 2n_oi$ is satisfied:

$$\left[Y_{0|2i-1}\right]^T = [Q]\,[R] \tag{3.98}$$

where $[R]$ is an upper triangular matrix and $[Q]$ is an orthogonal matrix with the property $[Q]^T\,[Q] = [I]$. From equation (3.98) follows, that the block Hankel matrix $\left[Y_{0|2i-1}\right]$ can be represented by the transpose of the QR decomposition:

$$\left[Y_{0|2i-1}\right] = [R]^T\,[Q]^T \tag{3.99}$$

For the more general case of the reference-based SSI-data with n_r reference sensors this equation can be re-written dividing the matrices in submatrices [107], [106]

$$[Y_{0|2i-1}] = \begin{array}{r|cccc|c|l} & n_r\,i & n_r & n_o - n_r & n_o(i-1) & j & \\ \hline n_r\,i & [R_{11}]^T & [0] & [0] & [0] & [Q_1]^T & n_r\,i \\ n_r & [R_{21}]^T & [R_{22}]^T & [0] & [0] & [Q_2]^T & n_r \\ n_o - n_r & [R_{31}]^T & [R_{32}]^T & [R_{33}]^T & [0] & [Q_3]^T & n_o - n_r \\ n_o(i-1) & [R_{41}]^T & [R_{42}]^T & [R_{43}]^T & [R_{44}]^T & [Q_4]^T & n_o(i-1) \end{array} \tag{3.100}$$

With the submatrices defined in equation (3.100), the projections of the row space of the "future" part of $\left[Y_{0|2i-1}\right]$ onto the row space of the "past" partition related to the reference sensors are obtained as [107], [106]

$$[\mathcal{P}_{i,ref}] = \begin{bmatrix} [R_{21}]^T \\ [R_{31}]^T \\ [R_{41}]^T \end{bmatrix} [Q_1]^T \tag{3.101}$$

$$[\mathcal{P}_{i-1,ref}] = \begin{bmatrix} [R_{41}]^T & [R_{42}]^T \end{bmatrix} \begin{bmatrix} [Q_1]^T \\ [Q_2]^T \end{bmatrix} \tag{3.102}$$

Even though the measured response sequence $\left[Y_{i|i}\right]$ which appears in the stochastic state-space equation (3.93) can be extracted directly from the block Hankel matrix, it can also be represented by means of the QR decomposition:

$$\left[Y_{i|i}\right] = \begin{bmatrix} [R_{21}]^T & [R_{22}]^T & [0] \\ [R_{31}]^T & [R_{32}]^T & [R_{33}]^T \end{bmatrix} \begin{bmatrix} [Q_1]^T \\ [Q_2]^T \\ [Q_3]^T \end{bmatrix} \tag{3.103}$$

In case that all sensors are considered as reference sensors ($n_r = n_o$), equations (3.100) to (3.103) simplify to

$$[Y_{0|2i-1}] = \begin{array}{r} \\ n_o\,i \\ n_o \\ n_o(i-1) \end{array} \begin{array}{c} \begin{array}{ccc} n_o\,i & n_o & n_o(i-1) \end{array} \\ \left[\begin{array}{ccc} [R_{11}]^T & [0] & [0] \\ [R_{21}]^T & [R_{22}]^T & [0] \\ [R_{31}]^T & [R_{32}]^T & [R_{33}]^T \end{array}\right] \end{array} \begin{array}{c} j \\ \left[\begin{array}{c} [Q_1]^T \\ [Q_2]^T \\ [Q_3]^T \end{array}\right] \end{array} \begin{array}{l} \\ n_o\,i \\ n_o \\ n_o(i-1) \end{array} \tag{3.104}$$

$$[\mathcal{P}_i] = \begin{bmatrix} [R_{21}]^T \\ [R_{31}]^T \end{bmatrix} [Q_1]^T \tag{3.105}$$

$$[\mathcal{P}_{i-1}] = \begin{bmatrix} [R_{31}]^T & [R_{32}]^T \end{bmatrix} \begin{bmatrix} [Q_1]^T \\ [Q_2]^T \end{bmatrix} \tag{3.106}$$

$$\left[Y_{i|i}\right] = \begin{bmatrix} [R_{21}]^T & [R_{22}]^T \end{bmatrix} \begin{bmatrix} [Q_1]^T \\ [Q_2]^T \end{bmatrix} \tag{3.107}$$

as also formulated in [116].

3.3 Frequency domain methods

3.3.1 Peak picking method

One of the simplest methods to estimate natural frequencies and mode shapes from ambient vibration measurements is the *peak picking* method that is sometimes also called *basic frequency method* [22], [116]. It is based on the assumption that the response close to a resonance is almost completely governed by a single mode:

$$\{q_{\omega_r}(t)\} \approx \{\psi_r\}\, q_r(t) \tag{3.108}$$

The output correlation matrix which is only related to the measured response $\{y(t)\}$ can then be approximated by [116]

$$[R_{yy}(\tau)] = \mathbf{E}\left[\{y(t+\tau)\}\,\{y(t)\}^T\right] = R_{q_r q_r}(\tau)\,\{\psi_r\}\,\{\psi_r\}^T \tag{3.109}$$

where $R_{q_r q_r}(\tau)$ is the auto-correlation function of the modal coordinate q_r. The spectral density matrix becomes then [106], [116]

$$[G_{yy}(\omega)] = G_{q_r q_r}(\omega)\,\{\psi_r\}\,\{\psi_r\}^H \tag{3.110}$$

From equation (3.110) one can deduce that each column of the spectral density matrix at resonance contains an unscaled estimate of mode shape $\{\psi_r\}$. In fact, these estimates are actually *operational deflection shapes* (ODS). However, for well separated modes these estimates can be considered as being close to unscaled mode shapes.

Natural frequencies are extracted as those values at which the spectral density functions have a peak, which gave the methodology the name. To improve the smoothness of the spectral estimates, averaged spectral density functions can be used [50]. Furthermore, the *output coherence functions*,

$$\gamma^2_{y_i y_j}(\omega) = \frac{G^2_{y_i y_j}(\omega)}{G_{y_i y_i}\,G_{y_j y_j}} \tag{3.111}$$

which are an indicator of the signal-to-noise ratio, are used to support the identification of spectral peaks as resonances. At resonances the coherence function should be close to 1.

An estimate of the modal damping ratio is typically derived by means of the half-power bandwidth method:

$$2\,\zeta = \frac{\omega_a^2 - \omega_b^2}{2\omega_r^2} \approx \frac{\Delta\omega}{\omega_r} \tag{3.112}$$

where the notation refers to the values indicated in figure 3.2.

The algorithm can be summarized as follows [116]:

1. Computation of the power spectral density matrix' trace which is the sum of the auto-spectral densities at frequency ω_r. This approach makes spectral components from all sensors visible what has the advantage, compared to the consideration of only a single signal's spectrum, that also modal components which have not significant amplitudes at some sensor locations become visible. The latter is, for example, important to be able to identify both vertical and lateral bending modes of beam-like structures from bidirectional measurements.

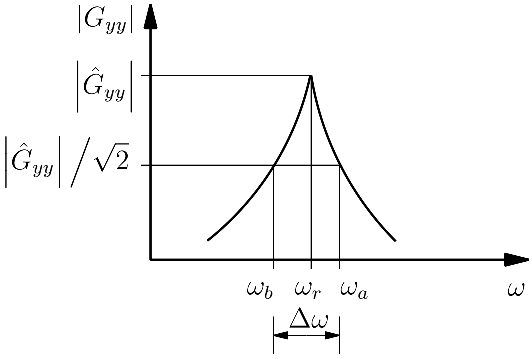

Figure 3.2: Illustration of the half-power bandwidth method

2. Selection of one column of the power spectral density matrix as mode shape estimate. Even though the choice of the coulmn could be theoretically arbitrary, it is important to choose a column that contains the cross-spectral densities with respect to a reference sensor that has been well excited in the respective mode, or in other words, which was not located close to a node of the mode shape.

3. Computation of the modal damping ratio by means of the half-power bandwidth method or an alternative technique.

The peak picking method is a relatively simple technique and can be a very useful tool for an estimation of modal parameters. However, the accuracy of the natural frequency depends on the frequency resolution of the spectral density function. As already pointed out, the estimates of the mode shapes are operational deflection shapes what means that they are actually a superposition of several modes. If there are close natural frequencies, the identified deflection shape may contain also considerable contributions of other modes than the one to be identified. Furthermore, the damping estimate obtained from the half-power bandwidth method is probably of limited accuracy [106], [117]. Especially in case of relatively small differences in frequency between neighbouring modes and if the damping cannot be considered as very low, the assumption of well separated modes (3.108) is not valid anymore.

3.3.2 Frequency domain decomposion method (FDD)

As explained in section 3.3.1, the identification results obtained by means of the peak picking method suffer from some limitations of the method. To overcome these drawbacks, the use of *frequency domain decomposition* (FDD) for modal identification was proposed in [22], [23]. It is related to the *complex mode identification function* (CMIF) that is derived from a singular value decomposition of FRF matrices [130], [51].

In [22] the theoretical background of the FDD technique has been described starting from the relation between the power spectral densities of the excitation and response, repectively, and the frequeny response function:

$$[G_{YY}(\omega)] = [H(\omega)]\,[G_{FF}(\omega)]\,[H(\omega)]^H \tag{3.113}$$

It has been derived then that the autospectral densities of the response can be represented as a decomposition into modal components

$$[G_{YY}(\omega)] = \sum_{r=1}^{n_m} \left(\frac{\{\psi_r\}\ \{g_r\}^T}{(\mathrm{i}\omega\ -\ \lambda_r)} + \frac{\{\psi_r\}^*\ \{g_r\}^H}{(\mathrm{i}\omega\ -\ \lambda_r^*)} \right) \tag{3.114}$$

which has a very similar structure as the modal representation of a frequency response function. The *operational reference factors* $\{g_r\}$ are here the equivalent to the modal participation factors in the FRF formulation. In a next step is stated that the first left singular vector of the singular value decomposition of the *power spectral density* (PSD) matrix at resonance

$$[G_{YY}(\omega_r)] = [U_r]\ [S_r]\ [V_r]^H = [U_r]\ [S_r]\ [U_r]^H \tag{3.115}$$

is an estimate of an unscaled mode shape assuming that the PSD matrix is of rank one which corresponds with a single degree-of-freedom system. In the case of close modes, the PSD matrix can be of higher rank. Than as many singular vectors as there are non-zero singular values can be considered as mode shape estimates.

An alternative approach for the derivation is given in [19]. It starts from the modal transformation (2.7) of the modal output

$$\{y(t)\} = [\Psi]\ \{y_m(t)\} \tag{3.116}$$

The output correlation matrix can be then written as

$$[R_{yy}(\tau)] = \mathbf{E}\left[\{y(t+\tau)\}\,\{y(t)\}^T\right] = [\Psi]\ [R_{y_m y_m}(\tau)]\ [\Psi]^T \tag{3.117}$$

where $[R_{y_m y_m}(\tau)]$ is the correlation matrix of the modal coordinates. As one can assume that the modal coordinates are uncorrelated, $[R_{y_m y_m}(\tau)]$ is a diagonal matrix. As power spectral density is defined as the Fourier transform of the correlation function, the output power spectral density matrix can be obtained from

$$[G_{YY}(\omega_r)] = [\Psi]\ [G_{y_m y_m}(\omega_r)]\ [\Psi]^H \tag{3.118}$$

Due to the assumption that the modal coordinates are uncorrelated, the autopower spectral density matrix is a diagonal matrix with the positive entries on its diagonal. Therefore, equation (3.118) has a comparable structure to the factorization in equation (3.115). This means, that the resulting relation

$$[G_{YY}(\omega_r)] = [U_r]\ [S_r]\ [U_r]^H \tag{3.119}$$

can be derived on different ways as proven in [19] where has been shown as well, that one can also perform an eigenvalue decomposition of the output correlation matrix to derive estimates of the mode shapes.

To identify the natural frequency and modal damping ratio, a portion of the PSD around the frequency corresponding to a selected peak of the first singular value curve is extracted. By computing the inverse Fourier transform of the extracted portion of the PSD an estimate of the modal contribution to the correlation function is obtained. From this correlation function the natural frequency is derived from the period of zero crossings and the modal damping ratio can be estimated from the logarithmic decrement of the decaying functions envelope. This procedure was already mentioned in [22]. In [23] the second step of the analysis is described more detailed. To select the base for the inverse Fourier transform, the correlation between the respective singular vectors in the vicinity of a selected peak of the singular value curve and the extracted mode shape estimate is investigated by means of the *modal assurance criterion* (MAC) which has been suggested first in [3] and discussed in literature, as for example in [2], [49]:

$$MAC(i,j) = \frac{\left|\{\psi_i\}^T \{\psi_j\}^*\right|^2}{\left(\{\psi_i\}^T \{\psi_i\}^*\right)\left(\{\psi_j\}^T \{\psi_j\}^*\right)} = \frac{\left|\{\psi_j\}^H \{\psi_i\}\right|^2}{\left(\{\psi_j\}^H \{\psi_j\}\right)\left(\{\psi_i\}^H \{\psi_i\}\right)} \tag{3.120}$$

The MAC is always a value within the range $0 \dots 1$, where a higher value indicates a higher degree of correlation between the two vectors. To select the range of the auto spectral density function to be selected for inverse Fourier transformation a search is started from the peak point to both sides. The search is terminated at respective lower and upper frequency bounds ω_l and ω_u if the MAC value between the selected mode shape and the respective singular vector becomes less than a pre-defined threshold.

Often the first step of the analysis, the estimation of mode shapes from the singular vectors and of natural frequencies as those values that are related to the peaks in the singular value curve is called frequency domain decomposition technique (FDD) while the extension by the second step, the consideration of the correlation function's modal component is referred to the name *enhanced frequency domain decomposition* (EFDD) technique.

A modification of the EFDD was suggested in [126] and further investigated in [125]. Instead of computing the spectral densities by means of the Fourier transforms of the measured output signals, for example as averaged spectra applying Welch's method, they are computed as the Fourier transforms of estimates of the correlation functions generated by the random decrement technique. To improve the quality of the damping estimates, in [152] a modification of the selected autospectral densities in the vicinity of the identified resonance prior to the inverse Fourier transormation was suggested.

This modification consists of a pre- and post-multiplication of the spectral estimates by the respective mode shape estimate which acts like a modal filter:

$$G^{enh}_{Y_iY_i}(\omega_l \leq \omega_r \leq \omega_u) \; = \; \{U_{r1}\}^H \; G_{Y_iY_i}(\omega_l \leq \omega_r \leq \omega_u) \; \{U_{r1}\} \tag{3.121}$$

This modification was introduced in [152] as *frequency-spacial domain decomposition* (FSDD) technique.

Another modification of the EFDD technique has been proposed in [78]. While the mode shapes are identified from the left singular vectors of the PSD matrix' singular value decomposition, the natural frequencies and damping coefficients are derived by curve fittig a the positive output power spectra.

3.3.3 Poly-reference least-squares complex frequency domain method (p-LSCF)

The *least-squares complex frequency* (LSCF) domain method in its original form was developed based on the representation of the frequency response function (FRF) as a common denominator model [62]. An extension of this approach to operational modal analysis was developed in [104].

However, one of the main shortcomings of the LSCF method is that the identification of close modes can cause difficulties [63], [109].

An improvement could be achieved by representing the frequency response function by a right matrix fraction description rather than by a common denominator model [63]. The applicability of this approach, which is called *poly-reference least-squares complex frequency domain method* (p-LSCF), to output-only measurements was derived in [33]. As mentioned above, the methodology which became also known under the name PolyMAX [109], [108],[110], was initially derived for the FRF that can be decomposed into its modal components [67]

$$[H(\omega)] = \sum_{r=1}^{n_m} \left(\frac{\{\psi_r\}\,\{l_r\}^T}{\mathrm{i}\omega - \lambda_r} + \frac{\{\psi_r\}^*\,\{l_r\}^H}{\mathrm{i}\omega - \lambda_r^*} \right) \tag{3.122}$$

where $\{\psi_r\}$ are the mode shapes while $\{l_r\}^T$ contains the modal participation factors of mode r. The poles λ_r are given as

$$\lambda_r,\, \lambda_r^* = -\zeta_r\,\omega_r \pm \mathrm{i}\omega_r\sqrt{1-\zeta_r^2}$$

As was shown in [33], the positive output power spectral density matrix can, under the assumption of white noise excitation, be described as well by a modal decomposition of a very similar structure as in equation (3.122)

$$\left[S_{yy}^{+}(\omega)\right] = \sum_{r=1}^{n_m} \left(\frac{\{\phi_r\}\,\{g_r\}^T}{\mathrm{i}\omega - \lambda_r} + \frac{\{\phi_r\}^*\,\{g_r\}^H}{\mathrm{i}\omega - \lambda_r^*} \right) \tag{3.123}$$

In contrary to the modal participation factors in equation (3.122), the *operational reference factors* $\{g_r\}$ have no direct physical meaning.

As described for the frequency response function in equation (2.169), one can also represent the positive output power spectral density matrix by a right matrix fraction description

$$\left[S_{yy}^{+}(\omega)\right] = [N_R(\omega)]\,[D_R(\omega)]^{-1} = \left[\sum_{j=0}^{p_N} \left[N_{R_j(\omega)}\right] z^j\right] \left[\sum_{j=0}^{p_D} \left[D_{R_j(\omega)}\right] z^j\right]^{-1} \tag{3.124}$$

Each row of matrix $\left[S_{yy}^{+}(\omega)\right]$ refers to one of n_o measured output signals while the columns are related to the n_r selected reference channels. If all channels are considered as references, $\left[S_{yy}^{+}(\omega)\right]$ is a square matrix of dimension $n_o \times n_o$. Any row o, $o = 1, 2, \ldots, n_o$ of matrix $\left[S_{yy}^{+}(\omega)\right]$ can be written as

$$\left\langle S_{yy_o}^{+}(\omega)\right\rangle = \langle N_o(\omega)\rangle\,[D_R(\omega)]^{-1} \tag{3.125}$$

where $\langle\cdot\rangle$ denotes a row vector and

$$\langle N_o(\omega)\rangle_{1\times n_r} = \sum_{j=0}^{p} z^j(\omega)\,\langle\beta_{oj}\rangle_{1\times n_r} \tag{3.126}$$

$$[D_R(\omega)]_{n_r\times n_r} = \sum_{j=0}^{p} z^j(\omega)\,[\alpha_j]_{n_r\times n_r} \tag{3.127}$$

with $z^j(\omega) = \left(e^{\mathrm{i}\omega\Delta t}\right)^j = e^{j\,(\mathrm{i}\omega\Delta t)}$. It is noted that the polynomial order of the numerator and of the denominator polynomials were set to the same value p. Furthermore, real-valued polynomial coefficients are assumed. For later use, the *polynomial coefficients* $\langle\beta_{oj}\rangle$ and $[\alpha_j]$ are assembled in matrices as follows:

$$[\beta_o]_{(p+1)\times n_r}=\begin{bmatrix}\langle\beta_{o0}\rangle\\ \langle\beta_{o1}\rangle\\ \vdots\\ \langle\beta_{op}\rangle\end{bmatrix}\quad [\alpha]_{n_r(p+1)\times n_r}=\begin{bmatrix}[\alpha_0]\\ [\alpha_1]\\ \vdots\\ [\alpha_p]\end{bmatrix}\quad [\theta]_{(n_r+n_o)(p+1)\times n_r}=\begin{bmatrix}[\beta_1]\\ [\beta_2]\\ \vdots\\ [\beta_{n_o}]\\ [\alpha]\end{bmatrix} \tag{3.128}$$

The objective is to identify all parameters collected in matrix $[\theta]$ such that the difference between the positive output power spectral density matrix $\left[S^+_{yy}(\omega_k)\right]$, computed based on equation (3.124) using these parameters, and an estimate $\left[\hat{S}^+_{yy}(\omega_k)\right]$ which was obtained from the measured response series is minimized for the discrete frequencies ω_k within a selected frequency range of interest $\omega_1 \le \omega_k \le \omega_{n_f}$. With this respect, the error function

$$\begin{aligned}\left\langle\varepsilon_o^{NLS}(\omega_k,[\theta])\right\rangle &= w_o(\omega_k)\left(\left\langle S^+_{yy_o}(\omega_k,[\theta])\right\rangle-\left\langle\hat{S}^+_{yy_o}(\omega_k)\right\rangle\right)\\ &= w_o(\omega_k)\left(\langle N_o(\omega_k,[\beta_o])\rangle\,[D_R(\omega_k,[\beta_o])]^{-1}-\left\langle\hat{S}^+_{yy_o}(\omega_k)\right\rangle\right)\end{aligned} \tag{3.129}$$

can be defined. By introducing the weighting coefficients $w_o(\omega_k)$ that refer to a specific output o and a certain frequency ω_k it is possible to take into account quality differences between the measured signals. The superscript NLS refers to the non-linear least squares character of equation errors (3.129). An objective function can then be obtained by combining the equation errors for all outputs and all frequencies:

$$\mathcal{E}^{NLS}([\theta])=\sum_{o=1}^{n_o}\sum_{k=1}^{n_f}\operatorname{tr}\left[\left\langle\varepsilon_o^{NLS}(\omega_k,[\theta])\right\rangle^H\left\langle\varepsilon_o^{NLS}(\omega_k,[\theta])\right\rangle\right]\longrightarrow\min \tag{3.130}$$

Minimizing equation (3.130) implies the search for the roots of the derivatives with respect to the unknown coefficients $[\theta]$ what leads to non-linear expressions. An approximation in form of a linear least-squares (LS) problem can be achieved by post-mulication of equation (3.129) by the denominator polynomial matrix $[D_R(\omega_k,[\beta_o])]$ which gives equation errors

$$\begin{aligned}\left\langle\varepsilon_o^{LS}(\omega_k,[\theta])\right\rangle &= w_o(\omega_k)\left(\langle N_o(\omega_k,[\beta_o])\rangle-\left\langle\hat{S}^+_{yy_o}(\omega_k)\right\rangle[D_R(\omega_k,[\beta_o])]\right)\\ &= w_o(\omega_k)\sum_{j=0}^{p}\left(z_j(\omega_k)\langle\beta_{oj}\rangle-z_j(\omega_k)\left\langle\hat{S}^+_{yy_o}(\omega_k)\right\rangle[\alpha_j]\right)\end{aligned} \tag{3.131}$$

By collecting all equation errors $\left\langle\varepsilon_o^{LS}(\omega_k,[\theta])\right\rangle$ referring to a single output channel in a matrix yields the system of equations

$$\left[E_o^{LS}(\omega_k,[\theta])\right]_{n_f\times n_r}=\begin{bmatrix}\left\langle\varepsilon_o^{LS}(\omega_1,[\theta])\right\rangle\\ \left\langle\varepsilon_o^{LS}(\omega_2,[\theta])\right\rangle\\ \vdots\\ \left\langle\varepsilon_o^{LS}(\omega_{n_f},[\theta])\right\rangle\end{bmatrix}=\begin{bmatrix}[X_o] & [Y_o]\end{bmatrix}\begin{bmatrix}[\beta_o]\\ [\alpha]\end{bmatrix} \tag{3.132}$$

with the matrices

$$[X_o]_{n_f\times(p+1)}=\begin{bmatrix}w_o(\omega_1)z_0(\omega_1) & w_o(\omega_1)z_1(\omega_1) & \dots & w_o(\omega_1)z_p(\omega_1)\\ w_o(\omega_2)z_0(\omega_2) & w_o(\omega_2)z_1(\omega_2) & \dots & w_o(\omega_2)z_p(\omega_2)\\ \vdots & \vdots & \dots & \vdots\\ w_o(\omega_{n_f})z_0(\omega_{n_f}) & w_o(\omega_{n_f})z_1(\omega_{n_f}) & \dots & w_o(\omega_{n_f})z_p(\omega_{n_f})\end{bmatrix} \tag{3.133}$$

$$[Y_o]_{n_f \times n_r(p+1)} = - \begin{bmatrix} w_o(\omega_1) z_0(\omega_1) \left\langle \hat{S}^+_{yy_o}(\omega_1) \right\rangle & \dots & w_o(\omega_1) z_p(\omega_1) \left\langle \hat{S}^+_{yy_o}(\omega_1) \right\rangle \\ w_o(\omega_2) z_0(\omega_2) \left\langle \hat{S}^+_{yy_o}(\omega_2) \right\rangle & \dots & w_o(\omega_2) z_p(\omega_2) \left\langle \hat{S}^+_{yy_o}(\omega_2) \right\rangle \\ \vdots & \dots & \vdots \\ w_o(\omega_{n_f}) z_0(\omega_{n_f}) \left\langle \hat{S}^+_{yy_o}(\omega_{n_f}) \right\rangle & \dots & w_o(\omega_{n_f}) z_p(\omega_{n_f}) \left\langle \hat{S}^+_{yy_o}(\omega_{n_f}) \right\rangle \end{bmatrix} \tag{3.134}$$

For the linearized equation errors an objective function similar to equation (3.130) can be formulated:

$$\mathcal{E}^{LS}([\theta]) = \sum_{o=1}^{n_o} \sum_{k=1}^{n_f} \operatorname{tr} \left[\left\langle \varepsilon_o^{LS}(\omega_k, [\theta]) \right\rangle^H \left\langle \varepsilon_o^{LS}(\omega_k, [\theta]) \right\rangle \right] \longrightarrow \min \tag{3.135}$$

which can be written with equation (3.132) as

$$\begin{aligned} \mathcal{E}^{LS}([\theta]) &= \sum_{o=1}^{n_o} \operatorname{tr} \left[\left[E_o^{LS}(\omega_k, [\theta]) \right]^H \left[E_o^{LS}(\omega_k, [\theta]) \right] \right] \\ &= \sum_{o=1}^{n_o} \operatorname{tr} \left[\begin{bmatrix} [\beta_o]^T & [\alpha]^T \end{bmatrix} \begin{bmatrix} [X_o]^H \\ [Y_o]^H \end{bmatrix} \begin{bmatrix} [X_o] & [Y_o] \end{bmatrix} \begin{bmatrix} [\beta_o] \\ [\alpha] \end{bmatrix} \right] \\ &= \operatorname{tr} \left[[\theta]^T [J]^H \cdot [J] [\theta] \right] \end{aligned} \tag{3.136}$$

where the matrix $[J]$ is

$$[J]_{n_o n_f \times (n_r + n_o)(p+1)} = \begin{bmatrix} [X_1] & [0] & \dots & [0] & [Y_1] \\ [0] & [X_2] & \dots & [0] & [Y_2] \\ \vdots & \vdots & \dots & \vdots & \vdots \\ [0] & [0] & \dots & [X_{n_o}] & [Y_{n_o}] \end{bmatrix} \tag{3.137}$$

Due to the above mentioned assumption of real valued coefficients θ, the product $[J]^H [J]$ can be replaced by its real part [108], [63] such that the objective function becomes

$$\mathcal{E}^{LS}([\theta]) = \operatorname{tr} \left[[\theta]^T \operatorname{Re} \left[[J]^H [J] \right] [\theta] \right] \tag{3.138}$$

The real part of the matrix product $[J]^H [J]$ is formed as

$$\operatorname{Re} \left[[J]^H [J] \right]_{(n_o+n_r)(p+1) \times (n_o+n_r)(p+1)} = \begin{bmatrix} [R_1] & [0] & \dots & [0] & [S_1] \\ [0] & [R_2] & \dots & [0] & [S_2] \\ \vdots & \vdots & \dots & \vdots & \vdots \\ [0] & [0] & \dots & [R_{n_o}] & [S_M] \\ [S_1]^T & [S_2]^T & \dots & [S_{n_o}]^T & [\sum_{o=1}^{n_o} [T_o]] \end{bmatrix} \tag{3.139}$$

with

$$\begin{aligned} [R_o]_{(p+1) \times (p+1)} &= \operatorname{Re} \left[[X_o]^H [X_o] \right] \\ [S_o]_{(p+1) \times n_r(p+1)} &= \operatorname{Re} \left[[X_o]^H [Y_o] \right] \\ [T_o]_{n_r(p+1) \times n_r(p+1)} &= \operatorname{Re} \left[[Y_o]^H [Y_o] \right] \end{aligned} \tag{3.140}$$

To minimize the objective function, its first derivatives with respect to the unknown parameters have to be set to zero. The partial derivatives of $\mathcal{E}^{LS}([\theta])$ can be found as [63], [108]

$$\left[\frac{\partial \mathcal{E}^{LS}([\theta])}{\partial\,[\beta_o]}\right] \;=\; 2\,\left([R_o]\,[\beta_o] \,+\, [S_o]\,[\alpha]\right)\,[0] \tag{3.141}$$

$$\left[\frac{\partial \mathcal{E}^{LS}([\theta])}{\partial\,[\alpha]}\right] \;=\; 2\sum_{o=1}^{n_o}\Big([S_o]^T\,[\beta_o] \,+\, [T_o]\,[\alpha]\Big) \;=\; [0] \tag{3.142}$$

Solving equation (3.141) for $[\beta_o]$

$$[\beta_o] \;=\; -\,[R_o]^{-1}\,[S_o]\,[\alpha] \tag{3.143}$$

and substituting into equation (3.142) yields

$$\left[2\sum_{o=1}^{n_o}\Big([T_o] \,-\, [S_o]^T\,[R_o]^{-1}\,[S_o]\Big)\right]\,[\alpha] \;=\; [\Xi]_{n_r(p+1)\times n_r(p+1)}\,[\alpha] \;=\; [0] \tag{3.144}$$

Since matrix $[\Xi]$ can be completely constructed based on the estimated output spectra, the denominator polynomial parameters $[\alpha]$ can be obtained by solving equation (3.144) in a least-squares sense. To avoid the trivial solution for $[\alpha]$, a constraint has to be introduced. One possibility is to require that one specific submatrix $[\alpha_j]$ is equal to a non-zero constant. It is suggested in [91] to choose the identity matrix as lowest order denominator polynomial order submatrix:

$$\begin{array}{r} \\ n_r \\ p\cdot n_r \\ \\ \end{array}
\begin{array}{c} \begin{array}{cc} n_r \quad & \quad p\cdot n_r \end{array} \\ \underbrace{\left[\begin{array}{c|c} [\Xi_{aa}] & [\Xi_{ab}] \\ \hline [\Xi_{ba}] & [\Xi_{bb}] \end{array}\right]}_{[\Xi]} \end{array}
\begin{array}{c} n_r \\ \underbrace{\left[\begin{array}{c} [I] \\ \hline [\alpha_1] \\ \vdots \\ [\alpha_p] \end{array}\right]}_{[\alpha]} \end{array}
\left.\begin{array}{c} \\ \\ \\ \end{array}\right\}[\alpha_b] =
\left[\begin{array}{c} [0] \\ \hline [0] \\ \vdots \\ [0] \end{array}\right] \tag{3.145}$$

From equation (3.145) can be seen that

$$[\alpha_b] \;=\; -\,[\Xi_{bb}]^{-1}\,[\Xi_{ba}]$$

and consequently

$$[\alpha] \;=\; \left[\begin{array}{c} [I] \\ -\,[\Xi_{bb}]^{-1}\,[\Xi_{ba}] \end{array}\right] \tag{3.146}$$

In [116] the highest order denominator polynomial submatrix of $[\alpha]$ was set to an identity matrix as constraint for the solution of equation (3.144) which results in

$$\begin{array}{r} \\ p\cdot n_r \\ n_r \\ \\ \end{array}
\begin{array}{c} \begin{array}{cc} p\cdot n_r \quad & \quad n_r \end{array} \\ \underbrace{\left[\begin{array}{c|c} [\Xi_{aa}] & [\Xi_{ab}] \\ \hline [\Xi_{ba}] & [\Xi_{bb}] \end{array}\right]}_{[\Xi]} \end{array}
\begin{array}{c} n_r \\ \underbrace{\left[\begin{array}{c} [\alpha_0] \\ \vdots \\ [\alpha_{p-1}] \\ \hline [I] \end{array}\right]}_{[\alpha]} \end{array}
\left.\begin{array}{c} \\ \\ \\ \end{array}\right\}[\alpha_a] =
\left[\begin{array}{c} [0] \\ \vdots \\ [0] \\ \hline [0] \end{array}\right] \tag{3.147}$$

Therefore one has

$$[\alpha_a] = -[\Xi_{aa}]^{-1}[\Xi_{ab}]$$

and

$$[\alpha] = \begin{bmatrix} [I] \\ -[\Xi_{aa}]^{-1}[\Xi_{ab}] \end{bmatrix} \tag{3.148}$$

The two described possibilities for the choice of constraints were investigated in [33]. It was shown there that the choice $[\alpha_p] = [I]$ leads to much clearer stabilisation diagrams. This term has not been introduced so far but will be explained in section 3.4.1.

With the denominator polynomial parameters $[\alpha]$ the numerator polynomial parameter matrices $[\beta_o]$ are obtained by substituting into equation (3.143).

The system poles are found as the roots of the denominator polynomial [39]. For their identification, the so-called *companion matrix* $[\mathcal{A}]$ is built from the denominator polynomial parameters [33]:

$$[\mathcal{A}] = \begin{bmatrix} -[\alpha_p]^{-1}[\alpha_{p-1}] & -[\alpha_p]^{-1}[\alpha_{p-2}] & \dots & -[\alpha_p]^{-1}[\alpha_1] & -[\alpha_p]^{-1}[\alpha_0] \\ [I] & [0] & \dots & [0] & [0] \\ \vdots & \vdots & \dots & \dots & \vdots \\ [0] & [0] & \dots & [I] & [0] \end{bmatrix} \tag{3.149}$$

From the solution of the eigenvalue problem

$$[\mathcal{A}]\,[\Psi_2] = [\Psi_2]\,[\Lambda] = [\Psi_2]\,[diag(\mu_r)] \tag{3.150}$$

the system poles μ_r and the operational reference factors $\{g_r\}$ can be retrieved.

$$\{\psi_{2,r}\} = \begin{Bmatrix} \mu_r^{p-1}\{g_r\} \\ \mu_r^{p-2}\{g_r\} \\ \vdots \\ \mu_r\{g_r\} \\ \{g_r\} \end{Bmatrix} \tag{3.151}$$

After the poles have been transformed from the z-domain into the Laplace domain by $\mu_r = e^{\lambda_r \Delta t} \Rightarrow \lambda_r = \frac{\ln(\mu_r)}{\Delta t}$, the natural frequencies and modal damping ratios can be calculated by means of equations (3.39) and (3.40) [39]:

$$\begin{aligned} \omega_r &= |\lambda_r| \\ \zeta_r &= -\frac{\mathrm{Re}\,[\lambda_r]}{|\lambda_r|} \end{aligned}$$

With these results, the mode shapes $[\Psi]$ as well as the lower and upper residuals $[LR]$, $[UR]$ that take into account contributions of modes outside the considered frequency range in the modal decomposition of the positive output spectral density matrix

$$\left[S_{yy}^{+}(\omega)\right] = \sum_{r=1}^{n_m}\left(\frac{\{\psi_r\}\{g_r\}^T}{\mathrm{i}\omega - \lambda_r} + \frac{\{\psi_r\}^*\{g_r\}^H}{\mathrm{i}\omega - \lambda_r^*}\right) + \mathrm{i}\,\omega\,[UR] + \frac{1}{\mathrm{i}\,\omega}[LR] \tag{3.152}$$

can be identified applying a *least-squares frequency domain* (LSFD) estimator [33].

It has been shown in [120], that the companion matrix $[\mathcal{A}]$ in equation(3.149) can be derived as the state matix of a state space system. This agrees with the solution for the system poles in equation (3.149) which is the same as used for all methods that identify the parameters of a state space model. The corresponding matrix $[C]$ that allows for the computation of the mode shapes as

$$[V] = [C]\,[\Psi]$$

is given by [120]

$$[C] = \Big[\; \big[[B_{p-1}] - [B_p]\,[\alpha_p]^{-1}\,[\alpha_{p-1}]\big] \quad \big[[B_{p-2}] - [B_p]\,[\alpha_p]^{-1}\,[\alpha_{p-2}]\big] \quad \dots \quad \big[[B_0] - [B_p]\,[\alpha_p]^{-1}\,[\alpha_0]\big] \;\Big] \tag{3.153}$$

where in matrix $[B_j]$ the row vectors $\langle\beta_{oj}\rangle$ for all n_o output channels referring to the same polynomial order j are collected:

$$[B_j] = \begin{bmatrix} \langle\beta_{1j}\rangle \\ \langle\beta_{2j}\rangle \\ \vdots \\ \langle\beta_{n_oj}\rangle \end{bmatrix} \qquad j = 0 \dots p \tag{3.154}$$

3.3.4 Stochastic frequency-domain subspace method

Similar to the SSI-data algorithm working in time domain, it is also possible to identify a state space model from output spectra by a stochastic subspace identification in frequency-domain [33]. The descriptions in this section follow the derivations in [33].

The stochastic discrete-time state-space model can be formulated in frequency-domain for any of n_f frequency lines as

$$\begin{aligned} z_k\,\{X_k\} &= [A]\,\{X_k\} + \{W_k\} && (3.155)\\ \{Y_k\} &= [C]\,\{X_k\} + \{V_k\} && (3.156)\\ & && (3.157) \end{aligned}$$

where $\{Y_k\}$ and $\{X_k\}$ refer to the *spectral vectors of the output and state vectors*, respectively, at spectral line k. The spectral frequency components of the *process and the measurement noise* at discrete frequency k are contained in the vectors $\{W_k\}$ and $\{V_k\}$ while z_k denotes the transformation variable

$$z_k = e^{\mathrm{i}2\pi\frac{k}{n_f}} \qquad k = 1, 2, \dots, n_f \tag{3.158}$$

Assuming that $\{W_k\}$ and $\{V_k\}$ describe zero mean circular complex independent and uniformly distributed noise, their covariance matrix is given by

$$\left[\mathbf{E}\left[\begin{Bmatrix} \{W_k\} \\ \{V_k\} \end{Bmatrix}\begin{bmatrix} \{W_k\}^H & \{V_k\}^H \end{bmatrix}\right]\right] = \begin{bmatrix} [Q] & [S] \\ [S]^H & [R] \end{bmatrix} \tag{3.159}$$

Successive p times multiplication of equation (3.156) by z_k and recursive substitution of equation (3.155) yields

$$z_k^p\,\{Y_k\} = [C]\,[A]^p\,\{X_k\} + [C]\,[A]^{p-1}\,\{W_k\} + [C]\,[A]^{p-2}\,\{W_k\}\,z_k + \dots + [C]\,\{W_k\}\,z_k^{p-1} + \{V_k\}\,z_k^p \tag{3.160}$$

Collecting the expressions in equation (3.160) for polynomial orders $p = 0, 1, \dots, i$ produces

$$\begin{Bmatrix} \{Y_k\} \\ z_k \{Y_k\} \\ z_k^2 \{Y_k\} \\ \vdots \\ z_k^{i-1} \{Y_k\} \end{Bmatrix} = [O_i] \, \{X_k\} + [\Gamma] \begin{Bmatrix} \{W_k\} \\ z_k \{W_k\} \\ z_k^2 \{W_k\} \\ \vdots \\ z_k^{i-1} \{W_k\} \end{Bmatrix} + \begin{Bmatrix} \{V_k\} \\ z_k \{V_k\} \\ z_k^2 \{V_k\} \\ \vdots \\ z_k^{i-1} \{V_k\} \end{Bmatrix} \tag{3.161}$$

with the extended observability matrix

$$[O_i] = \begin{bmatrix} [C] \\ [C]\,[A] \\ \vdots \\ [C]\,[A]^{i-1} \end{bmatrix} \tag{3.162}$$

and the lower triangular block Toeplitz matrix

$$[\Gamma] = \begin{bmatrix} [0] & [0] & \dots & [0] & [0] & [0] \\ [C] & [0] & \dots & [0] & [0] & [0] \\ [C]\,[A] & [C] & \dots & [0] & [0] & [0] \\ \vdots & \vdots & \dots & \vdots & \vdots & \vdots \\ [C]\,[A]^{i-2} & [C]\,[A]^{i-3} & \dots & [C]\,[A] & [C] & [0] \end{bmatrix} \tag{3.163}$$

If equation (3.161) is established for a model of order n at all frequency lines $k = 1, 2, \dots, n_f$ and collected in respective matrices, one obtains

$$[Y] = [O_i]\,[X] + [\Gamma]\,[W] + [V] \tag{3.164}$$

with the so-called *Vandermonde matrices*

$$[\mathcal{Y}]_{n_o i \times n_f} = \begin{bmatrix} \{Y_1\} & \{Y_2\} & \dots & \left\{Y_{n_f}\right\} \\ z_1 \{Y_1\} & z_2 \{Y_2\} & \dots & z_{n_f} \left\{Y_{n_f}\right\} \\ \vdots & \vdots & \dots & \vdots \\ z_1^{i-1} \{Y_1\} & z_2^{i-1} \{Y_2\} & \dots & z_{n_f^{i-1}} \left\{Y_{n_f}\right\} \end{bmatrix} \tag{3.165}$$

$$[\mathcal{W}]_{2Ni \times n_f} = \begin{bmatrix} \{W_1\} & \{W_2\} & \dots & \left\{W_{n_f}\right\} \\ z_1 \{W_1\} & z_2 \{W_2\} & \dots & z_{n_f} \left\{W_{n_f}\right\} \\ \vdots & \vdots & \dots & \vdots \\ z_1^{i-1} \{W_1\} & z_2^{i-1} \{W_2\} & \dots & z_{n_f^{i-1}} \left\{W_{n_f}\right\} \end{bmatrix} \tag{3.166}$$

$$[\mathcal{V}]_{n_o i \times n_f} = \begin{bmatrix} \{V_1\} & \{V_2\} & \dots & \left\{V_{n_f}\right\} \\ z_1 \{V_1\} & z_2 \{V_2\} & \dots & z_{n_f} \left\{V_{n_f}\right\} \\ \vdots & \vdots & \dots & \vdots \\ z_1^{i-1} \{V_1\} & z_2^{i-1} \{V_2\} & \dots & z_{n_f^{i-1}} \left\{V_{n_f}\right\} \end{bmatrix} \tag{3.167}$$

and the state matrix

$$[X]_{2N \times n_f} = \left[\begin{array}{cccc} \{X_1\} & \{X_2\} & \dots & \left\{X_{n_f}\right\} \end{array} \right] \tag{3.168}$$

The maximal polynomial order i has to be chosen such that

$$i > \frac{n}{n_f}$$

is satisfied.

It has been derived in [33] that the models determining the state space model can be estimated from the Vandermonde matrix $[\mathcal{Y}]$ in a similar way as from the block Hankel matrix of measured output in the SSI-data algorithm. For this, matrix $[\mathcal{Y}]$ is constructed with polynomial orders $-i \leq p < i$ and divided into two parts in the following way:

$$[\mathcal{Y}]_{2n_o i \times n_f} = \left[\begin{array}{cccc} z_1^{-i}\{Y_1\} & z_2^{-i}\{Y_2\} & \dots & z_{n_f}^{-i}\left\{Y_{n_f}\right\} \\ z_1^{-i+1}\{Y_1\} & z_2^{-i+1}\{Y_2\} & \dots & z_{n_f}^{-i+1}\left\{Y_{n_f}\right\} \\ \vdots & \vdots & \dots & \vdots \\ z_1^{-1}\{Y_1\} & z_2^{-1}\{Y_2\} & \dots & z_{n_f^{-1}}\left\{Y_{n_f}\right\} \\ \hline \{Y_1\} & \{Y_2\} & \dots & \left\{Y_{n_f}\right\} \\ z_1\{Y_1\} & z_2\{Y_2\} & \dots & z_{n_f}\left\{Y_{n_f}\right\} \\ \vdots & \vdots & \dots & \vdots \\ z_1^{i-1}\{Y_1\} & z_2^{i-1}\{Y_2\} & \dots & z_{n_f^{i-1}}\left\{Y_{n_f}\right\} \end{array} \right] = \left[\frac{[\mathcal{Y}_-]}{[\mathcal{Y}_+]} \right] \tag{3.169}$$

Very similarly as in the time-domain SSI-data method, the orthogonal projection of the row space of $[\mathcal{Y}_+]$ onto the row space of $[\mathcal{Y}_-]$ is computed to extract the extended observability matrix:

$$[\mathcal{Y}_+] / [\mathcal{Y}_-] = [O_i]\left[\hat{X}\right] \tag{3.170}$$

where $\left[\hat{X}\right]$ contains the Fourier spectra of the forward Kalman filter state sequence. The orthogonal projection (3.170) is obtained from the QR decomposition of $[\mathcal{Y}]^T$

$$\left[\begin{array}{c} [\mathcal{Y}_-] \\ [\mathcal{Y}_+] \end{array} \right] = \left[\begin{array}{cc} [R_{11}]^T & [0] \\ [R_{21}]^T & [R_{22}]^T \end{array} \right] \left[\begin{array}{c} [Q_1]^T \\ [Q_2]^T \end{array} \right] \tag{3.171}$$

$$[\mathcal{Y}_+] / [\mathcal{Y}_-] = [R_{21}]^T [Q_1]^T \tag{3.172}$$

Subsequently the extended observability matrix $[O_i]$ and the state estimates $\left[\hat{X}\right]$ are obtained by means of the singular value decomposition of $[\mathcal{Y}_+] / [\mathcal{Y}_-]$:

$$[\mathcal{Y}_+] / [\mathcal{Y}_-] = \left[\begin{array}{cc} [U_1] & [U_2] \end{array} \right] \left[\begin{array}{cc} [S_1] & [0] \\ [0] & [0] \end{array} \right] \left[\begin{array}{c} [V_1]^H \\ [V_2]^H \end{array} \right] = [U_1]\,[S_1]\,[V_1]^H \tag{3.173}$$

$$[O_i] = [W_1]^{-1}\,[U_1]\,[S_1]^{\frac{1}{2}} \tag{3.174}$$

$$\left[\hat{X}\right] = [S_1]^{\frac{1}{2}}\,[V_1]^H\,[W_2]^{-1} \tag{3.175}$$

The weighting matrices $[W_1]$, $[W_2]$ were introduced in the same way as in the SSI-data algorithm. One valid and typical choice are respective identity matrices. For the estimation of matrices $[A]$ and $[C]$ two options are suggested in [33]:

(a)
- Extraction of matrix $[C]$ as the first n_o rows of matrix $[O_i]$
- Extraction of the first $n_o(i-1)$ rows of matrix $[O_i]$ as $[O_{i,1}]$
- Extraction of the last $n_o(i-1)$ rows of matrix $[O_i]$ as $[O_{i,2}]$
- Computation of
$$[A] = [O_{i,1}]^{\dagger}\ [O_{i,2}]$$

(b) Solution of the state space equation

$$\begin{bmatrix} \left[z_k \hat{X}\right] \\ [Y] \end{bmatrix} = \begin{bmatrix} [A] \\ [C] \end{bmatrix} \left[\hat{X}\right] + \begin{bmatrix} [\rho_{W_k}] \\ [\rho_{V_k}] \end{bmatrix}$$

where the residua can be considered as the spectra of process and measurement noise.

3.4 Model order in parametric methods

3.4.1 Stabilisation diagrams

In the descriptions of parametric modal identification methods in sections 3.2 and 3.3 several mathematical models were introduced which have a certain order n. However, this model order is not known in advance. Accordingly, one of the challenges in the application of parametric methods to both experimental and operational modal analyses is the definition of an appropriate model order for a specific case study.

For example, in the covariance-driven stochastic subspace method (SSI-cov), the model order is linked to the number of non-zero singular values of the block Toeplitz matrix. However, this is a theoretical assumption which is usually not completely applicable to practical studies. There, all computed singular values are usually not zero. One recommendation is to search for a step in the sequence of singular values as an indicator to identify the appropriate model order. But if measured data is analysed, even such a clear step can often not be found. Therefore another approach has to become common practice not only for the SSI-cov method but for all parametric modal analysis methods in general.

Due to the difficulties in the a-priori definition of a model order, the solutions of a mathematical model used in a parametric method are usually computed for a series of assumed model orders. This leads to an overparameterisation and yields beside solutions related to physical modes also solutions that are called *spurious*. To distinguish between physical and spurious modes, one indicates the solutions in a *stabilisation diagram* as the one shown in figure 3.3. Each marker in the diagram refers to one solution of the model.

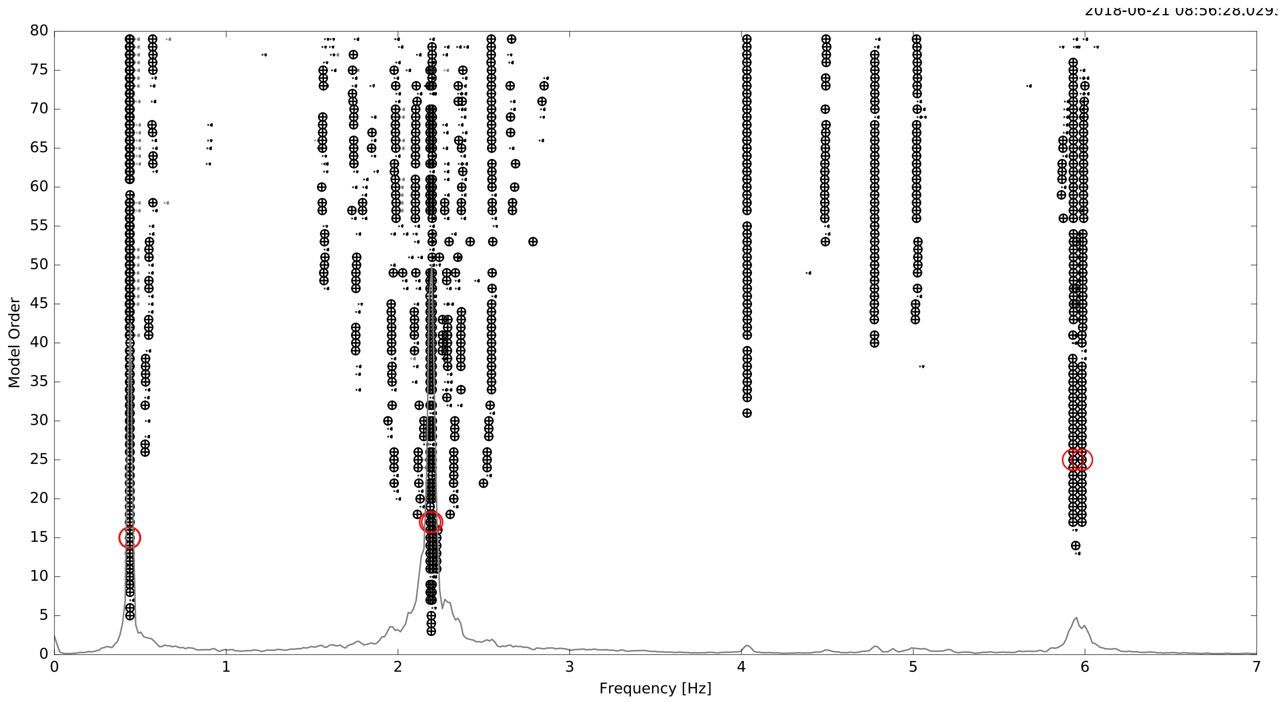

Figure 3.3: Example for a stabilisation diagram

As can be seen in figure 3.3, there are some solutions which occur repeatedly for many model orders while others seem to emerge rather randomly. The first group of solutions, which form column-like structures in the stabilisation diagram, are likely to be related to physical modes. These poles are also called *stable poles*. However, the "formation in columns", which means that the difference between the respective natural frequencies identified for the same mode but with different model orders is small, considers only one part of the modal parameters. To categorize a solution as "stable", not only the natural frequencies but also the modal damping ratios and mode shapes of solutions corresponding to model order k are compared to the respective parameters of the solutions for model order $k-1$. Typical stabilisation criteria are [106], [107], [116]:

$$\frac{|\omega_r(k) - \omega_r(k-1)|}{\omega_r(k-1)} \cdot 100\% \; < \; 1\% \tag{3.176}$$

$$\frac{|\zeta_r(k) - \zeta_r(k-1)|}{\zeta_r(k-1)} \cdot 100\% \; < \; 5\% \tag{3.177}$$

$$(1 \; - \; MAC\left(\{\phi_r(n)\}, \{\phi_r(n-1)\}\right)) \cdot 100\% \; < \; 1 \ldots 2\% \tag{3.178}$$

where MAC denotes the modal assurance criterion already introduced in equation (3.120). The thresholds in equations (3.176) to (3.178) are recommendations but not fixed values and can be adjusted by the analyst.

To reduce the number of spurious solutions occuring in the stabilisation diagram, further a-priori knowledge can be applied. So, poles that have negative damping can be excluded from the list of valid solutions. In case that light damping is expected, one can also define an upper limit for modal damping. For civil engineering structures this assumption is in most cases true, such that a limitation to damping coefficients in the range of, for example, $0 < \zeta \leq 15\%$ could be sensible.

3.4.2 Model order selection for parametric identification methods

The stabilisation diagram provides the analyst a tool to support the distinction between physical and spurious modes. However, assuming that a certain number of solutions forming a column in the stabilisation diagram could be identified as representatives of a certain mode, the challenge of selecting the correct model order remains.

One approach to identify the order of an innovation state-space model that was identified by means of the SSI-data method was initially proposed in [107], [106] and completely formulated in [31]. The algorithm is based on a transformation of the state vector similar to the modal transformation (2.7):

$$\{x_k\} \; = \; [\Psi] \; \{x_{m,k}\} \tag{3.179}$$

in which $[\Psi]$ contains the eigenvectors obtained from the eigenvalue decomposition of the state matrix $[A]$:

$$[A]\,[\Psi] \; = \; [\Psi] \; [\Lambda] \; \Longrightarrow \; [\Lambda] \; = \; [\Psi]^{-1} \; [A] \; [\Psi] \tag{3.180}$$

and $\{x_{m,k}\}$ denotes the modal state vector corresponding to instant of time k. Accordingly, the stochastic state-space model can be written as

$$\begin{aligned} [\Psi]\,\{x_{m,k+1}\} \; &= \; [A]\,[\Psi]\,\{x_{m,k}\} \; + \; \{w_k\} \; \Longrightarrow \; \{x_{m,k+1}\} \; = \; [\Psi]^{-1}\,[A]\,[\Psi]\,\{x_{m,k}\} \; + \; [\Psi]^{-1}\,\{w_k\} \\ \{y_k\} \; &= \; [C]\,[\Psi]\,\{\xi_k\} \; + \; \{v_k\} \end{aligned} \tag{3.181}$$

or

$$\begin{aligned}\{x_{m,k+1}\} &= [\Lambda]\{x_{m,k}\} + [\Psi]^{-1}\{w_k\} \\ \{y_k\} &= \left[\tilde{C}\right]\{x_{m,k}\} + \{v_k\}\end{aligned} \tag{3.182}$$

with

$$\left[\tilde{C}\right] = [C][\Psi] \tag{3.183}$$

Transferring equation (3.182) into an innovation state-space model yields

$$\left\{\hat{x}_{m,k+1|k}\right\} = [\Lambda]\left\{\hat{x}_{m,k|k-1}\right\} + \left[\tilde{\mathcal{K}}\right]\{e_k\} \tag{3.184}$$

$$\{y_k\} = \left[\tilde{C}\right]\left\{\hat{x}_{m,k|k-1}\right\} + \{e_k\} \tag{3.185}$$

where

$$\left[\tilde{\mathcal{K}}\right] = [\Psi]^{-1}[\mathcal{K}] \tag{3.186}$$

and $[\mathcal{K}]$ denotes the steady-state Kalman gain. The expected modal state vectors $\left\{\hat{x}_{m,k|k-1}\right\}$ can be computed by means of the Kalman filter. Solving equation (3.185) for $\{e_k\}$ and substituting the resulting expression into equation (3.184) gives for the innovation state-space model

$$\left\{\hat{x}_{m,k+1|k}\right\} = \left([\Lambda] - \left[\tilde{\mathcal{K}}\right]\left[\tilde{C}\right]\right)\left\{\hat{x}_{m,k|k-1}\right\} + \left[\tilde{\mathcal{K}}\right]\{y_k\} \tag{3.187}$$

$$\{y_k\} = \left[\tilde{C}\right]\left\{\hat{x}_{m,k|k-1}\right\} + \{e_k\} \tag{3.188}$$

Since the term $\left[\tilde{C}\right]\left\{\hat{x}_{m,k|k-1}\right\}$ in equation (3.188) is the *one-step-ahead predicted output* $\left\{\hat{y}_{k|k-1}\right\}$, the innovations $\{e_k\}$ can be considered as the prediction errors. Recalling equation (3.183) one recognizes that $\left[\tilde{C}\right]$ contains estimates of the mode shapes. Accordingly, one can decompose $\left\{\hat{y}_{k|k-1}\right\} = \left[\tilde{C}\right]\left\{\hat{x}_{m,k|k-1}\right\}$ into n_m modal components such that equation (3.188) becomes

$$\{y_k\} = \left[\tilde{C}\right]\left\{\hat{x}_{m,k|k-1}\right\} + \{e_k\} = \sum_{r=1}^{n_m}\left[\tilde{C}\right][I_r]\left\{\hat{x}_{m,k|k-1,r}\right\} + \{e_k\} = \sum_{r=1}^{n_m}\left\{\hat{y}_{k|k-1,r}\right\} + \{e_k\} \tag{3.189}$$

with $[I_r]$ being a matrix that has on its diagonal entries of 1 in those rows or columns that correspond to the eigenvalues of mode r. Since the eigensolutions occur as complex conjugate pairs, in each matrix $[I_r]$ two diagonal elements are set to 1. Merely in the case that an eigensolution is real, only one entry in $[I_r]$ is set to 1.

In the next step the observed outputs, the sums of the estimated modal output components $\{y_{mk}\} = \sum_{r=1}^{n_m}\left\{\hat{y}_{k|k-1,r}\right\}$ and the prediction errors $\{e_k\}$ are for all time steps $k = 1\dots n$ collected as columns in respective matrices:

$$\begin{aligned}\left[\begin{array}{cccc}\{y_1\} & \{y_2\} & \dots & \{y_n\}\end{array}\right] &= \left[\begin{array}{cccc}\{y_{m1}\} & \{y_{m2}\} & \dots & \{y_{mn}\}\end{array}\right] + \left[\begin{array}{cccc}\{e_1\} & \{e_2\} & \dots & \{e_n\}\end{array}\right] \\ [Y] &= [Y_m] + [Y_e]\end{aligned} \tag{3.190}$$

Post-multiplication of equation (3.190) by $[Y]^T$ yields the correlations between the measured response, the estimated modal components, the prediction errors and the measured response for all sensors.

$$[Y][Y]^T = [Y_m][Y]^T + [Y_e][Y]^T \tag{3.191}$$

Omitting all off-diagonal elements gives diagonal matrices containing the respective correlations for each sensor.

$$\left[[Y]\,[Y]^T\right]_{diag} = \left[[Y_m]\,[Y]^T\right]_{diag} + \left[[Y_e]\,[Y]^T\right]_{diag} \tag{3.192}$$

Multiplying equation (3.192) by the inverse of the left handside produces a normalised relation that allows for the extraction of the contribution of each identified mode r to the response measured by each sensor separately.

$$\begin{aligned} \left[[Y]\,[Y]^T\right]^{-1}_{diag} \left[[Y]\,[Y]^T\right]_{diag} &= \left[[Y]\,[Y]^T\right]^{-1}_{diag} \left[[Y_m]\,[Y]^T\right]_{diag} + \left[[Y]\,[Y]^T\right]^{-1}_{diag} \left[[Y_e]\,[Y]^T\right]_{diag} \\ [I] &= [diag(\Delta_m)] + [diag(\Delta_e)] \end{aligned} \tag{3.193}$$

Accordingly, the *global contribution of the estimated modal components* δ_m and the *global contribution of the prediction errors* δ_e to the total response can be derived as the mean value of the traces of matrices $[diag(\Delta_m)]$ and $[diag(\Delta_e)]$

$$\delta_m = \frac{1}{n}\,\mathrm{tr}\,[diag(\Delta_m)], \qquad \delta_e = \frac{1}{n}\,\mathrm{tr}\,[diag(\Delta_e)], \qquad \Rightarrow \delta_m + \delta_e = 1 \tag{3.194}$$

Both values, δ_m and δ_e can be computed for all model orders n. In [31] has been observed that the global contribution of the estimated modal components δ_m increases with raising model order. From a certain point, or region, the value δ_m remains almost constant. The point where the curve merges into the range of constant level is supposed to indicate the model order of the system. This conclusion was drawn [31] based on the observation that the global contribution of the prediction errors did not change significantly for model orders above the one identified as the system's model order even though the number of spurious solutions grows with increasing model order.

Several other criteria for the assessment of identified modal parameters are discussed in chapter 4. Furthermore, approaches of their application to the selection of stable poles within automated modal analysis are described there.

3.5 Special topics related to OMA algorithms

3.5.1 Consideration of non-stochastic components in the excitation

Operational modal analysis is based on the fundamental assumption that the considered system is excited by unmeasured white noise excitation. However, this assumption is in practical applications not satisfied. Even though it may be sufficient for an operational modal analysis to assure that the structure is excited at all degrees-of-freedom by unmeasured dynamic forces with broad-band frequency characteristics in the frequency range of interest, situations can occur in which also these conditions are not true. These situations can either be wanted or unwanted.

In the *wanted* case one can think of forced vibration tests in which, for example, shakers, impulse hammers or a drop weight system are used to generate a measured excitation acting on the structure. At the same time, the structure is excited by traffic loads and ambient influences such as wind, micro-seismicity or wave forces. Consequently, it would be desireble to combine the concepts of experimental and operational modal analyses (EMA), (OMA). These algorithms are also called *operational modal analysis in presence of exogenous inputs* (OMAX) [60].

The second group of situations, the *unwanted* cases, occurs, for example, if the measurements have to be taken under service conditions which include the operation of devices such as rotating machinery. Typical examples of this situation are wind energy plants or industrial facilities with respective machinery. There it is important to distiguish between components in the signals that contain information due to the harmonic excitation and those parts related to the modal behaviour of the structure. This becomes especially crucial if the harmonic components have frequencies close to resonance.

3.5.1.1 Data-driven combined deterministic-stochastic subspace identification

The discrete-time state-space model of a system subjected to both deterministic, measured forces and stochastic loading is given by equations (2.124):

$$\begin{aligned} \{x_{k+1}\} &= [A]\{x_k\} + [B]\{u_k\} + \{w_k\} \\ \{y_k\} &= [C]\{x_k\} + [D]\{u_k\} + \{v_k\} \end{aligned} \tag{3.195}$$

In equations (3.195) the process noise $\{w_k\}$ incorporates the effects of the unmeasured excitation while measurement noise is described by $\{v_k\}$. Based on the assumption that both $\{w_k\}$ and $\{v_k\}$ are white noise random processes with zero mean, their covariance matrices related to two instants of time k_1 and k_2 are as also given in equation (2.125)

$$\left[\mathbf{E}\left[\left\{\begin{array}{c} \{w_{k_1}\} \\ \{v_p\} \end{array}\right\}\left[\begin{array}{cc} \{w_{k_2}\}^T & \{v_{k_2}\}^T \end{array}\right]\right]\right] = \left[\begin{array}{cc} [Q] & [S] \\ [S]^T & [R] \end{array}\right] \delta_{k_1 k_2} \tag{3.196}$$

A combined deterministic-stochastic subspace identification method has been presented in [138], [136] and [137]. The algorithm described in [138] has been extended for the reference-based case in [121]. The original version of the method that uses all channels of a measurement as reference signals can be considered as a special case of the reference-based method. Therefore, the algorithm proposed in [121] is illustrated in the following. It starts with the separation of both the state vector and the measured response into a deterministic and a stochastic part, referring to the respective excitation sources:

$$\{x_k\} = \{x_{k,d}\} + \{x_{k,s}\} \tag{3.197}$$

$$\{y_k\} = \{y_{k,d}\} + \{y_{k,s}\} \tag{3.198}$$

where the subscripts d and s refer to the deterministic and stochastic part, respectively. Accordingly, the state space model can also be divided into two parts:

$$\begin{aligned} \{x_{k+1,d}\} &= [A]\{x_{k,d}\} + [B]\{u_k\} \\ \{y_{k,d}\} &= [C]\{x_{k,d}\} + [D]\{u_k\} \end{aligned} \tag{3.199}$$

and

$$\begin{aligned} \{x_{k+1,s}\} &= [A]\{x_{k,s}\} + \{w_k\} \\ \{y_{k,s}\} &= [C]\{x_k k, s\} + \{v_k\} \end{aligned} \tag{3.200}$$

The derivation in [121] is related to those of the SSI-data method decribed in section 3.2.4.2. It includes as well respective projections of row spaces of block Hankel matrices constructed from measured data. However, it involves not only the block Hankel matrix of the measured output data $\left[Y_{0|2i-1}\right]$ but also the block Hankel matrix of the measured input data $\left[U_{0|2i-1}\right]$. If the first n_r rows of each block row of $\left[Y_{0|2i-1}\right]$ contain the respective sections of the reference channels while the remaining $n_o - n_r$ rows of a block row are filled with the signals not considered as references, the structure of this two block Hankel matrix is given by

$$\left[Y_{0|2i-1}\right] = \frac{1}{\sqrt{j}}\;
\begin{array}{r|cccc|l}
 & \longleftarrow & & j & \longrightarrow & \\
 & \{y_0^{ref}\} & \{y_1^{ref}\} & \dots & \{y_{j-1}^{ref}\} & \\
 & \{y_1^{ref}\} & \{y_2^{ref}\} & \dots & \{y_j^{ref}\} & \\
i & \vdots & \vdots & \dots & \vdots & \text{“past”} \\
 & \{y_{i-1}^{ref}\} & \{y_i^{ref}\} & \dots & \{y_{i+j-2}^{ref}\} & \\
\hline
n_r & \{y_i^{ref}\} & \{y_{i+1}^{ref}\} & \dots & \{y_{i+j-1}^{ref}\} & \\
\hline
n_o - n_r & \{y_i^{\sim ref}\} & \{y_{i+1}^{\sim ref}\} & \dots & \{y_{i+j-1}^{\sim ref}\} & \\
\hline
 & \{y_{i+1}\} & \{y_{i+2}\} & \dots & \{y_{i+j}\} & \text{“future”} \\
i-1 & \vdots & \vdots & \dots & \vdots & \\
 & \{y_{2i-1}\} & \{y_{2i}\} & \dots & \{y_{2i+j-2}\} &
\end{array}
= \left[\begin{array}{c} \left[Y_p^{ref}\right] \\ \hline \left[Y_{i|i}^{ref}\right] \\ \hline \left[Y_{i|i}^{\sim ref}\right] \\ \hline \left[Y_f^{-}\right] \end{array}\right] \tag{3.201}$$

The block Hankel matrix $\left[U_{0|2i-1}\right]$ is constructed similarly from the n_u measured input signals:

$$
\left[U_{0|2i-1}\right] = \frac{1}{\sqrt{j}}
\begin{array}{c|cccc|c}
 & \multicolumn{4}{c}{\longleftarrow \; j \; \longrightarrow} & \\
 & \{u_0\} & \{u_1\} & \ldots & \{u_{j-1}\} & \\
 & \{u_1\} & \{u_2\} & \ldots & \{u_j\} & \\
i & \vdots & \vdots & \ldots & \vdots & \text{“past”} \\
 & \{u_{i-1}\} & \{u_i\} & \ldots & \{u_{i+j-2}\} & \\
\hline
n_u & \{u_i\} & \{u_{i+1}\} & \ldots & \{u_{i+j-1}\} & = \\
\hline
i-1 & \{u_{i+1}\} & \{u_{i+2}\} & \ldots & \{u_{i+j}\} & \\
 & \vdots & \vdots & \ldots & \vdots & \text{“future”} \\
 & \{u_{2i-1}\} & \{u_{2i}\} & \ldots & \{u_{2i+j-2}\} &
\end{array}
\left[\begin{array}{c} [U_p] \\ \hline \left[U_{i|i}\right] \\ \hline \left[U_f^-\right] \end{array}\right]
\qquad (3.202)
$$

Similarly as for the SSI-data algorithm, an efficient implementation can be achieved by employing a respective QR decomposition of the block Hankel matrices:

$$
\left[\begin{array}{c} \left[U_{0|2i-1}\right] \\ \left[Y_{0|2i-1}\right] \end{array}\right]
=
\left[\begin{array}{c} [U_p] \\ \left[U_{i|i}\right] \\ \left[U_f^-\right] \\ \left[Y_p^{ref}\right] \\ \left[Y_{i|i}^{ref}\right] \\ \left[Y_{i|i}^{\sim ref}\right] \\ \left[Y_f^-\right] \end{array}\right]
= [R]^T \, [Q]^T
$$

$$
= \left[\begin{array}{ccccccc}
[R_{11}]^T & [0] & [0] & [0] & [0] & [0] & [0] \\
[R_{21}]^T & [R_{22}]^T & [0] & [0] & [0] & [0] & [0] \\
[R_{31}]^T & [R_{32}]^T & [R_{33}]^T & [0] & [0] & [0] & [0] \\
[R_{41}]^T & [R_{42}]^T & [R_{43}]^T & [R_{44}]^T & [0] & [0] & [0] \\
[R_{51}]^T & [R_{52}]^T & [R_{53}]^T & [R_{54}]^T & [R_{55}]^T & [0] & [0] \\
[R_{61}]^T & [R_{62}]^T & [R_{63}]^T & [R_{64}]^T & [R_{65}]^T & [R_{66}]^T & [0] \\
[R_{71}]^T & [R_{72}]^T & [R_{73}]^T & [R_{74}]^T & [R_{75}]^T & [R_{76}]^T & [R_{77}]^T \\
\end{array}\right]
\begin{array}{l} n_u i \\ n_u \\ n_u(i-1) \\ n_o i \\ n_r \\ n_o - n_r \\ n_o(i-1) \end{array}
\left[\begin{array}{c} [Q_1]^T \\ [Q_2]^T \\ [Q_3]^T \\ [Q_4]^T \\ [Q_5]^T \\ [Q_6]^T \\ [Q_7]^T \end{array}\right]
\qquad (3.203)
$$

$$
\begin{array}{ccccccc|c}
n_u i & n_u & n_u(i-1) & n_o i & n_r & n_o - n_r & n_o(i-1) & j
\end{array}
$$

While in the reference-based SSI-data algorithm the orthogonal projection $[\mathcal{P}_{i,ref}] = [Y_f] \,/\, [\mathbf{Y_{p,ref}}]$ was considered, in the reference-based combined deterministic-stochastic subspace method the obligue projection [138] of the row space of $[Y_f]$ onto the joint row space of $[U_p]$ and $\left[Y_p^{ref}\right]$ in the direction of the row space of $[U_f]$ is computed [121]:

$$
[\mathcal{O}_i] = [Y_f] \Big/_{[U_f]} \left[\begin{array}{c} [\mathbf{U_p}] \\ [\mathbf{Y_{p,ref}}] \end{array}\right] \qquad (3.204)
$$

Since an *oblique projection* is a numerically ill-conditioned problem, $[\mathcal{O}_i]$ is pre- und post-multiplied by appropriate weighting matrices $[W_1]$ and $[W_2]$, respectively, such that $[W_1]\,[\mathcal{O}_i]\,[W_2]$ describes an orthogonal projection, [121] with reference to [56]. If the weighting matrices $[W_1]$ and $[W_2]$ are chosen to be identity matrices, the weighted projection $[W_1]\,[\mathcal{O}_i]\,[W_2]$ can be obtained by means of the result of the QR decomposition (3.203) as

$$[W_1]\,[\mathcal{O}_i]\,[W_2] \;=\; \left[\;\left(\left[\left[R_{U_p}\right][R_\gamma] \;+\; \left[R_{Y_{p,ref}}\right][R_\delta]\right][\Pi]\right) \,\middle|\, \left(\left[R_{Y_{p,ref}}\right][R_{44}]^T\right)\;\right][Q_\alpha] \tag{3.205}$$

where $\left[R_{U_p}\right]$ and $\left[R_{Y_{p,ref}}\right]$ are obtained as respectively the first $n_f i$ and last $n_o i$ columns of

$$\left[\;\left[R_{U_p}\right] \,\middle|\, \left[R_{U_f}\right] \,\middle|\, \left[R_{Y_{p,ref}}\right]\;\right] \;=\; [R_\alpha]\;[R_\beta]^{-1} \tag{3.206}$$

and

$$[\Pi] \;=\; [I]_{2n_u i\times 2n_u i} \;-\; [R_\varepsilon]^T\;\left[[R_\varepsilon]\,[R_\varepsilon]^T\right]^{-1}\;[R_\varepsilon] \tag{3.207}$$

with

$$[R_\alpha] \;=\; \begin{bmatrix} [R_{51}]^T & [R_{52}]^T & [R_{53}]^T & [R_{54}]^T \\ [R_{61}]^T & [R_{62}]^T & [R_{63}]^T & [R_{64}]^T \\ [R_{71}]^T & [R_{72}]^T & [R_{73}]^T & [R_{74}]^T \end{bmatrix} \tag{3.208}$$

$$[R_\beta] \;=\; \begin{bmatrix} [R_{11}]^T & [0] & [0] & [0] \\ [R_{21}]^T & [R_{22}]^T & [0] & [0] \\ [R_{31}]^T & [R_{32}]^T & [R_{33}]^T & [0] \\ [R_{41}]^T & [R_{42}]^T & [R_{43}]^T & [R_{44}]^T \end{bmatrix} \tag{3.209}$$

$$[R_\gamma] \;=\; \begin{bmatrix} [R_{11}]^T & [0] & [0] \end{bmatrix} \tag{3.210}$$

$$[R_\delta] \;=\; \begin{bmatrix} [R_{41}]^T & [R_{42}]^T & [R_{43}]^T \end{bmatrix} \tag{3.211}$$

$$[R_\varepsilon] \;=\; \begin{bmatrix} [R_{21}]^T & [R_{22}]^T & [0] \\ [R_{31}]^T & [R_{32}]^T & [R_{33}]^T \end{bmatrix} \tag{3.212}$$

$$[Q_\alpha] \;=\; \begin{bmatrix} [Q_1] & [Q_2] & [Q_2] & [Q_4] \end{bmatrix} \tag{3.213}$$

The order n can be determined as the number of non-zero singular values of the singular value decomposition

$$[W_1]\;[\mathcal{O}_i]\;[W_2] \;=\; \begin{bmatrix} [U_1] & [U_2] \end{bmatrix} \begin{bmatrix} [S_1] & [0] \\ [0] & [0] \end{bmatrix} \begin{bmatrix} [V_1]^T \\ [V_2]^T \end{bmatrix} = [U_1]\,[S_1]\,[V_1]^T \tag{3.214}$$

The extended observability matrix is then

$$[O_i] \;=\; [U_1]\;[S_1]^{\frac{1}{2}} \tag{3.215}$$

With matrix $[O_{i-1}]$, which is obtained by omitting the last n rows of $[O_i]$, one can define

$$[\mathcal{T}_l] \;=\; \begin{bmatrix} [O_{i-1}]^\dagger\,[R_\zeta] \\ [R_\theta] \end{bmatrix} \tag{3.216}$$

and

$$[\mathcal{T}_r] \;=\; \begin{bmatrix} [O_i]^\dagger\,[R_\eta] \\ [R_\kappa] \end{bmatrix} \tag{3.217}$$

with

$$[R_\zeta] = \left[\begin{array}{cccccc} [R_{71}]^T & [R_{72}]^T & [R_{73}]^T & [R_{74}]^T & [R_{75}]^T & [R_{76}]^T \end{array} \right] \tag{3.218}$$

$$[R_\eta] = \left[\begin{array}{cccccc} [R_{51}]^T & [R_{52}]^T & [R_{53}]^T & [R_{54}]^T & [R_{55}]^T & [0] \\ [R_{61}]^T & [R_{62}]^T & [R_{63}]^T & [R_{64}]^T & [R_{65}]^T & [R_{66}]^T \\ [R_{71}]^T & [R_{72}]^T & [R_{73}]^T & [R_{74}]^T & [R_{75}]^T & [R_{76}]^T \end{array} \right] \tag{3.219}$$

$$[R_\theta] = \left[\begin{array}{cccccc} [R_{51}]^T & [R_{52}]^T & [R_{53}]^T & [R_{54}]^T & [R_{55}]^T & [0] \\ [R_{61}]^T & [R_{62}]^T & [R_{63}]^T & [R_{64}]^T & [R_{65}]^T & [R_{66}]^T \end{array} \right] \tag{3.220}$$

$$[R_\kappa] = \left[\begin{array}{cccccc} [R_{21}]^T & [R_{22}]^T & [0] & [0] & [0] & [0] \\ [R_{31}]^T & [R_{32}]^T & [R_{33}]^T & [0] & [0] & [0] \end{array} \right] \tag{3.221}$$

Matrices $[A]$ and $[C]$ can be extracted as the first n columns of the product $[\mathcal{S}] = [\mathcal{T}_l]\,[\mathcal{T}_r]^\dagger$:

$$[\mathcal{S}] = \left[\left[\begin{array}{c} [A] \\ [C] \end{array} \right] \middle| \left[K_{[U_f]} \right] \right] = [\mathcal{T}_l]\;[\mathcal{T}_r]^\dagger \tag{3.222}$$

Estimates of the noise covariance matrices can be calculated as

$$\left[\begin{array}{cc} [Q] & [S] \\ [S]^T & [R] \end{array} \right] = [[\mathcal{T}_l] - [\mathcal{S}]\,[\mathcal{T}_r]]\;[[\mathcal{T}_l] - [\mathcal{S}]\,[\mathcal{T}_r]]^T = \left[[\mathcal{T}_l] - [\mathcal{T}_l]\,[\mathcal{T}_r]^\dagger\,[\mathcal{T}_r]\right]\;\left[[\mathcal{T}_l] - [\mathcal{T}_l]\,[\mathcal{T}_r]^\dagger\,[\mathcal{T}_r]\right]^T \tag{3.223}$$

The natural frequencies, modal damping ratios and mode shapes are retrieved by applying the same relations that are also used in the output-only SSI algorithms which are repeated here for the sake of completeness.

$$[A] = [\Psi]\,[\Lambda_d]\,[\Psi]^{-1} = [\Psi]\,[diag(\mu_r)]\,[\Psi]^{-1} \tag{3.224}$$

$$\lambda_r = \frac{\ln(\mu_r)}{\Delta t} \tag{3.225}$$

$$\omega_r = |\lambda_r| \tag{3.226}$$

$$\zeta_r = -\frac{\mathrm{Re}\,[\lambda_r]}{|\lambda_r|} \tag{3.227}$$

$$[V] = [C]\;[\Psi] \tag{3.228}$$

3.5.1.2 Stochastic combined deterministic-stochastic frequency-domain subspace identification

Similarly as described in the previous section for the SSI-data algorithm, the stochastic frequency-domain subspace identification method presented in section 3.3.4 can also be extended to a combined deterministic-stochastic algorithm. In the following the analysis is explained based on the descriptions in [33]. The model to be identified is the *combined deterministic-stochastic frequency-domain state-space model*

$$z_k\,\{X_k\} = [A]\,\{X_k\} + [B]\,\{U_k\} + \{W_k\} \tag{3.229}$$

$$\{Y_k\} = [C]\,\{X_k\} + [D]\,\{U_k\} + \{V_k\} \tag{3.230}$$

$$\tag{3.231}$$

If measured input data is available one can, similarly to the definition in equation (3.169) for the measured output, organize the discrete input Fourier spectra in a Vandermonde matrix:

$$[\mathcal{U}]_{2n_u i \times n_f} = \left[\begin{array}{cccc} z_1^{-i}\{U_1\} & z_2^{-i}\{U_2\} & \dots & z_{n_f}^{-i}\left\{U_{n_f}\right\} \\ z_1^{-i+1}\{U_1\} & z_2^{-i+1}\{U_2\} & \dots & z_{n_f}^{-i+1}\left\{U_{n_f}\right\} \\ \vdots & \vdots & \dots & \vdots \\ z_1^{-1}\{U_1\} & z_2^{-1}\{U_2\} & \dots & z_{n_f^{-1}}\left\{U_{n_f}\right\} \\ \hline \{U_1\} & \{U_2\} & \dots & \left\{U_{n_f}\right\} \\ z_1\{U_1\} & z_2\{U_2\} & \dots & z_{n_f}\left\{U_{n_f}\right\} \\ \vdots & \vdots & \dots & \vdots \\ z_1^{i-1}\{U_1\} & z_2^{i-1}\{U_2\} & \dots & z_{n_f^{i-1}}\left\{U_{n_f}\right\} \end{array}\right] = \left[\begin{array}{c} [\mathcal{U}_-] \\ \hline [\mathcal{U}_+] \end{array}\right] \tag{3.232}$$

The main theorem of the combined deterministic-stochastic frequency-domain subspace identification [33] states that the obligue projection [138] of the row space of $[Y_+]$ onto the joint row space of $[U_-]$ and $[Y_-]$ in the direction of the row space of $[U_+]$ can be considered as the product of the extended observability matrix

$$[O_i] = \begin{bmatrix} [C] \\ [C]\,[A] \\ \vdots \\ [C]\,[A]^{i-1} \end{bmatrix} \tag{3.233}$$

and the spectra of the forward Kalman filter state estimates

$$\left[\hat{X}\right] = \left[\ \left[\hat{X}_1\right]\ \left[\hat{X}_2\right]\ \dots\ \left[\hat{X}_{n_f}\right]\ \right] \tag{3.234}$$

if the number of considered frequency lines n_f tends to infinity:

$$[Y_+] \big/_{[U_+]} \begin{bmatrix} [\mathbf{U}_-] \\ [\mathbf{Y}_-] \end{bmatrix} \longrightarrow [O_i]\left[\hat{X}\right] \text{ for } n_f \to \infty \tag{3.235}$$

This projection can be calculated efficiently by means of a respective QR decomposition

$$\begin{bmatrix} [Y_+] \\ [U_+] \\ [U_-] \\ [Y_-] \end{bmatrix} = \begin{bmatrix} [R_{11}]^T & [0] & [0] & [0] \\ [R_{21}]^T & [R_{22}]^T & [0] & [0] \\ [R_{31}]^T & [R_{32}]^T & [R_{33}]^T & [0] \\ [R_{41}]^T & [R_{42}]^T & [R_{43}]^T & [R_{44}]^T \end{bmatrix} \begin{bmatrix} [Q_1]^T \\ [Q_2]^T \\ [Q_3]^T \\ [Q_4]^T \end{bmatrix} = [R]^T\,[Q]^T \tag{3.236}$$

as

$$[\mathcal{O}_i] = [Y_+] \big/_{[U_+]} \begin{bmatrix} [\mathbf{U}_-] \\ [\mathbf{Y}_-] \end{bmatrix} = [R_c]\,[\mathcal{R}]\,[[R_a]\,[\mathcal{R}]]^{\dagger}\,[R_a]\,[Q] \tag{3.237}$$

with

$$[\mathcal{R}] = \left[[I] - [R_b]^H \left[[R_b]\,[R_b]^H\right]^{\dagger}[R_b]\right] \tag{3.238}$$

and

$$
\begin{aligned}
[R_a] &= \begin{bmatrix} [R_{31}]^T & [R_{32}]^T & [R_{33}]^T & [0] \\ [R_{41}]^T & [R_{42}]^T & [R_{43}]^T & [R_{44}]^T \end{bmatrix} && (3.239) \\
[R_b] &= \begin{bmatrix} [R_{21}]^T & [R_{22}]^T & [0] & [0] \end{bmatrix} && (3.240) \\
[R_c] &= \begin{bmatrix} [R_{11}]^T & [0] & [0] & [0] \end{bmatrix} && (3.241) \\
& && (3.242)
\end{aligned}
$$

The extended observability matrix and the state estimates are obtained based on the sigular value decomposition of the computed projection

$$[\mathcal{O}_i] = \begin{bmatrix} [U_1] & [U_2] \end{bmatrix} \begin{bmatrix} [S_1] & [0] \\ [0] & [0] \end{bmatrix} \begin{bmatrix} [V_1]^T \\ [V_2]^T \end{bmatrix} = [U_1]\,[S_1]\,[V_1]^T \tag{3.243}$$

from the non-zero singular values and the respective singular vectors

$$
\begin{aligned}
[O_i] &= [U_1]\,[S_1]^{\frac{1}{2}} && (3.244) \\
\left[\hat{X}\right] &= [S_1]^{\frac{1}{2}}\,[V_1]^H && (3.245)
\end{aligned}
$$

With $[Y]$, $[Y]$ and $\left[\hat{X}\right]$ the system matrices $[A]$, $[B]$, $[C]$ and $[D]$ may then be extracted from the least squares solution of the state space model

$$\begin{bmatrix} \left[z_k \hat{X}\right] \\ [Y] \end{bmatrix} = \begin{bmatrix} [A] & [B] \\ [C] & [D] \end{bmatrix} \left[\hat{X}\right] + \begin{bmatrix} [\rho_{W_k}] \\ [\rho_{V_k}] \end{bmatrix} \tag{3.246}$$

The noise covariance matrices can then be calculated from the residuals of the least squares solution:

$$\begin{bmatrix} [Q] & [S] \\ [S]^H & [R] \end{bmatrix} = \frac{1}{n_f} \begin{bmatrix} [\rho_{W_k}] \\ [\rho_{V_k}] \end{bmatrix} \begin{bmatrix} [\rho_{W_k}]^H & [\rho_{V_k}]^H \end{bmatrix} \tag{3.247}$$

From the system matrices the modal parameters are derived by means of equations (3.224) to (3.228).

It is noted that the computation of the spectral estimates involves either bias if weighting by applying a window function such as a Hanning window is used or errors due to transient influences of initial and final values of a block if these are not equal. The latter influences can be taken into account by extending the inputs by z_k [33].

3.5.1.3 Presence of harmonic components in the response signals

As the name *operational* modal analysis already indicates, the structures under consideration are tested under operational conditions. Especially if machinery with rotating or reciprocating components is contributing to the unmeasured excitation of the structure, the fundamental assumption of all operational modal analysis methods – white noise, or at least broad band excitation – is violated. As a result, the measured signals contain harmonic components that have a negative influence on the quality of the results obtained by several identification methods. While, for example, stochastic subspace identification still delivers correct estimates of the modal parameters [76], [77], the results obtained from methods such as the EFDD or LSCE can be biased, especially if harmonic components are close to resonance [77], [99].

Several techniques to identify the presence and frequency of harmonic components in the measured response signals were investigated in [75]. Within the study was observed that the probability density function of a band-pass filtered response signal close to a resonance is normally distributed while the one of a harmonic component shows two distinct peaks tending to infinity at the positive and negative amplitude values of the harmonic function. To quantify the comparison the shape of the distribution of a considerd probability density function to that of a normal distribution, the *kurtosis* γ_2 which is defined as the fourth central moment of a statistical variable y

$$\gamma_2 = \mathbf{E}\left[\left(\frac{y-\mu_y}{\sigma_y}\right)^4\right] = \frac{\mathbf{E}\left[(y-\mu_y)^4\right]}{\sigma_y^4} \tag{3.248}$$

is employed. Since the kurtosis of an arbitrary normal distribution is always $\gamma_2 = 3$ [97], the deviation ε of the kurtosis of a considered probability density function from 3, which is also called *excess* [97] is used as an indicator to identify harmonic components in a signal.

The following algorithm for the identification of harmonic components in a series of measured output signals has been proposed in [76], [77].

1. Scaling of all signals $\{y_i\}$ to unit variance and shift to zero mean
2. Narrow bandpass filtering of every signal for all frequencies f_k
3. Computation of the (kurtosis) excess $\varepsilon(\gamma_{i,k}) = \frac{\mathbf{E}\left[\left(\{y_i\}-\mu_{y_i}\right)^4\right]}{\sigma_{y_i}^4} - 3$ of all signals filtered around frequency f_k
4. Calculation of the mean of the excess ε_k for each frequency f_k
5. Determination of the median m_ε of the excess of all frequencies which should theoretically be 0
6. Computation of the deviation of the excess ε_k for each frequency from the median m_ε: if the deviation exceeds a certain threshold, the distribution of the probability density function around f_k is different from the majoraty of all frequencies, the respective spectral component can be considered as outlier.

In case of a modal identification by means of the frequency-domain decomposition method, it is suggested to exclude the outliers from further analyses. The power spectral densities at the respective frequencies are estimated by linear interpolation between adjacent values [76], [77]. A procedure which reduces the computational effort by a statistical analysis of the singular values computed within the FDD algorithm in order to identify potential frequency lines on which the kurtosis-based analysis is applied has been suggested in [7]. This pre-selection limits the runs of the algorithm described above to only very few frequency lines rather than the whole frequency range.

Based on the assumption that the presence of harmonic components in a measured signal and their frequencies have already been identified, an extension of the least-square complex exponential method (LSCE) was proposed in [99]. This extension consists of the description of the known harmonic components of frequency ω_h by two additional lines in Prony's equations

$$\begin{bmatrix} 0 & \sin(\omega_h\Delta t) & \dots & \sin(\omega_h(2n_m-1)\Delta t) \\ 1 & \cos(\omega_h\Delta t) & \dots & \cos(\omega_h(2n_m-1)\Delta t) \end{bmatrix} \begin{Bmatrix} \beta_0 \\ \beta_1 \\ \vdots \\ \beta_{(2n_m-1)} \end{Bmatrix} = -\begin{Bmatrix} \sin(2n_m\omega_h\,\Delta t) \\ \cos(2n_m\omega_h\,\Delta t) \end{Bmatrix} \tag{3.249}$$

taking into consideration that each harmonic component leads to two addinional roots $\mu_h = e^{\pm i\omega_h\Delta t}$. Accordingly, if there are n_h known harmonic components in the signals, the system of equations (3.23) formed by a Hankel matrix with n_R block rows of which each has L rows, is extended by $2n_h$ lines of the type (3.249) such that the following system of equation emerges

$$\left[\begin{array}{ccc|ccc} R_0 & \dots & R_{2n_h-1} & R_{2n_h} & \dots & R_{2n_m-1} \\ \vdots & \dots & \vdots & \vdots & \dots & \vdots \\ R_{Ln_R-1} & \dots & R_{Ln_R+2n_h-2} & R_{Ln_R+2n_h-2} & \dots & R_{Ln_R+2n_m-2} \\ \hline 0 & \dots & \sin(\omega_1(2n_h-1)\Delta t) & \sin(\omega_1 2n_h\Delta t) & \dots & \sin(\omega_1(2n_m-1)\Delta t) \\ 1 & \dots & \cos(\omega_1(2n_h-1)\Delta t) & \cos(\omega_1 2n_h\Delta t) & \dots & \cos(\omega_1(2n_m-1)\Delta t) \\ \vdots & \dots & \vdots & \vdots & \dots & \vdots \\ 0 & \dots & \sin(\omega_{n_h}(2n_h-1)\Delta t) & \sin(\omega_{n_h} 2n_h\Delta t) & \dots & \sin(\omega_{n_h}(2n_m-1)\Delta t) \\ 1 & \dots & \cos(\omega_{n_h}(2n_h-1)\Delta t) & \cos(\omega_{n_h} 2n_h\Delta t) & \dots & \cos(\omega_{n_h}(2n_m-1)\Delta t) \end{array}\right] \left\{\begin{array}{c} \beta_0 \\ \beta_1 \\ \vdots \\ \beta_{2n_h-1} \\ \beta_{2n_h-1} \\ \hline \beta_{2n_h} \\ \vdots \\ \beta_{2n_m-1} \end{array}\right\}$$

$$= \left\{\begin{array}{c} R_{2n_m} \\ \vdots \\ R_{Ln_R+2n_m-1} \\ \hline \sin(\omega_1 2n_m\Delta t) \\ \cos(\omega_1 2n_m\Delta t) \\ \vdots \\ \sin(\omega_{n_h} 2n_m\Delta t) \\ \cos(\omega_{n_h} 2n_m\Delta t) \end{array}\right\} \tag{3.250}$$

or

$$\begin{bmatrix} [R_A]_{Ln_R\times 2n_h} & [R_B]_{Ln_R\times(2n_m-2n_h)} \\ [H_A]_{2n_h\times 2n_h} & [H_B]_{2n_h\times(2n_m-2n_h)} \end{bmatrix} \begin{Bmatrix} \{b_A\}_{2n_h} \\ \{b_B\}_{2n_m-2n_h} \end{Bmatrix} = \begin{Bmatrix} \{R_C\}_{Ln_R} \\ \{H_C\}_{2n_h} \end{Bmatrix} \tag{3.251}$$

Equation (3.251) can be split into two systems of equations:

$$[R_A]\,\{b_A\} + [R_B]\,\{b_B\} = \{R_C\} \tag{3.252}$$

$$[H_A]\,\{b_A\} + [H_B]\,\{b_B\} = \{H_C\} \tag{3.253}$$

It is proposed in [99] first to solve equation (3.253) for $\{b_A\}$

$$\{b_A\} = [H_A]^{-1}\,\{\{H_C\} - [H_B]\,\{b_B\}\} \tag{3.254}$$

and to substitute the right handside into equation (3.252).

$$\Big[[R_B] - [R_A]\,[H_A]^{-1}\,[H_B]\Big]\,\{b_B\} = \{R_C\} - [R_A]\,[H_A]^{-1}\,\{H_C\} \tag{3.255}$$

The least-squares solution $\{b_B\}$ of equation (3.255) is then used to compute $\{b_A\}$ with equation (3.254). The vectors $\{b_A\}$ and $\{b_B\}$ contain together the complete set of coefficients $\beta_0 \ldots \beta_{2n_m-1}$ which are used to retrieve the modal parameters as described in section 3.2.1.1. The solutions of the harmonics will appear in the stabilisation diagram as modes with zero damping.

3.6 Examples for the performance of operational modal analysis

3.6.1 Two degree-of-freedom system

The two degree-of-freedom system that has been introduced in chapter 2 is recalled here. Figure 3.4 shows the considered two-storey frame with its two degrees-of freedom as well as the two calculated mode shapes of the undamped system. The respective modal parameters of the system are given as follows:

$$\begin{aligned} f_1 &= 1.706\,Hz \qquad & \zeta_1 &= 0.02 = 2.00\% \qquad & [\Phi] = \begin{bmatrix} 1 & -0.851 \\ 0.425 & 1 \end{bmatrix} \\ f_2 &= 3.320\,Hz & \zeta_2 &= 0.01 = 1.00\% & \end{aligned}$$

The eigenvectors were scaled such that the maximal amplitude of each mode shape equals one.

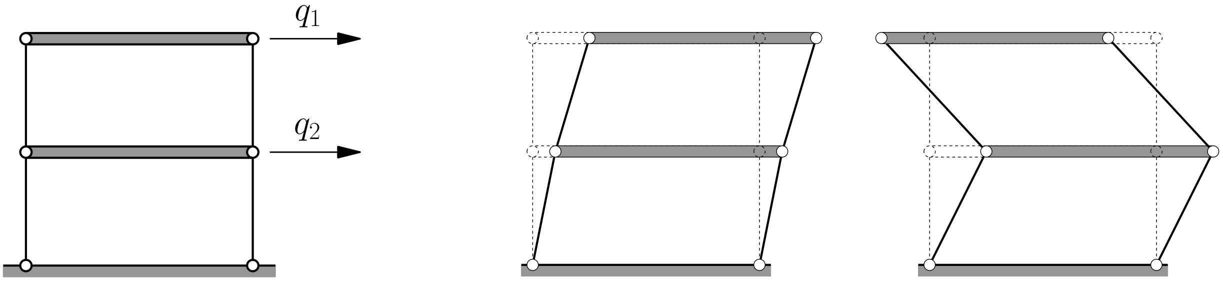

system geometry mode 1 mode 2

Figure 3.4: Two storey frame system: definition of degrees-of-freedom and the two mode shapes

To illustrate the performance of several OMA methods, the simulated response to the noise excitation in example 2.10 has been used. The time series have a length of

$$204800\,\text{samples} \times \frac{1}{128}s = 1600\,s = 26\,min\,40\,s.$$

In the following, the analysis of this data by means of four methods is described. For all parametric methods the following stabilisation criteria were used:

- deviation in frequency = 1%
- deviation in damping = 5 %
- minimal $MAC = 0.98$

For all analyses related to the 2 degree-of-freedom system in this section, both channels are regarded as reference channels.

3.6.1.1 Poly-reference least square complex exponential (p-LSCE) method

For the analysis of the response data by means of the poly-reference least square complex exponential (p-LSCE) method, the following algorithmic parameters were chosen:

$$\begin{array}{lcl} \text{decimation of the time series by factor 4} \longrightarrow \Delta t & = & \frac{1}{32}\,s \\ \text{length of correlation series} & = & 2 \times 60 \;=\; 120 \text{ samples} \\ \text{maximal model order} & = & 60 \end{array}$$

In figure 3.5 the stabilisation diagram obtained with these parameters are shown. If all poles are plotted, one recognises numerous solutions. However, if only the stable poles are visualised, the diagram becomes much clearer.

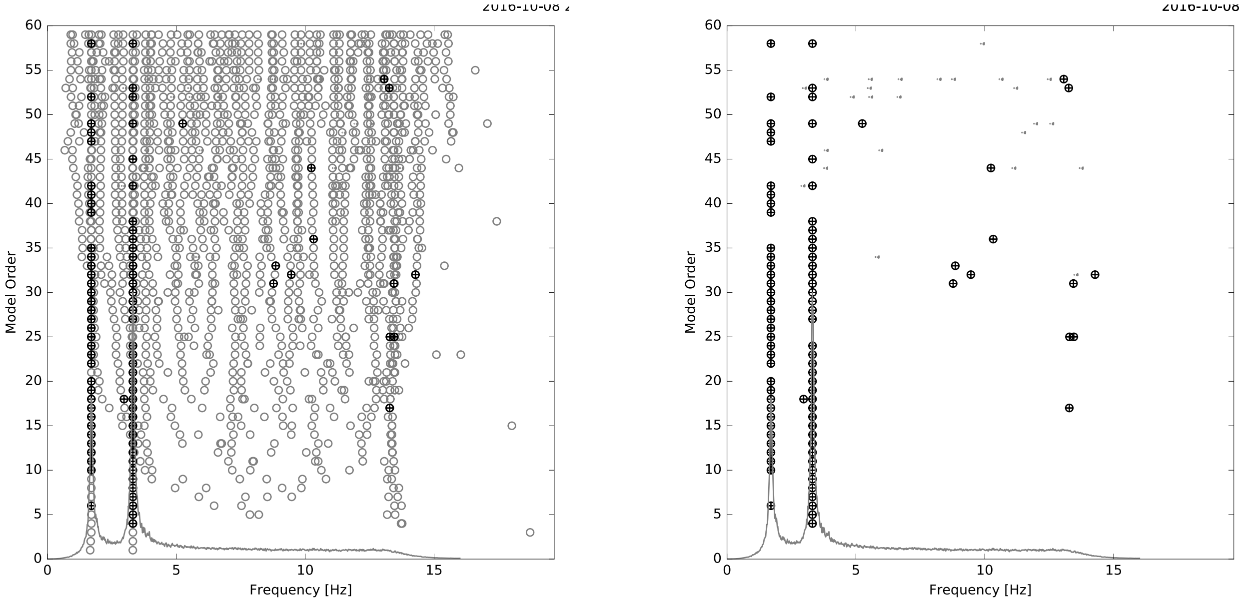

(a) all poles (b) stable poles only

Figure 3.5: Two storey frame system: stabilisation diagram obtained by means of the p-LSCE method

If all natural frequencies and modal damping ratios related to the two obvious modes are collected and plotted in the frequency-damping plane, the diagram in figure 3.6 is obtained. There two very clear clusters with hardly varying frequencies and relatively small deviations in damping can be identified. Respective statistical data for the two modes is listed in table 3.1.

The two mode shapes are visualised in figure 3.7. In the following subsections describing the results identified by other OMA methods, the plot of mode shapes would be absolutely repetitive and is therefore renounced there.

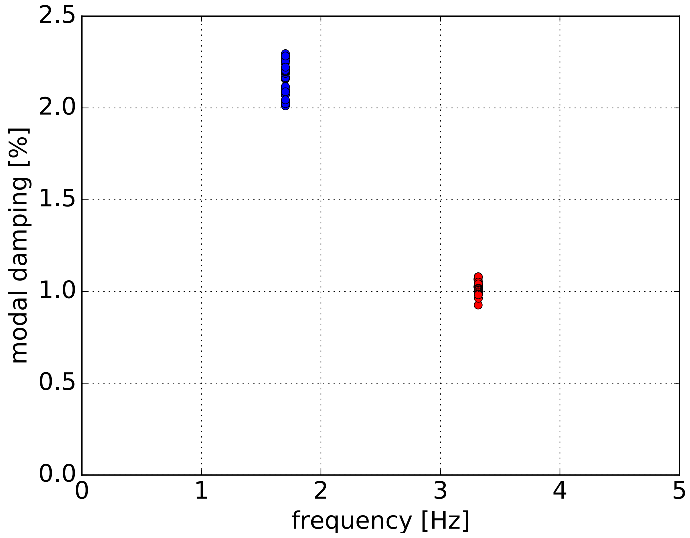

Figure 3.6: Two storey frame system: stable solutions related to the two modes obtained by means of the p-LSCE method in the frequency-damping plane

parameter	minimum	maximum	median	mean	standard deviation	COV
f_1	1.701 Hz	1.704 Hz	1.703 Hz	1.703 Hz	0.0006 Hz	0.0331 %
f_2	3.313 Hz	3.318 Hz	3.316 Hz	3.316 Hz	0.0011 Hz	0.0346 %
ζ_1	2.011 %	2.296 %	2.165 %	2.151 %	0.0795 %	3.6975 %
ζ_2	0.926 %	1.080 %	1.014 %	1.016 %	0.0321 %	3.159 %

Table 3.1: Two storey frame system: statistical parameters of the natural frequencies and modal damping ratios identified by means of the p-LSCE method (COV = coefficient of variation)

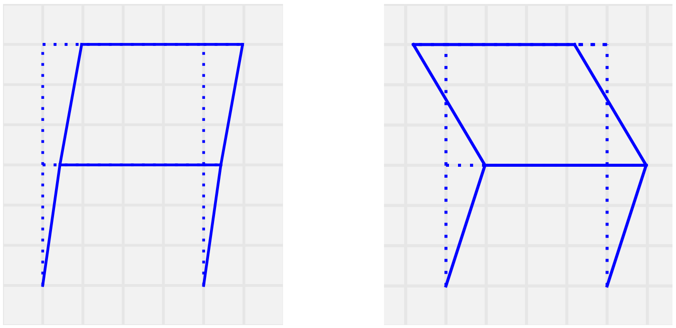

mode 1 mode 2

Figure 3.7: Two storey frame system: mode shapes identified by means of the p-LSCE method

3.6.1.2 Covariance-driven stochastic subspace identification (SSI-cov) method

The parameters used in the analysis of the simulated response data of the 2-DOF system were

decimation of the time series by factor 4 $\longrightarrow \Delta t = \frac{1}{32}\,s$

bumber of block rows = number of block columns of the block Toeplitz matrix $= 60$

maximal model order $= 60$

With these parameters, the stabilisation diagrams shown in figure 3.8 were obtained. One can observe that the number of stable solutions for the two modes of the system were identified for almost all model orders starting at the 4th model order.Even though there are also some spurious solutions that are indicated as stable poles, they can be very well distinguished from the solutions related to the physical modes of the considered system.

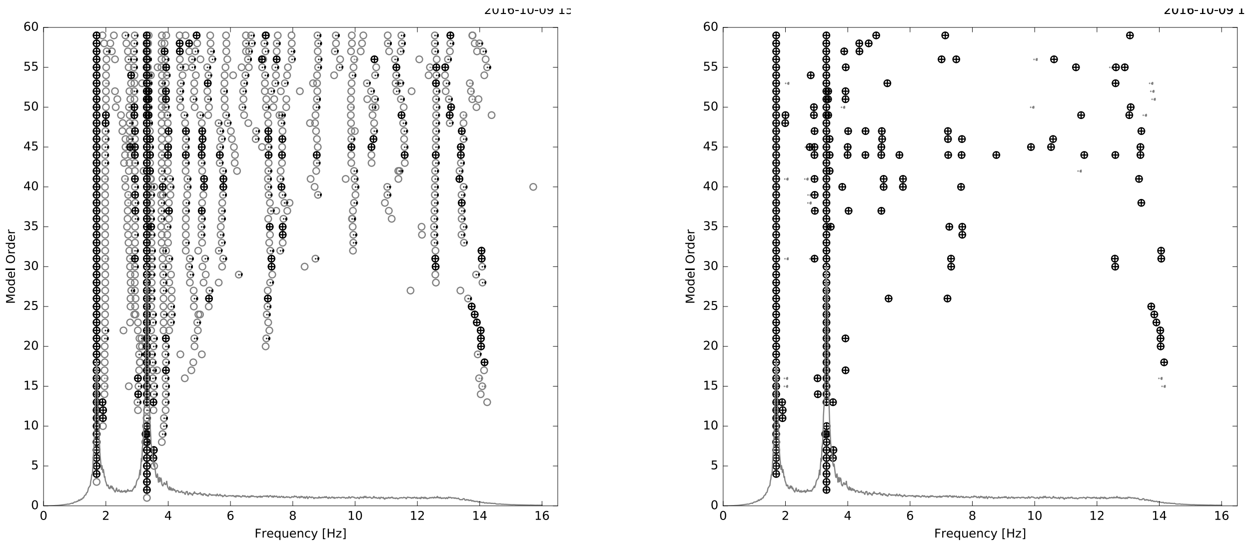

(a) all poles (b) stable poles only

Figure 3.8: Two storey frame system: stabilisation diagram obtained by means of the SSI-cov method

parameter	minimum	maximum	median	mean	standard deviation	COV
f_1	1.702 Hz	1.703 Hz	1.703 Hz	1.703 Hz	0.0005 Hz	0.0265 %
f_2	3.310 Hz	3.322 Hz	3.316 Hz	3.316 Hz	0.0022 Hz	0.0668 %
ζ_1	2.106 %	2.204 %	2.148 %	2.151 %	0.018 %	0.841 %
ζ_2	1.013 %	1.092 %	1.038 %	1.038 %	0.0153 %	1.473 %

Table 3.2: Two storey frame system: statistical parameters of the natural frequencies and modal damping ratios identified by means of the SSI-cov method (COV = coefficient of variation)

Figure 3.9 suggests that the deviations both in frequency and damping are very small for all solutions referring to the two physical modes. It can also be observed that the damping values assumed for the simulation are slightly overestimated in the identification. These two observations are quantified by the information given in table 3.2.

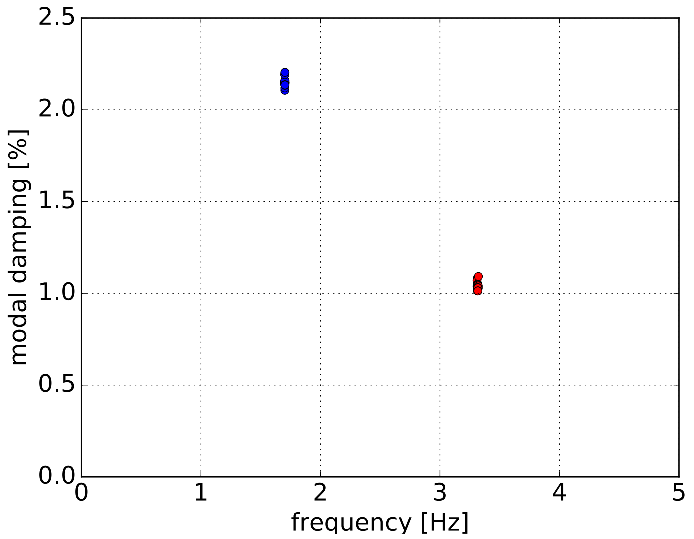

Figure 3.9: Two storey frame system: stable solutions related to the two modes obtained by means of the SSI-cov method in the frequency-damping plane

3.6.1.3 Data-driven stochastic subspace identification (SSI-data) method

To reduce the size of the block Hankel matrix to be decomposed within the analysis by the SSI-data algorithm, the time series were in this case decimated by a factor of 8, which resulted in a sampling rate of $\frac{128}{8} = 16\,Hz$. Further, the length of the time windows collected in the Hankel matrix was set to 13880 samples which corresponds to a time interval of 867.5 s or 14 min and 27.5 s. Accordingly, the truncated data taken into account covered a shorter time than the signals processed in the previous analyses. In detail, the parameters used in this study were:

$$\begin{array}{lcl} \text{decimation of the time series by factor 8} \longrightarrow \Delta t & = & \frac{1}{16}\,s \\ \text{number of block rows of the block Hankel matrix} & = & 2 \times 60 = 120 \\ \text{maximal model order} & = & 60 \end{array}$$

With these settings, the stabilisation diagrams presented in figure 3.10 were obtained. It can be noticed that the number of columns marking stable solutions is by far larger than the number of actual physical modes which indicates an overfit of the process model. In such a case mode selection can become difficult, especially if multiple stable poles that suggest identical mode shapes are grouped close to a physical mode. This situation also occurs for the 2-DOF system considered here if the number of block rows is increased as illustrated in figure 3.11 (b). At several model orders the stabilisation diagram looks similar to one of a system with closely spaced modes. However, here the respective mode shapes are almost identical, the major difference can only be seen in the identified damping ratios. For simulated data one can relatively easily distinguish solutions related to a physical mode from a spurious solution. For a purely experimental study the preliminary knowledge about the system is, naturally, not available which complicates the correct identification significantly.

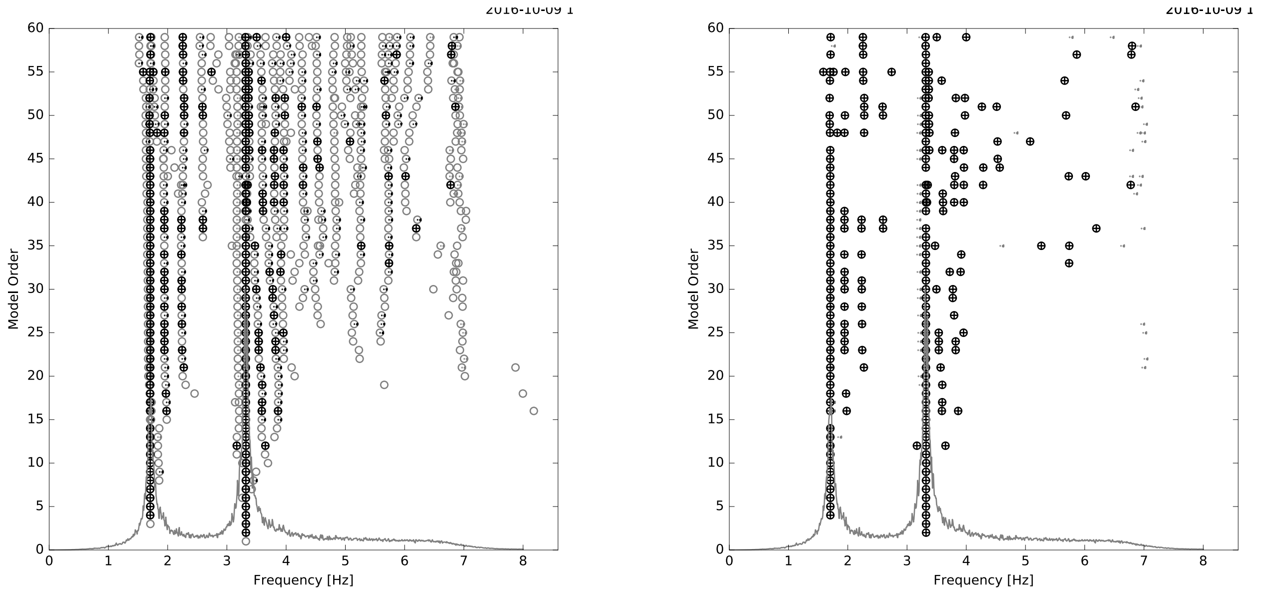

(a) all poles

(b) stable poles only

Figure 3.10: Two storey frame system: stabilisation diagram obtained by means of the SSI-data method

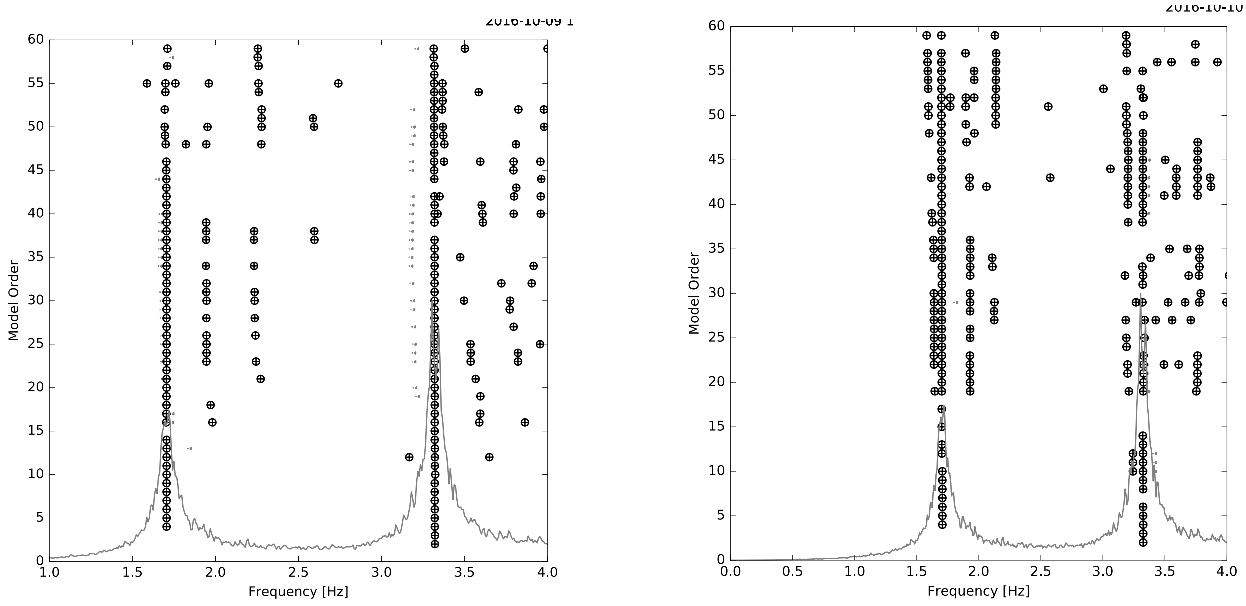

(a) (b)

Figure 3.11: Two storey frame system: stabilisation diagram obtained by means of the SSI-data method, (a) detail of figure 3.10 (b), (b) based on an analysis of a block Hankel matrix with 240 block rows

From the visualisation of the solutions related to the two physical modes in the frequency-damping plane, figure 3.12, it becomes obvious that the scatter of the damping ratios is larger than in the results obtained for this case study by means of the SSI-cov method. The statistical data in table 3.3 quantify this observation.

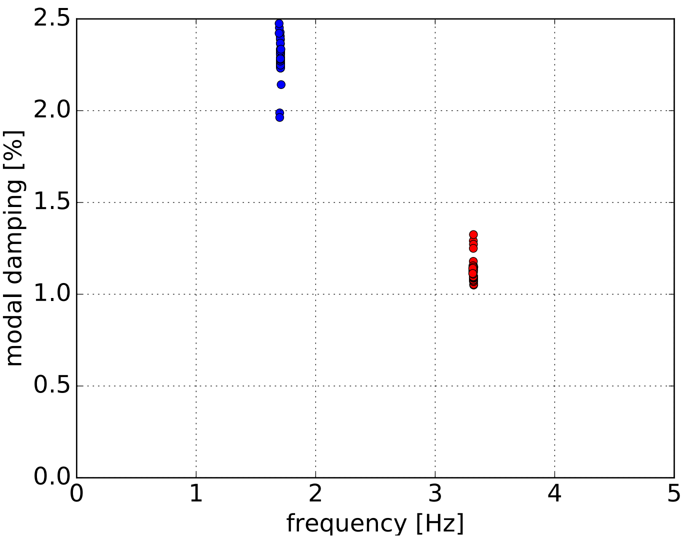

Figure 3.12: Two storey frame system: stable solutions related to the two modes obtained by means of the SSI-data method in the frequency-damping plane

parameter	minimum	maximum	median	mean	standard deviation	COV
f_1	1.694 Hz	1.711 Hz	1.706 Hz	1.705 Hz	0.0032 Hz	0.1848 %
f_2	3.314 Hz	3.323 Hz	3.319 Hz	3.319 Hz	0.0019 Hz	0.0574 %
ζ_1	1.963 %	2.535 %	2.283 %	2.293 %	0.096 %	4.193 %
ζ_2	1.050 %	1.325 %	1.118 %	1.122 %	0.0532 %	4.7432 %

Table 3.3: Two storey frame system: statistical parameters of the natural frequencies and modal damping ratios identified by means of the SSI-data method (COV = coefficient of variation)

3.6.1.4 Frequency domain decomposition (FDD) method

The results of a modal identification by means of the FDD method are influenced by the properties of the spectral density functions, especially their frequency resolution which is determined by the length of the sections of the time series sections, and by the estimate of the correlation functions from which the natural frequencies and modal damping ratios are derived.

In this example, the spectral desities were computed according to Welch's method extracting sections of 10240 samples from the simulated response series and an overlap of 25 %. The peaks in the curve of the first singular values were selected manually. In the search of the frequency range that is related to the same mode as the peak value, data points which had a $MAC \geq 0.99$ with the mode shape of the peak value were excepted. Figure 3.13 shows the diagram with the singular values, the detected peaks and the associated frequency ranges.

The identified natural frequencies and modal damping ratios with their statistical parameters are summarized in table 3.4 whereas it needs to be mentioned that the number of samples here consists always of two samples as eauch value has been determined for one channel (or degree-of-freedom). Each value of the natural frequencies related to one channel was computed as the mean value of the inverse of the periods estimated as the time between the two closest zero crossings with positive slope of the respective autocorrelation function. The four autocorrelation functions are plotted in figure 3.14.

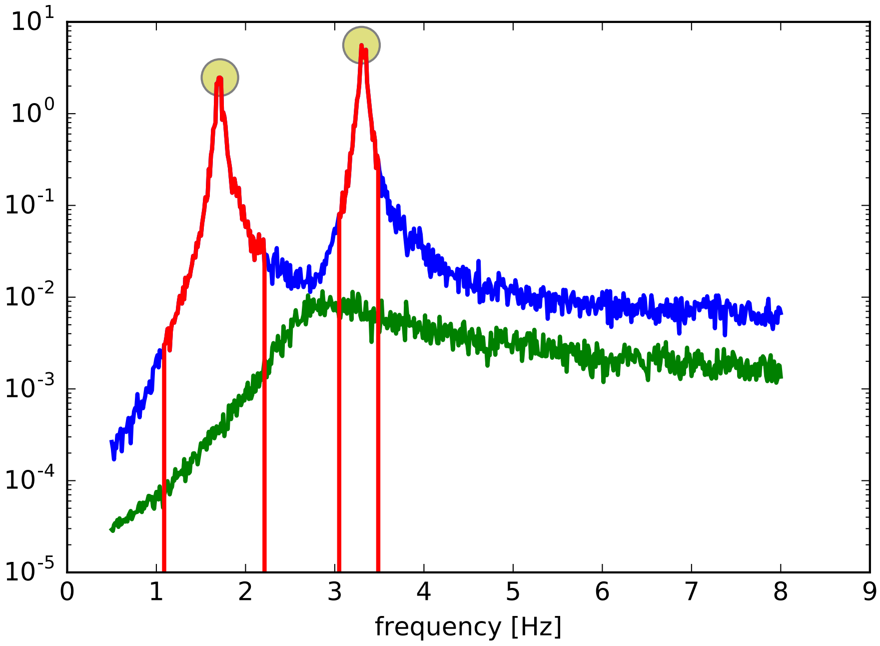

Figure 3.13: Two storey frame system: singular values of the spectral density matrices including the identified peaks (circled) and the corresponding frequency ranges (marked in red)

parameter	mean	standard deviation	COV
f_1	1.704 Hz	0.00056 Hz	0.033 %
f_2	3.326 Hz	0.00019 Hz	0.0057 %
ζ_1	2.246 %	0.014 %	0.614 %
ζ_2	1.191 %	0.018 %	1.570 %

Table 3.4: Two storey frame system: statistical parameters of the natural frequencies and modal damping ratios identified by means of the FDD method (COV = coefficient of variation)

degree-of-freedom 1, mode 1 degree-of-freedom 1, mode 2

degree-of-freedom 2, mode 1 degree-of-freedom 2, mode 2

Figure 3.14: Two storey frame system: autocorrelation functions estimated for the two channels and the two modes, respectively

3.6.2 Practical example: Modal analysis of a model beam

3.6.2.1 Description of the system

To demonstrate the performance of several modal identification methods in their application to a practical system, measured data that has been acquired in laboratory tests with a beam was chosen as an example. The considered system is a 3 m long steel beam with a standard rectangular hollow cross-section 100×60×3 mm. One objective in the choice of this study was to minimise the uncertainties that can be caused by the experimental setup. As boundary conditions are always one of the most uncertain parameters in physical models, it was decided to simulate free-free support conditions for the beam. Practically this was achieved by hanging the beam on two elastic cords. The response of the system was measured by accelerometers in vertical direction at 12 locations equidistantly distributed along the longitudinal axis of the beam. An overview of the system and the experimental setup is given in figure 3.15 in form of a sketch and in figure 3.16 as a photograph in plan view. To enhance the signal-to-noise ratio, an impulse hammer was used to apply multiple impacts at several locations of the beam.

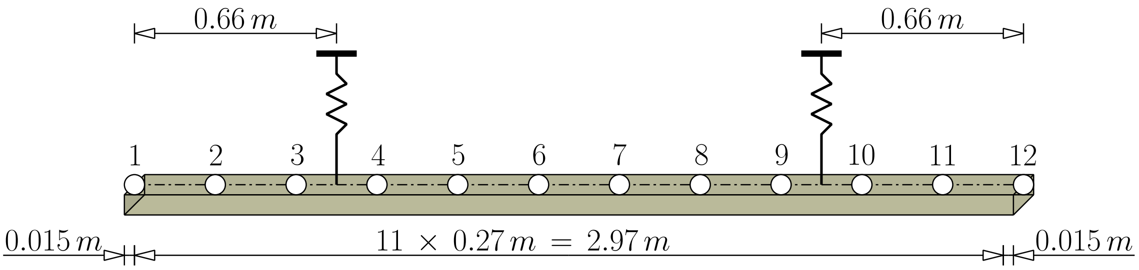

Figure 3.15: Sketch of the analysed beam with simulated free-free support

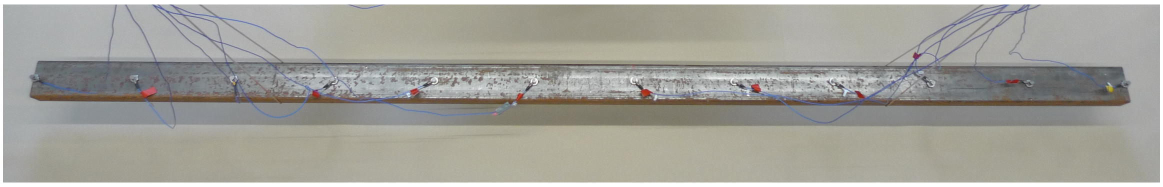

Figure 3.16: Experimental setup of the beam with simulated free-free support

A second advantage of the chosen system is the availability of an analytical solution for the natural frequencies ω_r and mode shapes ψ_r which can be used to validate the experimental results:

$$\omega_r = \left(\frac{\alpha_r}{L}\right)^2 \sqrt{\frac{EI}{\rho A}} \tag{3.256}$$

$$\psi_r(x) = \sinh\frac{\alpha_r}{L}x + \sin\frac{\alpha_r}{L}x - \left(\cosh\frac{\alpha_r}{L}x + \cos\frac{\alpha_r}{L}x\right)\frac{\sinh\alpha_r - \sin\alpha_r}{\cosh\alpha_r - \cos\alpha_r} \tag{3.257}$$

where L is the beam's length and

$$\alpha_r = \frac{(2r+1)\pi}{2} \tag{3.258}$$

For the first five bending modes in vertical direction one obtains with the parameters

$$\begin{aligned} E &= 2.05 \times 10^{11}\,\frac{N}{m^2} \\ I &= 55.7\,cm^4 \\ A &= 9.14\,cm^2 \\ \rho &= 7850\,\frac{kg}{m^3} \end{aligned}$$

the natural frequencies and mode shapes summarised in table 3.5.

3.6.2.2 Description of the tests

As mentioned above, the system was excited by means of an impulse hammer. It becomes obvious from the Fourier spectrum of the applied force shown in figure 3.17 that the excitation clearly covers a broad frequency band. Accordingly, one can expect that all modes presented in table 3.5 are sufficiently excited for their identification. From the spectrum of the accelerations measured at measuring point No. 1, i.e. at one end of the beam, that is shown in figure 3.18 one can deduce that at least the five modes presented in table 3.5 could be identified in the frequency range up to 750 Hz from the measured signals.

Here the results of the analysis of a test with a duration of 92 seconds are presented and discussed. Accordingly, the number of periods of the mode with the expected lowest natural frequency of nearly 50 Hz within the observed time window is approximately 4500. This agrees also with recommendations given in literature such as [27].

To be able to cover a frequency range up to 1 kHz, a sampling rate of 4096 Hz was chosen. This gives even the possibility to investigate the effects obtained by decimating the measured

nat. frequencies	mode shapes
49.54 Hz	
137.61 Hz	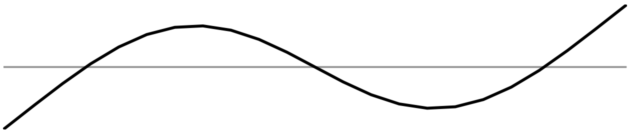
269.72 Hz	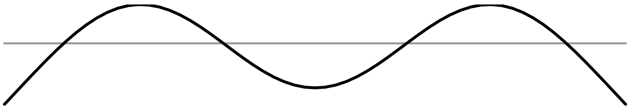
445.86 Hz	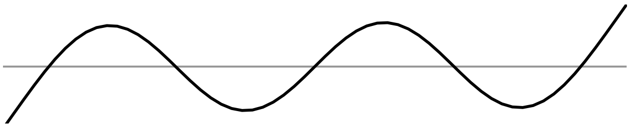
666.04 Hz	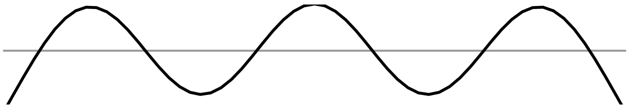

Table 3.5: Analytical solutions of the first five natural frequencies and bending mode shapes for the considered beam

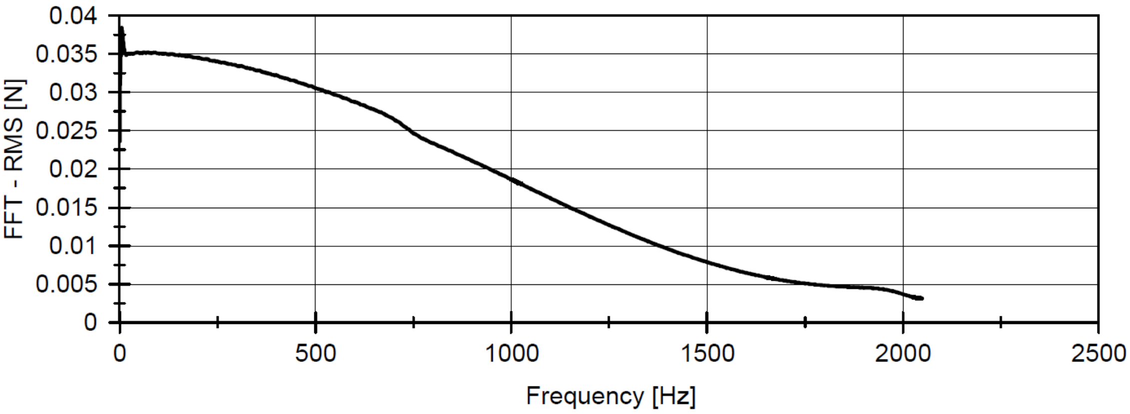

Figure 3.17: Fourier spectrum of the impulse excitation applied to the beam in laboratory tests

time series. In the following sections results obtained by means of three parametric methods with varying algorithmis parameters are presented and discussed.

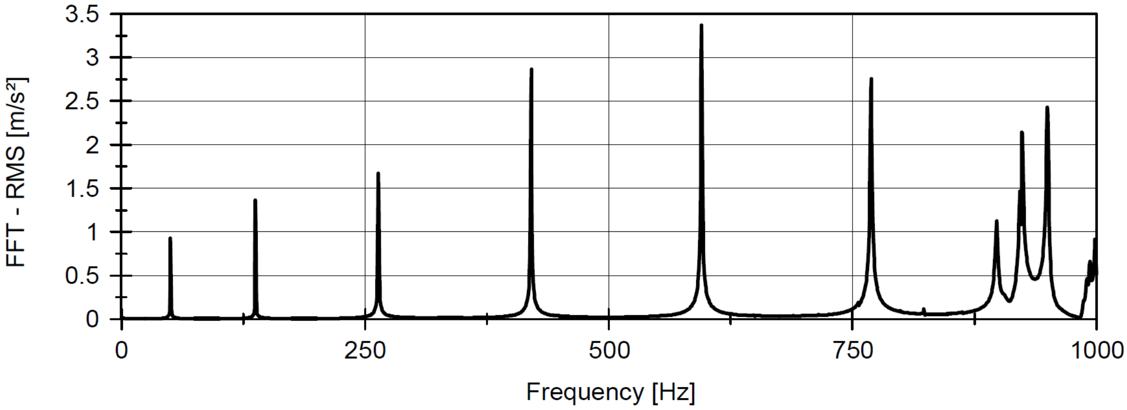

Figure 3.18: Fourier spectrum of the acceleration response at measuring point No. 1 during the laboratory tests

3.6.2.3 Modal Identification with the poly-reference least squares complex exponential (p-LSCE) method

As the investigation of the influence of all possible parameters to be set for the analysis of the acquired time series by means of the poly-reference least squares complex exponential (p-LSCE) method would become too complex, here only the number of reference channels and the effect of decimating the data has been considered in the following. Therefore, the maximal model order and the length of correlation series were fixed for all cases as

$$\begin{aligned} &\text{ength of correlation series} &&= 2 \times 50 = 100 \text{ samples} \\ &\text{maximal model order} &&= 50 \end{aligned}$$

while the reference channels and the degree of decimation were varied. With respect to decimation it was distinguished between the options to use the time series with their original sampling rate of 4096 Hz and to decimate the signals by a factor of 2 which resulted in a sampling rate of 2048 Hz. Further, the calculations were performed, on the one hand, with the correlation functions with respect to all channels and using only channels 1 and 12, that correspond to the sensors at the two ends of the beam, on the other hand. This resulted in four different combinations of analysis parameters. The stablisation diagrams for these four cases are shown in tables 3.6 and 3.7.

From the stabilisation diagrams in tables 3.6 and 3.7 one can conclude for this example, that the decimation of the signals leads to an increase of solutions in the considered frequency range. This does not only apply to the number of solutions in general but partly also to the number of stable solutions. Further, the reduction of the used references for the correlations to the selected channels 1 and 12 does not only reduce the computational effort but also results in "clearer" stabilisation diagrams, i.e. more stable soultions corresponding to physical modes of the investigated beam.

To quantify the uncertainties in the identified modal parameters, all solutions that could be clearly assigned to the same physical mode were considered. As not from all stabilisation diagrams stable solutions could be selected for each mode, also some solutions which were not classified as stable solution were taken into account if they still could be clearly assigned

1) all channels, no decimation

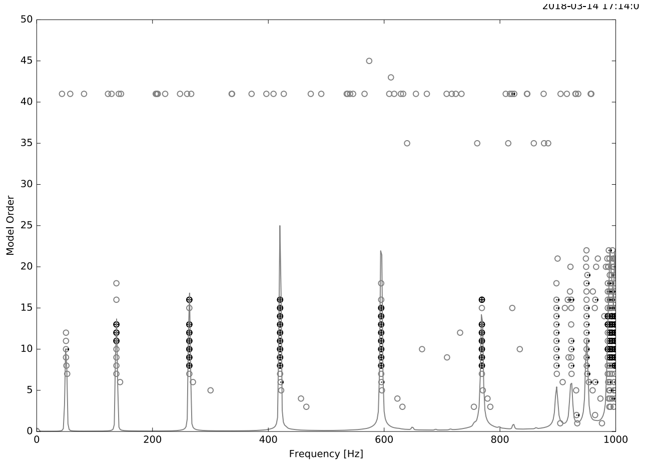

2) channels 1 & 12 as reference, no decimation

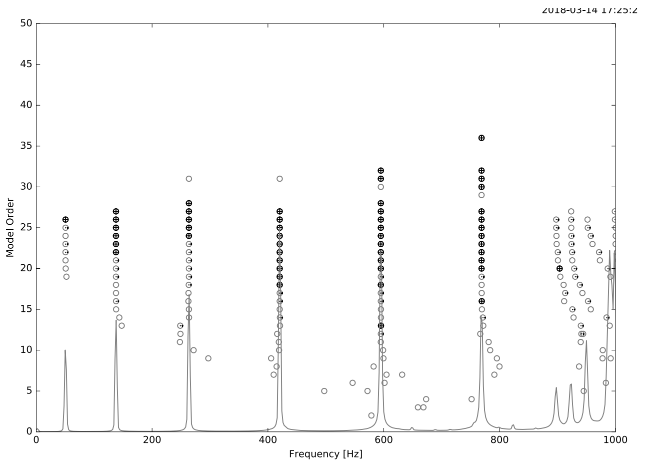

3) all channels, decimation to SR = 2048 Hz

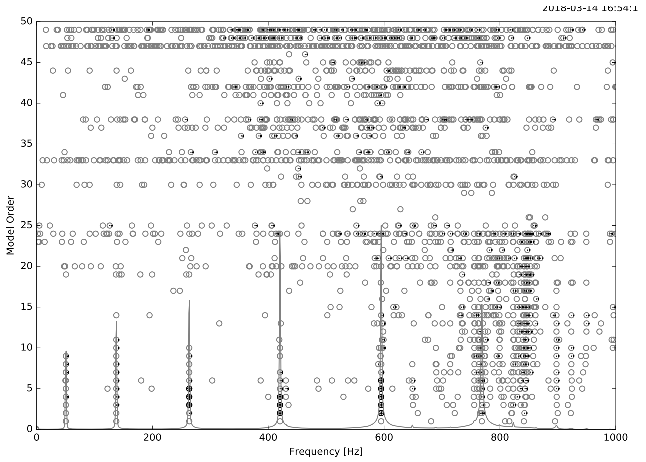

4) channels 1 & 12 as reference, decimation to SR = 2048 Hz

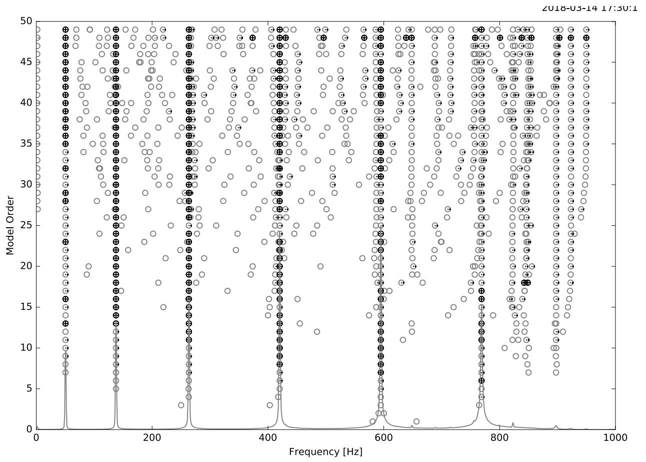

Table 3.6: Laboratory beam: Stabilisation diagrams generated by means of the p-LSCE method for the four different analysis cases, all calculated solutions

to a specific mode. For example, from table 3.7 one can deduce that there were only very few stable solutions for the first two physical modes available from most of the analyses. In these cases, also solutions which showed damping ratios with a relatively small deviation from neighbouring solutions and MPC values (see section 4.1.1) very close to 1 were taken into account. Still then, for some analyses only very few solutions could be selected. Nevertheless, also the statistical parameters of these estimates in table 3.9 give quantitative information with respect to the scatter of the respective parameters that can be already qualitatively obtained from the diagrams in table 3.8. These results also confirm the impression evoked by the stabilisation diagrams, that the identification for which the signals were decimated to a sampling rate of 2048 Hz and which only used the correlation functions with respect to channels 1 and 12 give the highest level of confidence in this example.

1) all channels, no decimation

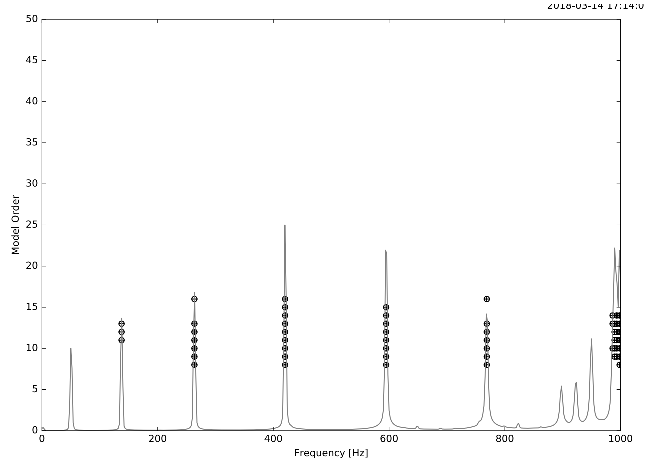

2) channels 1 & 12 as reference, no decimation

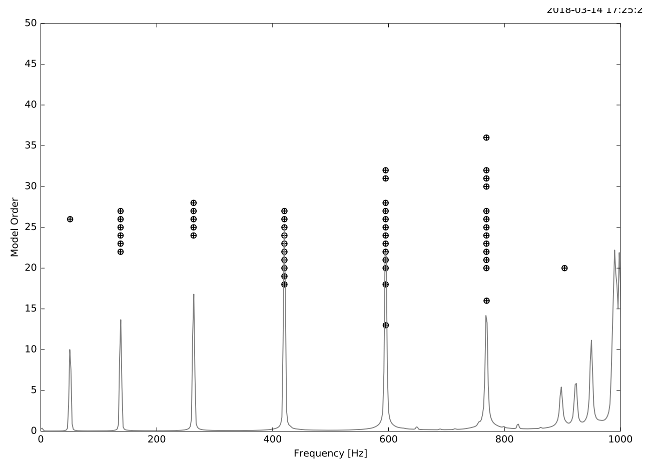

3) all channels, decimation to SR = 2048 Hz

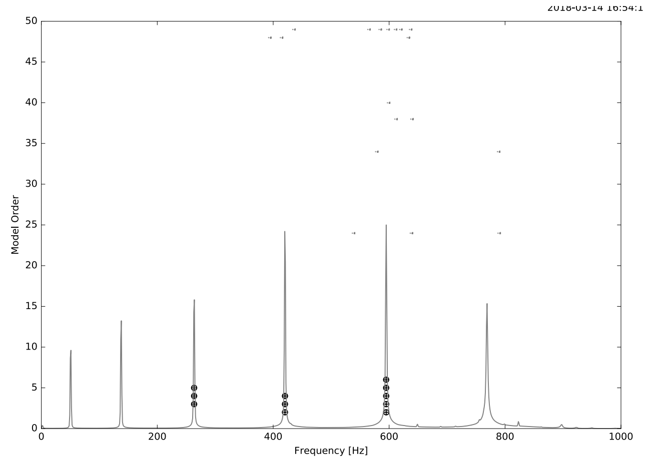

4) channels 1 & 12 as reference, decimation to SR = 2048 Hz

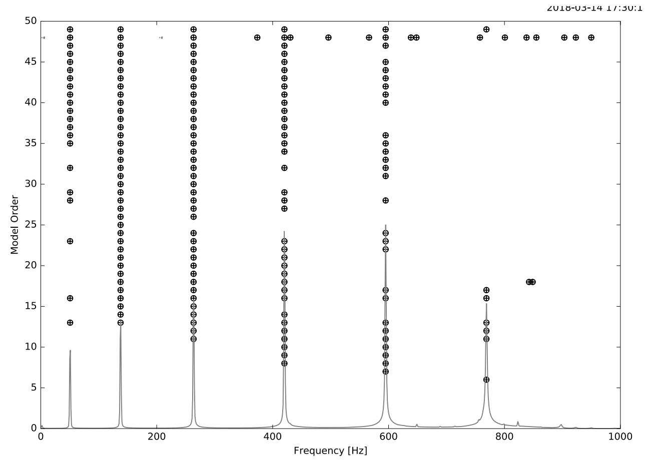

Table 3.7: Laboratory beam: Stabilisation diagrams generated by means of the p-LSCE method for the four different analysis cases, only stable solutions

1) all channels, no decimation 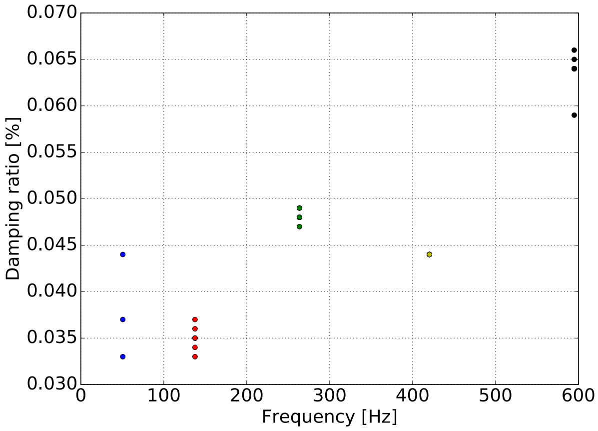	2) channels 1 & 12 as reference, no decimation 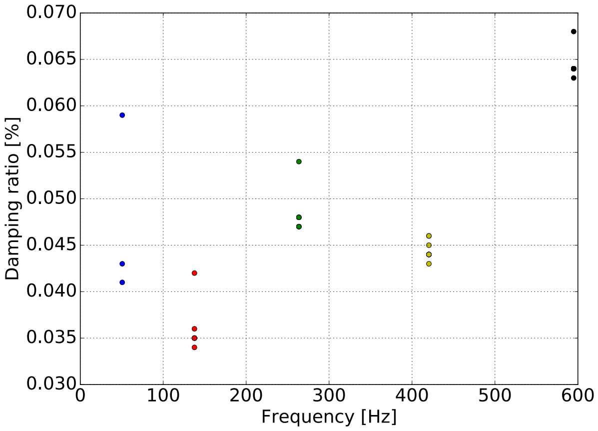
3) all channels, decimation to SR = 2048 Hz 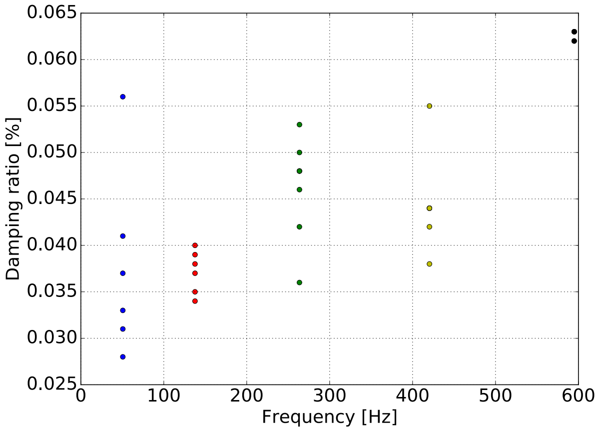	4) channels 1 & 12 as reference, decimation to SR = 2048 Hz 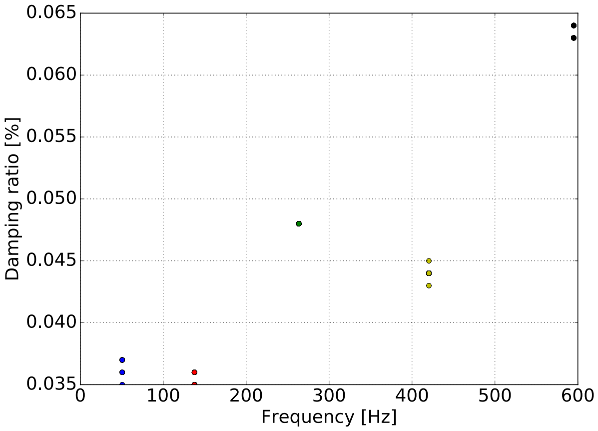

Table 3.8: Laboratory beam: solutions generated by means of the p-LSCE method for the four different analysis cases in the damping-frequency plane

		reference channels: all, no decimation	reference channels: 1 & 12, no decimation	reference channels: all, decimation: SR = 2048 Hz	reference channels: 1 & 12, decimation: SR = 2048 Hz
f_1	mean	50.583 Hz	50.579 Hz	50.582 Hz	50.582 Hz
	COV	1.9e-3 %	2.5e-3 %	1.8e-2 %	5.6e-4 %
f_2	mean	137.648 Hz	137.649 Hz	137.648 Hz	137.648 Hz
	COV	7.8e-4 %	7.5e-4 %	2.5e-3 %	1.1e-4 %
f_3	mean	263.598 Hz	263.598 Hz	263.592 Hz	263.597 Hz
	COV	2.1e-4 %	9.6e-4 %	7.2e-3 %	1.3e-4 %
f_4	mean	420.341 Hz	420.343 Hz	420.344 Hz	420.342 Hz
	COV	5.9e-4 %	1.2e-3 %	2.1e-3 %	2.0e-4 %
f_5	mean	594.953 Hz	594.959 Hz	594.939 Hz	594.960 Hz
	COV	2.6e-3 %	5.3e-4 %	5.0e-3 %	2.7e-4 %
ζ_1	mean	0.038 %	0.048 %	0.038 %	0.037 %
	COV	11.963 %	16.899 %	24.412 %	1.772 %
ζ_2	mean	0.035 %	0.036 %	0.037 %	0.035 %
	COV	3.415 %	6.288 %	5.690 %	1.249 %
ζ_3	mean	0.048 %	0.048 %	0.046 %	0.048 %
	COV	1.303 %	4.347 %	10.560 %	0.00 %
ζ_4	mean	0.044 %	0.044 %	0.044 %	0.044 %
	COV	0.00 %	1.854 %	10.751 %	0.502 %
ζ_5	mean	0.064 %	0.064 %	0.063 %	0.063 %
	COV	2.572 %	1.683 %	0.752 %	0.753 %

Table 3.9: Laboratory beam: mean values and COV of the identified natural frequencies and modal damping ratios for the four cases of signal processing by means of the p-LSCE method

3.6.2.4 Modal Identification with the covariance-driven stochastic subspace identification (SSI-cov) method

In this section, the results of modal analyses by means of the SSI-cov algorithm are described. Within these analyses two aspects were considered: a) the use of reference channels and b) the change of the sampling rate by decimating the acquired time series. The size of the block Toeplitz matrix was kept constant with 200 block columns and rows in all cases. Further, the maximal model order was chosen to be 100 in all analyses.

The presentation of the results is limited to the first five bending modes which are shown in table 3.5 as solutions of the analytical approach. To demonstrate, how the results are influenced by using only the covariances with respect to selected reference channels in the block Toeplitz matrix and by changing the sampling rate and accordingly the time window length for the correltation analyses, four different identifications are compared:

1. use of all channels for the calculation of the covariances and no decimation of the time series.
2. use of channels 1 and 12, i.e. the data measured at the two ends of the beam, as references for the covariances and no decimation of the time series.
3. use of all channels for the calculation of the covariances and decimation of the time series by factor 2 ⟶ new *sampling rate* (SR): 2048 Hz.
4. use of channels 1 and 12, i.e. the data measured at the two ends of the beam, as references for the covariances and decimation of the time series by factor 2 ⟶ new sampling rate (SR): 2048 Hz.

The stabilisation diagrams for these four cases are shown in table 3.10. In these plots only stable solutions are shown. One can observe that in this example the difference of the stabilisation diagrams between the cases in which the covariances of all channels were used and those where channels 1 and 12 were used as references appear to be not significant. However, the decimation of the signals apparently leads to more spurious solutions. On the other hand, the decimation has the effect that the modes of lower order show stable solutions already at relatively low model orders.

With respect to the selection of the "best" model order, it is helpful to have an impression about how much the solutions corresponding to different model orders vary. Therefore, the solutions are given in the damping-frequency plane in table 3.11. In these diagrams for all stable solutions that could be associated to physical modes, the modal damping ratios are related to the respective identified natural frequencies. The mean values and coefficients of variantion of the quantities represented in the diagrams are given in table 3.12.

From the stabilisation diagrams has been deduced that decimating the time series had obviously a positive effect on the identification, especially of modes at lower frequencies. Even though far more solutions for each mode were taken into account in the cases with decimated time series, the diagrams in table 3.11 clearly show that the respective identified parameters scatter significantly less than in the results obtained without decimating the measured data. The coefficients of variation of the identified natural frequencies are below 0.01 % while the identified modal damping ratios in most cases show larger deviations from each other. In this context,

1) all channels, no decimation 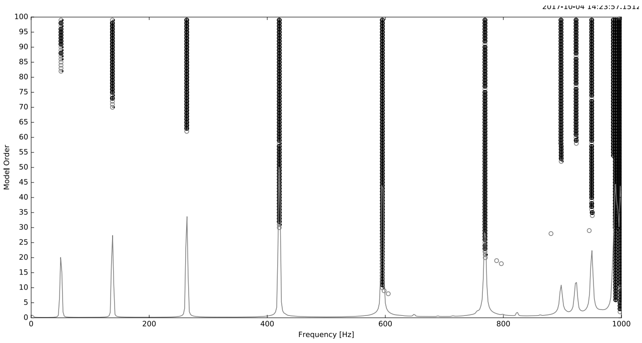 	2) channels 1 & 12 as reference, no decimation 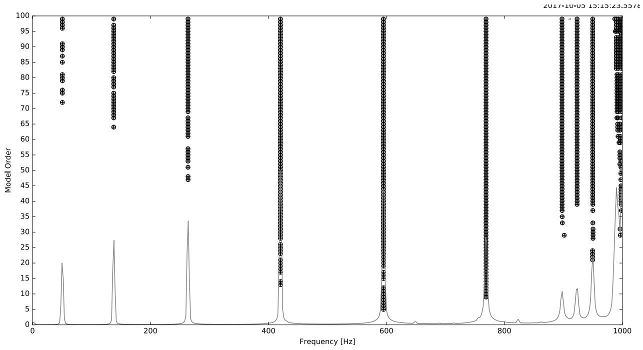
3) all channels, decimation to SR = 2048 Hz 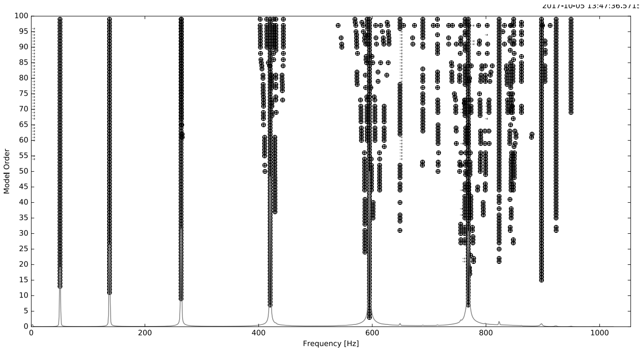 	4) channels 1 & 12 as reference, decimation to SR = 2048 Hz 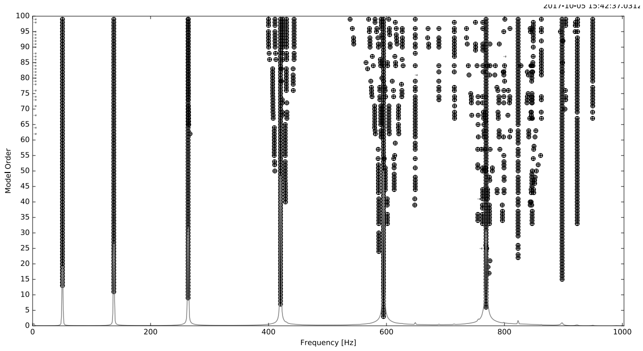

Table 3.10: Laboratory beam: Stabilisation diagrams generated by means of the SSI-cov method for the four different analysis cases

however, needs to be mentioned that the damping of the beam is very weak and small deviations of the absolute values easily result in larger relative deviations.

If only the covariances with respect to the two selected reference channels are used to build the covariance matrices instead of taking into account all covariance relations, it can be observed for this example, that the results, in particular the modal damping ratios, are in most cases slightly more scattered. These conclusions from the diagrams in table 3.11 are quantified by the respective statistical values given in table 3.12.

1) all channels, no decimation 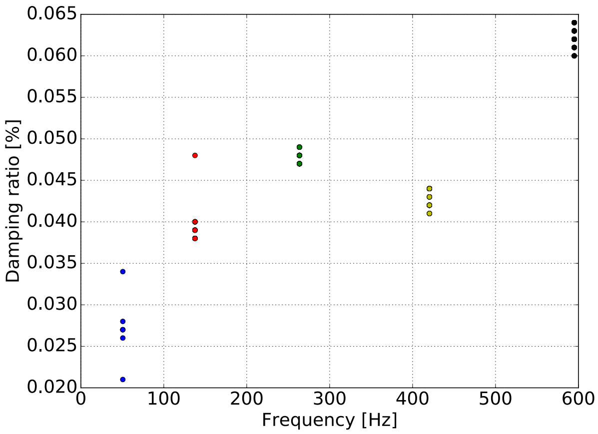 	2) channels 1 & 12 as reference, no decimation 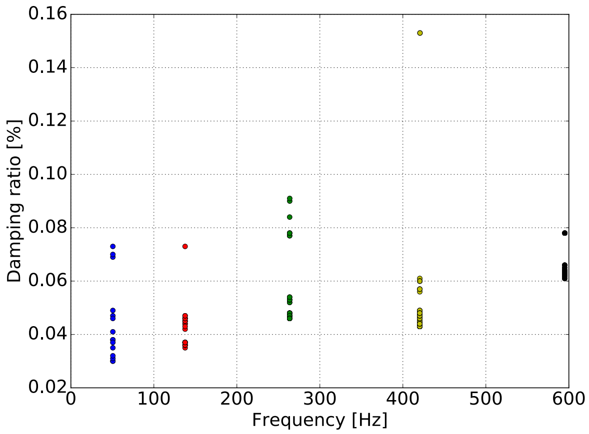
3) all channels, decimation to SR = 2048 Hz 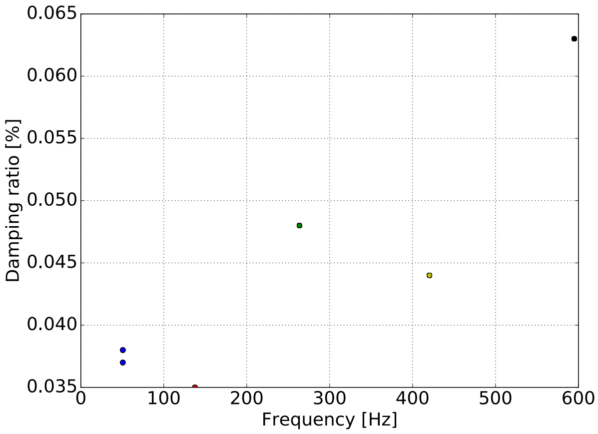 	4) channels 1 & 12 as reference, decimation to SR = 2048 Hz 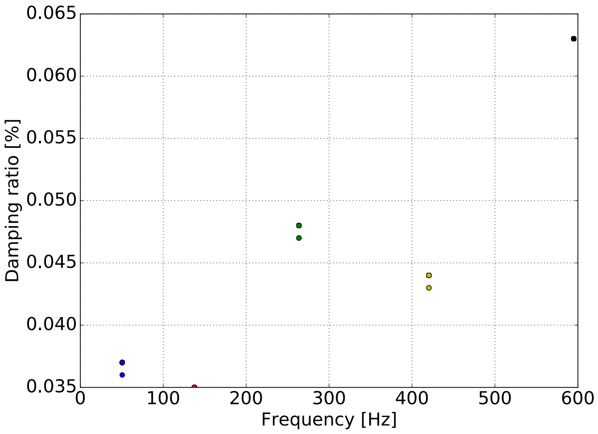

Table 3.11: Laboratory beam: solutions generated by means of the SSI-cov method for the four different analysis cases in the damping-frequency plane

		reference channels: all, no decimation	reference channels: 1 & 12, no decimation	reference channels: all, decimation: SR = 2048 Hz	reference channels: 1 & 12, decimation: SR = 2048 Hz
f_1	mean	50.582 Hz	50.583 Hz	50.583 Hz	50.583 Hz
	COV	6.9e-4 %	9.7e-4 %	0.00 %	0.00 %
f_2	mean	137.646 Hz	137.646 Hz	137.648 Hz	137.648 Hz
	COV	1.5e-3 %	2.9e-3 %	0.00 %	0.00 %
f_3	mean	263.597 Hz	263.598 Hz	263.594 Hz	263.594 Hz
	COV	4.8e-4 %	6.4e-3 %	2.0e-4 %	3.4e-4 %
f_4	mean	420.336 Hz	420.351 Hz	420.340 Hz	420.340 Hz
	COV	7.4e-4 %	1.0e-2 %	1.1e-4 %	1.1e-4 %
f_5	mean	594.964 Hz	594.976 Hz	594.956 Hz	594.956 Hz
	COV	1.4e-3 %	6.3e-3 %	7.9e-5 %	7.8e-5 %
ζ_1	mean	0.027 %	0.044 %	0.037 %	0.037 %
	COV	12.978 %	32.34 %	1.328 %	0.288 %
ζ_2	mean	0.039 %	0.041 %	0.035 %	0.035 %
	COV	4.964 %	17.39 %	0.00 %	0.00 %
ζ_3	mean	0.048 %	0.054 %	0.048 %	0.048 %
	COV	1.546 %	24.20 %	0.00 %	0.372 %
ζ_4	mean	0.043 %	0.049 %	0.044 %	0.044 %
	COV	2.454 %	34.51 %	0.00 %	0.402 %
ζ_5	mean	0.063 %	0.064 %	0.063 %	0.063 %
	COV	1.519 %	6.672 %	0.00 %	0.00 %

Table 3.12: Laboratory beam: mean values and COV of the identified natural frequencies and modal damping ratios for the four cases of signal processing by means of the SSI-cov method

3.6.2.5 Modal Identification with the data-driven stochastic subspace identification (SSI-data) method

As has been shown in the previous two sections, the results of an operational modal analysis by means of parametric methods can depend very much on the choice of algorithmis parameters. Similarly as for the p-LSCE and the SSI-cov methods, the influence of signal decimation and use of reference signals is now also investigated for the application of the SSI-data algorithm in this section.

For the analyses described in the following the number of block rows of the Hankel matrix was fixed to 150, the modal parameters were identified for models up to a maximal order of 200. As variable parameters with influence on the identification algorithm, the degree of decimation as well as the choice of reference signals were selected. With the two options of considering all channels and channels 1 & 12 as references and three different sampling rates after decimation

- 4096 Hz – no decimation,
- 2048 Hz – decimation by factor 2,
- 1024 Hz – decimation by factor 4,

six different cases of analysis were obtained. In table 3.13 the stabilisation diagrams for these six analyses are shown.

Again, the discussion of the results is also limited here to the first five modes, i.e. to a frequency range up to 600 Hz. In the stabilisation diagrams in table 3.13 only stable solutions are indicated. A spectrum is included in each diagram to give an orientation at which frequencies solutions corresponding to physical modes are to expect.

From observing the stabilisation diagrams one can draw the following conclusions with respect to the considered frequency range.

- The number of spurious solutions increases with an increasing degree of decimation.
- Decimating the signals results also in more stable solutions starting from very low model orders.
- Clearly stable solutions corresponding to mode 2 at ≈ 137.6 Hz can be hardly found for sampling rates of 4096 and 2048 Hz.
- The second mode can be only identified with sufficient confidence if the signals had been decimated to a sampling rate of 1024 Hz. However, in this case the fifth mode is not included in the frequency range covered by the analysis.

To obtain an overview about how much the identified modal parameters for the respective modes vary in the six analysis cases, the modal damping ratios were plotted over frequency in table 3.14. These diagrams show a trend that the scatter of the damping ratios is reduced if the signals are decimated. Further, the use the two chosen reference reference channels leads as well for most of the modes to smaller deviations of the modal damping ratios identified for different model orders. Even though these observations do not apply to all cases and all modes, the

1) all channels, no decimation 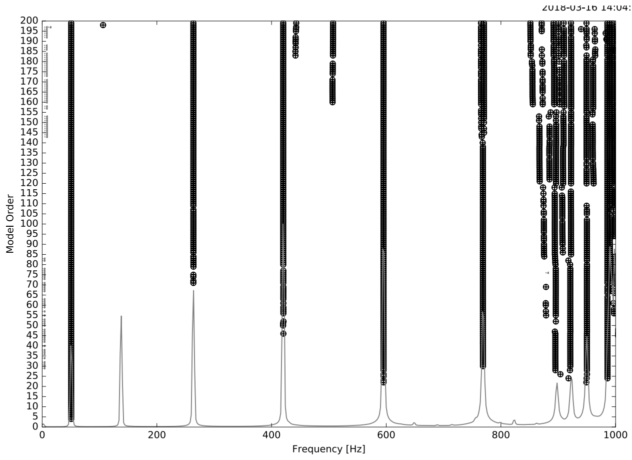 	2) channels 1 & 12 as reference, no decimation 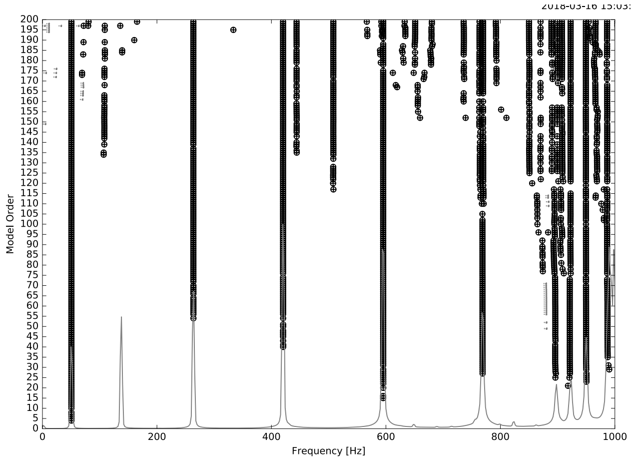
3) all channels, decimation to SR = 2048 Hz 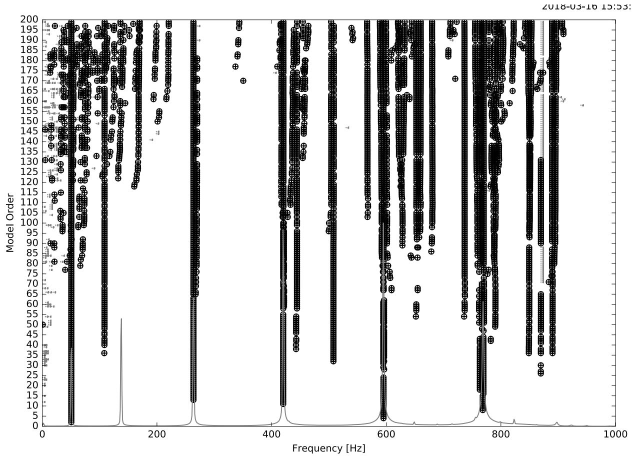 	4) channels 1 & 12 as reference, decimation to SR = 2048 Hz 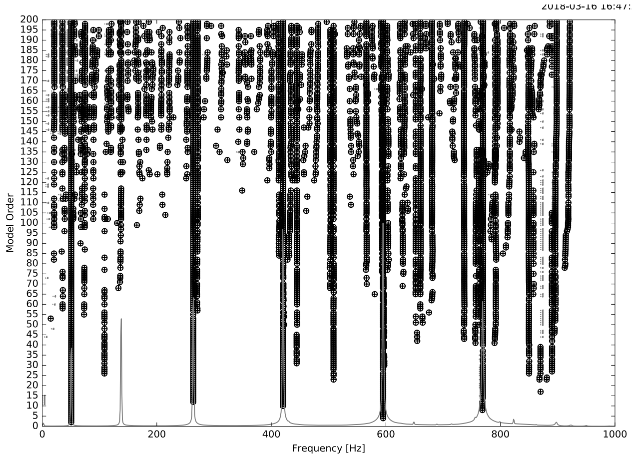
5) all channels, decimation to SR = 1024 Hz 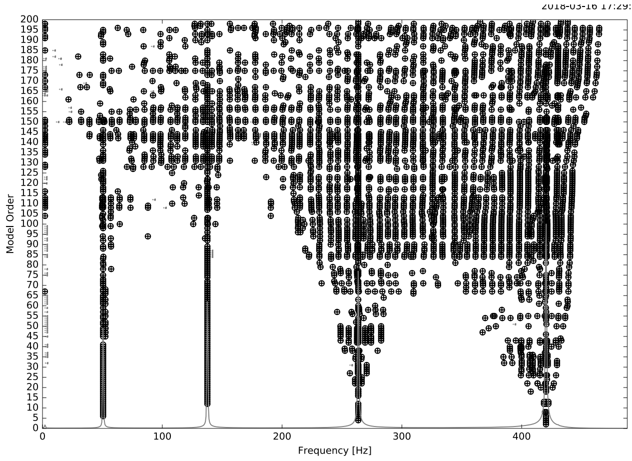 	6) channels 1 & 12 as reference, decimation to SR = 1024 Hz 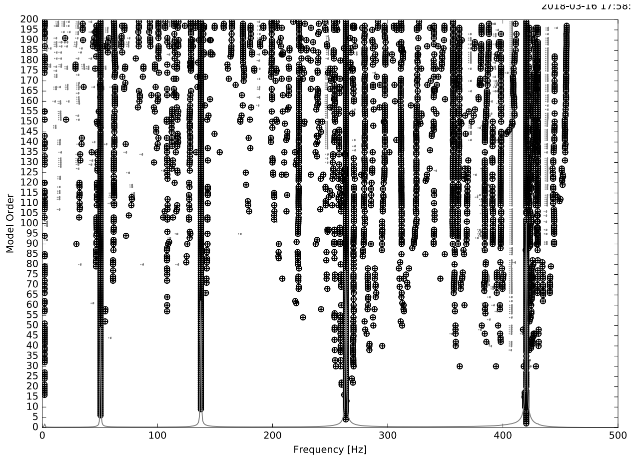

Table 3.13: Laboratory beam: Stabilisation diagrams generated by means of the SSI-data method for the six different analysis cases

mentioned trends are visible and quantified in table 3.15 which summarises the mean values and coefficients of variation of the identified natural frequencies and modal damping ratios corresponding to the first five modes.

1) all channels, no decimation

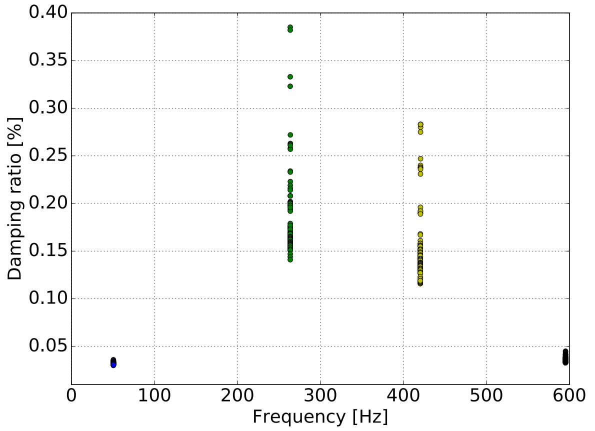

2) channels 1 & 12 as reference, no decimation

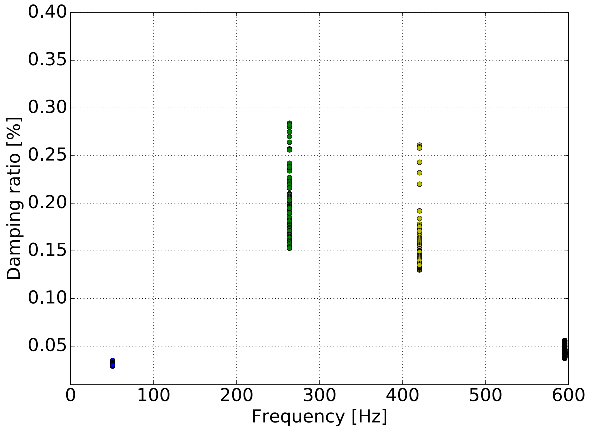

3) all channels, decimation to SR = 2048 Hz

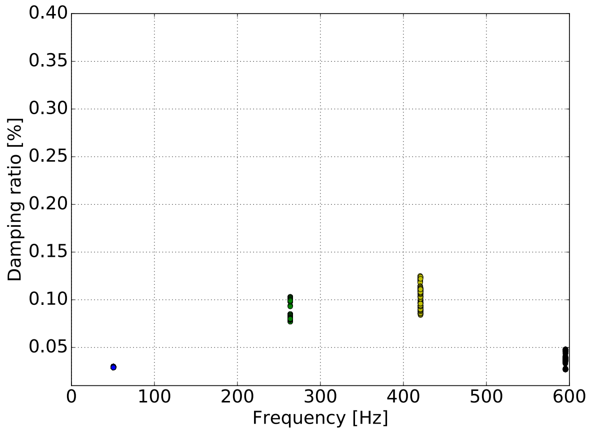

4) channels 1 & 12 as reference, decimation to SR = 2048 Hz

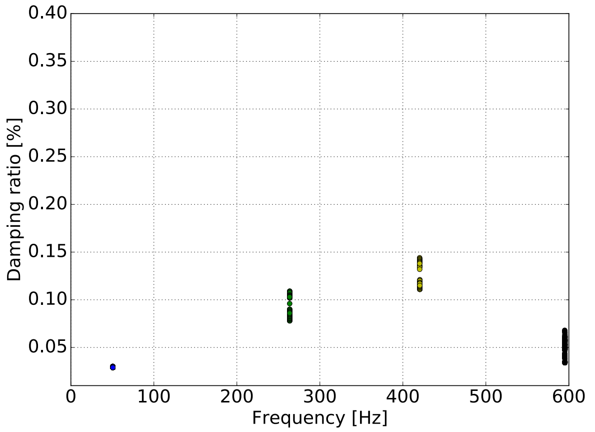

5) all channels, decimation to SR = 1024 Hz

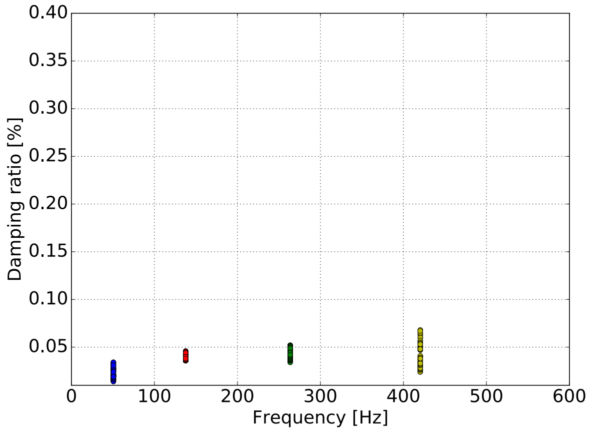

6) channels 1 & 12 as reference, decimation to SR = 1024 Hz

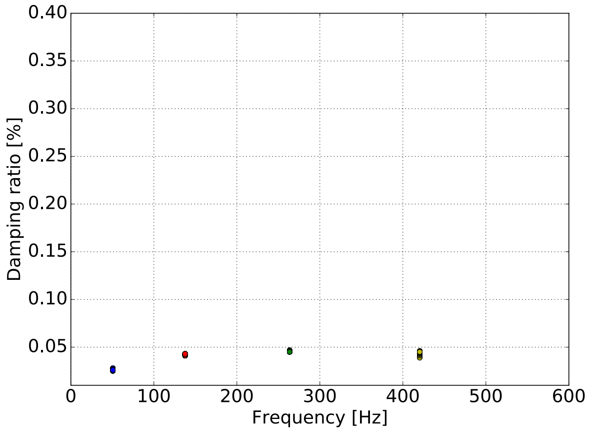

Table 3.14: Laboratory beam: solutions generated by means of the SSI-data method for the six different analysis cases in the damping-frequency plane

		reference channels: all, no decimation	reference channels: 1 & 12, no decimation	reference channels: all, decimation: SR = 2048 Hz	reference channels: 1 & 12, decimation: SR = 2048 Hz	reference channels: all, decimation: SR = 1024 Hz	reference channels: 1 & 12, decimation: SR = 1024 Hz
f_1	mean	50.584 Hz	50.585 Hz	50.585 Hz	50.585 Hz	50.586 Hz	50.585 Hz
	COV	1.2e-3 %	9.7e-4 %	2.4e-4 %	0.00 %	5.6e-3 %	9.7e-4 %
f_2	mean	–	–	–	137.733 Hz	137.652 Hz	137.655 Hz
	COV	–	–	–	0.137 %	3.5e-3 %	4.2e-4 %
f_3	mean	263.685 Hz	263.629 Hz	263.678 Hz	263.658 Hz	263.606 Hz	263.601 Hz
	COV	1.2e-2 %	1.3e-2 %	5.1e-3 %	2.3e-3 %	5.3e-3 %	3.7e-4 %
f_4	mean	420.400 Hz	420.345 Hz	420.476 Hz	420.362 Hz	420.328 Hz	420.337 Hz
	COV	1.8e-2 %	7.6e-3 %	4.1e-2 %	1.9e-2 %	1.3e-2 %	9.3e-4 %
f_5	mean	595.270 Hz	595.250 Hz	595.213 Hz	595.180 Hz	–	–
	COV	2.6e-3 %	2.3e-3 %	9.3e-3 %	1.4e-2 %	–	–
ζ_1	mean	0.031 %	0.031 %	0.029 %	0.029 %	0.023 %	0.026 %
	COV	2.993 %	3.082 %	1.336 %	1.293 %	23.02 %	2.189 %
ζ_2	mean	–	–	–	1.075 %	0.038 %	0.042 %
	COV	–	–	–	11.82 %	6.813 %	1.366 %
ζ_3	mean	0.180 %	0.185 %	0.086 %	0.090 %	0.043 %	0.046 %
	COV	23.99 %	17.24 %	9.656 %	8.929 %	10.936 %	0.891 %
ζ_4	mean	0.150 %	0.151 %	0.106 %	0.121 %	0.039 %	0.044 %
	COV	24.75 %	17.09 %	11.13 %	8.203 %	27.707 %	3.089 %
ζ_5	mean	0.0351 %	0.043 %	0.038 %	0.050 %	–	–
	COV	6.306 %	8.483 %	15.48 %	16.95 %	–	–

Table 3.15: Laboratory beam: mean values and COV of the identified natural frequencies and modal damping ratios for the six cases of signal processing by means of the SSI-data method

3.6.2.6 Comparison of the results obtained by means of three parametric methods

In the three previous subsections about the modal identifications performed based on signals that were measured during vibration tests on a steel beam has been reported. In this subsection, these results are again summarised to give a comparative overview about the performance of the different algorithms in this example. It is emphasised that here only the observations from a single study are presented. They cannot be generalised and directly transferred to other studies as there are always various factors influencing the results of an operational modal analysis.

To obtain a comparative overview about the mentioned identification results, the mean values and coefficients of variation of the identified modal parameters given in tables 3.9, 3.12 and 3.15 are graphically represented in respective diagrams. One set of diagrams is exemplarily given here for mode 3 in figures 3.19 and 3.20. The respective diagrams for all considered modes are collected in appendix A.

As has become already obvious in the previous subsections, the relative deviations of identified natural frequencies are considerably smaller than those of the identified modal damping ratios. This does not only apply to the values obtained for different model orders of a single identification as expressed by the coefficients of variation (COV) in the diagrams but also to the mean values calculated from the identified modal parameter sets corresponding to the same mode.

For example, the mean values of the natural frequencies related to all modes identified by means of the p-LSCE and the SSI-cov algorithms vary less than 0.01 % from each other. This is also the case for the values identified by means of the SSI-data method for modes 1 and 2, with the restriction for mode 2 to the analyses for which the signals were decimated to a sampling rate (SR) of 1024 Hz. For modes 3 and 4 the scatter of the mean values of the natural frequencies identified by means of the SSI-data algorithm does not exceed a range of about 0.04 %, for mode 5 the respective limit is less than 0.06 %.

With the exceptions of the SSI-data results for mode 2 (SR = 2048 Hz, reference channels 1 & 12) and mode 4 (SR = 2048 Hz, all channels as reference), the coefficients of variation of the solutions corresponding to the respective mode in one analysis are smaller than 0.02 %. This means that the uncertainties related to the identification of the natural frequencies by means of different methods and analysis parameters are in a similar range as those of the respective solutions of a single computation in this example.

Apart from very few exceptions, the mean values of the modal damping ratios identified by means of the p-LSCE and SSI-cov algorithms vary within a range smaller than 10 %. Compared to the values mentioned in context with natural frequencies, this may appear to be a large scatter. However, it needs to be mentioned that the absolute values are very small and the uncertainties of identified modal damping ratios are usually always higher compared to those related to natural frequencies. Additionally, the absolute values of modal damping ratios are several dimensions smaller than those of natural frequencies. Accordingly, a relative deviation of several per cent of damping ratios in the range as identified in this study are still very small absolute values.

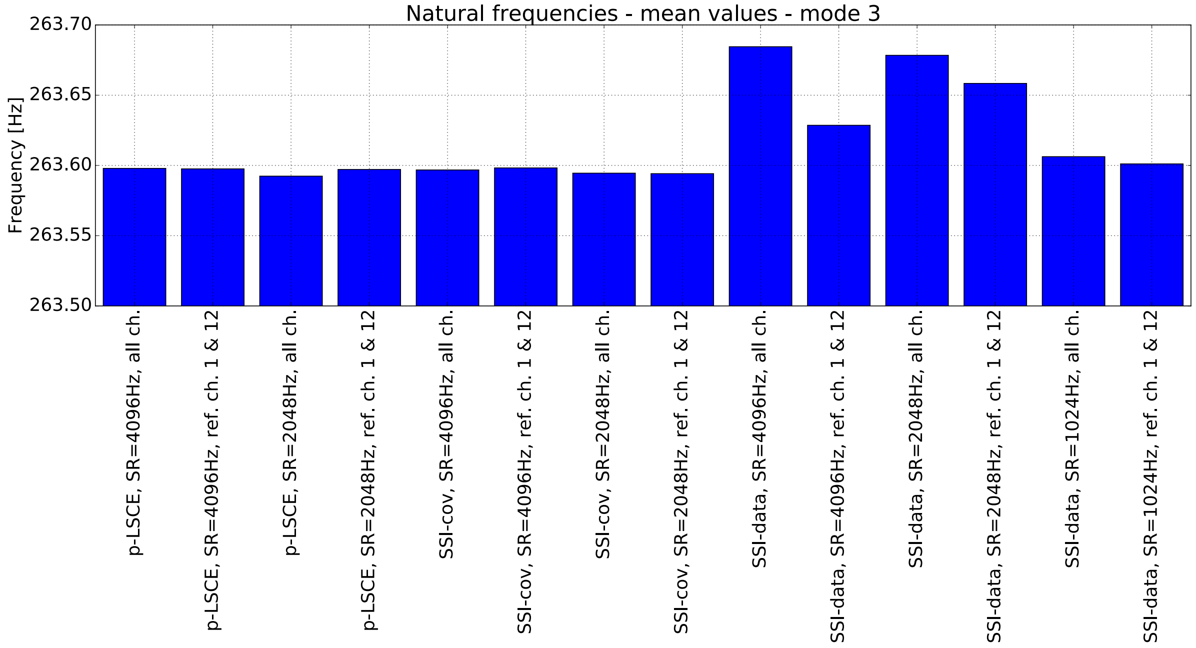

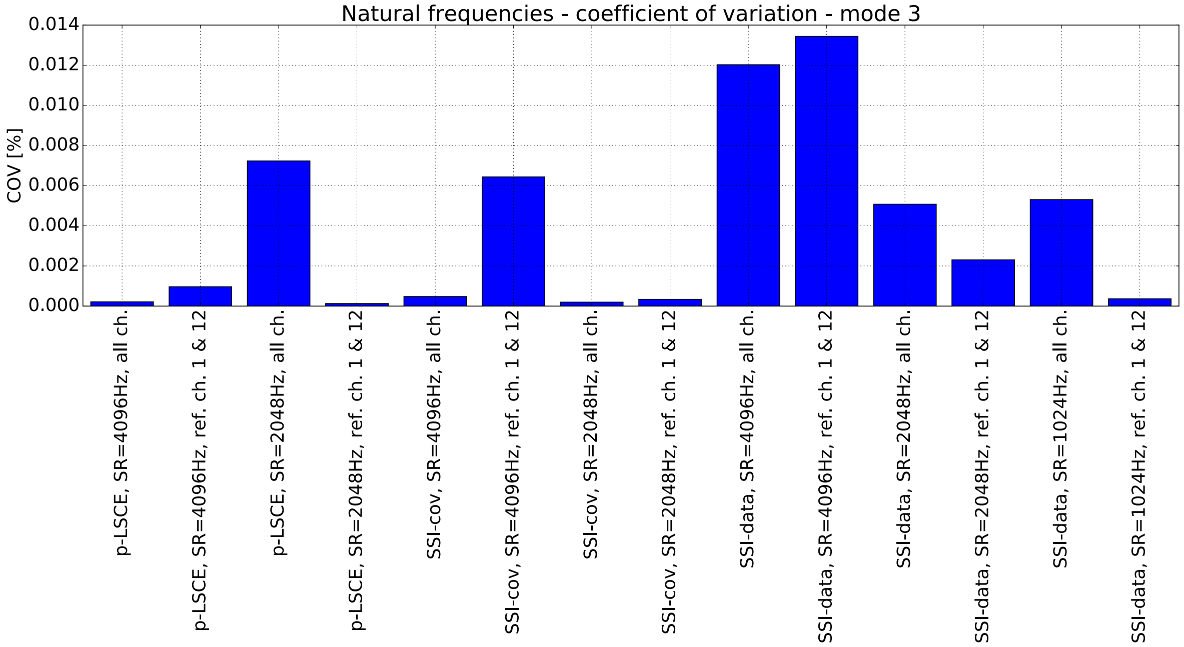

Figure 3.19: Laboratory beam: mean values and COV of the natural frequencies identified for mode 3 by means of different OMA methods using various parameters

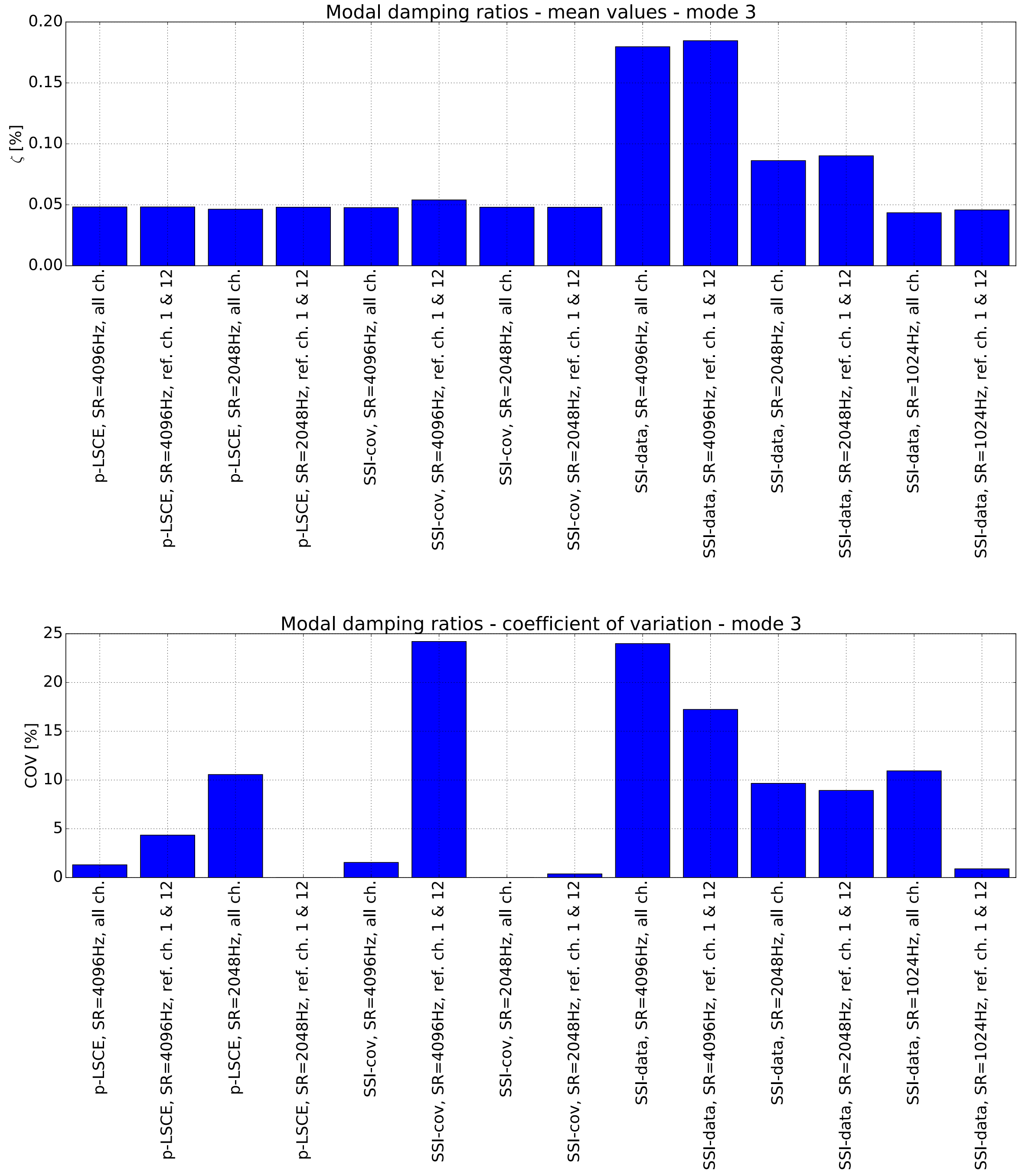

Figure 3.20: Laboratory beam: mean values and COV of the modal damping ratios identified for mode 3 by means of different OMA methods using various parameters

With the exception of the first mode, the damping ratios identified from the time series with sampling rates of 4096 Hz and 2048 Hz by means of the SSI-data method are in average higher than the corresponding values obtained by means of the p-LSCE and SSI-cov methods. Another interesting observation from the results obtained from the SSI-data analyses is that the influence of the reduction to the two selected reference channels is much smaller than the effect generated by decimating the signals.

The coefficients of variation related to the identified modal damping ratios are rather irregular and reach values between 0 and up to 35 %. A trend or conclusive relation can hardly been observed.

Even though the results summarised in this subsection apply exclusively to the analyses of a single example, one can conclude that such a comparative study of modal parameters that were identified by means of different methods gives the analyst valuable information about the level of confidence with respect to the results. This information can be further used, for example, as input parameter to a stochastic model updating. It is also important in applications where identified modal parameters are used to detect modifications of a considered system due to changes of environmental and service conditions or damage. In such cases considerations as presented here are recommended.

Chapter 4

Postprocessing of modal parameter estimates

After the identification of a mathematical model – in case of parametric identification methods – and the identification of modal parameters, it is important to assess the quality of the results. On the one hand the knowledge about the quality of the analyses provides a measure of confidence into the results, on the other hand measures of quality can be used for the distinction between physical and spurious modes obtained by means of a parametric method and in the selection of a respective soltution from a set of solutions calculated for different model orders. Especially the latter aspect will be discussed in the context with automised procedures for operational modal analysis in chapter 5. However, before an introduction into automised operational modal analysis will be given, several approaches and metrics to assess the quality of the identified results and to quantify the uncertainties will be discussed in section 4.1. Sections 4.2 and 4.3 give an overview about some aspects with respect to the combination of incomplete mode shapes obtained from tests with different setups and the representation of identified mode shapes. The issue of the quantification of uncertainties of a single estimate of modal parameters is discussed in section 4.4 where also a respective algorithm for SSI methods is described.

4.1 Validation of identified modal parameters

Even though an assessment of the quality of identified modal parameters is important regardless which method has been used, this aspect plays a significant role especially in the context with parametric methods. As already explained in section 3.4.1, stabilisation diagrams are a very common and useful tool supporting the distinction between physical and spurious modes. To categorise modal solutions into the group of stable poles, commonly relative deviations of natural frequencies and damping ratios are used as well as the modal assurance criterion, MAC. Respective criteria have been introduced in equations (3.176) to (3.178). These indicators are very adjuvant within the pole selection process. However, to select a specific solution out of a group of poles assigned as stable or to quantify the trustworthiness of the results, further criteria which provide additional information should be applied. In the following sections several such indicators and approaches are introduced.

4.1.1 Indicators for validation of modal parameters

4.1.1.1 Physical interpretation

In many cases the analyst sould have expectations about the visual appearance of mode shapes either from a numerical model or simply based on experience with similar structures. Therefore a graphical representation of the identified mode shapes is an intuitive but always very helpful tool and indicator. Some aspects with respect to the visualisation of mode shapes are discussed in section 4.3.

Another, rather simple criterion is the consideration of modal damping. There may be solutions with negative damping values. Due to the common expectation that the investigated systems should have positive damping, modal solutions with negative damping can be excluded from the group of valid results. Furthermore, zero damping can be usually considered as an indicator for harmonic components in the signals caused either by excitations such as rotating machinery or by contamination of the electrical signals. Accordingly, one should be careful, for example, with the interpretation of modes identified at the AC voltage frequency of the public electricity network which is $50\,Hz$ in European countries. In several countries the AC voltage frequency of the railway catenary system is $16.7\,Hz$. Therefore, a careful distinction between physical modes and harmonic components at this frequency may become a challenge in the analysis of railway bridges.

Structures tested in civil engineering can have damping values of less than $1\,\%$, but commonly damping values greater than $20\,\%$ should not be expected. Therefore, modal parameter sets with very high damping values can also be eliminated from further considerations.

4.1.1.2 Modal complexity

Operational modal analysis, as well as experimental modal analysis, will usually result in complex modes. Physically, a complex mode means that the phase angles of the degrees-of-freedom are not exactly either 0° or 180°. This means, that the amplitude values are reached at different instants at the different degrees-of-freedom during the vibration in a single mode. Reasons for complex modes are [49]

- non-proportional damping of the structure and
- close modes which means that the natural frequencies of two modes *“are separated by an amount which is less than the prevailing damping in either or both modes”* [49].
- repeated roots meaning that different modes have the same natural frequency, which is typical for systems with double or rotational symmetry.

For most civil engineering structures nearly-proportional damping can be assumed. Accordingly, the degree of complexity of their modes can be expected as rather low. An exception are certainly tower-like structures with double or rotationally symmetric cross sections. Apart from this group of systems, it has become common practice in civil engineering to take the degree of modal complexity as a measure of quality of identified modes.

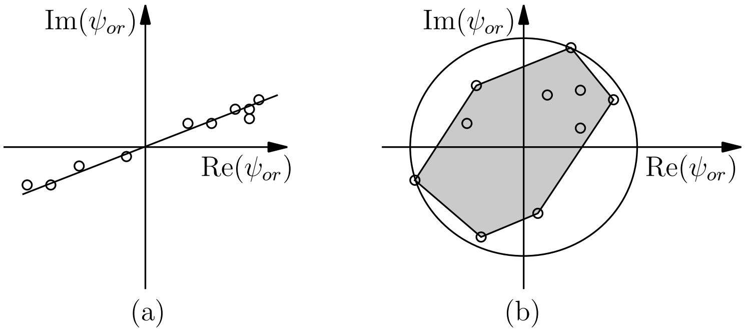

Figure 4.1: Representation of elements of complex mode shapes in an Argand diagram: (a) nearly real mode, (b) complex mode

A popular visual representaion of the complexity of a mode shape is the presentation of the elements of a mode shape in a so-called Argand diagram as in figure 4.1. The elements of the eigenvectors of a real mode should all have the same phase angle θ_r. Accordingly, they are supposed to form a straight line in the Argand diagram as indicated in 4.1(a).

Two measures of complexity, called *modal complexity factors* (MCF), were defined in [73]. The first of the two indicators, $MCF1$ is defined as the maximal absolute of all phase differences between two mode shape elements of a single eigenvector normalised by the mean phase difference:

$$MCF1 = \sum_{o=1}^{n_o-1} (n_o - o) \frac{max(|\theta_{ir} - \theta_{jr}|)}{\sum_{j=1}^{n_o} \sum_{j=1,j\neq i}^{n_o} (|\theta_{ir} - \theta_{jr}|)} \tag{4.1}$$

in which the phase differences are limited to 90°.

The second measure, $MCF2$ takes also into account the magnitudes of the mode shape estimates. It is defined as the ratio between the area of a circle around the origin of the Argand diagram with the radius of the maximal magnitude of the mode shape elements and the area enclosed by the envelope around the mode shape elements in the Argand diagram. One restriction in the construction of the enclosing polygon is that no interior angle can be greater than 180°. This approach is illustrated in figure 4.1(b).

Another indicator which may be rather natural from figure 4.1(a) is the *mean phase deviation* (MPD) [67]. The *mean phase* (MP), which is the angle between the horizontal axis and the straight line in figure 4.1(a), can be computed as

$$MP_r = \frac{\sum_{o=1}^{n_o} w_o \theta_{or}}{\sum_{o=1}^{n_o} w_o} \tag{4.2}$$

For the calculation it has to be ensured that the phase angles θ_{or} are within the range $0 \leq \theta_{or} \leq 90°$. Common choices for the weighting factors w_o are $w_o = 1$ for equal weighting or $w_o = |\phi_{or}|$ to give elements with larger modal amplitude a stronger weight.

The mean phase deviation becomes then with equation (4.2)

$$MPD_r = \sqrt{\frac{\sum_{o=1}^{n_o} w_o \left(\theta_{or} - MP_r\right)^2}{\sum_{o=1}^{n_o} w_o}} \tag{4.3}$$

For normal modes the MPD should be close to zero. It has been stated in [122] that the formulae given above may not be appropriate if mode shape elements have a large imaginary and a small real part. With this motivation, alternative expressions were derived in [122].

In [103] the *modal phase collinearity* (MPC) was proposed as a measure for spacial consistency of identified mode shapes. The analysis starts with subtracting the complex mean value of the considered mode shape from all elements of this mode shape [67]:

$$\left\{\tilde{\psi}_r\right\} = \{\psi_r\} - \frac{\sum_{o=1}^{n_o} \psi_{or}}{n_o} \tag{4.4}$$

Then the covariances between the real and imaginary parts of vector $\left\{\tilde{\psi}_r\right\}$ can be estimated as

$$\begin{aligned} S_{RR,r} &= \operatorname{Re}\left\{\tilde{\psi}_r\right\}^T \operatorname{Re}\left\{\tilde{\psi}_r\right\} \\ S_{II,r} &= \operatorname{Im}\left\{\tilde{\psi}_r\right\}^T \operatorname{Im}\left\{\tilde{\psi}_r\right\} \\ S_{RI,r} &= \operatorname{Re}\left\{\tilde{\psi}_r\right\}^T \operatorname{Im}\left\{\tilde{\psi}_r\right\} \end{aligned}$$

which can be used to construct the respective covariance matrix:

$$\left[S_r^2\right] = \begin{bmatrix} S_{RR,r} & S_{RI,r} \\ S_{RI,r} & S_{II,r} \end{bmatrix} \tag{4.5}$$

The eigenvalues of $[S_r^2]$ are given by

$$\lambda_{1,2} = \frac{S_{RR,r} + S_{II,r}}{2} \pm S_{RI,r}\sqrt{\frac{\left(S_{II,r} - S_{RR,r}\right)^2}{4S_{RI,r}^2} + 1} \tag{4.6}$$

With these eigenvalues the modal phase collinearity is defined by [103], [133]

$$MPC_r = \left(2\frac{\lambda_1}{\lambda_1 + \lambda_2} - 0.5\right)^2 = \left(\frac{\lambda_1 - \lambda_2}{\lambda_1 + \lambda_2}\right)^2 \tag{4.7}$$

The MPC values are in the range $0 \leq MPC \leq 1$, where 1 indicates normal or real modes. Furthermore, it has been shown in [133] that the MPC can also be expressed as the MAC of a mode shape with its conjugate.

It should be noticed that the definition of MPC in [67] and [122] deviates from equation (4.7), it is equivalent to

$$M\hat{P}C_r = \frac{\lambda_1}{\lambda_1 + \lambda_2} \tag{4.8}$$

if the expressions for λ_1 and λ_2 in equation 4.6 [103] are used.

4.1.1.3 Modal contribution to total response

Already in section 3.4.2 the idea to use information about the contribution of a single identified mode to the total measured response has been discussed in context with the selection of model order in parametric identification methods. This concept has also been the base for the development of the so-called *modal transfer norm* MTN as an indicator to separate physical from spurious modal parameter sets in the stabilisation diagram belonging to a combined deterministic-stochastic subspace identification in [121].

In [122], the modal transfer norm has been investigated in more detail. The indicator is based on the modal decompostion of the frequency response function (FRF) for situations with deterministic excitation and of the positive output power spectral density ($S^+_{yy}(\omega)$) if the input is of stochastic nature. At resonance the response of a system should be dominated by a single mode. This statement can be quantified by means of the largest singular value s_{max} of the respective FRF or positive output power spectral density matrices. Accordingly, the modal transfer norm has been defined in [122] for the two cases of deterministic, denoted by superscript d, and stochastic input, indicated by superscript s, as

$$MTN^d_{\infty r} = s_{max}\left([H_{mob}(\omega_{r,d})]\right) = s_{max}\left(\frac{1}{e^{\mathrm{i}\omega_{d,r}\,\Delta t} - \lambda_{d,r}}\;\{\psi_r\}\,\{l_{d,r}\}^T\right) \tag{4.9}$$

$$MTN^s_{\infty r} = s_{max}\left(\left[S^+_{\dot{y}\dot{y}}(\omega_{r,d})\right]\right) = s_{max}\left(\left(\frac{1}{e^{\mathrm{i}\omega_{d,r}\,\Delta t} - \lambda_{d,r}} + \frac{1}{2\,\lambda_{d,r}}\right)\{\psi_r\}\,\{g_{d,r}\}^T\right) \tag{4.10}$$

where $\omega_{r,d}$ is the rth natural circular frequency of the damped system while $\{\psi_r\}$ is the corresponding mode shape. The dicrete-time modal participation and operational reference vectors are denoted by $\{l_{d,r}\}$ and $\{g_{d,r}\}$, respectively. Furthermore, the eigenvalues of the discrete-time model $\lambda_{d,r}$ are related to the eigenvalues of the continuous-time model $\lambda_{c,r}$ by

$$\lambda_{d,r} = e^{\lambda_{c,r}\Delta t} = e^{(-\omega_r\zeta_r + \mathrm{i}\,\omega_r\sqrt{1-\zeta_r^2})\Delta t} \tag{4.11}$$

Equations (4.9) and (4.10) refer to the assumption of measured velocities. If a part or all response signals were measured as displacements or accelerations, the corresponding mode shape components have to be, respectively, divided or multiplied by $\lambda_{c,r}$.

In [122] the application of the modal transfer norm is proposed as an indicator in the pole selection process in the sense that solutions related to low MTN values are omitted in the stabilisation diagram. This behaviour is justified with reference to [57] and [132] by pole/zero cancellation in all components of an FRF for spurious solutions.

Moreover, it is suggested to use the MTN as stabilisation criterion or as a measure for mode distinction within the formulation of relative differences:

$$\Delta MTN_{\infty j,k} = \frac{|MTN_{\infty j} - MTN_{\infty k}|}{\max\left(|MTN_{\infty j}|\,,|MTN_{\infty k}|\right)} \tag{4.12}$$

As mentioned above, a combined version of the modal transfer norm has been suggested in [121]. However, due to the fact that the FRF and the positive output power spectral density have not only different physical units but are often also of different orders of magnitude, a combined application of the two criteria (4.9) and (4.10) instead of the application of the combined criterion is recommended in [122].

4.2 Merging of incomplete modal parameter sets

If a structure is monitored over a longer period all sensors are usually installed once and remain at their measurement locations over the whole monitoring period. However, if ambient vibration tests are performed either on-site or in the laboratory within a shorter test campaign, it is common practice to arrange the sensor locations in a number of setups. This procedure has two major practical advantages if conventional vibration sensors are used:

1. It provides the possibility to instrument more measurement points than the technical equipment would allow in a single setup. This means that the number of measurement points is not limited to the number of sensors or channels of a data acquisition system avaliable in a certain institution.
2. Furthermore, it may be far less time consuming to install a reasonable number of sensors with respective cables and to move a part of sensors several times instead of installing the whole equipment for measurements at the same number of locations in a single setup.

In the last decade the application of laser scanning vibrometers for modal analysis has become increasingly popular, especially for laboratory tests. The nature of this technique is that vibrations can be measured subsequently at a large number of points. In most applications laser scanning vibrometry is used together with measured input signals such that the modal parameters can be identified by means of classical experimental modal analysis techniques. However, laser scanning vibrometers have also been used for operational modal analysis as reported, for example in [104], [144], [131]. Several mode merging strategies for the application to data acquired with a 3D laser scanning vibrometer were developed and compared in [94].

Regardless, which type of sensors are used in multi-setup vibration tests, to be able to identify mode shapes that contain modal displacements at all measured degrees-of-freedom it is necessary to define at least one reference sensor which remains at the same location during all tests and a strategy how the incomplete mode shapes obtained from the different setups can be merged to a complete mode shape. Even though it is sufficient to keep the reference sensors at one location for at least two different setups before they can be moved to their next position, as discribed in [86] as jumping frog method, it is probably most common not to change the reference sensors' postions for a whole series of ambient vibration tests. The jumping frog strategy requires a very careful documentation and great caution in the data analysis. Even if it may have advantages such that one can, for example, move the whole measurement equipment more or less together if long bridges are investigated, especially in the case of multi-span bridges it might become difficult to correctly identify all mode shapes which can have close natural frequencies if the reference sensors are moved to locations at which some modes show only very low modal amplitudes.

Even though the jumping frog strategy offers the advantage of reducing the overall testing time it requires great care in the test design, the documentation and the data processing. Therefore the great majority of ambient vibration tests are carried out with fixed reference sensors. Accordingly, this concept is also assumed in the following descriptions of strategies for merging incomplete modal information from different measurement setups. Three different approaches to merge incomplete modal information obtained from multi-setup ambient vibration tests with fixed reference sensors are discussed in the following sections.

In operational modal analysis input signals are not measured. Accordingly, the assumption of stationarity of the excitation for all tests that were performed successively cannot necessarily be verified. Actually, the assumption of non-stationarity is far more likely. As, for example, described in [104] and [105], one can distiquish between the following non-stationarities:

1. excitation level instability,
2. excitation color or mode participation instability and
3. data inconsistency.

While the effect of excitation level instability, which theoretically simply results in different amplitudes of a linear time-invariant system, can be compensated by appropriate scaling of modal components obtained from different setups, the second non-stationarity requires further considerations. Excitation color instability, which refers not only to the frequency content but also to the spacial distribution, leads to a violation of the assumption of equal excitation of all identified modes in any setup and therefore to varying identifiabilities. This may even cause that some modes cannot be identified from some data sets. By means of particular approaches these effects can be taken into account in the analysis.

Data inconsistency means in this context that the fundamental assumption of time-invariability is not satisfied. This means, that the analysed system is subject to inadvertent changes during the tests. Typical examples for such changes are

- mass loading effects, for example due to traffic loads or moving sensors – typical if lightweight structures are investigated,
- changes due to environmental effects such as temperature or humidity changes and
- nonlinearities stimulated, for example by changing excitation level.

These types of non-stationarities are not considered here. It is assumed that the systems behave linearly and are time-invariant over the testing period.

4.2.1 Post separate estimation re-scaling (PoSER) technique

Natural frequencies, modal damping ratios and incomplete mode shapes can be identified from any set of simultaneously acquired time series by means of either method described in chapter 3. After scaling of the incomplete mode shapes with respect to the reference sensors they can be combined to an estimate of the global mode shapes. This procedure, that is named *post separate estimation re-scaling* (PoSER) [91] is graphically illustrated in figure 4.2.

For the scaling procedure, one setup k has to be selected as reference. The modal components $\left\{\psi_{rov,r}^{(j)}\right\}$ identified for the roving sensors from all other setups j are multiplied by a scaling coefficient $\alpha_r^{(j\to k)}$:

$$\left\{\psi_{rov,r}^{(j\to k)}\right\} = \alpha_r^{(j\to k)} \left\{\psi_{rov,r}^{(j)}\right\} \tag{4.13}$$

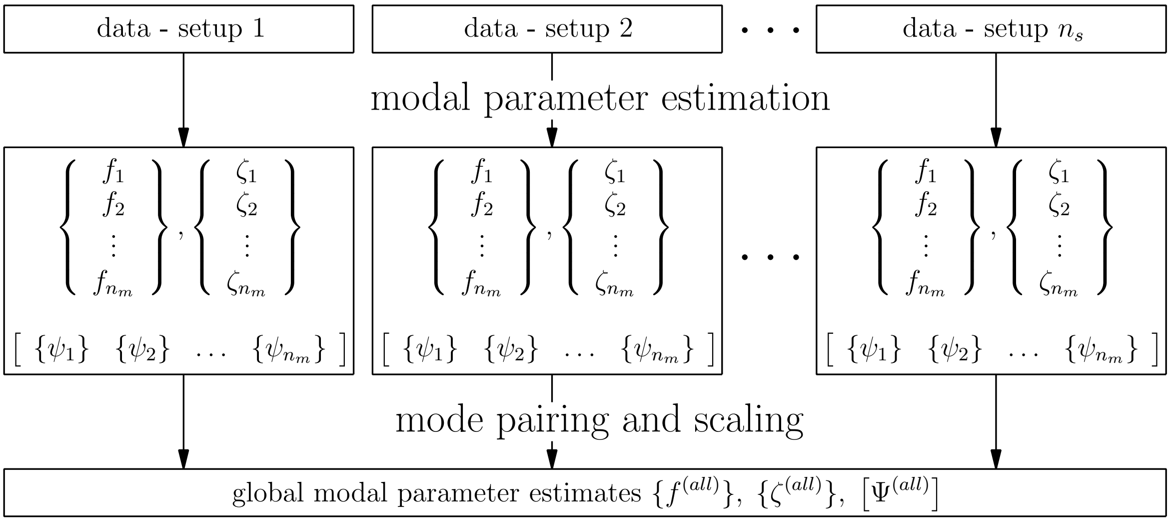

Figure 4.2: Schematic representation of the post separate estimation re-scaling (PoSER) approach

with

$$\alpha_r^{(j\to k)} = \frac{\left\{\psi^{(j)}_{ref,r}\right\}^H \left\{\psi^{(k)}_{ref,r}\right\}}{\left\{\psi^{j}_{ref,r}\right\}^H \left\{\psi^{(j)}_{ref,r}\right\}} \tag{4.14}$$

where the subscripts rov and ref refer to the roving and reference sensors' channels, respectively, while the superscripts in parentheses are related to the setups. The global mode shape estimate of mode r is then formed by the incomplete modal components from n_s setups as

$$\{\psi_{glob,r}\} = \left\{\begin{matrix} \left\{\psi^{(k)}_{ref,r}\right\} \\ \left\{\psi^{(1\to k)}_{rov,r}\right\} \\ \left\{\psi^{(2\to k)}_{rov,r}\right\} \\ \vdots \left\{\psi^{(n_s\to k)}_{rov,r}\right\} \end{matrix}\right\} \tag{4.15}$$

Global estimates of natural frequencies and modal damping ratios can be generated by averaging the results from all setups. Furthermore, the scatter of the estimates can be also considered as a measure of confidence into the respective value.

Apart from the already mentioned difficulties that may arise from a varying identifiability of specific modes, processing and selection of modal solutions from different setups can become elaborate and tedious, especially if many setups were used in the tests and the analyses are not automated. On the other hand, separate processing of the data obtained from different setups allows an insight into uncertainty of modal estimates from single setups or possible systematic changes of modal parameters over the whole test period. If, for example tests are performed over a complete day, changes of the natural frequency due to the temperature development within the structure may be observed.

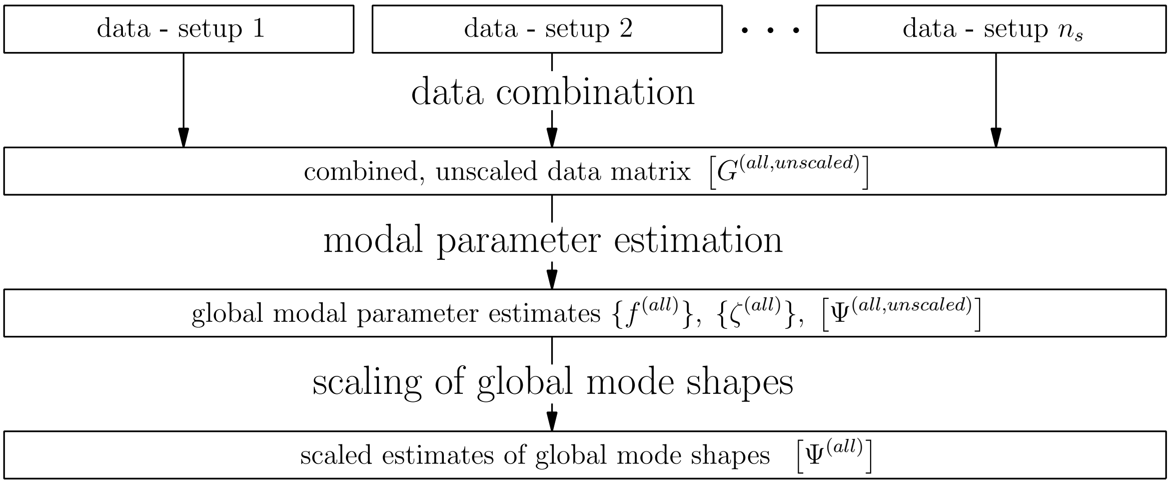

Figure 4.3: Schematic representation of the post global estimation re-scaling (PoGER) approach

4.2.2 Post global estimation re-scaling (PoGER) technique

As described, for example, in [104] and [91], it is also possible to combine power spectral density matrices or correlation matrices from all measured setups to one matrix $\left[G^{(all)}\right]$ to which a respective modal parameter estimation method is applied. The modal vectors contain both reference and roving sensor degrees-of-freedom from all setups. The respective components corresponding to the roving sensors need to be scaled and combined to global mode shapes according to the procedure in equations (4.13) to (4.15) after selecting one setup as reference setup. This approach is also named *post global estimation re-scaling* (PoGER) technique and illustrated in figure 4.3.

A clear advantage of the PoGER algorithm is that only a single stabilisation diagram is created and analyzed. Problems with a weak identification of specific modes from single setups due to insufficient excitation or inappropriate sensor placement may be compensated by a good identifiability from data acquired in other setups.

On the other hand the matrices to be used for modal identification become very large and may cause memory problems. However, this issue will become decreasingly important with the development of increasingly powerful computer technology. Another disadvantage of the global analysis of data from all setups is that uncertainties of the analysis cannot be quantified with respect to individual setups without further considerations.

4.2.3 Pre global estimation re-scaling (PreGER) technique

Instead of applying the re-scaling to the identified mode shapes at the end of the analyses, one can also apply scsaling within the process of data assembling into respective matrices required for a particular modal identification method. In [104] and [91] this strategy is called *pre global estimation re-scaling* (PreGER). The general procedure is visualised in figure 4.4.

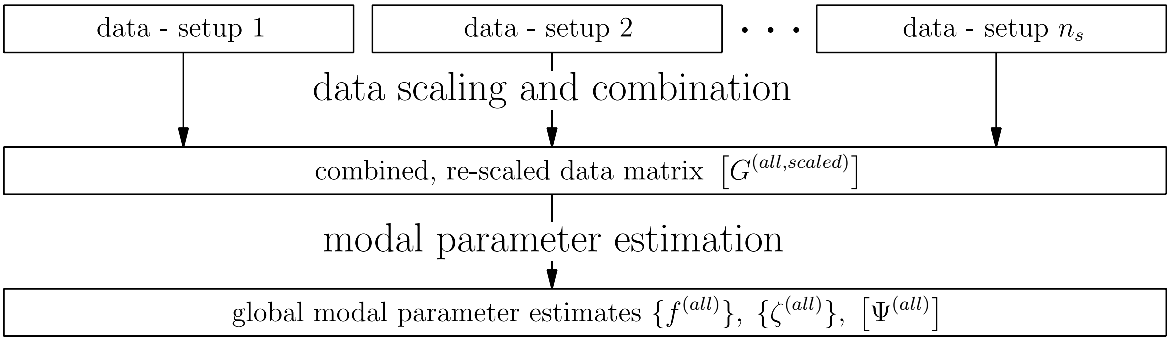

Figure 4.4: Schematic representation of the pre global estimation re-scaling (PreGER) approach

If the scaling of the measured data, that is necessary if the excitation of the structure cannot be assumed as stationary over all setups, is performed prior to the modal parameter estimation, the specifics of the applied identification algorithm have to be taken into account. For modal analyses in frequency-domain that are based on spectral density matrices an approach for scaling and assembly of a global re-scaled spectral density matrix has been proposed in [104] and [105]. Assuming that one setup k has been chosen as reference setup, the cross spectral densities corresponding to the roving sensors obtained from setup j, $\left[S_{rov}^{(j)}(\omega)\right]$, can be scaled with respect to the reference setup by means of the cross spectral densities related to the reference sensors obtained from setup j, $\left[S_{ref}^{(j)}(\omega)\right]$, as

$$\left[S_{rov}^{(j\rightarrow k)}(\omega)\right] = \left[S_{rov}^{(j)}(\omega)\right] \left[S_{ref}^{(j)}(\omega)\right]^{-1} \left[S_{ref}^{(k)}(\omega)\right] \tag{4.16}$$

To reduce the risk that the quality of the identified global modal parameters suffers from poor spectral estimates of an arbitrarily chosen reference setup k due to non-stationarities, the reference $\left[S_{ref}^{(k)}(\omega)\right]$ in equation (4.16) can be replaced by an average of the cross spectral densities of all n_s setups.

$$\left[S_{rov}^{(j\rightarrow \Sigma)}(\omega)\right] = \left[S_{rov}^{(j)}(\omega)\right] \left[S_{ref}^{(j)}(\omega)\right]^{-1} \frac{1}{n_s} \sum_{k=1}^{n_s} \left[S_{ref}^{(k)}(\omega)\right] \tag{4.17}$$

This choice is also supposed to result in a generally higher signal-to-noise ratio of the re-scaled data matrices [104], [105]. The global re-scaled cross spectral density matrix $\left[S^{(all\rightarrow\Sigma)}(\omega)\right]$ is then formed by stacking the reference cross spectral densities and those obtained for the roving sensors' data of all setups after respective scaling.

$$\left[S^{(all\rightarrow\Sigma)}(\omega)\right] = \begin{bmatrix} \frac{1}{n_s}\sum_{k=1}^{n_s}\left[S_{ref}^{(k)}(\omega)\right] \\ \left[S_{rov}^{(1\rightarrow\Sigma)}(\omega)\right] \\ \left[S_{rov}^{(2\rightarrow\Sigma)}(\omega)\right] \\ \vdots \\ \left[S_{rov}^{(n_s\rightarrow\Sigma)}(\omega)\right] \end{bmatrix} \tag{4.18}$$

An algorithm for scaling the respective entries into the block Hankel or block Toeplitz matrix used in the covariance-driven stochastic subspace method has been suggested in [95] and [96]. It is based on the scaling of the covariances calculated from all setups by means of controllability matrices related to the respective setup and a controllability matrix that has been computed from a selected reference setup. A clarification of this algorithm has been given in [47].

The algorithm that was originally derived for the covariance-driven stochastic subspace identification (SSI-cov) has been extended to its applicability to the data-driven stochastic subspace identification (SSI-data) in [43]. In both cases, the merging algorithms lead to global Hankel or Toeplitz matrices which are the base for a global modal parameter estimation by means of a respective SSI method.

A very thorough discussion of merging strategies can be found in [42]. There the previously mentioned algorithms were generalised for any subspace algorithm. Furthermore, several algorithms were derived to improve the computational performance. Additional extensions of the algorithms lead to one merging algorithm that does not provide a global Hankel matrix but already a global extended observability matrix – algorithm 4.4 in [42], algorithm 2 in [45]. For the case that a large number of sensors and a large number of setups were used during the tests, an algorithm which results in the estimate of global system matrices of the state-space model $[A]$, $[C]$ – algorithm 4.5 – is recommended in [42]. In the following the algorithm that produces an estimate of the global extended observability matrix $\left[O_i^{(all)}\right]$ in an implementation for the SSI-cov/ref method is explained.

Similarly as in the procedure described by equations (4.16) to (4.18), the information corresponding to roving sensors of any setup will be scaled with respect to the reference sensors' information from a single setup. Therefore, it is assumed that the block Toeplitz matrix related to any setup j

$$\left[T_{1|i}^{(j)}\right] = \begin{bmatrix} \left[R_i^{(j)}\right] & \left[R_{i-1}^{(j)}\right] & \dots & \left[R_1^{(j)}\right] \\ \left[R_{i+1}^{(j)}\right] & \left[R_i^{(j)}\right] & \dots & \left[R_2^{(j)}\right] \\ \vdots & \vdots & \dots & \vdots \\ \left[R_{2i-1}^{(j)}\right] & \left[R_{2i-2}^{(j)}\right] & \dots & \left[R_i^{(j)}\right] \end{bmatrix} \tag{4.19}$$

is constructed by covariance matrices with the channels sorted in a way that the n_{ref} reference and the n_{rov} roving sensors' covariances are summarised in respective subblocks:

$$\left[R_h^{(j)}\right] = \begin{array}{c c} \overleftrightarrow{\;n_{ref}\;} & \\ \left[\begin{array}{c} \left[R_h^{(j,ref)}\right] \\ \hline \left[R_h^{(j,rov)}\right] \end{array}\right] & \begin{array}{l} \updownarrow n_{ref} \\ \updownarrow n_{rov} \end{array} \end{array} \tag{4.20}$$

According to equations (3.66) to (3.68), an estimate of the extended observability matrix is obtained from a singular value decomposition of the block Toeplitz matrix:

$$\left[T_{1|i}^{(j)}\right] = \left[U^{(j)}\right]\left[S^{(j)}\right]\left[V^{(j)}\right]^T = \begin{bmatrix} \left[U_1^{(j)}\right] & \left[U_2^{(j)}\right] \end{bmatrix} \begin{bmatrix} \left[S_1\left[U_1^{(j)}\right]\right] & [0] \\ [0] & [0] \end{bmatrix} \begin{bmatrix} \left[V_1^{(j)}\right]^T \\ \left[V_2^{(j)}\right]^T \end{bmatrix} \tag{4.21}$$

as

$$\left[O_i^{(j)}\right] = \left[W_1^{(j)}\right]\left[U_1^{(j)}\right]\left[S_1^{(j)}\right]^{\frac{1}{2}} = \begin{bmatrix} \left[C^{(j)}\right] \\ \left[C^{(j)}\right]\left[A^{(j)}\right] \\ \vdots \\ \left[C^{(j)}\right]\left[A^{(j)}\right]^{i-1} \end{bmatrix} \tag{4.22}$$

with the weighting matrix $\left[W_1^{(j)}\right]$ which is often chosen to be the identity matrix. As the model order is not known, one can select the dimensions of $\left[U_1^{(j)}\right]$ and $\left[S_1^{(j)}\right]$ such that they correspond to the largest model order to be taken into account in a stabilisation diagram. To obtain later the extended observability matrix for a specific model order p, one has only to extract the first p columns of $\left[O_i^{(j)}\right]$.

The block rows of the extended observability matrix are sorted in the same way as those of the block Toeplitz matrix which means that, for example, the first block row can be written as

$$\left[C^{(j)}\right] = \left[\begin{array}{c} \left[C^{(j,ref)}\right] \\ \hline \left[C^{(j,rov)}\right] \end{array}\right] \tag{4.23}$$

This structure allows for a dissambling of the extended observability matrix into two parts which are related to the reference and roving sensors, respectively:

$$\begin{tikzcd} \left[O_i^{(j)}\right] \arrow[r] \arrow[dr] & \left[O_i^{(j,ref)}\right] \\ & \left[O_i^{(j,rov)}\right] \end{tikzcd}$$

where

$$\left[O_i^{(j,ref)}\right] = \begin{bmatrix} \left[C^{(j,ref)}\right] \\ \left[C^{(j,ref)}\right]\left[A^{(j,ref)}\right] \\ \vdots \\ \left[C^{(j,ref)}\right]\left[A^{(j,ref)}\right]^{i-1} \end{bmatrix} \quad \text{and} \quad \left[O_i^{(j,rov)}\right] = \begin{bmatrix} \left[C^{(j,rov)}\right] \\ \left[C^{(j,rov)}\right]\left[A^{(j,rov)}\right] \\ \vdots \\ \left[C^{(j,rov)}\right]\left[A^{(j,rov)}\right]^{i-1} \end{bmatrix} \tag{4.24}$$

After having selected one setup k as reference setup, the roving sensor-related extended observability matrices of all other $n_s - 1$ setups are re-scaled with respect to setup k:

$$\left[O_{i,RS}^{(j,rov)}\right] = \left[O_i^{(j,rov)}\right]\left[O_i^{(j,ref)}\right]^{\dagger}\left[O_i^{(k,ref)}\right] \tag{4.25}$$

such that a global extended observability matrix that contains information related to all sensor locations can be assembled as

$$\left[O_{i,RS}^{(all)}\right] = \begin{bmatrix} \left[C^{(all)}\right] \\ \left[C^{(all)}\right]\left[A^{(all)}\right] \\ \vdots \\ \left[C^{(all)}\right]\left[A^{(all)}\right]^{i-1} \end{bmatrix} \tag{4.26}$$

with

$$\left[C^{(all)}\right] = \begin{bmatrix} \left[C^{(k,ref)}\right] \\ \left[C^{(1,rov)}\right] \\ \left[C^{(2,rov)}\right] \\ \vdots \\ \left[C^{(n_s,rov)}\right] \end{bmatrix} \quad \text{and} \quad \left[A^{(all)}\right] = \begin{bmatrix} \left[A^{(k,ref)}\right] \\ \left[A^{(1,rov)}\right] \\ \left[A^{(2,rov)}\right] \\ \vdots \\ \left[A^{(n_s,rov)}\right] \end{bmatrix} \tag{4.27}$$

The global modal parameters are then identified from the global extended observability matrix $\left[O_{i,RS}^{(all)}\right]$ in the same way as described in section 3.2.4.1. Even though this is not mentioned in [42] and [45], one can also perfom the re-scaling with respect to an average of the matrices $\left[O_i^{(j,ref)}\right]$ rather than to $\left[O_i^{(k,ref)}\right]$ that is related to an arbitrarily chosen setup k.

It is remarked that the pre global estimation re-scaling (PreGER) approach has the same advantages and limitations as the post global estimation re-scaling (PoGER) strategy. However, the global matrix from which the modal parameters are extracted in the PreGER technique has a smaller dimension because only one set of rows corresponding to the reference sensors are contained while the global matrix used in the PoGER algorithm contains the complete information of all sensors from each setup.

In [47] the different merging strategies were applied to the modal parameter estimation of a large bridge. In their conclusions the authors attest similar performance of both PoGER and PreGER algorithms. Similar studies were described in [104]. A slightly better performance of the PreGER technique was observed there in the case that not the reference sensor cross spectral densities of a specific setup but the averaged cross spectral densities from all setups were used for the re-scaling.

4.3 Visualisation of mode shapes

Mode shapes can be interpreted as deflection shapes of a structure vibrating at specific resonance frequencies. This means that each mode is connected to specific geometrical characteristics of the vibration. These characteristics are of importance for engineers since modal deflections are, for example, also related to internal stresses that can, in the extreme case, even lead to damage. Accordingly, a graphical representation of mode shapes is very valuable in engineering.

From a modal parameter estimation usually complex mode shapes are obtained. They are either represented by their real and imaginary parts or by their magnitudes and phase angles. In case of real modes the phase angle at a specific degree-of-freedom is either 0° or 180° which means that all degrees-of-freedom pass through their amplitudes at the same time. However, if a mode is complex, the phase angles deviate usually from these values which means that the maximal displacements are reached at different degrees-of-freedom at different instants of time. The only way to visualise such characteristics appropriately in context with the geometry of the structure is an animation.

Even though such animations can be very nicely presented by computer applications, results of a study are usually disseminated in form of reports that do not provide the inclusion of moving pictures. Therefore, the common way of illustrating mode shapes are static plots of the deformed structure. This procedure requires a real-valued representation of the complex mode shapes.

Several approaches for the realisation of complex modes can be found in literature. A short overview as well as further analyses with respect to relations between real-valued approximations $[\Psi_R]$ and the respective complex modes $[\Psi_C]$ by a linear transformation

$$[\Psi_R] \,=\, [\Psi_C]\,[T] \tag{4.28}$$

as it was, according to [72], proposed in [100], are, for example, given in [71]. Many of them were actually motivated by the demand of a possibility to compare mode shapes identified from tests with those computed for a numerical model. Since numerical modal solutions are in most cases related to an undamped system, the computed mode shapes are normally real vectors.

One possiblity to plot a mode shape, especially for weakly damped systems for which the phase angles deviate only very slightly from 0° or 180° is to scale the magnitudes of the complex mode shapes by the cosine of the phase angle. This results in a picture looking like a snapshot taken from an animation.

A more rigorous approach is to multiply the magnitude values of a complex mode shape by the sign of the phase angle's cosine which means that all phase angles $-90° < \theta < 90°$ are forced to a phase angle of 0° while those components with $-180° \leq \theta \leq -90°$ or $90° \leq \theta \leq 180°$ are assigned to a phase angle of 180°. Even though this is a very rough approximation it is acceptable for lightly damped systems and has been widely used. In [72] it is even called the *standard method*.

Another possibility to represent a transformation in the sense of equation (4.28)is, to form the sum of the real part of the complex modal matrix and a correction matrix [72]:

$$[\Psi_R] \,=\, \mathrm{Re}\,[\Psi_C] \,+\, \mathrm{Im}\,[\Psi_C]\left[\mathrm{Re}\,[\Psi_C]^T\,\mathrm{Re}\,[\Psi_C]\right]^{-1}\mathrm{Re}\,[\Psi_C]^T\,\mathrm{Im}\,[\Psi_C] \tag{4.29}$$

As a measure of correlation between a complex mode shape and its realised eigenvector, the modal assurance criterion between the two vectors can be employed:

$$MAC\left(\psi_R,\psi_C\right) \,=\, \frac{\left|\{\psi_R\}^T\,\{\psi_C^*\}\right|^2}{\{\psi_R\}^T\,\{\psi_R\}\,\{\psi_C\}^T\,\{\psi_C^*\}} \tag{4.30}$$

In [72] is suggested to replace the approximation of a realised mode shape $\{\psi_R\}$, which may have been generated by any approach, by an improved approximation that consists of the original approximation and a correction vector $\{\epsilon\} \,=\, f_\gamma\,\{\gamma\}$

$$\{\psi_R\} \,+\, \{\epsilon\} \tag{4.31}$$

where $\{\gamma\}$ is an arbitrary real vector and f_γ denotes a scalar coefficient. Equation (4.30) becomes then

$$MAC\left(\psi_R+\epsilon,\psi_C\right) \,=\, \frac{\left|\{\psi_R\}^T\,\{\psi_C^*\} \,+\, f_\gamma\,\{\gamma\}^T\,\{\psi_C^*\}\right|^2}{\left(\{\psi_R\}^T\,\{\psi_R\}+2f_\gamma\,\{\gamma\}^T\,\{\psi_R\}+f_\gamma^2\,\{\gamma\}^T\,\{\gamma\}\right)\,\left(\{\psi_C\}^T\,\{\psi_C^*\}\right)} \tag{4.32}$$

which can be transformed into a polynomial fraction in f_γ:

$$MAC\left(\psi_R+\epsilon,\psi_C\right) \,=\, \frac{A \,+\, Bf_\gamma \,+\, Cf_\gamma^2}{D \,+\, Ef_\gamma \,+\, Ff_\gamma^2} \tag{4.33}$$

with

$$\begin{aligned} A &= z_1\, z_1^* & D &= \{\psi_R\}^T \{\psi_R\}\; z_3 \\ B &= z_1 z_2^* + z_1^* z_2 & E &= 2\,\{\gamma\}^T \{\psi_R\}\; z_3 \\ C &= z_2 z_2^* & F &= \{\gamma\}^T \{\gamma\}\; z_3 \end{aligned}$$

and

$$z_1 = \{\psi_R\}^T \{\psi_C^*\} \qquad z_2 = \{\gamma\}^T \{\psi_C^*\} \qquad z_3 = \{\psi_C\}^T \{\psi_C^*\}$$

To identify the coefficient f_γ such that the correlation between the two vectors $\{\phi_R\}$ and $\{\phi_C\}$ becomes maximal, the respective partial derivative of equation (4.33) has to be set to zero:

$$\frac{\partial MAC\left(\psi_R + \epsilon, \psi_C\right)}{\partial f_\gamma} = \frac{(CE - BF)\, f_\gamma^2 \;+\; 2\,(CD - AF)\, f_\gamma \;+\; (BD - AE)}{\left(D + E f_\gamma + F f_\gamma^2\right)^2} = 0 \tag{4.34}$$

Provided that the denominator is non-zero, the coefficient f_γ is obtained by solving the quadratic numerator polynomial

$$f_{\gamma_{1,2}} = \frac{(AF - CD)}{(CE - BF)} \pm \sqrt{\frac{(AF - CD)^2}{(CE - BF)^2} - \frac{(BD - AE)}{(CE - BF)}} \tag{4.35}$$

Whether or not an improvement of an approximation $\{\psi_R\}$ can be achieved by the described procedure depends also on the choice of vector $\{\gamma\}$. In [72] the use of

$$\gamma_i = \frac{|\psi_{C,i}|}{\cos\theta_i} \tag{4.36}$$

for the ith element of vector $\{\gamma\}$ was proposed. To find the maximal correlation between complex and realised mode shapes, the described enhancing procedure can be embedded within an optimisation which iteratively selects $\{\gamma\}$ and calculates the corresponding coefficient f_γ.

A transformation procedure for mode shape realisation that is based on the equation of motion and its state space representaion was suggested in [53] and [54]. The concept of this approach starts from extracting a part from the eigenvalue problem of the state space formulation described by equation (2.38)

$$\left[\; [M]^{-1}[K] \quad [M]^{-1}[C_2] \;\right] \left[\begin{array}{ccc} \{\psi_1\} & \dots & \{\psi_N\} \\ \lambda_1\{\psi_1\} & \dots & \lambda_N\{\psi_N\} \end{array} \right] = -\left[\; \lambda_1^2\{\psi_1\} \quad \dots \quad \lambda_N^2\{\psi_N\} \;\right] \tag{4.37}$$

The corresponding eigenvalue problem of the undamped system (2.4) can be re-written as

$$[M]^{-1}[K]\;\{\phi_r\} = \omega_r^2\;\{\phi_r\} \tag{4.38}$$

From a modal parameter identification the complex eigenvectors $\{\psi_r\}$ with their eigenvalues λ_r and the natural circular frequencies ω_r are available. The result of a mode shape realisation should correspond to the eigenvector $\{\phi_r\}$ in equation (4.38). By comparing equations (4.37) and (4.38) it becomes obvious that the matrix $[M]^{-1}[K]$ is a common element. If this matrix could be identified from the estimates of the complex mode shapes and eigenvalues by means of equation (4.37) it would be possible to obtain realised mode shapes as the solution of the eigenvalue problem (4.38). However, this would require that the part of the modal matrix that is available from modal parameter estimation is invertible which is generally not the case. Therefore an algorithm that uses a so-called *modal truncation* to overcome this problem is suggested in [53] and [54].

Provided that the number of sensors n_o, or instrumented degrees-of-freedom, is larger than the number of identified modes, which is indeed the case in many practical applications, a transformation matrix $[T]$ can be obtained from the left singular vectors of the singular value decomposition of the identified n_m mode shapes' real parts.

$$\left[\begin{array}{cccc} \mathrm{Re}\{\psi_1\} & \mathrm{Re}\{\psi_2\} & \dots & \mathrm{Re}\{\psi_{n_m}\} \end{array}\right] = [U]\,[S]\,[V]^T \tag{4.39}$$

Matrix $[T]_{n_o \times n_m}$ consists of the first n_m columns of matrix $[U]$ and has the property

$$[T]^T\,[T] = [I]$$

It is used to transform the complex modal vectors from physical to reduced coordinates:

$$\left\{\tilde{\psi}_r\right\} = [T]^T\,\{\psi_r\} \tag{4.40}$$

With these complex modal vectors in reduced coordinates, equation (4.37) can be re-written as

$$\underbrace{\left[\begin{array}{cc} \left[\tilde{M}\right]^{-1}\left[\tilde{K}\right] & \left[\tilde{M}\right]^{-1}\left[\tilde{C}_2\right] \end{array}\right]}_{\left[\tilde{A}^{\downarrow}\right]} \left[\begin{array}{ccc} \left\{\tilde{\psi}_1\right\} & \dots & \left\{\tilde{\psi}_N\right\} \\ \lambda_1\left\{\tilde{\psi}_1\right\} & \dots & \lambda_N\left\{\tilde{\psi}_N\right\} \end{array}\right] = -\left[\begin{array}{ccc} \lambda_1^2\{\psi_1\} & \dots & \lambda_N^2\{\psi_N\} \end{array}\right] \tag{4.41}$$

which can be solved for $\left[\tilde{A}^{\downarrow}\right]$. Matrix $\left[\tilde{M}\right]^{-1}\left[\tilde{K}\right]$ which is obtained as the first n_m columns of $\left[\tilde{A}^{\downarrow}\right]$ is subsequently used to solve the eigenvalue problem

$$\left[\tilde{M}\right]^{-1}\left[\tilde{K}\right]\left\{\tilde{\phi}_r\right\} = \tilde{\omega}_r^2\left\{\tilde{\phi}_r\right\} \tag{4.42}$$

In the last step the real modal vectors in reduced coordinates are extended to physical coordinates by means of the transformation matrix $[T]$

$$\left\{\tilde{\psi}_{R_r}\right\} = [T]\left\{\tilde{\phi}_r\right\} \tag{4.43}$$

It is important that the real parts of the complex eigenvectors, which are used to compute the transformation matrix, contain sufficient information about the mode shapes [54]. In this context is recommended to scale the complex modes prior to the realisation such that the respective largest component is $1 + 0\mathrm{i}$. Furthermore, one indicator for the consistency of an analysis according to this algorithm is the agreement between the identified natural circular frequency ω_r and $\tilde{\omega}_r$ which is obtained as solution of the eigenvalue problem of the reduced system.

4.4 Uncertainty quantification

In experimental and operational modal analyses an absolutely true result is not available. All results are estimates with some degree of uncertainty. To obtain an impression how confidable the estimates of modal parameters are, the uncertainties have to be quantified.

Usually uncertainty is expressed by means of statistical values such as variance or its square root, the standard deviation. A statistical analysis normally requires a representatively large number of samples of a random variable. However, from a single test only one data set is available. In this case the term *uncertainty* requires further specification.

One possible interpretation is that one has identified a certain number of estimates for the same mode, for example from different model orders corresponding to a certain parametric identification method. These solutions for one mode are collected in a so-called cluster, a concept which will be enlarged upon in context with automated operational modal analyses in chapter 5. Of course, it is then possible to compute mean values and standard deviations of the respective modal parameters as described, for example in [142].

But this interpretation does not provide information about the quality of any single estimate of modal parameters which belongs to the considered cluster. A quantified information about the uncertainties of any identified frequency, modal damping ratio and mode shape corresponding to a certain model order would be very useful. Measures as the variance of an identified natural frequency can be used in further analyses such as a stochastic updating of finite element models or the evaluation of modal parameter fluctuations due to, for example, environmental or service conditions.

Since modal parameter estimation involves in most cases several stages, uncertainties are inherited from one step of analysis to the next. Therefore the uncertainties of a parameter at final stage, meaning natural frequencies, modal damping ratios and mode shapes, depend basically on two factors:

1. the uncertainties at the individual stages of analysis, quantified by respective covariances, and
2. the sensitivities, which express to which extent a functional value varies due to a small change of a variable it depends on, of intermediate results at a certain stage of analysis with respect to the output of a previous computational step.

An algorithm for the quantification of uncertainty propagation in modal parameter estimation by means of ARMA models was developed in [4] and [5]. In [112] the computation of covariances of modal parameters identified based on a common denominator frequency-domain model were described continuing the derivations presented in [61].

For the covariance-driven stochastic subspace identification a procedure for the computation of uncertainties in modal parameter estimation has been derived in [123]. Using the results of this algorithm, computational schemes that are more efficient and can also be applied to other stochastic subspace identification methods were evolved in [46].

All algorithms mentioned so far were developed for single setup analyses. An extension that allows the application to analyses of multiple setups by means of the SSI-PreGER methodology, as developed in [42], [45] and described in section 4.2.3, was proposed in [44].

In the following an algorithm is described that quantifies the uncertainties within a modal parameter estimation by means of stochastic subspace identification according to [46] and its application within the analysis of multiple setups as suggested in [44].

4.4.1 Algorithm to quantify uncertainties of modal parameters obtained from a single setup by means of SSI

Step 1: Covariance estimation for the subspace matrix

The covariance matrix of the respective subspace matrices used in different SSI methods are computed based on dividing the measured time series into n_b statistically independent blocks of length j_b such that $n_b \cdot j_b = j$, where j denotes the length of the blocks used in the respective SSI algorithm. In case of the data-driven SSI, j equals the number of columns of the block Hankel matrix $\left[Y_{0|2i-1}\right]$ whereas it is the number of samples taken into account for the computation of the block covariance matrices in SSI-cov.

Reference-based data-driven SSI (SSI-data/ref)

Instead of generating the respective Hankel matrices for each of the n_b data blocks separately, they can also be obtained by splitting matrix $\left[Y_{0|2i-1}\right]$ into blocks with j_b columns each:

$$\left[Y_{0|2i-1}\right] = \Big[\ \overbrace{\overbrace{[Y_1]}^{j_b}\ \ \overbrace{[Y_2]}^{j_b}\ \ \dots\ \ \overbrace{[Y_{n_b}]}^{j_b}}^{j_b}\ \Big] \tag{4.44}$$

For each of these blocks respective covariance matrices $\left[\widehat{\Sigma}_{Y_k}\right]$ can be computed. The estimate of the covariance matrix of the subspace matrix $\left[Y_{0|2i-1}\right]$ is then computed as the covariance of the sample mean of the n_b covariance matrices

$$\left[\widehat{\Sigma}_{Y_{0|2i-1}}\right] = \frac{1}{n_b(n_b-1)} \sum_{k=1}^{n_b} \left(\left[\left[\widehat{\Sigma}_{Y_k}\right] - \left[\overline{\widehat{\Sigma}}_{Y_k}\right]\right] \left[\left[\widehat{\Sigma}_{Y_k}\right] - \left[\overline{\widehat{\Sigma}}_{Y_k}\right]\right]^T \right) \tag{4.45}$$

with the mean of the n_b covariance matrices

$$\left[\overline{\widehat{\Sigma}}_{Y_k}\right] = \frac{1}{n_b} \sum_{k=1}^{n_b} \left[\widehat{\Sigma} Y_k\right] \tag{4.46}$$

Reference-based covariance-driven SSI (SSI-cov/ref)

Similarly as described in the previous section for the subspace matrix of the SSI-data algorithm, n_b block Toeplitz matrices $\left[\widehat{T}^{ref}_{1|i-1,k}\right]$ containing the covariances between a set of measured reference signals and the shifted time series of all sensors can be estimated based on signal blocks of length j_b rather than j where again $n_b \cdot j_b = j$. The mean block Toeplitz matrix is then obtained as

$$\left[\overline{\widehat{T}}^{ref}_{1|i-1}\right] = \frac{1}{n_b} \sum_{k=1}^{n_b} \left[\widehat{T}^{ref}_{1|i-1,k}\right] \tag{4.47}$$

Introducing the vec(·) operator, that stacks the columns of a matrix, a covariance estimate of the block Toeplitz matrix can be computed as

$$\left[\widehat{\Sigma}_{T^{ref}_{1|i-1}}\right] = \frac{1}{n_b(n_b-1)} \sum_{k=1}^{n_b} \left(\left\{ \mathrm{vec}\left(\left[\widehat{T}^{ref}_{1|i-1,k}\right] - \left[\overline{\widehat{T}}^{ref}_{1|i-1}\right] \right) \right\} \left\{ \mathrm{vec}\left(\left[\widehat{T}^{ref}_{1|i-1,k}\right] - \left[\overline{\widehat{T}}^{ref}_{1|i-1}\right] \right) \right\}^{T} \right) \tag{4.48}$$

After the construction of the respective subspace matrix which means

- for SSI-data the projection

  $$[\mathcal{H}_{data}] = [\mathcal{P}_i] = [Y_f] \,/\, [\mathbf{Y_p}] = [Y_f]\,[Y_p]^T \left[[Y_p]\,[Y_p]^T\right]^{\dagger} [Y_p]$$

  and

- for SSI-cov the block Toeplitz matrix

  $$[\mathcal{H}_{cov}] = \left[T^{ref}_{1|i-1,k}\right]$$

the algorithms follow the same operations. Therefore, the *subspace matrices* are not distinguished any more and receive the common notation $[\mathcal{H}]$ in the following.

Step 2: Covariance estimation for the system matrices $[A]$ and $[C]$

Since the system matrices $[A]$ and $[C]$ are derived from the observability matrix $[O_i]$, first the propagation of a *perturbation* $\Delta\,[\mathcal{H}]$ to a perturbation $\Delta\,[O_i]$ of the observability matrix is investigated. The following descriptions follow as well the derivations in [46] which are based on [112] and [123].

The vectorised perturbations of the observability matrix due to small perturbations of the subspace matrix are expressed by means of the *sensitivity matrix* $[J_{O_i,\mathcal{H}}]$:

$$\mathrm{vec}\left(\Delta\,[O_i]\right) = [J_{O_i,\mathcal{H}}]_{(i+1)n_o n\times(i+1)n_o j n_{ref}}\ \Delta\,[\mathcal{H}] \tag{4.49}$$

where

- i = number of block rows of $[\mathcal{H}]$
- j = number of block columns of $[\mathcal{H}]$
- n = respective model order
- n_o = number of all sensors
- n_{ref} = number of reference sensors

To obtain the sensitivity matrix for a certain model order n, the singular values s_k together with the respective left and right singular vectors $\{u_k\}$ and $\{v_k\}$ are required.

$$\begin{aligned} [J_{O_i,\mathcal{H}}] \; = \; & \tfrac{1}{2}\left[[I]_n \otimes [U_1]\,[S_1]^{-\frac{1}{2}}\right][\mathcal{S}_4]\begin{bmatrix} \{\{v_1\}\otimes\{u_1\}\}^T \\ \vdots \\ \{\{v_n\}\otimes\{u_n\}\}^T \end{bmatrix} \\ & + \left[[S_1]^{\frac{1}{2}}\right] \otimes \begin{bmatrix} [I]_{(i+1)n_o} & [0]_{(i+1)n_o \times j n_{ref}} \end{bmatrix} \begin{bmatrix} [B_1]^{\dagger}\,[C_1] \\ \vdots \\ [B_n]^{\dagger}\,[C_n] \end{bmatrix} \end{aligned} \tag{4.50}$$

where $\otimes$ denotes the *Kronecker product* as described, for example, in [18], [119]. The *selection matrix* $[\mathcal{S}_4]$ is given by

$$[\mathcal{S}_4] \; = \; \sum_{k=1}^{n}\left[\mathcal{E}^{n^2,n}_{(k-1)n+k,k}\right] \tag{4.51}$$

where a matrix $\left[\mathcal{E}^{a,b}_{l,m}\right]$ is defined as a matrix of dimension $a \times b$ that is zero apart from element (l,m) which is 1.

Similar to equation (4.49), the propagation of perturbations in the observability matrix $[O_i]$ to the system matrices $[A]$ and $[C]$ can be described by

$$\mathrm{vec}\,(\Delta\,[A]) \; = \; [J_{A,O_i}]_{n^2 \times (i+1)n_o n}\;\Delta\,[O_i] \tag{4.52}$$

and

$$\mathrm{vec}\,(\Delta\,[C]) \; = \; [J_{C,O_i}]_{n_o n \times (i+1)n_o n}\;\Delta\,[O_i] \tag{4.53}$$

with the sensitivity matrices

$$\begin{aligned} [J_{A,O_i}] \; = \; & \left([I]_n \otimes \left[O_i^{\uparrow}\right]^{\dagger}[\mathcal{S}_2]\right) - \left([A]^T \otimes \left[O_i^{\uparrow}\right]^{\dagger}[\mathcal{S}_1]\right) \\ & + \left(\left[\left[O_i^{\downarrow}\right]^T[\mathcal{S}_2] - [A]^T\left[O_i^{\uparrow}\right]^T[\mathcal{S}_2]\right] \otimes \left[\left[O_i^{\uparrow}\right]^T\left[O_i^{\uparrow}\right]\right]^{-1}\right)\left[\mathcal{P}_{(i+1)n_o,n}\right] \end{aligned} \tag{4.54}$$

$$[J_{C,O_i}] = [I]_n \otimes \begin{bmatrix} [I]_{n_o} & [0]_{n_o \times n_o i} \end{bmatrix} \tag{4.55}$$

The selection matrices $[\mathcal{S}_1]$, $[\mathcal{S}_2]$ and the *permutation matrix* $[\mathcal{P}_{a,b}]$ are defined as

$$[\mathcal{S}_1] \; = \; \begin{bmatrix} [I]_{n_o i} & [0]_{n_o i \times n_o} \end{bmatrix} \tag{4.56}$$

$$[\mathcal{S}_2] \; = \; \begin{bmatrix} [0]_{n_o i \times n_o} & [I]_{n_o i} \end{bmatrix} \tag{4.57}$$

$$[\mathcal{P}_{a,b}] \; = \; \sum_{l=1}^{a}\sum_{m=1}^{b}\left[\mathcal{E}^{a,b}_{l,m}\right] \otimes \left[\mathcal{E}^{b,a}_{m,l}\right] \tag{4.58}$$

while matrices $\left[O_i^{\uparrow}\right]$ and $\left[O_i^{\downarrow}\right]$ are extracted from the observability matrix as

$$\left[O_i^{\uparrow}\right] = \begin{bmatrix} [C] \\ [C]\,[A] \\ \vdots \\ [C]\,[A]^{p-1} \end{bmatrix} \qquad \left[O_i^{\downarrow}\right] = \begin{bmatrix} [C]\,[A] \\ [C]\,[A]^2 \\ \vdots \\ [C]\,[A]^{p} \end{bmatrix} \tag{4.59}$$

An estimate of the covariances of the vectorized system matrices $[A]$ and $[C]$ can be computed by means of the subspace matrix' covariance matrix and the sensitivity matrices defined in equations (4.50), (4.54),(4.55):

$$[\Sigma_{A,C}] = \operatorname{cov}\left(\left[\begin{array}{c} \operatorname{vec}([A]) \\ \operatorname{vec}([C]) \end{array}\right]\right) = \left[\begin{array}{c} [J_{A,O_i}] \\ [J_{C,O_i}] \end{array}\right] [J_{O_i,\mathcal{H}}]\,[\Sigma_{\mathcal{H}}]\,[J_{O_i,\mathcal{H}}]^T \left[\begin{array}{cc} [J_{A,O_i}]^T & [J_{C,O_i}]^T \end{array}\right] \quad (4.60)$$

Step 3: Estimation of the modal parameters' covariances

In the third step the propagation of a perturbation in matrices $[A]$ and $[C]$ to the modal parameters is investigated. Assuming that μ_r and $\{\theta_r\}$ are, respectively, the rth eigenvalue and right eigenvector of matrix $[A]$ such that the respective eigenvalue of the corresponding continuous-time state transition matrix $[A_c]$ is obtained as

$$\lambda_r = \frac{\ln(\mu_r)}{\Delta t}$$

Furthermore, the mode shapes are assumed to be normalised such that the kth element $\psi_{r,k} = 1 + 0\mathrm{i}$ which means that any element of the mode shape has been scaled as

$$\psi_{r,j} = \frac{\theta_{r,j}}{\theta_{r,k}}$$

The perturbations in the natural frequency, modal damping ratio and mode shape of the rth mode propagated from a perturbation in the vectorised system matrices are

$$\begin{aligned} \Delta f_r &= \{J_{f_r,A}\}^T \operatorname{vec}(\Delta\,[A]) \\ \Delta \zeta_r &= \{J_{\zeta_r,A}\}^T \operatorname{vec}(\Delta\,[A]) \\ \Delta\{\psi_r\} &= [J_{\psi_r,A,C}] \left[\begin{array}{c} \operatorname{vec}(\Delta\,[A]) \\ \operatorname{vec}(\Delta\,[C]) \end{array}\right] \end{aligned}$$

with the sensitivities

$$\left[\begin{array}{c} \{J_{f_r,A}\}^T \\ \{J_{\zeta_r,A}\}^T \end{array}\right] = \left[\begin{array}{c} \{J_{f_r,\mu_r}\}^T \\ \{J_{\zeta_r,\mu_r}\}^T \end{array}\right] \left[\begin{array}{c} \operatorname{Re}(\{J_{\lambda_r,A}\}^T) \\ \operatorname{Im}(\{J_{\lambda_r,A}\}^T) \end{array}\right] \quad (4.61)$$

$$[J_{\psi_r,A,C}] = \frac{1}{\theta_{r,k}} \left([I]_{n_o} - \left[\begin{array}{ccc} [0]_{n_o\times(k-1)} & \{\psi_r\} & [0]_{n_o\times(n_o-k)} \end{array}\right]\right) \left[\begin{array}{c|c} [C]\,[J_{\psi_r,A}] & \{\theta_r\}^T \otimes [I]_{n_o} \end{array}\right] \quad (4.62)$$

and

$$\left[\begin{array}{c} \{J_{f_r,\mu_r}\}^T \\ \{J_{\zeta_r,\mu_r}\}^T \end{array}\right] = \frac{1}{\Delta t\ |\mu_r|^2\,|\lambda_r|} \left[\begin{array}{cc} \frac{1}{2\pi} & 0 \\ 0 & \frac{100\%}{|\lambda_r|^2} \end{array}\right] \left[\begin{array}{cc} \operatorname{Re}(\lambda_r) & \operatorname{Im}(\lambda_r) \\ -\operatorname{Im}(\lambda_r)^2 & \operatorname{Re}(\lambda_r)\operatorname{Im}(\lambda_r) \end{array}\right] \left[\begin{array}{cc} \operatorname{Re}(\mu_r) & \operatorname{Im}(\mu_r) \\ -\operatorname{Im}(\mu_r) & \operatorname{Re}(\mu_r) \end{array}\right] \quad (4.63)$$

At the end, the covariances of the modal parameters of two modes r_1 and r_2 are obtained from these sensitivities and the covariances of the system matrices:

$$\operatorname{cov}\left(\left\{\begin{array}{c} f_{r_1} \\ \zeta_{r_1} \end{array}\right\}, \left\{\begin{array}{c} f_{r_2} \\ \zeta_{r_2} \end{array}\right\}\right) = \left[\begin{array}{cc} \left\{J_{f_{r_1},A}\right\}^T & \{0\}^T_{n_on} \\ \left\{J_{\zeta_{r_1},A}\right\}^T & \{0\}^T_{n_on} \end{array}\right] [\Sigma_{A,C}] \left[\begin{array}{cc} \left\{J_{f_{r_2},A}\right\}^T & \{0\}^T_{n_on} \\ \left\{J_{\zeta_{r_2},A}\right\}^T & \{0\}^T_{n_on} \end{array}\right]^T \quad (4.64)$$

$$\operatorname{cov}\left(\left\{\begin{array}{c}\operatorname{Re}(\{\phi_{r_1}\})\\ \operatorname{Im}(\{\phi_{r_1}\})\end{array}\right\},\left\{\begin{array}{c}\operatorname{Re}(\{\phi_{r_2}\})\\ \operatorname{Im}(\{\phi_{r_2}\})\end{array}\right\}\right) = \left[\begin{array}{c}\operatorname{Re}(\left[J_{\phi_{r_1},A,C}\right])\\ \operatorname{Im}(\left[J_{\phi_{r_1},A,C}\right])\end{array}\right]\left[\Sigma_{A,C}\right]\left[\begin{array}{c}\operatorname{Re}(\left[J_{\phi_{r_2},A,C}\right])\\ \operatorname{Im}(\left[J_{\phi_{r_2},A,C}\right])\end{array}\right]^T \tag{4.65}$$

4.4.2 Efficient algorithm for the computation of covariances

Some of the matrices occurring in the algorithm in section 4.4.1 can be of significant size such that the operations become computationally very costly and considerable memory can be required. This gave the motivation for the development of a computationally more efficient implementation for the computation of covariance estimates of the modal parameters in [46].

Step 1: Factorisation of the subspace matrix' covariance matrix

Using the general notation $[\mathcal{H}]$ for the subspace matrix, as introduced in section 4.4.1, equations (4.45) and (4.48) can be re-written as

$$\left[\hat{\Sigma}_{\mathcal{H}}\right] = \frac{1}{n_b(n_b-1)}\sum_{k=1}^{n_b}\left(\left[[\mathcal{H}_k]-\left[\overline{\mathcal{H}}_k\right]\right]\left[[\mathcal{H}_k]-\left[\overline{\mathcal{H}}_k\right]\right]^T\right) \tag{4.66}$$

With the definitions

$$\left[\tilde{\mathcal{H}}_k\right] = [\mathcal{H}_k]-\left[\overline{\mathcal{H}}_k\right] \tag{4.67}$$

and

$$[\mathcal{T}] = \frac{1}{\sqrt{n_b(n_b-1)}}\left[\begin{array}{cccc}\left[\tilde{\mathcal{H}}_1\right] & \left[\tilde{\mathcal{H}}_2\right] & \ldots & \left[\tilde{\mathcal{H}}_{n_b}\right]\end{array}\right] \tag{4.68}$$

one can express equation (4.66) also as

$$\left[\hat{\Sigma}_{\mathcal{H}}\right] = [\mathcal{T}]\,[\mathcal{T}]^T \tag{4.69}$$

Since the number of data blocks n_b which can be extracted from the measured time series is limited such that $n_b < (i+1)n_o j n_{ref}$, matrix $[\mathcal{T}]$ has usually less columns than the covariance matrix $\left[\hat{\Sigma}_{\mathcal{H}}\right]$.

Step 2: Sensitivity of the observability matrix

For model order k, the left and right singular vectors $\{u_k\}$, $\{v_k\}$ and the corresponding singular value s_k are obtained from a singular value decomposition of the subspace matrix $[\mathcal{H}]$. Associated with the respective model order k, the following matrices are defined:

$$\begin{aligned}
[\mathcal{K}_k] &= \left[[I]_{in_{ref}} + \left[\begin{array}{c}[0]_{(in_{ref}-1)\times in_{ref}}\\ 2\,\{v_k\}^T\end{array}\right] - \frac{1}{s_k^2}\,[\mathcal{H}]^T\,[\mathcal{H}]\right]^{-1} && (4.70)\\
\left[\tilde{\mathcal{B}}_k\right] &= \left[[I]_{(i+1)n_o} + \frac{1}{s_k}\,[\mathcal{H}]\,[\mathcal{K}_k]\left(\frac{1}{s_k}\,[\mathcal{H}]^T - \left[\begin{array}{c}[0]_{(in_{ref}-1)\times(i+1)n_o}\\ \{u_k\}^T\end{array}\right]\right)\frac{1}{s_k}\,[\mathcal{H}]\,[\mathcal{K}_k]\right] && (4.71)\\
[\mathcal{T}_{k,1}] &= \left[[I]_{jn_{ref}}\otimes\{u_k\}^T\right]\,[\mathcal{T}] && (4.72)\\
[\mathcal{T}_{k,2}] &= \left[\{v_k\}^T\otimes[I]_{(i+1)n_o}\right]\,[\mathcal{T}] && (4.73)
\end{aligned}$$

With these definitions, the product of the sensitivity matrix of $\left[\tilde{J}_{O_i,\mathcal{H}}\right]$ with matrix $[\mathcal{T}]$ related to the kth singular value can be calculated by

$$\left(\left[\tilde{J}_{O_i,\mathcal{H}}\right][\mathcal{T}]\right)_k = \frac{1}{2\sqrt{s_k}}\{u_k\}\left(\{v_k\}^T[\mathcal{T}_{k,1}]\right) + \frac{1}{\sqrt{s_k}}\left[\tilde{\mathcal{B}}_k\right]\begin{bmatrix}[\mathcal{T}_{k,2}]-\{u_k\}\left(\{u_k\}^T[\mathcal{T}_{k,2}]\right)\\ [\mathcal{T}_{k,1}]-\{v_k\}\left(\{v_k\}^T[\mathcal{T}_{k,1}]\right)\end{bmatrix} \tag{4.74}$$

Step 3: Sensitivities of the system matrices $[A]$ and $[C]$

For the following computational steps the auxiliary matrices $[\mathcal{Q}_1]$, $[\mathcal{Q}_2]$, $[\mathcal{Q}_3]$ and $[\mathcal{Q}_4]$ are defined:

$$[\mathcal{Q}_1] = \left([I]_n\otimes\left[O_i^{\uparrow}\right]^T[\mathcal{S}_1]\right)\left[\tilde{J}_{O_i,\mathcal{H}}\right][\mathcal{T}] = \begin{bmatrix}\left[O_i^{\uparrow}\right]^T[\mathcal{S}_1]\left(\left[\tilde{J}_{O_i,\mathcal{H}}\right][\mathcal{T}]\right)_1\\ \vdots\\ \left[O_i^{\uparrow}\right]^T[\mathcal{S}_1]\left(\left[\tilde{J}_{O_i,\mathcal{H}}\right][\mathcal{T}]\right)_n\end{bmatrix} \tag{4.75}$$

$$[\mathcal{Q}_2] = \left([I]_n\otimes\left[O_i^{\downarrow}\right]^T[\mathcal{S}_1]\right)\left[\tilde{J}_{O_i,\mathcal{H}}\right][\mathcal{T}] = \begin{bmatrix}\left[O_i^{\downarrow}\right]^T[\mathcal{S}_1]\left(\left[\tilde{J}_{O_i,\mathcal{H}}\right][\mathcal{T}]\right)_1\\ \vdots\\ \left[O_i^{\downarrow}\right]^T[\mathcal{S}_1]\left(\left[\tilde{J}_{O_i,\mathcal{H}}\right][\mathcal{T}]\right)_n\end{bmatrix} \tag{4.76}$$

$$[\mathcal{Q}_3] = \left([I]_n\otimes\left[O_i^{\uparrow}\right]^T[\mathcal{S}_2]\right)\left[\tilde{J}_{O_i,\mathcal{H}}\right][\mathcal{T}] = \begin{bmatrix}\left[O_i^{\uparrow}\right]^T[\mathcal{S}_2]\left(\left[\tilde{J}_{O_i,\mathcal{H}}\right][\mathcal{T}]\right)_1\\ \vdots\\ \left[O_i^{\uparrow}\right]^T[\mathcal{S}_2]\left(\left[\tilde{J}_{O_i,\mathcal{H}}\right][\mathcal{T}]\right)_n\end{bmatrix} \tag{4.77}$$

$$[\mathcal{Q}_4] = \left([I]_n\otimes\begin{bmatrix}[I]_{n_o} & [0]_{n_o\times in_o}\end{bmatrix}\right)\left[\tilde{J}_{O_i,\mathcal{H}}\right][\mathcal{T}] = \begin{bmatrix}\begin{bmatrix}[I]_{n_o} & [0]_{n_o\times in_o}\end{bmatrix}\left(\left[\tilde{J}_{O_i,\mathcal{H}}\right][\mathcal{T}]\right)_1\\ \vdots\\ \begin{bmatrix}[I]_{n_o} & [0]_{n_o\times in_o}\end{bmatrix}\left(\left[\tilde{J}_{O_i,\mathcal{H}}\right][\mathcal{T}]\right)_n\end{bmatrix} \tag{4.78}$$

$$[\mathcal{Q}_5] = [I]_n\otimes\left(\left[O_i^{\uparrow}\right]^T\left[O_i^{\uparrow}\right]\right)^{-1} \tag{4.79}$$

With these definitions and the permutation matrix $[\mathcal{P}_{n,n}]$, as defined in equation (4.58), the products of the sensitivities of the system matrices $[A]$ and $[C]$ with respect to perturbations in the observability matrix and matrix $\left(\left[\tilde{J}_{O_i,\mathcal{H}}\right][\mathcal{T}]\right)$ can be computed by

$$[J_{A,O_i}]\left[\tilde{J}_{O_i,\mathcal{H}}\right][\mathcal{T}] = [\mathcal{Q}_5]\left(-\left([A]^T\otimes[I]_n\right)\left([\mathcal{P}_{n,n}]+[I]_{n^2}\right)[\mathcal{Q}_1]+[\mathcal{P}_{n,n}][\mathcal{Q}_2]+[\mathcal{Q}_3]\right) \tag{4.80}$$

$$[J_{C,O_i}]\left[\tilde{J}_{O_i,\mathcal{H}}\right][\mathcal{T}] = [\mathcal{Q}_4] \tag{4.81}$$

The covariances of system matrices $[A]$ and $[C]$ are obtained by means of the results of equations (4.80) and (4.81):

$$[\Sigma_{A,C}] = [U_{A,C}]\,[U_{A,C}]^T \tag{4.82}$$

with

$$[U_{A,C}] = \begin{bmatrix}[J_{A,O_i}]\\ [J_{C,O_i}]\end{bmatrix}\left[\tilde{J}_{O_i,\mathcal{H}}\right][\mathcal{T}] \tag{4.83}$$

Step 4: Covariance estimates of the modal parameters

It has been shown in [46] that covariance estimates of the modal parameters can be generated without explicitely computing the covariances of the system matrices $[\Sigma_{A,C}]$ but only the respective sensitivities. If $\{\chi_r\}$ is the rth left eigenvector of matrix $[A]$

$$\{\chi_r\}^H [A] = \mu_r \{\chi_r\}^H$$

the auxiliary sensitivity matrix product

$$[J_{\mu_r,A}]\,[J_{A,O_i}]\left[\tilde{J}_{O_i,\mathcal{H}}\right][\mathcal{T}] = \frac{1}{\{\chi_r\}^H \{\theta_r\}} \{\chi_r\}^H \left(\left[O_i^{\uparrow}\right]^T \left[O_i^{\uparrow}\right]\right)^{-1} [\mathcal{Q}_r] \tag{4.84}$$

can be defined where $[\mathcal{Q}_r]$ denotes the auxiliary matrix

$$[\mathcal{Q}_r] = \left(\{\theta_r\}^T \otimes [I]_n\right)\left(-\mu_r\left([\mathcal{P}_{n,n}] + [I]_{n^2}\right)[\mathcal{Q}_1] + [\mathcal{P}_{n,n}]\,[\mathcal{Q}_2] + [\mathcal{Q}_3]\right) \tag{4.85}$$

The covariances of the natural frequencies and modal damping ratios are eventually obtained by means of equation (4.84) as

$$\operatorname{cov}\left(\left\{\begin{array}{c} f_{r_1} \\ \zeta_{r_1} \end{array}\right\}, \left\{\begin{array}{c} f_{r_2} \\ \zeta_{r_2} \end{array}\right\}\right) = \left[U_{f_{r_1},\zeta_{r_1}}\right]\left[U_{f_{r_2},\zeta_{r_2}}\right]^T \tag{4.86}$$

with

$$[U_{f_r,\zeta_r}] = \left[\begin{array}{c} \{J_{f_r,\mu_r}\}^T \\ \{J_{\zeta_r,\mu_r}\}^T \end{array}\right]\left[\begin{array}{c} \mathrm{Re}([J_{\mu_r,A}]\,[J_{A,O_i}]\left[\tilde{J}_{O_i,\mathcal{H}}\right][\mathcal{T}]) \\ \mathrm{Im}([J_{\mu_r,A}]\,[J_{A,O_i}]\left[\tilde{J}_{O_i,\mathcal{H}}\right][\mathcal{T}]) \end{array}\right] \tag{4.87}$$

in which the sensitivities $\{J_{f_r,\mu_r}\}$ and $\{J_{\zeta_r,\mu_r}\}$ were defined in equation (4.63).

The covariances between two mode shapes $\{\psi_{r_1}\}$ and $\{\psi_{r_2}\}$ can be calculated following a similar algorithm.

$$\operatorname{cov}\left(\left\{\begin{array}{c} \mathrm{Re}\left(\{\psi_{r_1}\}\right) \\ \mathrm{Im}\left(\{\psi_{r_1}\}\right) \end{array}\right\}, vect \begin{array}{c} \mathrm{Re}\left(\{\psi_{r_2}\}\right) \\ \mathrm{Im}\left(\{\psi_{r_2}\}\right) \end{array}\right) = \left[U_{\psi_{r_1}}\right]\left[U_{\psi_{r_2}}\right]^T \tag{4.88}$$

Matrices $[U_{\psi_r}]$ are formed from the real and imaginary parts of

$$\begin{aligned} [\Upsilon] &= [J_{\psi_r,A,C}]\left[\begin{array}{c} [J_{A,O_i}] \\ [J_{C,O_i}] \end{array}\right]\left[\tilde{J}_{O_i,\mathcal{H}}\right][\mathcal{T}] \\ &= \frac{1}{\psi_{r,k}}\left([I]_{n_o} - \left[\begin{array}{ccc} [0]_{n_o\times(k-1)} & \{\psi_r\} & [0]_{n_o\times(n_o-k)} \end{array}\right]\right) \\ &\quad \left([C]\,[J_{\psi_r,A}]\,[J_{A,O_i}]\left[\tilde{J}_{O_i,\mathcal{H}}\right][\mathcal{T}] + \left(\{\psi_r\}^T \otimes [I]_{n_o}\right)[J_{C,O_i}]\left[\tilde{J}_{O_i,\mathcal{H}}\right][\mathcal{T}]\right) \end{aligned} \tag{4.89}$$

as

$$[U_{\psi_r}] = \left[\begin{array}{c} \mathrm{Re}\left([\Upsilon]\right) \\ \mathrm{Im}\left([\Upsilon]\right) \end{array}\right] \tag{4.90}$$

In equation (4.89) the following expressions can be substituted:

$$\begin{aligned} [J_{\psi_r,A}]\,[J_{A,O_i}]\left[\tilde{J}_{O_i,\mathcal{H}}\right][\mathcal{T}] &= \left(\mu_r [I]_n - [A]\right)^{\dagger}\left([I]_n - \frac{1}{\{\chi_r\}^H \{\psi_r\}}\{\psi_r\}\{\chi_r\}^H\right) \\ &\quad \left(\left[O_i^{\uparrow}\right]^T \left[O_i^{\uparrow}\right]\right)^{-1} [\mathcal{Q}_r] \end{aligned} \tag{4.91}$$

$$[J_{C,O_i}]\left[\tilde{J}_{O_i,\mathcal{H}}\right][\mathcal{T}] = [\mathcal{Q}_4] \tag{4.92}$$

Chapter 5

Automated postprocessing

From the previous chapters can be concluded that modal analysis, both experimental and operational, is a complex field of engineering that usually requires computationally demanding analyses and a relatively high level of experience. Especially the latter aspect gives motivation to provide tools that support the analyst in the identification of modal parameters from data acquired in vibration tests. While the actual analysis of the measured data can be very well formalised, several steps of the postprocessing, in particular the selection of modes from results obtained by means of parametric methods typically requires a certain degree of experience.

Even though the results of automatic procedures should always be critically assessed, the replacement of tasks, that are traditionally perfomed manually, by sophisticated numerical tools is often not only desirable but even necessary. This applies especially to the identification of modal parameters from multiple measurements as in the case of continuous structural monitoring. Therefore, several approaches have been developed to facilitate the postprocessing of modal analyses.

In general, one can distiquish between two different objectives of automation in the context with modal analysis:

- *automated modal identification*, that mainly refers to the selection of physical modes from a single analysis, and
- *automated mode tracking* if modes identified from different tests or analyses need to be assigned to each other correctly as required, for example, in continuous monitoring.

In this chapter both objectives will be considered separately even if the applied methods can be very similar.

5.1 Automated modal identification

As mentioned above, automated modal identification, refers in first place to the selection of physical modes which means in the decision which solutions of the analysis are considered as physical modes. In the case of nonparametric modal analysis, such as the frequency domain decomposition (FDD) method, the equivalent manual process is the selection of peaks in the singular values or power spectra. For the results of parametric modal analyses, modal selection is related to stabilisation diagrams from which the analyst has to choose which solutions should be considered as related to physical modes and which are spurious. Accordingly, the approaches to automate the modal selection process are different for the two groups of modal analysis and are therefore also distinguished in the following sections.

A comprehensive overview about different automated modal identification techniques is given, for example, in [91], [116] and [92]. In this chapter several methods are summarised that are related to some of the most established operational modal analysis techniques.

5.1.1 Automated nonparametric modal identification

On of the most established nonparametric operational modal identification techniques is probably the frequency domain decomposition (FDD) technique which is described in section 3.3.2. The respective modal selection process is based on the identification of peaks in the diagram of singular values of the power spectral matrices versus frequency. Consequently, the first step of an automated modal identification with the FDD method consists of the detection of peaks in the series of the first singular values.

However, as not all peaks are necessarily related to physical modes, a distinction from peaks related to noise or harmonic components in the signals is required. The identification of harmonics has already been addressed in section 3.5.1.3. The concept described there can also be applied in the context with mode selection within an automated FDD analysis.

For the separation of peaks related to noise, a procedure that compares the similarity between the first singular vectors in the vicinity of a peak with the one corresponding to the detected peak has been suggested in [21] and [6]. If the peak is related to a physical mode, the first singular vectors $\{u_1(f)\}$ at frequencies f in the vicinity to the frequency at the peak f_0 should be very similar to the related first singluar vector $\{u_1(f_0)\}$ which is an estimate of the corresponding mode shape. This is not the case for a peak related to noise components in the signals. As a measure that quantifies this similarity, the modal coherance

$$d(f_0) = \{u_1(f)\}^H \{u_1(f_0)\} \tag{5.1}$$

that is very similar to the MAC, has been suggested in [21] and [6]. If this value is close to unity, it indicates a high similarity between the two considered vectors. To classify a singluar vector $\{u_1(f)\}$ as similar to $\{u_1(f_0)\}$, a threshold value of approximately $d(f_0) \geq 0.8$ is proposed in [6] while in [21] this threshold is set to

$$d(f_0) \geq \frac{n}{\sqrt{n_o}} \tag{5.2}$$

where n is a number within the range of 3 to 5 and n_o denotes the number of channels used for the analysis.

These criteria are also used to define a so-called modal domain, a frequency range in which the respective mode is dominant. The size of the modal domain is then used to decide whether a peak is considered as related to a physical mode or not. The algorithm of automated modal selection based on an FDD analysis can be summarised in the following steps:

1. Identification of peaks in the first singular values of the power spectral matrices versus frequency,
2. Decision if a respective peak is related to a physical mode,
3. Definition of the modal domain around the peak,
4. Continuation of the search until all identified peaks have been considered or a pre-defined number of modes to be identified were selected.

The algorithm summarised above follows the intuitive manual procedure of mode selection in an FDD analysis which also starts with a peak detection. However, the automation of the peak selection requires the definition of threshold values which may need time-demanding calibration in advance. To overcome this drawback, an alternative procedure has been suggested in [116]. The method, that is called LEONIDA in [116], is based on the analysis of the first singular vectors obtained from the analysis of j independent time sequences extracted from a single measurement or several separate records. This means that for each measurement or sequence extracted from a single measurement a series of first singular vectors is obtained for each frequency line of the power spectral densities in a first step. Afterwards one set of results is chosen as reference with which the MAC values of the remaining first sigular vectors corresponding to the respective frequency lines are calculated. To reduce the effects of noise in the resulting functions of MAC with respect to frequency, these functions are averaged which can be represented as plot of averaged MAC values versus frequency.

Within the bandwidth of a mode the obtained curve should have a value close to one and be nearly horizontal. Furthermore, it can is assumed that the deviations between the MAC values computed based on the results from different measurements should be very small within the bandwidth of a mode. Correspondingly, the following limits are defined for the identification of modes by means of the LEONIDA approach according to [116]:

- The average MAC value should be greater than 0.95:

$$\frac{1}{j}\sum_{i=1}^{j} MAC_i(f) \; > \; 0.95 \tag{5.3}$$

- The standard deviation of the MAC value at a single frequency should be less than 0.01:

$$\sigma_{(MAC)}(f) < 0.01 \tag{5.4}$$

- The average of the first derivative of the MAC value should be less than 0.01:

$$\frac{1}{j}\sum_{i=1}^{j} \frac{\mathrm{d}MAC_i(f)}{\mathrm{d}f} \; < \; 0.01 \tag{5.5}$$

- The standard deviation of the first derivative of the MAC value should be less than 0.01:

$$\sigma_{\left(\frac{\mathrm{d}_{MAC(f)}}{\mathrm{d}_f}\right)} \; < \; 0.01 \tag{5.6}$$

With these criteria a sequence of bandwidths corresponding to modes can be obtained. Subsequently, the natural frequencies of the corresponding modes are identified by means of peak detection of the first singular values of the power spectral densities within the respective bandwidths. An estimate of the corresponding mode shape is the respective singular vector.

This alternative algorithm of automated modal identification based on an FDD analysis can accordingly be summarised in the following steps:

1. Splitting of the measured time series into j sequences or choice of measured time series to be analised at once.
2. Calculation of the power spectral density matrices for each of the considered sequences and subsequent singular value decomposition.
3. Selection of a set of reference singular values and vectors.
4. Computation of the MAC values between all first singular vectors corresponding to all frequency lines with respect to the first singular vectors of the corresponding reference solution.
5. Calculation of the mean values and standard deviations of the MAC value sequences computed for each frequency line.
6. Identification of the bandwidths of modes by means of the criteria given in equations (5.3) to (5.6).
7. Identification of the modal parameters of each mode corresponding to the identified bandwidth.

The quality of the modal parameters identified by means of the described methodolgy, as the results of an FDD analysis in general, depends on the frequency resolution and record length [116].

5.1.2 Automated parametric modal identification

The identification of modes by means of a parametric method is related to the selection of solutions for a respective mathematical model. The most important tool in this context is the stabilisation diagram. This graphical representation of the identification results facilitates the distinction between physical modes and spurious solutions and forms the base for the identification of "stable poles" by means of several criteria such as those described in chapter 4.

As the manual selection of solutions related to physical modes from the stabilisation diagram corresponds with the identification of stable poles, algorithms of automated modal identification based on parametric modal analysis methods usually try to mimic the decision of an analyst whether a solution is related to a physical mode or is spurious. This means that the solutions that are visualised in a manual analysis in a stabilisation diagram have to be assigned to a certain number of physical modes and spurious solutions. For this classification, most approaches suggested for automatic modal identification apply cluster analysis algorithms. Therefore a short introduction into cluster analysis is provided in the following subsection before several methods for an automated modal selection are described.

5.1.2.1 Cluster analysis

The objective of cluster analysis is the classification of a given set of objects with specific properties into a number of groups with common features which are called clusters. All objects gathered in one cluster should show maximal similarity while the different clusters should be separated with maximal diversity.

Numerous algorithms for cluster analysis have been described in literature. They can be classified into the two major groups of *hierarchical* and *nonhierarchical* clustering algorithms [66].

In **hierarchical clustering** procedures, it is decided $(n_{ob} - 1)$times by means of a similarity measure how the given n_{ob} objects are combined. In the case of an *agglomerative* method, each object forms a single cluster at the beginning of the analysis which are merged subsequently to one single cluster containing all objects at the end. Methods that work in the opposite direction which means that they start from a single cluster that is step by step divided into n_{ob} single-member sub-clusters are called *divisive* algorithms.

Apart from the direction of the anaylsis, both agglomerative and divisive algorithms act very similarly. For the sake of simplicity and as in most applications agglomerative algorithms are used [66], the principal steps of anaylsis are briefly described only for this group of procedures in the following.

An agglomerative hierarchical cluster analysis consists of three major steps [14]:

1. Selection and calculation of the similarity measures,
2. Choice and application of the linkage method,
3. Decision about the number of clusters.

In the first step of the analysis a specific similarity measure or distance needs to be defined and calculated for each possible pair of objects. The results are collected in a distance or similarity matrix. Depending on the variable types, different similarity measures can be used. For metric variables, usually matrix norms such as the Euclidean distance, the City block or Manhatten distance, the Minkowski distance and the Q- or Pearson correlation coefficient are used [14], [66], [84], [48].

Based on the values of the distance or similarity measures, the objects are collected into groups of objects with maximal similarity until they are all included in a single cluster. The most common linkage methods for hierarchical clustering are *single linkage*, *complete linkage*, *average linkage*, *ward's* and *centroid methods*. The different linkage methods are not further discussed here. The interested reader is referred to respective textbooks about cluster analysis.

As hierarchical cluster analysis is a procedure that generates a series of clusters from a series of single-member clusters to a single cluster in a sequence that can be visualised in a tree-like diagram, also called dendogram, it is not clear a priori which number of clusters is most appropriate. In an automatic analysis, the decision about the level of analysis at which the "best" set of clusters has been achieved requires a suitable criterion. The definition of this criterion is also one of the most crucial issues in context with automated modal identification.

The most applied methods of the group of **nonhierarchical cluster analysis** techniques belong to the class of **partitioning methods**. An anylsis by means of a partitioning algorithm begins, unlike hierarchical clustering, with the definition of the number of clusters. This means, that the analyst needs to decide before the analysis starts, into how many groups the data shall be split. By means of an appropriate algorithem, the objects are than assigned into the clusters. In general, a partitioning analysis consists of the following two major steps [66]:

1. Specification of the cluster seeds,
2. Assignment of the objects to the clusters.

Cluster seeds denote here the cluster centroids assumed for the start of a partioning cluster analysis. They can be either specified by the analyst or generated by applying some numerical methodology. In case of the first option, an *analyst specified selection* is chosen, a preliminary analysis of the data is required. The choice is influenced, on the one hand, by subjective decision criteria, but it also allows, on the other hand, to use expert knowledge.

Alternatively, the cluster seeds can be obtained from a *sample generating* procedure. There exist different possibilities. For example, the cluster seeds can be selected from the given objects randomly. Another possibility is that the given objects are sorted according to some criterion and then split into groups of equal size for which then the centroids are computed as seeds for the cluster analysis.

Which ever method is chosen to generate the cluster seeds, it should be mentioned that the result of any assignment technique that is applied then, strongly depends on the choice of the initial set of cluster seeds.

For the assignment of the objects into K clusters by means of a partitioning cluster analysis several algorithms exist that are also referred to as K*-means clustering* [66]. In the following, the principal ideas of some of these algorithms are briefly introduced.

One of the probably most straightforward ways is to predefine maximal distance values and assign all objects which have a distance to a certain cluster seed that is smaller than the specified threshold into the respective cluster. All objects which do not satisfy the threshold condition will be excluded. In [66] it is distinguished between *sequential* and *parallel* threshold methods. As the name indicates, the first procedure considers all cluster seeds sequentially. This means that all objects that satisfy the threshold condition will be assigned to the considered cluster and excluded from further analyses. In case that the distance to another cluster seed that has not yet been considered is smaller, it will not be re-assigned as it already belongs to one cluster. This shortcoming is avoided in a parallel threshold analysis that assigns an object to the cluster for which the respective distance to the cluster seed is minimal.

As both the parallel and sequential threshold methods exclude all objects that do not satisfy a prespecified criterion, they can be suitable methods for certain applications, especially if very good preliminary knowledge with respect to the cluster centroids is available.

By means of the two described threshold methods, each object is assigned once and cannot be re-assigned to another cluster. At the end of the analysis the originally set cluster seeds do not necessarily have to be the centroids of the respective clusters. Therefore, it seems natural to use the centroids of the clusters as a new set of cluster seeds for a second assignment of those objects that may be closer to another cluster. This procedure can then be repeated iteratively to reduce the variability of the clusters which leads to an *optimisation*. One very common algorithm applied to partitioning clustering analysis is the substitution method [14].

So far, only partitioning methods were considered that allow for assigning an object solely to a single cluster. One can call this a *hard partitioning*. However, there may be situations when objects may have similarities to more than one cluster. To cope with this problem, the class of **fuzzy clustering** algorithms has been developed. As these algorithms can also be applied to automated modal analysis, the principles are explained here as well.

For fuzzy partitioning it is also assumed that the complete set of objects has to be separated into C clusters. Unlike for a hard partitioning, an object can be member of more than one cluster with different contribution or weight. How strong an object is related to the different clusters is expressed by a so-called *membership function*. The values of all membership functions u_{ik} are collected in the so-called *fuzzy partition matrix* $[U_i]$ where either the rows or the columns refer to the objects and the second dimension to the centroids or *cluster prototypes* as they are also called in context with fuzzy clustering. All values of the membership functions are within the interval $[0, 1]$. The sum of these values referring to any single object must be 1.

The basic approach for fuzzy clustering is given by the *fuzzy C-means* algorithm. Similarly as for K-means clustering, or hard partitioning, a sequence of C cluster centroids $\{v_i\}$ which are also called *cluster prototypes* in context with fuzzy clustering need to be defined. They are typically combined as columns in a matrix $[V_i]$. The n_d data sets $\{x_k\}$ collected in matrix $[X]$ are then iteratively assigned to the clusters such that the objective function

$$J\left([X], [U_i], [V_i]\right) = \sum_{i=1}^{C} \sum_{k=1}^{n_d} \left(u_{ik}\right)^m \, d^2\left(\{x_k\} - \{v_i\}\right) \tag{5.7}$$

is minimised. The exponent m of the membership values u_{ik} determines the fuzziness of the resulting clusters and is often set to the value of $m = 2$ [127]. In equation (5.7), $d^2\left(\{x_k\} - \{v_i\}\right) = d_{ik}^2$ denotes a distance function

$$d_{ik}^2 = \left(\{x_k\} - \{v_i\}\right)^T \left[A^i\right] \left(\{x_k\} - \{v_i\}\right) \tag{5.8}$$

where $[A^i]$ is a norm matrix. If $[A^i]$ is set to an identity matrix, d_{ik}^2 becomes the Euclidean norm.

The Fuzzy C-means algorithms can by summarised by the following steps [127], [1]:

1. Initialisation: Choice of
    - the number of clusters C,
    - the fuzzy parameter m,
    - the termination criterion ε_t,
    - the maximal number of iterations T and
    - the partition matrix $[U_i]$ such that the afore mentioned requirements are satisfied.
2. Update of the cluster prototypes
3. Calculation of the distances

4. Update of the partition matrix

These analyses are repeated t times until either the threshold is not exceeded anymore, $\left|\left|[U_i]_t - [U_i]_{t-1}\right|\right| < \varepsilon$ or the chosen maximal number of iterations has been achieved, $t \geq T$.

Two features of the Fuzzy C-means algorithms are

1. that it forms exclusively hyperspherical partitions and
2. that all clusters have equal importance which results in almost the same density of members in each cluster.

To overcome these limitations, two extensions of the Fuzzy C-Means algorithm were developed [127], [1].

The first extension is given by the Gustafson-Kessel algorithm [64]. It utilises different weighting factors for the clusters. This is obtained by computing the norm matrix $[A_i]$ based on the fuzzy covariance matrix such that instead of the Euclidean norm the Mahalonobis distance is used. As a result, the Gustafson-Kessel algorithm can capture ellipsoidal properties of clusters.

To allow also for different desities of the clusters, Gath and Geva suggested to weight the Mahalonobis distance that is used in the Gustafson-Kessel algorithm by an exponential term which is based on a prior probability function. For further detailes with respect to fuzzy clustering algorithms, the interested reader is referred to the literature, as for example [127] and [1].

5.1.2.2 Methodologies for automated parametric modal estimation using cluster analysis

Methods based on hierarchical clustering and partitioning

As mentioned earlier, most approaches that were developed for an automated modal parameter estimation based on parametric identification methods apply cluster analysis to select the respective solutions out of all poles computed by a respective analysis. This process replaces the manual selection of modal solutions by means of a stabilisation diagram. Therefore, the information represented in a stabilisation diagram provides the base for any automated mode selection procedure based on a parametric modal estimation method. However, as the solutions contain also numerous poles that are not associated with physical modes, much research has been focused on three major aspects to improve the quality of automatically identified modal parameters as indicated in [91]:

- modal identification algorithms that generate clearer stabilisation diagrams,
- the development and consideration of additional parameters to improve the information base for the selection of modal solutions and
- methodologies for an automatic analysis to select the solutions corresponding to physical modes from the information represented in a stabilisation diagram.

The first point is related not only to the choice of a specific identification method but also to the respective parameters that can influence the results of an analysis considerably.

As already described in sections 3.4, 4.1 and 4.4, several methods and indicators have been suggested that can be used to assess the quality of a modal parameter estimate. The application of these and other mode validation criteria as well as further considerations within an automated pole selection are implied by the second aspect. They may be used at different stages of the analysis. One can exclude some spurious solutions already by a preliminary selection at an early stage from being taken into account within later clustering or incorporate them into the metrics utilised in the clustering procedure.

An automatic mode selection procedure that can be applied to the results of any parametric modal identification method has been presented in [91] and [92]. It is based on hierarchical clustering. For the distance between two parameter sets i and k only the natural frequencies and mode shapes are considered:

$$d_{ik} = w_f \left| \frac{f_i - f_k}{f_k} \right| + w_\varphi \left(1 - MAC(\varphi_i, \varphi_k)\right) \tag{5.9}$$

where w_f and w_φ are weighting factors related to the natural frequencies and mode shapes, respectively. In the studies described in [91] and [92] both factors were set to 1. As criterion for the termination of the hierarchical clustering an upper limit for the distance between any data set and the closest data set within the same cluster is defined. It is recommended to use the stabilisation criteria to define the termination limit. Afterwards, outliers are removed from all clusters using a criterion based on the modal damping values: only those data sets with modal damping ratios within the range

$$(\zeta_{Q_1} - 1.5\,\zeta_{IQR}) \;\ldots\; (\zeta_{Q_3} + 1.5\,\zeta_{IQR}) \tag{5.10}$$

are retained. In equation 5.10, ζ_{Q_1} and ζ_{Q_3} denote the lower and upper quartile modal damping ratios and ζ_{IQR} is the respective interquartile range of the modal damping ratios.

A similar approach for the application to results of a modal identification by means of the Eigensystem Realisation Algorithm (ERA) has been presented in [150]. Prior to the grouping of poles into mode sets employing hierarchical clustering, spurious solutions are removed by means of a modal similarity index MSI that compares two modes i and k based on natural frequencies and modal damping ratios:

$$MSI_{i,k} = \frac{w_f}{\mathrm{d}f} \frac{|f_i - f_k|}{\max(f_i, f_k)} + \frac{w_\zeta}{\mathrm{d}\zeta} \frac{|\zeta_i - \zeta_k|}{\max(\zeta_i, \zeta_k)} \tag{5.11}$$

where w_f and w_ζ denote respective weighting factors for natural frequencies and damping ratios while $\mathrm{d}f$ and $\mathrm{d}\zeta$ are described in [150] as tolerance values for the relative estimates of natural frequencies and damping ratios, respectively. The following values for these quatities are suggested in [150]: $w_f = 0.7$, $w_\zeta = 0.3$, $\mathrm{d}f = 0.01$ and $\mathrm{d}\zeta = 0.05$.

As distance measure for the hierarchical clustering a function is used in [150] that incorporates the MSI, the modal assurance criterion and a mode energy level MEL which is derivated from an identified frequency response function that requires also the measurement of the excitation. In the case of operational modal analysis, the mode energy level MEL may be replaced by the modal transfer norm.

An enhanced approach has been suggested in [122]. It consists of three major stages:

1. Classification of all poles into
    - possibly physical modes and
    - certainly spurious modes.

    This classification is performed in three steps:

    (a) Computation of as many relevant single-mode validation criteria as possible

    (b) Classification of poles as possibly physical and certainly spurious modes:
    In this step all poles are partitioned into two clusters by employing K-means clustering with $K = 2$. The metrics used as distance measure is based on so-called soft validation criteria. Those solutions that are categorised as certainly spurious modes are excluded from further analysis.

    (c) Application of so-called hard validation criteria to all possibly physical modes:
    In this step remaining solutions that include modal parameters such as very high or non-positive damping ratios and that do not occur in complex conjugate pairs are dismissed.

2. Collection of all retained possibly physical modes in groups that correspond to similar modes employing hierarchical clustering:

    (a) Use of a distance measure between two clusters i and k that is based on the continuos-time eigenvalues λ_{ci} and λ_{ck} and the modal assurance criterion:

    $$d_{i,k} = \frac{|\lambda_{ci} - \lambda_{ck}|}{\max\left(|\lambda_{ci}|, |\lambda_{ck}|\right)} + 1 - MAC(\varphi_i, \varphi_k) \tag{5.12}$$

    (b) Successive merging of the two closest clusters using the average distance between all elements of two respective clusters as their mutual distance

    (c) Termination of the hierarchical clustering if the minimal distance between two clusters $d(i,k)$ exceeds the threshold $\tilde{d}$ that is obtained from the mean value μ_p and standard deviation σ_p of the distance measures of each possibly physical mode from the respective closest mode computed in the previous clustering stage:

    $$d(i,k) \geq \tilde{d} = \mu_p \, \sigma_p \tag{5.13}$$

    This means that the threshold for terminating the hierarchical clustering does not require a definition or intervention by the analyst but is calculated automatically.

3. Selection of the final set of physical modes by partioning the retained clusters of stage 2 and a set of empty clusters into two final clusters of physical and spurious modes, respectively. Eventually, from each mode set of the physical modes one representative solution is selected, for example the one with median damping ratio or the one with the largest MPC value.

Methods using fuzzy clustering techniques

An automated procedure that uses up to six variables based on modal parameters identified in frequency domain from input-output tests is described in [143]. Instead of a hard partitioning the application of the fuzzy C-means algorithm is suggested for the selection of physical modes. For the decision to which cluster a mode belongs, if the algorithm suggests multiple membership, a minimal value of the respective membership function of 0.5 has been defined as a hard criterion. A very similar approach that includes even up to 8 variables in the calculation of the distance values has been described in [140]. The practical application of the methodology proposed in [143] has been illustrated, for example, in [88] and [89].

A very detailed analysis of the application of different fuzzy clustering algorithms to operational modal analysis from in-flight test data is described in [127]. It has been shown that the choice of the number of clusters and the cluster prototype initialisation are the most important factors in a fuzzy cluster analysis. In the example, the assignment of the solutions to different clusters was based on natural frequencies and damping ratios only. However, in general, further parameters could be intergrated into the proposed methodology. Clusters which showed a large scatter of their members were excluded by introducing a measure for compactness of a cluster. Eventually, each pole that remained after excluding several solutions is assigned to the cluster in which it has the highest membership.

The application of Fuzzy C-means clustering to the automatic modal identification from acceleration data acquired by long-term monitoring has been described in [32]. The authors observed that the identified poles form clusters of non-spherical or non-circular but strongly ellipsoidal shapes if plotted in the frequency-damping plane. Alternative to the application of the more complex Gustafson-Kessel algorithm in [32], not the modal parameters but the real and imaginary parts of the identified complex eigenvalues are considered and gathered in clusters using Fuzzy C-means clustering since the data analysed in the presented examples shows less ellipsoidal characteristics in the Z-plane than in the frequency-damping plane. Mode shapes were also not included in the automatic modal selection as the data sets included only a limited number of channels.

5.1.2.3 Methodologies for automated parametric modal estimation using alternative mode selection techniques

Cluster analysis requires the calculation and comparison of all possible distances between each possible pair of data points within the considered domain. In case of automated parametric modal identification this refers to all modal solutions obtained from a respective analysis. As the number of identified modal solutions can be considerable, cluster analysis may become computationally very expensive. Therefore, several authors suggested alternative approaches to group the modal solutions into respective clusters.

Clustering by means of Delauny triangulation

In [65] has been suggested to apply a Delauny triangulation to the modal solutions represented in the frequency-damping plane. This technique is widely used, for example to automatically generate a mesh for finite element models. Here, the modal solutions retained after preliminary removal of obviously spurious solutions by means of a criterion based on the mean phase deviation, MPD, are plotted in the frequency-damping plane and connected by lines such that a closed grid of triangles is formed.

Afterwards, the sizes of all triangles are evaluated by comparing the differences in frequency and damping between two corner points with a pre-defined value that represents a certain percentage of the lowest frequency and damping values, respectively, of all three corner points of the considered triangle. Furthermore, it is examined if the three MAC values corresponding to each triangle are higher than a pre-defined threshold. Triangles that do not satisfy all criteria are deleted.

This procedure should result in separated groups of triangles connected to each other. These groups can still contain solutions that belong to different modes. Therefore, an additional analysis is performed that starts from the highest model order and assigns all solutions at descending order to the respective mode to which the distance in terms of frequency, damping and mode shape is minimal.

Eventually, clusters that contain fewer members than half of the maximal model order are deleted as well. So, the procedure for automated modal selection proposed in [65] can be summarised by the following steps:

1. removal of solutions that show Mean Phase Deviations (MPD) above a certain threshold,
2. Delauny triangulation of the remaining solutions in the frequency-damping plane,
3. erasure of triangles by means of size-related criteria,
4. identification of groups of connected triangles,
5. assignment of solutions within each group of connected triangles to respective modes,
6. selection of those modes that were identified at least at 50% of the considered model orders.

The application of this algorithm has been described in [65] by means of data acquired on an offshore wind turbine structure.

Clustering with subdivided stabilisation diagrams

While a cluster analysis usually involves all available data sets, in [15] a methodology is proposed that splits the modal solutions that can be visualised in a stabilisation diagram into subgroups. As in most approaches, only solutions that satisfy all pre-defined stabilisation criteria are considered. A second data reduction is achieved by excluding all solutions with modal damping ratios outside a range typical for the considered type of structure. In [15] it has been suggested to retain all solutions with $0 \leq \zeta \leq 15\%$.

After this first data reduction, the frequency range of interest of the stabilisation diagram is split into a certain number of frequency bands which are named *bins* in [15]. These bins should overlap in frequency by 50 %. As frequency bandwidth of these bins $\Delta f = \frac{f_{max}}{500}$ is recommended in [15] assuming that the frequency band of interest ranges from 0 to f_{max}.

In the next stage of analysis, one bin is considered after the other. Before proceeding it is checked whether the ratio of the number of stable poles in the respective bin to the total number of model orders considered is not less than $\frac{1}{3}$. If this condition is not satisfied, the respective bin is excluded from further analyses. Next, the MPC values of all remaining modal solutions in the respective bin are checked. Poles with $MPC < 0.7$ are not taken into account in further steps.

To identify multiple modes within a single bin, the MAC values related to each possible pair of distinct poles are calculated. Afterwards, all parameter sets that with $MAC > 0.7$ are grouped and considered as being related to the same mode forming one cluster.

Due to the bins' frequency overlap of 50 % each identified mode is likely to be recognised in two adjacent bins. To assign any mode only two one bin, it is suggested in [15] to compute the distance of all cluster members already grouped by means of the afore mentioned MAC criterion to the centre of the respective bin in the frequency-damping plane. The centre of a bin is in this case defined by the bin's centre frequency and the median modal damping ratio of all poles contained in the bin. A cluster is than assigned to the bin to which any of it's members shows the minimal distance value.

Finally all clusters are considered again to check if any two clusters possibly represent the same mode and should be merged. For this purpose, the inter-cluster distances are computed using the distance measure [15]:

$$d_{i,k} = \mu_p \frac{\sqrt{2 - 2\left(f_i f_k + \zeta_i \zeta_k + \left|\{\varphi_i\}^T \{\varphi_k\}\right|\right)}}{\sqrt{f_i^2 + \zeta_i^2 + \{\varphi_i\}^T \{\varphi_i\}}\sqrt{f_k^2 + \zeta_k^2 + \{\varphi_k\}^T \{\varphi_k\}}} \tag{5.14}$$

where f_i, f_k, ζ_i, ζ_k, $\{\varphi_i\}$ and $\{\varphi_k\}$ denote the natural frequency, modal damping ratio and mode shapes related to clusters i and k, respectively. If the respective inter-cluster distance is below a certain threshold value, the two clusters can be considered as representing the same mode and are merged. As threshold values 0.1 and 0.16 are recommended in [15] for, respectively, very low and relatively high signal-to-noise ratios in the measured data.

With respect to the inter-cluster distance defined in equation (5.14) it must be assumed that the mode shapes, natural frequencies and modal damping ratios must be scaled in a certain way such that the radicand in the numerator does not become negative. Unfortunately, this scaling is not mentioned in [15].

5.1.3 Automated mode tracking

Automated modal identification can be used to facilitate the analysis of any data set acquired during structural dynamic tests. However, the main motivation for the development of the procedures described in section 5.1 is the completely automatic analysis of large amounts of data that have been acquired, for example, during a long-term structural monitoring. Another important application can be the multiple analysis of a set of data using different parameters influencing the respective algorithm.

In these cases also the results of separate analyses have to be related to each other. For example, in the case of long-term structural monitoring one is interested in the evolution of modal parameters to identify effects of environmental conditions on the considered structure or to detect structural damage or deterioration. It is obvious that it is very important in this context, that the modal parameters to be compared but identified in separate analyses are related to the same physical mode of the structure. This can be very challenging, especially if the structure has some very close modes or if some modes are not well identified in some of the analyses. It may also be possible that, for example, a natural frequency of a certain mode increases due to system changes from one observation to a later instant to an extent that it has a value greater than the natural frequency of a higher-order mode at the first time. Such an effect may be caused by decreasing temperatures leading to frost which often results in stiffening effects.

Accordingly, a multiple automated modal analysis must also be able to track the identified modes correctly. As natural frequencies are not necessarily sufficient to track modes correctly, it seems natural to include the mode shapes. This has also been suggested, for example, in [41] where the modal assurance criterion MAC is used to assign the modes identified from different observations correctly. The successful application of the MAC in the context of long-term monitoring of a bridge has been reported in [92] where the mode shapes identified at any observation instant have been compared by means of the MAC with a set of reference modes identified at the beginning of the monitoring. Additionally, these comparisons are limited to frequency bands of ±15% of the respective reference frequencies assuming that the natural frequencies do not change more than 15 % due to varying environmental and operational conditions.

The application of the MAC is probably successful if data from a sufficient number of sensor locations is available. However, a monitoring system does not always have many sensors but only few or even only one. If it is not possible to distinguish the shapes of the modes identified from the measured signals clearly, the MAC is also not a sufficient criterion that can be used for a robust mode tracking. Therefore, in [143] is suggested to track the modes identified from two different observations by a distance measure that is based on respective residue matrices. The major limitation of this approach is that it requires the measurement of the excitation which is not available from operational modal tests. Only if an identical excitation can be ensured, for example in regular inspections, the suggested distance measure can be used as also stated in [143]. However, this is probably a rather exceptional situation for applications of operational modal analysis.

A methodology that does not compare the mode shapes but uses only natural frequencies has been described in [40]. It involves the modal transfer norm MTN which is a measure of contribution of a specific mode to the observed response. The procedure given in [40] suggests to sort the modes identified at one instant of time according to the descending order of their modal transfer norms. Starting with the mode with the highest modal transfer norm, one mode after another is assigned to the mode with the closest natural frequency identified from the previous observation. The respective mode corresponding with the previous observation is excluded from further search after having been assigned. This procedure is reasonable from the point of view that modes, which contribute to the observed structural response most, receive major attention. However, if a certain mode has not been identified either from the current or the previous identification, the modal assignment without consideration of this mode shape may become incorrect.

Chapter 6

Practical applications of operational modal analysis

The application of different operational modal analysis (OMA) techniques to numerically simulated vibration response data and to signals acquired in laboratory tests has been described already in section 3.6. Three further studies with respect to the practical application of OMA are presented in this chapter. The respective examples were selected to discuss specific issues that are also related to certain aspects of uncertainties in modal identification.

In the first example the performance of different OMA methods in the identification of modal parameters of a structure with very close modes is considered. The choice of algorithmic parameters and their respective influence on the obtained results is the major topic of the second case study. Uncertainties that may arise in the correct assignment of mode shapes identified from tests with sparse spacial resolution at structures showing modes dominated by deformations of specific structural members are discussed in the third application.

6.1 Operational modal analysis of a rotationally symmetric structure

In this section several parametric modal identification methods are applied to response data that was acquired during ambient vibration tests with an antenna mast. The considered structure is an almost 40 metres tall steel mast with circular tubular cross-section. It consists of four segments with diameters decreasing from bottom to top that are connected by bolted flanges. The graphical representation of a finite element model and a photograph are shown in figure 6.1.

There are two aspects in this example which make this case study interesting:

1. Due to the axial symmetry of the cross section, the structural bending modes occur as pairs with orthogonal mode shapes at theoretically identical natural frequencies.

2. The system has very weak damping.

Due to limited accessibility and restrictions with respect to available time for the tests, only two measuring points were instrumented with accelerometers oriented into two perpendicular lateral directions, respectively. The locations of the accelerometers are indicated in figures 6.1 and 6.2.

During the ambient vibration tests, the dynamic response of the mast was measured simulataneously at both measuring locations. The dominant excitation of the structure was caused by moderate wind. As the two measuring points were instrumented at the same time, the measurement contained four channels. The data analysed here, was acquired over a measurement duration of 1400 seconds at a sampling rate of 250 Hz.

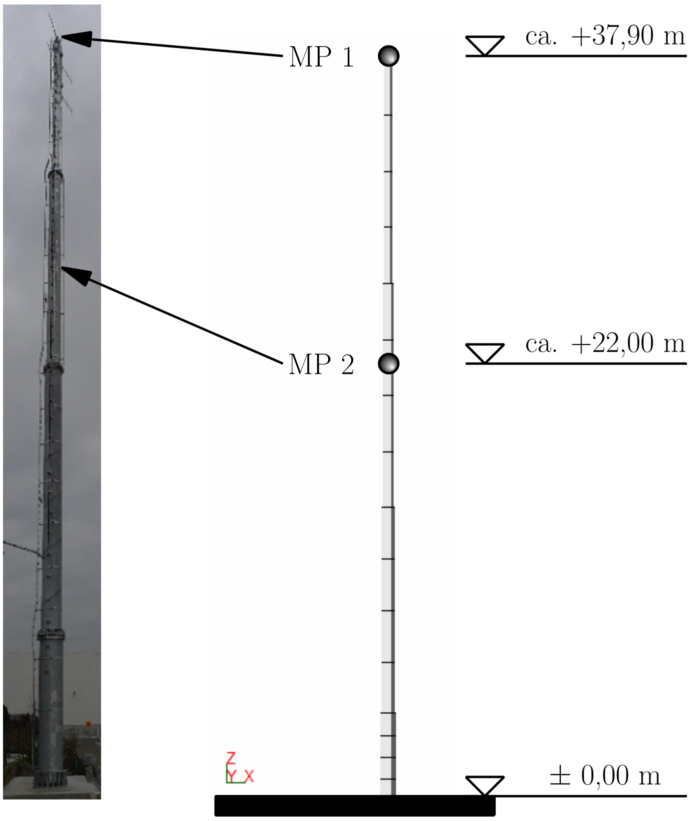

Figure 6.1: Antenna mast: photograph and finite element model

The measured accelerations were analysed by means of several OMA methods. In the analyses by means of parametric methods, the following stabilisation criteria were utilised:

- deviation in frequency = 1%
- deviation in damping = 5 %
- minimal $MAC = 0.98$

To validate the damping estimates obtained from the modal analyses, also free vibration tests were performed. In these tests the structure was excited to vibrations in a specific mode by rhythmic pulling on a rope that was attached to the mast at measuring point 2 as indicated

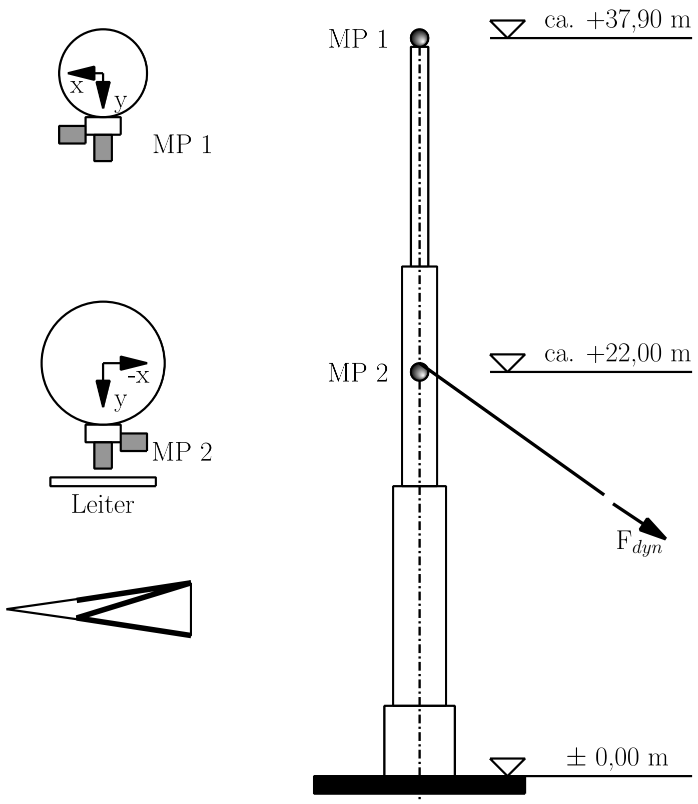

Figure 6.2: Antenna mast: unscaled geometry and location of measuring points

in figure 6.2. When the response had reached a level considerably above the ambient vibration response the excitation was stopped. From the free vibration curves the logarithmic damping decrement and subsequently the modal damping ratio of the respective excited mode were identified. Figure 6.3 shows an example of such a free vibration response curve together with the two exponential envelopes fitted to the positive and negative peak values, respectively.

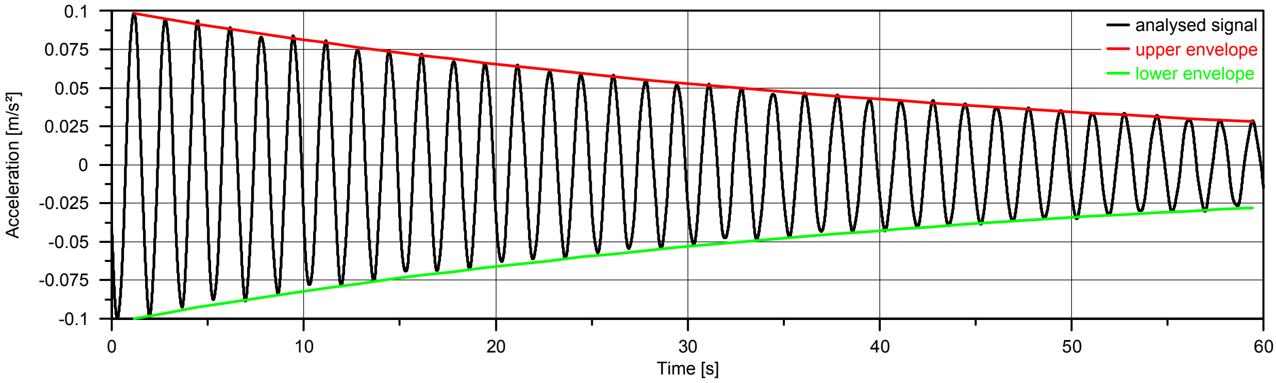

Figure 6.3: Antenna mast: typical free vibration response curve with fitted envelopes for damping estimation

From the free vibration response curves related to tests in which the structure was excited to resonance vibrations in either one of the first or second order bending modes, the modal damping ratios summarised in table 6.1 were identified. In some of the tests the structure was excited more than once. Therefore, the respectively analysed time frame is mentioned in table 6.1 as well. The values obtained from different tests vary within a certain range. Nevertheless, they give a reasonable estimate of the dimension that should be expected for the damping ratios that can be identified by means of an operational modal analysis. Therefore the results from the free vibration tests will be used in the following sections as respective references.

Table 6.1: Antenna mast: modal damping ratios identified from the free vibration curves

Test No.	Time sequence	frequency	modal damping ratio
2	25...85 s	0.604 Hz	0.60 %
2	115...165 s	0.602 Hz	0.47 %
3	30...80 s	2.220 Hz	0.15 %
3	170...200 s	2.221 Hz	0.14 %
3	300...350 s	2.220 Hz	0.17 %
3	440...520 s	2.220 Hz	0.15 %
4	40...110 s	2.220 Hz	0.16 %
5	70...130 s	0.601 Hz	0.57 %
6	70...130 s	0.601 Hz	0.57 %

In a preliminary study a finite element model of the mast was generated by means of 16 beam elements with tubular cross-sections and three mass points taking the additional masses at the connections between the four sections into account. Further, the influence of additional elements such as antenna cables, the ladder, antennas and respective auxiliary elements on the dynamic behaviour of the system were simplified by adding a distributed mass to the beam elements.

As geometric imperfections of the rotationally symmetric geometry and influences of unsymmetric mass distribution of non-structural members were not considered in the model, the numerical modal analysis considering the first eight modes resulted in four mode pairs with respective identical natural frequencies and orthogonal mode shapes. The computed modal parameters of the undamped system are summarised in table 6.2. From the graphical representations of the mode shapes, it becomes obvious that an instrumentation of only two measuring points is, of course, not sufficient to represent all eight bending mode shapes appropriety. However, with complementary knowledge from the numerical study, a clear assignment of the incomplete identified mode shapes to respective physical mode shapes is well possible in this case study. In the following sections, analyses of the measured time series by means of several identification methods and the respective results are presented.

Table 6.2: Natural frequencies and mode shapes of the antenna mast computed with the finite element model

f_n [Hz]	isometry	xz-plane	yz-plane	xy-plane
0.606	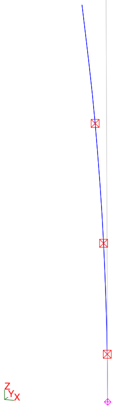	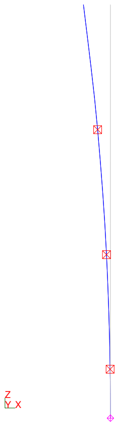	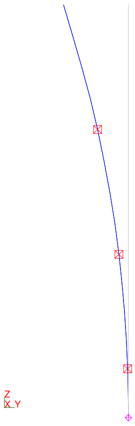	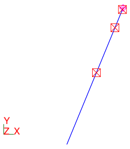
0.606	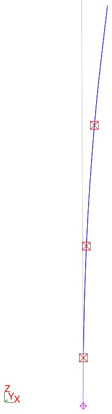	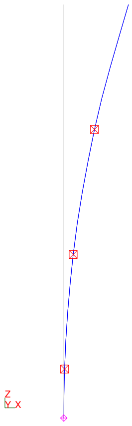	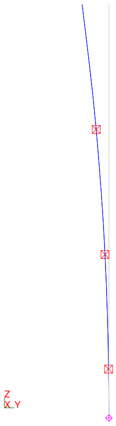	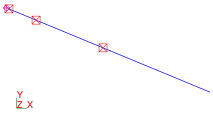
2.241	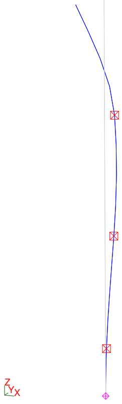	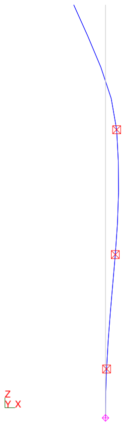	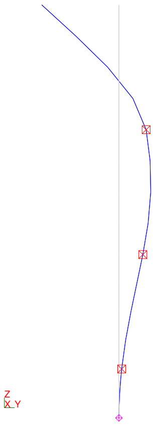	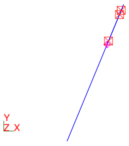

Table 6.2: Natural frequencies and mode shapes of the antenna mast computed with the finite element model (cont.)

f_n [Hz]	isometry	xz-plane	yz-plane	xy-plane
2.241	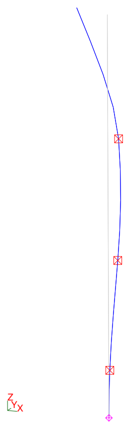	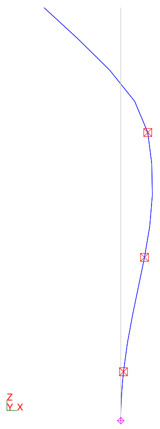	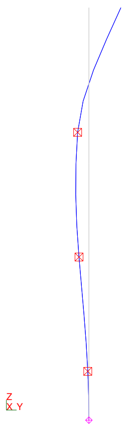	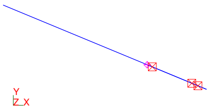
5.143	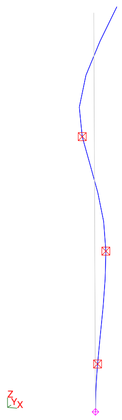	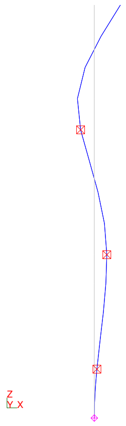	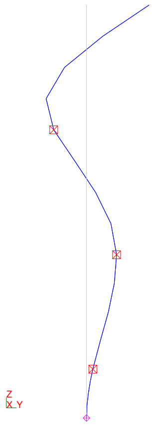	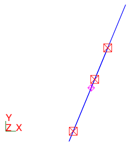
5.143	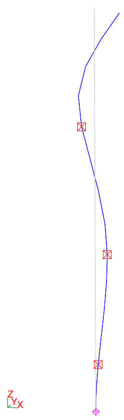	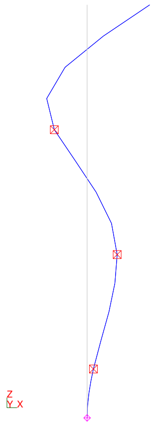	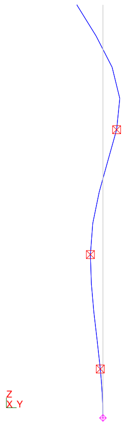	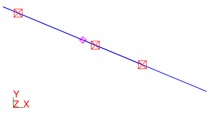

Table 6.2: Natural frequencies and mode shapes of the antenna mast computed with the finite element model (cont.)

f_n [Hz]	isometry	xz-plane	yz-plane	xy-plane
11.249	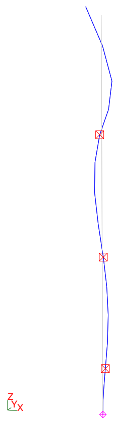	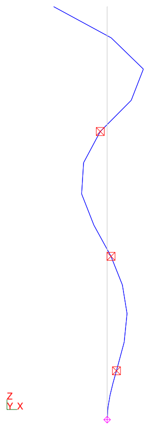	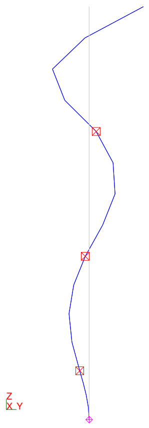	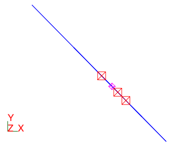
11.249	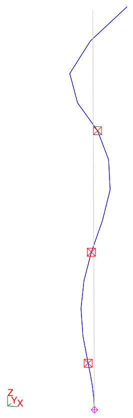	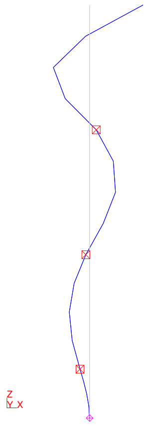	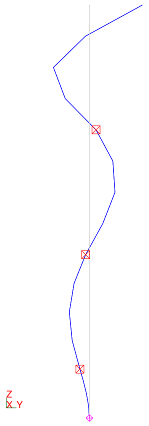	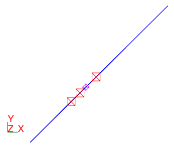

6.1.1 Analysis by means of the covariance-driven stochastic subspace identification (SSI-cov) method

For the analysis of the data measured at two locations of the mast in two horizontal directions, respectively, the following parameters were chosen:

decimation of the time series by factor 4 $\longrightarrow f_s$ = 62.5 Hz
number of block rows = number of block columns of the block Toeplitz matrix = 200
maximal model order = 50

By analysing the measured time series using all four channels as references, the stabilisation diagrams given in figure 6.4 were generated. It can be very well seen, that several modes obviously occur at very close frequencies. A zoom into the low frequency range shows that the solutions at about 0.6 Hz form two columns of stable poles related to two distinct modes. Only very few solutions are not marked as stable poles. This can be interpreted as an indicator for a successful system identification based on measured data of appropriate quality.

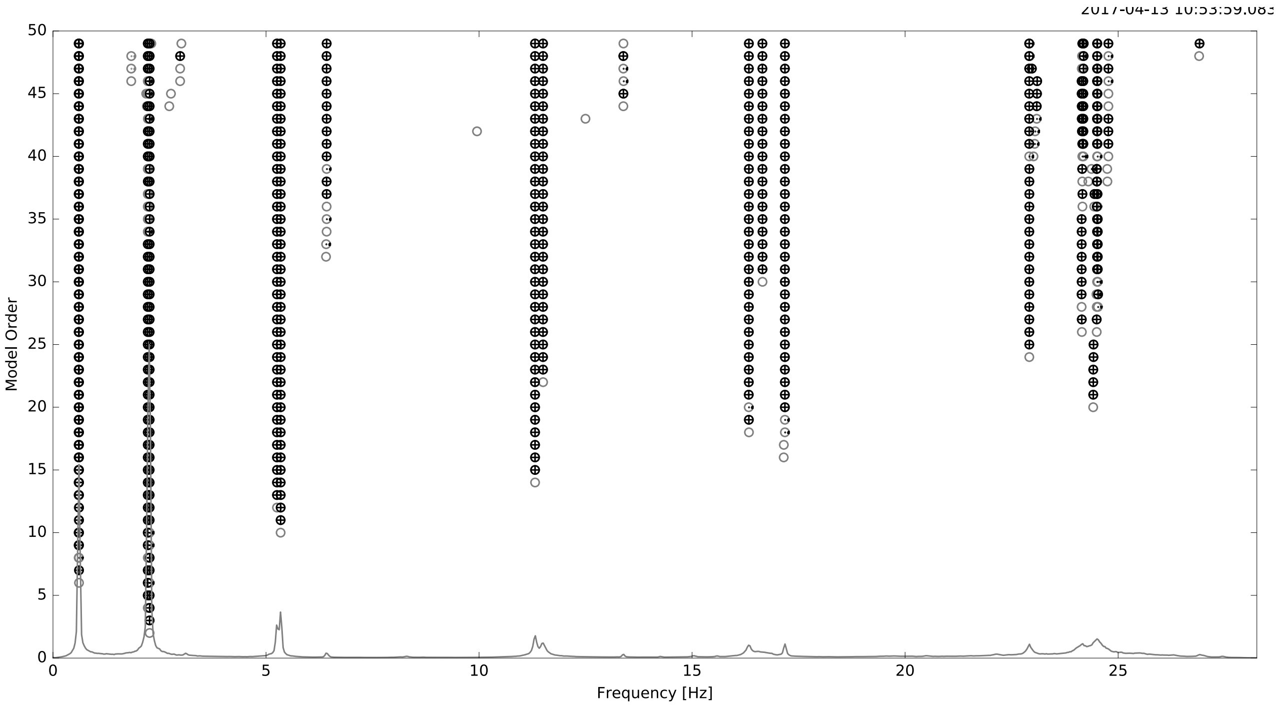

(a) total frequency range

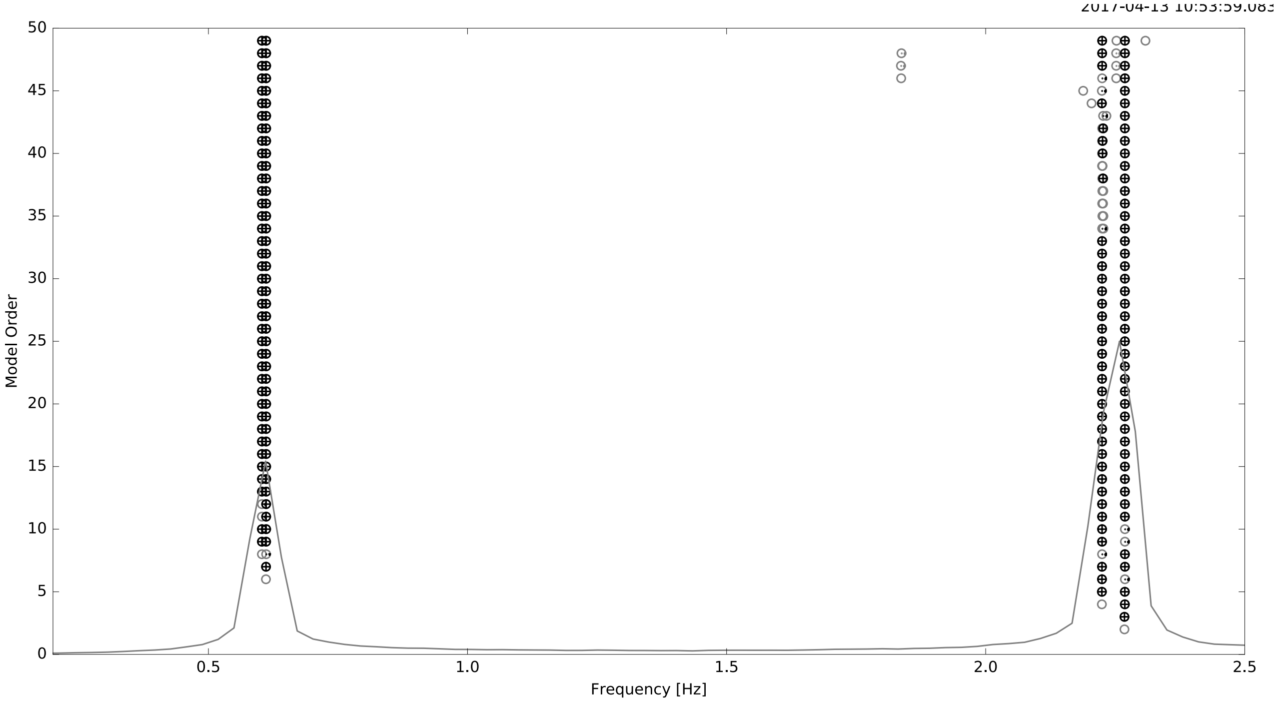

(b) zoom into low frequency range

Figure 6.4: Antenna mast system: stabilisation diagram obtained by means of the SSI-cov method

Table 6.3: Antenna mast system: modal parameters of the first eight bending modes identified by means of the SSI-cov method, solutions obtained for model order 30

f_n [Hz] ζ_n [%]	mode shapes identified	 numerical	f_n [Hz] ζ_n [%]	mode shapes identified	 numerical
0.603 Hz 0.461 %	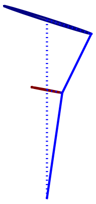		0.611 Hz 0.412 %	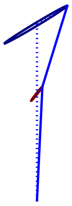	
2.225 Hz 0.090 %	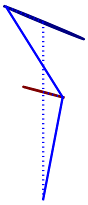		2.269 Hz 0.059 %	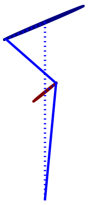	
5.258 Hz 0.109 %	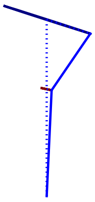		5.344 Hz 0.092 %	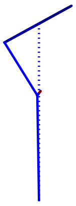	
11.314 Hz 0.184 %	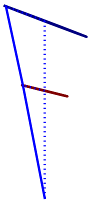		11.502 Hz 0.337 %	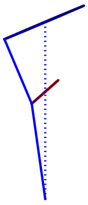	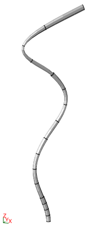

The identified natural frequencies, modal damping ratios and mode shapes extracted for model order 30 are given in table 6.3.

The mean values and coefficients of variation of both the natural frequencies and modal damping ratios identified for the first 8 modes are summarised in table 6.4. The underlying data is represented graphically in figure 6.5. In this diagramm one can very well recognise the different clusters with very small scatter containing the solutions of one mode.

A comparison between the damping ratios identified by means of the SSI-cov analysis and obtained from the free vibration tests (table 6.1) shows a good agreement. The damping ratios extracted from the free vibration curves are slightly higher than those identified by means of the SSI-cov algorithm. One reason for these deviations could be that the amplitudes due to the excitation by rhythmic pulling of the rope were higher than those during the ambient vibration tests. The vibrations at larger amplitudes may have activated slightly higher energy dissipation, for example in connections. Nevertheless, the detected differences are relatively small.

Table 6.4: Antenna mast system: mean values and coefficients of variation (COV) of the modal parameters of the first eight bending modes identified by means of the SSI-cov method

mode No.	$\bar{f}_r$	COV(f_r)	$\bar{\zeta}_r$	COV(ζ_r)
1	0.603 Hz	0.00 %	0.460 %	1.215 %
2	0.611 Hz	0.00 %	0.410 %	0.365 %
3	2.225 Hz	0.00 %	0.091 %	3.954 %
4	2.269 Hz	0.00 %	0.060 %	2.326 %
5	5.258 Hz	0.00 %	0.109 %	2.580 %
6	5.344 Hz	0.00 %	0.091 %	1.356 %
7	11.314 Hz	3.5e-3 %	0.186 %	0.961 %
8	11.502 Hz	0.00 %	0.337 %	0.358 %

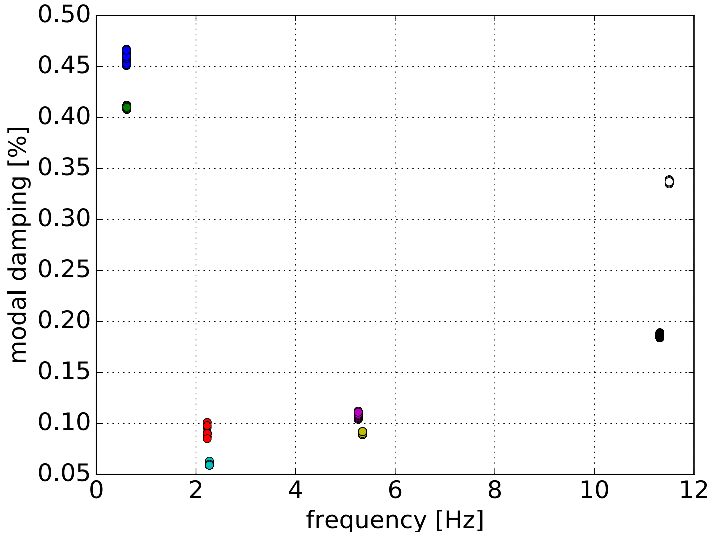

Figure 6.5: Antenna mast: natural frequencies and modal damping ratios identified by means of the SSI-cov method

6.1.2 Analysis by means of the data-driven stochastic subspace identification (SSI-data) method

The time series that were analysed by means of the SSI-cov method have also been used for a modal analysis by means of the SSI-data algorithm. For the results presented in this section the following parameters were chosen:

decimation of the time series by factor 4 $\longrightarrow f_s = 62.5\,Hz$
number of block rows = number of block columns of the block Hankel matrix $= 400$
maximal model order $= 50$

With these parameters the stabilisation diagram shown in figure 6.6 has been obtained. Again the solutions corresponding to the pairwise orthogonal modes with very close frequencies can be very well identified. The mode shapes look qualitatively very similar to those identified by means of the SSI-cov method which are given in table 6.3. Therefore, these graphical representations of the identified mode shapes are not repeated here.

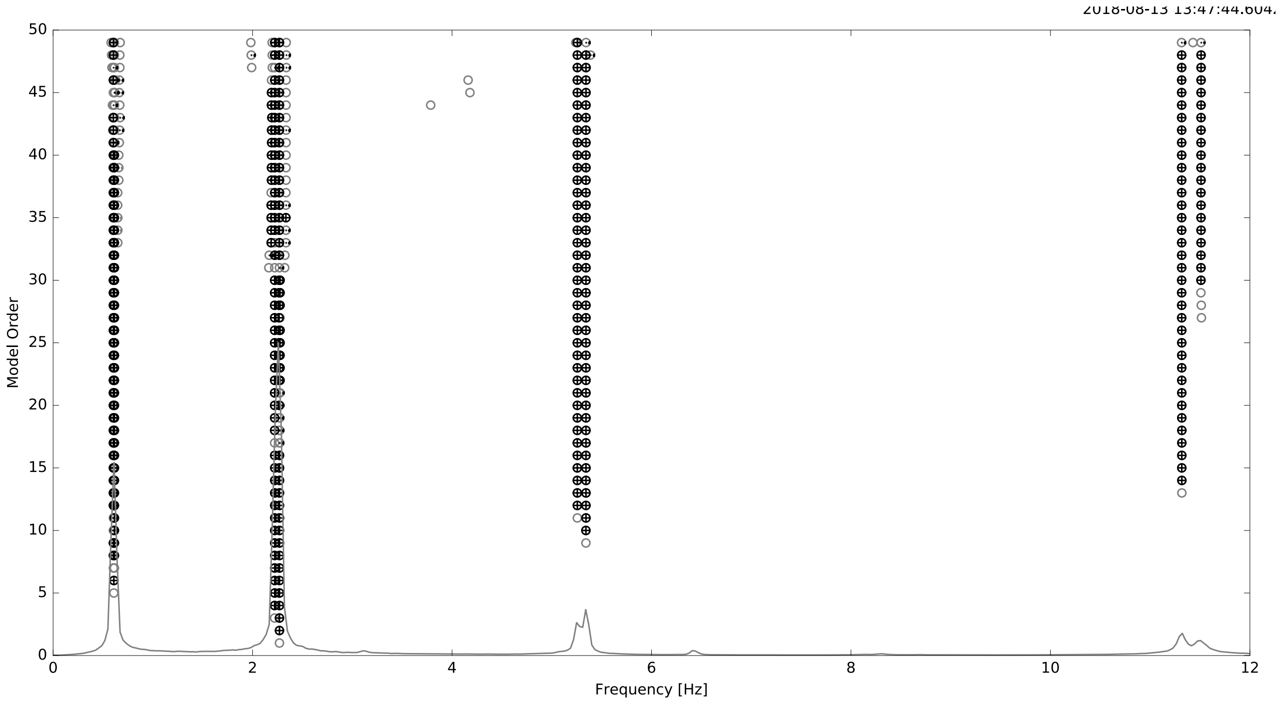

Figure 6.6: Antenna mast system: stabilisation diagram obtained by means of the SSI-data method

The mean values of the natural frequencies and modal damping ratios identified with the SSI-data method as well as the corresponding coefficients of variation are summarised in table 6.5. In figure 6.7 the identified modal parameters for which the respective statistical values were calculated, are shown.

The identified modal parameters are very similar to those obtained by means of the covariance-driven SSI. Some deviations of the uncertainties of the estimated modal damping ratios can be noticed. In particular for the first two modes, the coefficients of variation are slightly higher.

Table 6.5: Antenna mast system: mean values and coefficients of variation (COV) of the modal parameters of the first eight bending modes identified by means of the SSI-data method

mode No.	$\bar{f}_r$	COV(f_r)	$\bar{\zeta}_r$	COV(ζ_r)
1	0.604 Hz	0.00 %	0.355 %	3.455 %
2	0.614 Hz	2.79e-2 %	0.610 %	1.489 %
3	2.222 Hz	2.15e-2 %	0.124 %	0.306 %
4	2.270 Hz	7.55e-3 %	0.091 %	1.026 %
5	5.256 Hz	0.00 %	0.086 %	1.109 %
6	5.343 Hz	0.00 %	0.073 %	1.012 %
7	11.316 Hz	5.30e-3 %	0.137 %	2.378 %
8	11.510 Hz	3.24e-3 %	0.320 %	1.266 %

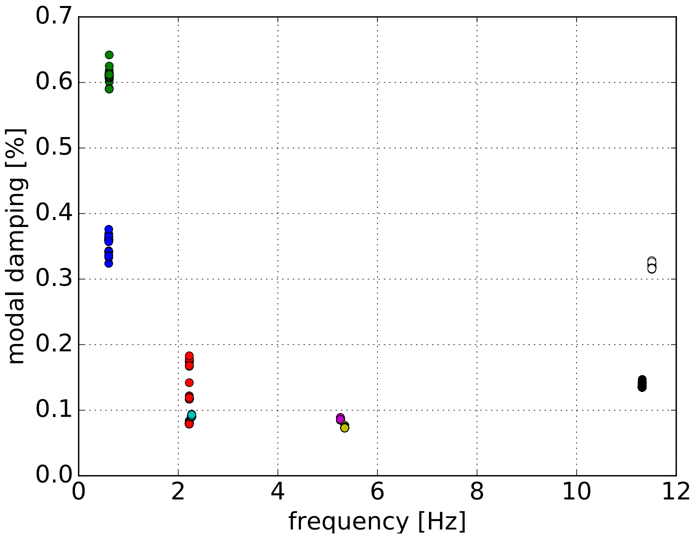

Figure 6.7: Antenna mast: natural frequencies and modal damping ratios identified by means of the SSI-data method

6.1.3 Analysis by means of the poly-reference least square complex exponential (p-LSCE) method

The application of the p-LSCE algorithm to the data measured at the antenna mast showed that the results that could be obtained with this method for this example lead to far fewer stabil solutions than the two considered SSI algorithms. In particular the identified mode shapes devitated in many cases from model order to model order while the modal damping ratios and natural frequencies showed a much better stabilisation behaviour. These observations could not be significantly improved by choosing different analysis parameters. The results presented in the following were obtained using as analysis parameters

$$\begin{array}{lcl} \text{length of correlation series } 2N & = & 2 \times 250 \; = \; 500 \text{ samples and} \\ \text{maximal model order} & = & 50 \end{array}$$

The corresponding stabilisation diagram is given in figure 6.8. In this case not only stable but all solutions are shown. Further, the stabilisation threshold for the MAC was reduced compared to the value chosen for the analyses with the SSI methods. For the solutions in figure 6.8 the following stabilisation criteria were defined:

- deviation in frequency $= 1\%$
- deviation in damping $= 5\ \%$
- minimal $MAC = 0.90$

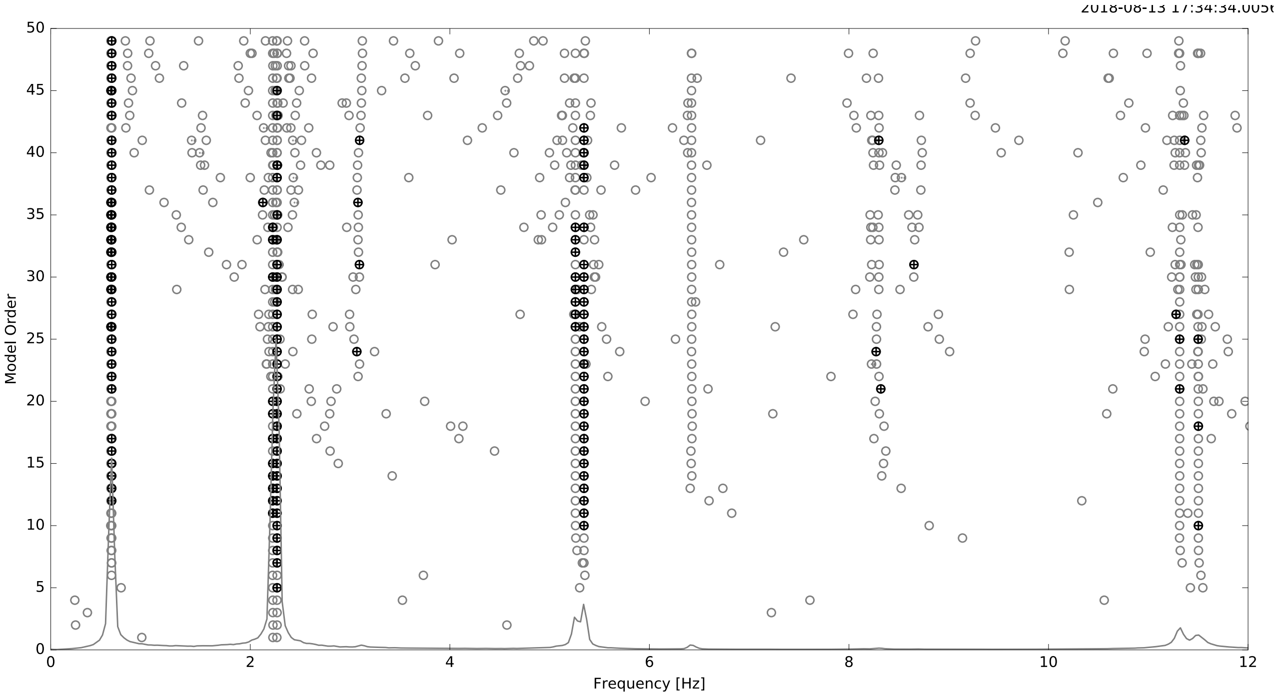

Figure 6.8: Antenna mast system: stabilisation diagram obtained by means of the p-LSCE method

To obtain meaningful results for the statistical analysis of the natural frequencies not only respective stabil solutions were selected. Instead the selection was based on two criteria related to the mode shapes:

- The mode shape should be consistent with the shapes known from the identification by means of the SSI methods and
- Due to the low damping values a small degree of complexity should be expected; therefore only results with an $MPC > 0.95$ were taken into account.

Based on this approach, the natural frequencies and modal damping ratios indicated in figure 6.9 with the statistical parameters collected in table 6.6 were obtained. Not only the identified natural frequencies but also the modal damping values are in a similar range as the respective results obtained applying the SSI methods to the same measured data. However, as mentioned before the mode shapes estimated by means of the p-LSCE method from the time series measured at the antenna mast show in many cases a relatively high degree of complexity and deviating shapes from model order to model order.

These observations let one conclude that the separation of the mode shapes corresponding to very close natural frequencies is difficult if the p-LSCE method is applied to the ambient vibration data that was used in this study. Apart from relatively high and non-proportional damping, a well known reason for complex modes are very close natural frequencies and double symmetry of the considered structure [49]. Even though the damping of the steel cantilever is relatively low, its almost perfect circular cross-section causes paired modes with nearly identical natural frequencies which can lead to the identification of modes with a relatively high degree of complexity that can be quantified for example by low values of the modal phase collinearity MPC as described in section 4.1.1.

Table 6.6: Antenna mast system: mean values and coefficients of variation (COV) of the modal parameters of the first eight bending modes identified by means of the p-LSCE method

mode No.	$\bar{f}_r$	COV(f_r)	$\bar{\zeta}_r$	COV(ζ_r)
1	0.603 Hz	0.00 %	0.453 %	1.351 %
2	0.611 Hz	6.41e-2 %	0.419 %	2.677 %
3	2.225 Hz	0.00 %	0.087 %	3.434 %
4	2.269 Hz	1.67e-2 %	0.059 %	7.917 %
5	5.258 Hz	0.00 %	0.112 %	0.657 %
6	5.344 Hz	0.00 %	0.093 %	1.308 %
7	11.314 Hz	4.42e-3 %	0.188 %	0.579 %
8	11.501 Hz	7.78e-3 %	0.345 %	0.799 %

6.1.4 Comparison of the estimated modal parameters for the antenna mast

As described in the previous sections, the natural frequencies identified by means of the three applied parametric methods agree almost perfectly. The deviations between the respective mean values are in the range of fractiles of one per cent. Similarly, the scatter of the identified natural frequencies, quantified by the coefficients of variation are negligible.

Even though the uncertainties of the identified modal damping ratios are usually greater than those related to natural frequencies, the values obtained in this study agree very well. In figure 6.10 the mean values and standard deviations of the identified modal damping ratios are illustrated. One can observe that the respective values identified by means of the SSI-cov and

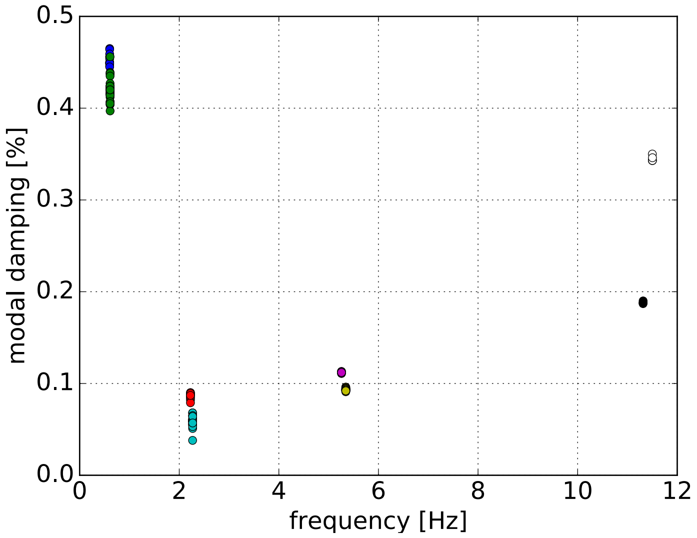

Figure 6.9: Antenna mast: natural frequencies and modal damping ratios identified by means of the p-LSCE method

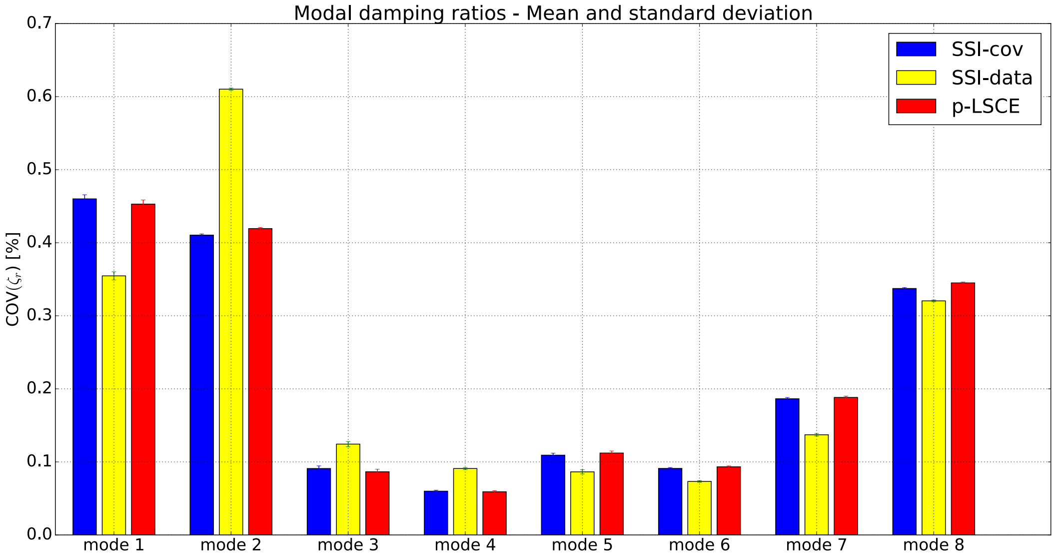

Figure 6.10: Antenna mast: comparison of the modal damping ratios identified with different methods

p-LSCE methods are almost identical for all modes. Only the results estimated with the SSI-data algorithm deviate slightly stronger. However, these deviations are in most cases within an acceptable range.

The standard deviations indicated in the diagram in figure 6.10 by the small range lines at the top end of the bars are hardly noticeable which can be interpreted as an indicator for a high degree of confidence. As mentioned earlier, the modal damping ratios identified from the free vibration curves generated by exciting the structure at the natural frequencies of modes 1, 2, 3, and 4 are also within the range of the values obtained by the applied modal analysis algorithms. This observation also confirms as well the reliability of the identification results.

Nevertheless, it needs to be mentioned that the selection of the solutions presented here has been performed manually taking a certain degree of experience into account. An automatic selection procedure may have led to different results. Especially in the case of the p-LSCE method an automatic clustering algorithm would proably have failed in the identification of some of the modes. In this respect further research and development is still needed.

6.2 Algorithmic uncertainties in the operational modal analysis of a bridge deck

In section 6.1 the results obtained by means of different parametric identification methods are compared. It has been discussed that the modal parameters identified for different model orders varied to a certain extent. However, for each exemplary analysis by means of a certain OMA method only one set of algorithmic parameters has been applied. The influence of the choice of parameters such as the number of block columns of the block Toeplitz matrix created within an SSI-cov analysis or the length of the correlation series used in the p-LSCE algorithm have not been addressed so far. This question is the focus of this section.

By means of the example of ambient vibration tests that were performed on a railway bridge, it is illustrated, how the uncertainties of the modal parameters identified by means of the SSI-cov method behave in relation to the chosen number of block columns in the block Toeplitz matrix. This is one of the governing parameters of the SSI-cov algorithm. Similar studies could be generated for other parameters that are related to further identification methods. However, here only one such example is given as an introduction into the field of algorithmic uncertainties in operational modal analysis.

The chosen case study is a railway bridge with a single span of 32.50 meters. It spans over a small river and accommodates two tracks on ballast bed. The superstructure consists of two separate cross-sections of which each carries one track as illustrtated in figure 6.11. The main structure of the bridge deck consists of two times four pre-stressed composite beams that were connected to two monolithic beams by in-situ concrete. More details about the construction of such a so-called PREFLEX bridge deck as well as further information about the bridge are given, for example, in [149]. Photographs of the bridge are shown in figures 6.12 and 6.13.

Even though the two parts of the superstructure are statically independent, the ballast is continuous over the complete cross-section. This results in a certain degree of coupling of the two parts of the bridge deck. Accordingly, the dynamic behaviour of the bridge considered here is similar to the one that has been observed for many typical filler-beam railway bridges as described, for example in [148], [30] and [147].

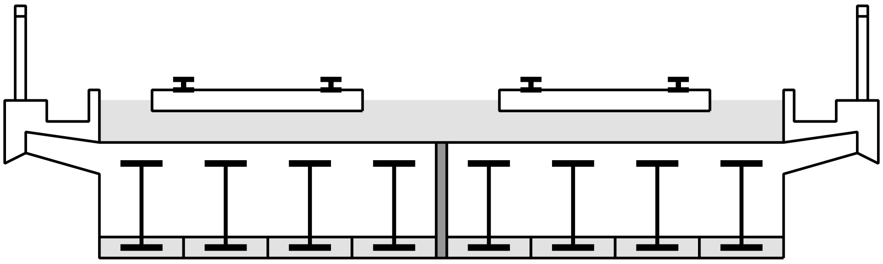

Figure 6.11: Investigated railway bridge: cross-section of the bridge deck

Figure 6.12: Investigated railway bridge: Tracks on ballast (left) and side view (right)

6.2.1 Description of the ambient vibration tests

Also in this study the ambient vibration tests were carried out as a one-day campaign. As the ballast covered the complete bridge deck and the railway traffic across the bridge could not be interrupted for the tests, all sensors had to be installed on the bottom side of the bridge. Since longitudinal and lateral movements and deformations of the bridge deck are of minor importance compared to the bending and torsional deformation, the sensors were only installed for measurements of accelerations in vertical direction. Figure 6.13 gives an impression of the installation of the accelerometers.

In figure 6.13 one can very well see that the bottom side of the bridge deck was relatively easily accessible. However, this was only the case at the banks to both sides of the river. The installation of sensors over the river bed would have required a higher technical effort that could not be provided for a one-day campaign.

Figure 6.13: Investigated railway bridge: sensor installation at the bottom side of the bridge deck

To obtain a spacial resolution that was sufficient to visualise bending and torsional mode shapes of up to 3rd or 4th order, 40 measuring points were defined. As not all these locations could be instrumented at the same time, the tests were organised in six setups. Four measuring locations were selected as reference points were the accelerometers were kept during all tests. At the remaining 36 measuring points, six roving sensors were placed in six setups. Figure 6.14 gives an overview about the respective locations of the sensors in the six setups.

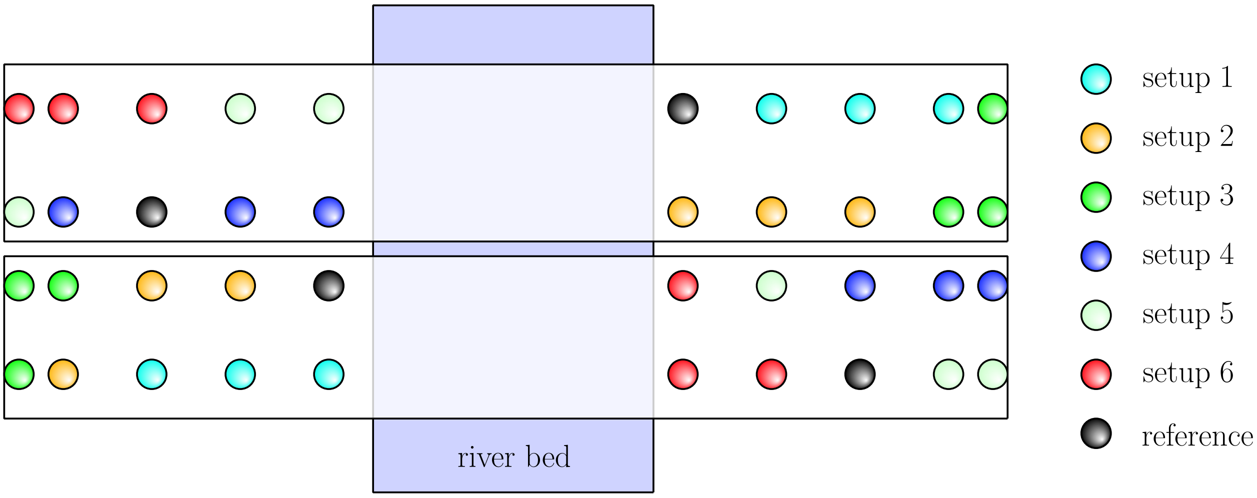

Figure 6.14: Investigated railway bridge: sketch of measuring points instrumented in six setups in plan view

For the response measurements seismic accelerometers with a nominal sensitivity of 1 $\frac{V}{g}$ were used. To improve the degree of excitation for as many modes as possible and to increase the signal-to-noise ratio, multiple impulses were imposed to the bridge deck from underneath during the measurements.

Ambient vibration response data on short and medium span railway bridges should always be acquried without the influence of trains passing over the bridge. With moving trains on the bridge the assumption of time-invariance of the considered system is strongly violated. Consequently, the ambient vibration tests could only be performed during intervals between train passages. The density of traffic consisting of both freight and passenger trains was comparatively high. Therefore, the duration of each measurement was limited to about three minutes.

6.2.2 Modal identification

First a modal identification by means of the reference-based covariance-driven stochastic subspace identification (SSI-cov/ref) method was performed. The four channels corresponding to the reference sensors were also used as reference signals in the modal analysis of the data acquired in the six setups. During the ambient vibration tests, the time series were acquired with a sampling rate of 2084 Hz. For the modal identification the measured data was decimated by a factor of 16 to a sampling rate of 128 Hz.

Within the modal analyses both the post separate estimation re-scaling (PoSER) and the post global estimation re-scaling (PoGER) methods were applied to merge the modal parameters estimated for the six test setups. In both cases it was possible to identify 14 modes. Table 6.7 summarises point estimates of mode shapes and natural frequencies of these 14 modes. Even though information about modal deflections in the central part of the span is not available due to limited accessibility, the identified mode shapes can still be well assigned to the bending and torsional modes of respective order.

Further, the identified mode shapes indicate the weak coupling of the two superstructures by the continuous ballast. All identified mode shapes, bending modes of first to fourth order and torsional modes up to third order, occur in two forms. Once the two superstructures move in phase and once in anti-phase. The lower natural frequencies always correspond to the respective version of a mode that includes less relative movements in the interface between the two superstructures. This observation is very reasonable as it confirms the contribution of both the continuous ballast and the elastic filling in the joint gap between the two composite superstructures to the stiffness of the bridge deck.

With the identified natural frequencies and mode shapes collected in table 6.7 a good set of information about the modal behaviour of the bridge deck was available. In the next step the relation between the number of blocks considered in the generation of the block-Toeplitz matrix within the modal identification by means of the SSI-cov method and the identified modal parameters should be investigated. In this study, the numbers of block columns and block rows were chosen to be equal. They were varied in a range from 100 to 440 with increments of 10. From each block-Toeplitz matrix, system matrices for state space models of an order up to 200 were derived.

This investigation required numerous repetitions of both computations and selections of modal solutions. To facilitate these analyses, an automatic procedure was developed. Within this procedure the information related to the different test setups was merged by means of the post global estimation re-scaling (PoGER) method. In this way, only one stabilisation diagram was obtained for each chosen number of block columns/rows.

The selection of modal solutions to be taken into account in the statistic analyses had to be automated as well. In this study, the respective sets of modal parameters were compared with the natural frequencies and mode shapes presented in table 6.7. Additionally, to assure that only identified modal solutions with physical relevance are comprised, it was examined if the modal damping ratios were within a given range. Accordingly, the following selection criteria had to be satisfied:

- $0.95 f_{r,ref} \leq f_{r,i} \leq 1.05 f_{r,ref}$,
- $0.00 \leq \zeta_{r,i} \leq 0.10$,
- $MAC(\varphi_{r,ref}, \varphi_{r,i}) > 0.95$.

In these criteria $f_{r,i}$ and $f_{r,ref}$ refer to the rth natural frequency of solution i and of the reference solutions, respectively. Further, $\zeta_{r,i}$ denotes the modal damping ratio of mode r of solution i, while $MAC(\varphi_{r,ref}, \varphi_{r,i})$ is the respective MAC value between the reference shape $\varphi_{r,ref}$ and the one of solution i, $\varphi_{r,i}$.

All sets of modal parameters corresponding to different model orders satisfying these criteria were then used to derive respective statistical parameters for each chosen number of block columns/rows.

Table 6.7: Investigated railway bridge deck: summary of identified mode shapes and point estimates of the natural frequencies

f = 3.52 Hz 1st order bending, in phase 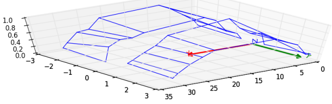	f = 7.04 Hz 1st order bending, anti-phase with torsion 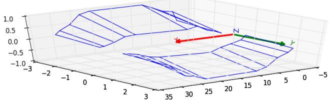	f = 11.77 Hz 2nd order bending, in phase 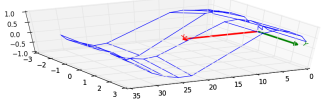
f = 11.97 Hz 1st order torsion, anti-phase 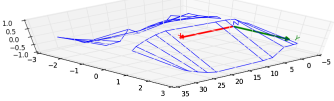	f = 14.96 Hz 2nd order bending, anti-phase 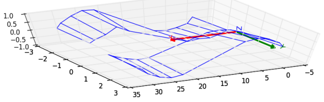	f = 21.24 Hz 1st order torsion, in phase 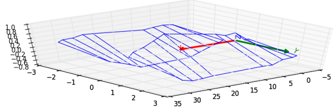
f = 23.89 Hz 3rd order bending, in phase 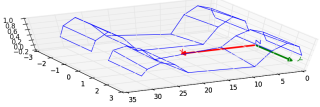	f = 25.68 Hz 3rd order bending, anti-phase 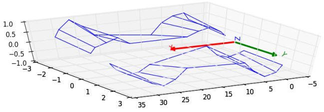	f = 26.90 Hz 2nd order torsion, anti-phase 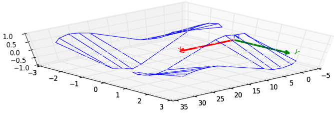
f = 31.40 Hz 2nd order torsion, in phase 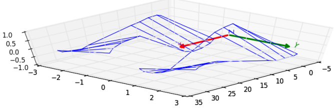	f = 38.88 Hz 4th order bending, in phase 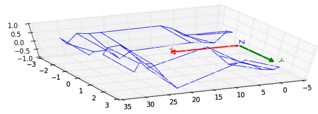	f = 40.01 Hz 4th order bending, anti-phase 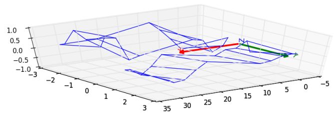
f = 53.37 Hz 3rd order torsion, anti-phase 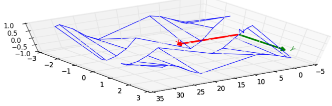	f = 55.14 Hz 3rd order torsion, in phase 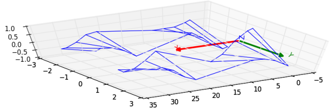	

6.2.3 Statistic analysis of the identified modal parameters

For each set of estimated modal parameters corresponding to one number of block rows/columns in the block Toeplitz matrix and one mode, the mean values and coefficients of variation were computed. The resulting values are presented in table 6.8. These results give an impression on how much the identified modal parameters may vary depending on the choice of the algorithmic parameters and the selected model order. However, this summary does not give an information about relations between the uncertainties and the choice of the number of block rows/columns of the block-Toeplitz matrix.

In figure 6.15 is shown for two modes, how the identified natural frequencies and modal damping ratios may differ depending on the chosen number of block columns / rows of the block-Toeplitz matrix and model order. In the case of the first mode, relatively clear trends for both the natural frequencies and damping ratios are suggested by the results while a decrease of variance in the results with increasing number of block columns of the block-Toeplitz matrix can be observed in the diagrams corresponding to the mode with $\bar{f}_r = 26.89$ Hz .

Table 6.8: Mean values and coefficients of variation of the natural frequencies ($\bar{f}_r$, $COV(f_r)$) and modal damping ratios ($\bar{\zeta}_r$, $COV(\zeta_r)$) identified with the SSI-cov method

$\bar{f}_r$ [Hz]	$COV(f_r)$ [%]	$\bar{\zeta}_r$ [%]	$COV(\zeta_r)$ [%]
3.50	0.18	1.12	29.22
7.00	0.46	2.79	17.25
11.78	0.27	3.52	11.37
11.99	0.15	1.14	15.90
14.94	0.41	4.70	11.34
21.24	0.38	3.20	16.64
23.95	0.25	3.50	4.38
25.67	0.10	2.27	4.72
26.89	0.13	1.24	15.69
31.41	0.36	1.46	46.80
39.07	0.58	3.43	11.38
40.00	0.12	2.05	7.62
53.35	0.09	1.56	13.77
55.11	0.18	2.16	30.79

To quantify the uncertainties in the results represented in figure 6.15, the mean values and coefficients of variation of both the natural frequencies and modal damping ratios identified for the two modes were computed for all chosen numbers of block columns. The respective results are displayed in figures 6.16 and 6.17.

In fact, the data presented in these diagrams seems to confirm the impression that was qualitatively obtained from figure 6.15 in a quantified way. Both the mean values and uncertainties tend to converge with increasing number of block columns of the block-Toeplitz matrix to a certain value. For some other modes a similar behaviour could be observed in this

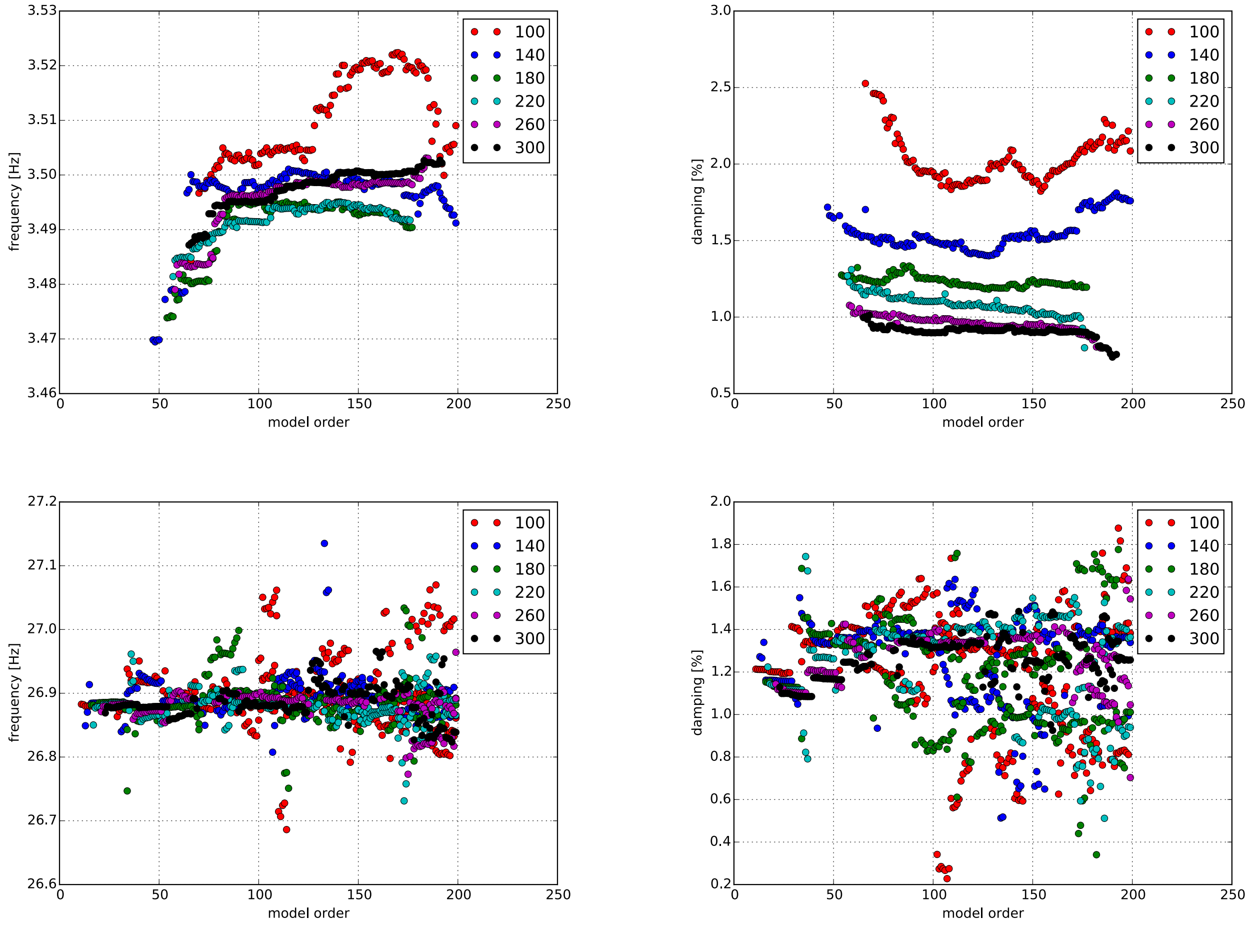

Figure 6.15: Natural frequencies and modal damping ratios of the modes with $\bar{f}_r = 3.50$ Hz (top) and $\bar{f}_r = 26.89$ Hz (bottom) identified with the SSI-cov for 100, 140, 180, 220, 260 and 300 block columns

case study, however, not for all modes. In this context it needs to be mentioned that not all modes were very well identified in all analyses. This gives reason to the conclusions that

1. the observation of convergence of both mean values and coefficients of variation of the identified modal parameters with increasing number of block columns of the block-Toeplitz matrix cannot be generalised and
2. it can be assumed that there exist relations between the degree of excitation of a certain mode during the test, the quality of the measured data, the chosen algorithmic parameters and the uncertainties in the identified modal parameters.

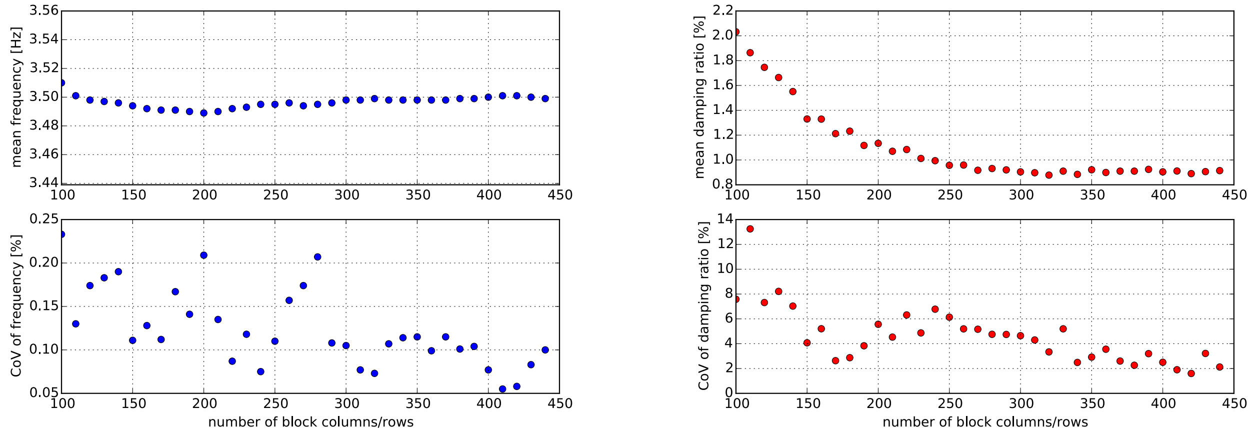

Figure 6.16: Mean values and corresponding coefficients of variation of the natural frequencies (left) and modal damping ratios (right) identified with the SSI-cov for the mode with $\bar{f}_r = 3.50$ Hz for all chosen numbers of block columns

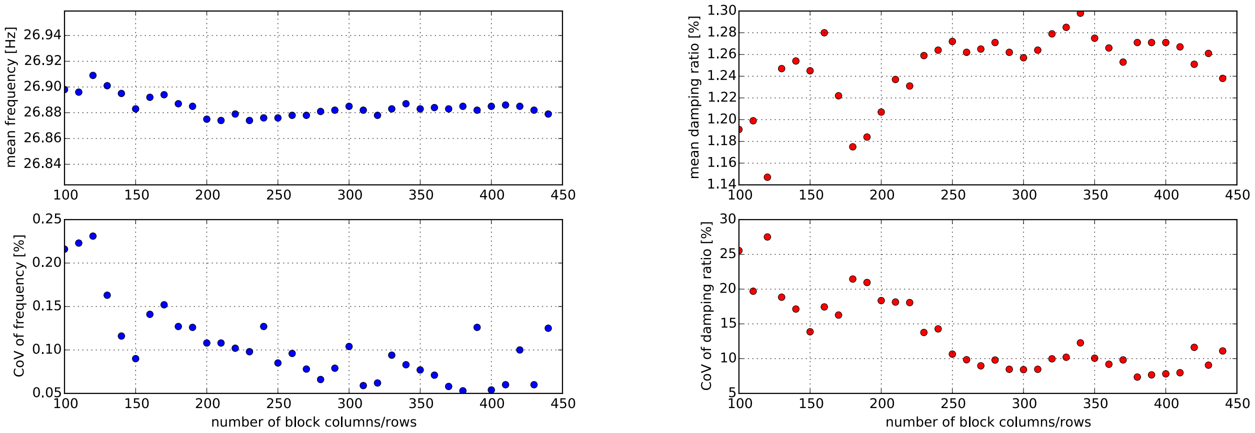

Figure 6.17: Mean values and corresponding coefficients of variation of the natural frequencies (left) and modal damping ratios (right) identified with the SSI-cov for the mode with $\bar{f}_r = 26.89$ Hz for all chosen numbers of block columns

6.3 Operational modal analysis at structures with locally dominated modes

6.3.1 Problem description

As has been already mentioned in section 6.1 technical and economical reasons may lead to uncertainties in the identification of mode shapes when only very few locations of the structure can be instrumented during ambient vibration tests. One possibility to overcome this problem to a certain extent is the comparison of the experimental results with those of a numerical modal analysis using a finite element model or, if possible, analytical functions.

However, this approach has also its limitations. This is especially the case for structures consisting of multiple structural elements such as, for example, cable-stayed, suspension or tied-arch bridges. In these cases there are several modes that are dominated by deformations of the bridge deck and others that rather pertain to the members of the suspension system. In ambient vibration tests, often sensors can be only placed on the deck of such a bridge. This means that the spacial information of the identified mode shape is not only limited, but for some parts of the structure, which may have a strong local modal behaviour, no information is available.

Even if the number of measuring points on the bridge deck is sufficient to clearly identify also bending mode shapes of higher order, one problem may arise from the fact that an operational modal analysis can only provide unscaled mode shapes. There may be the situation that there are modes that are dominated by local vibrations, for example of the hangers of a tied-arch bridge. In this case the bridge deck will also move in a shape that is similar to the mode shape of the bridge deck which has the closest natural frequency to the local mode of the hanger.

This problem is graphically illustrated in figure 6.18 by means of two close modes obtained from a numerical modal analysis of a finite element model of a tied-arch bridge. In the left column of the figure the shape of a mode that ist clearly dominated by hanger vibrations is shown, while in the right column the modal amplitudes of the bridge deck are much larger in relation to the hanger vibrations. The vibration shape of the bridge deck is in both modes qualitatively almost identical.

From an operational modal analysis based on measurements with sensors located only on the bridge deck, one could hardly distinguish between the two mode shapes. Due to the fact that the frequencies are also very similar, it would also be difficult to derive the correct information by means of a finite element model. The order of the two modes can be easily reverse for the numerlical model and the physical structure contingent on uncertainties in the correct description of parameters describing mass and stiffness in the numerical model. Therefore, it would be strongly recommended also to install sensors at the hangers of the bridge if they are accessible. A description of such a practical application is reported in [124].

Similar problems may arise in the operational modal identification of guyed masts if the cables cannot be instrumented. Addionally, the modal analysis of these structures becomes even more challenging as these masts have commonly a double symmetric cross-section. In the following sections a respective case study and a proposal for an approach to distiguish between modes dominated by vibrations of the mast and the cables, respectively, are presented.

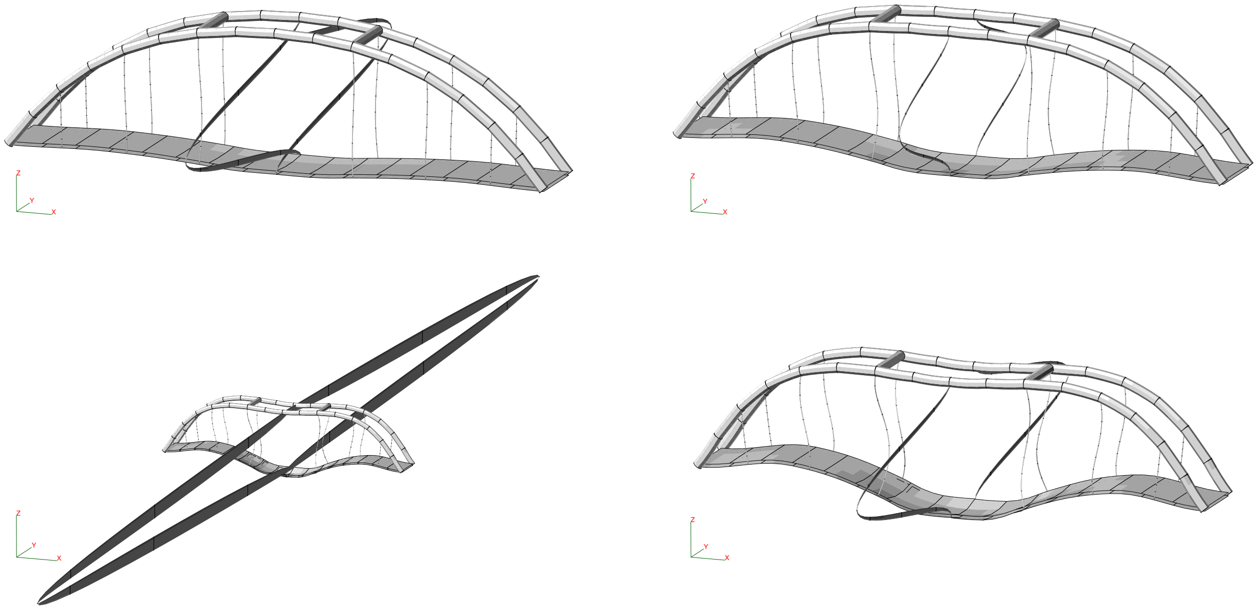

Figure 6.18: Numerical model of a tied-arch bridge: two mode shapes with almost identical deflections of the bridge deck: left - mode dominated by hanger vibrations, right - mode dominated by deck vibrations (amplification: top – 200, bottom – 400)

6.3.2 Description of the investigated guyed mast

The considered structure is an almost 200 metres tall steel mast with circular tubular cross-section that is supported at four levels by steel cables spanning in three vertical planes. These three planes are oriented at angles of 0°,120° and 240°. In figure 6.19 the mast with its cables is shown.

A guyed mast can be considered as vertically oriented beam with a hinged support at one end and several elastic supports provided by the cables. The stiffnes of the elastic supports is determind by the cross-section, material and longitudinal forces of the cables. Accordingly, the modal behaviour of the mast is strongly influenced by the properties of the cables. In the case of the structure considered here that was built in 1960, all available information was exclusively based on design documents.

6.3.3 Description of the ambient vibration tests

Focus of the investigation was the modal behaviour of the mast. This means that the state of the cables was not of primary interest in this study. However, as already mentioned, the cables and the mast are both parts of the complex system. The dynamic behaviour of the structure depends on the interaction between cables and mast.

Further, for the tests only limited time was available to access different measuring points on the structure and it was not possible to install sensors at the cables during this test campaign.

Figure 6.19: Guyed mast with anchoring at four levels

Taking these restrictions into account, it was decided to instrument three measuring points with accelerometers directed into two perpendicular lateral directions, respectively. The locations of the accelerometers are indicated in figure 6.20. They were chosen based on the results of a numerical modal analysis by means of a finite element model. As can be seen in figure 6.20, all three measuring points were located at platforms situated right above the connections of cables to the mast.

According to preliminary numerical analyses, natural natural frequencies below 0.5 Hz had to be expected. Therefore, seismic accelerometers with a sensitivity of 10 $\frac{V}{g}$ were used to measure the structural response due to ambient excitiation over a total period of about 25 minutes with a sampling rate of 128 Hz.

For expected natural frequencies below 0.5 Hz, 25 minutes are a relatively short duration of test. However, the test duration could not be extended due to organisational and technical limitations. Another aspect that needs to be mentioned is that operational modal analysis assumes that the considered system has a time-invariant dynamic behaviour during the observation time. In case of a guyed mast, the dynamic behaviour depends on the stiffness provided by the cables which is strongly geometrically nonlinear and is also influenced by respective weather conditions. If wind speed and direction change significantly during a test, it can be expected that the assumption of time-invariant system behaviour is violated. During the tests, the wind was moderate and its direction was relatively constant

6.3.4 Results of the ambient vibration tests

An operational modal analysis was performed applying the covariance-driven Stochastic Subspace Identification method. Within the pre-processing step, the measured time series was decimated by a factor of 4 such that the sampling rate of the analysed data was 32 Hz.

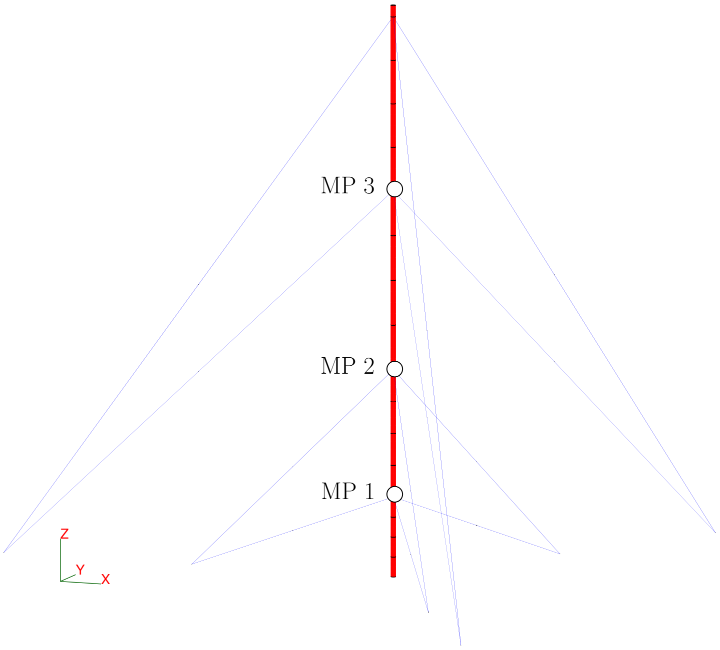

Figure 6.20: Guyed mast: sketch with measuring points (MP)

Based on a block Toeplitz matrix that was built with 200 block columns and rows, solutions for system models of order up to 100 were computed. Figure 6.21 shows the stabilisation diagram for the frequency range up to 2 Hz. Here numerous stable solutions are apparent and let expect a large number of modes to be present within this frequency range.

From this stabilisation diagram, 12 solutions were selected that are likely to correspond to physical modes of the structure. The corresponding natural frequencies, modal damping ratios and mode shapes of these point solutions are collected in table 6.9.

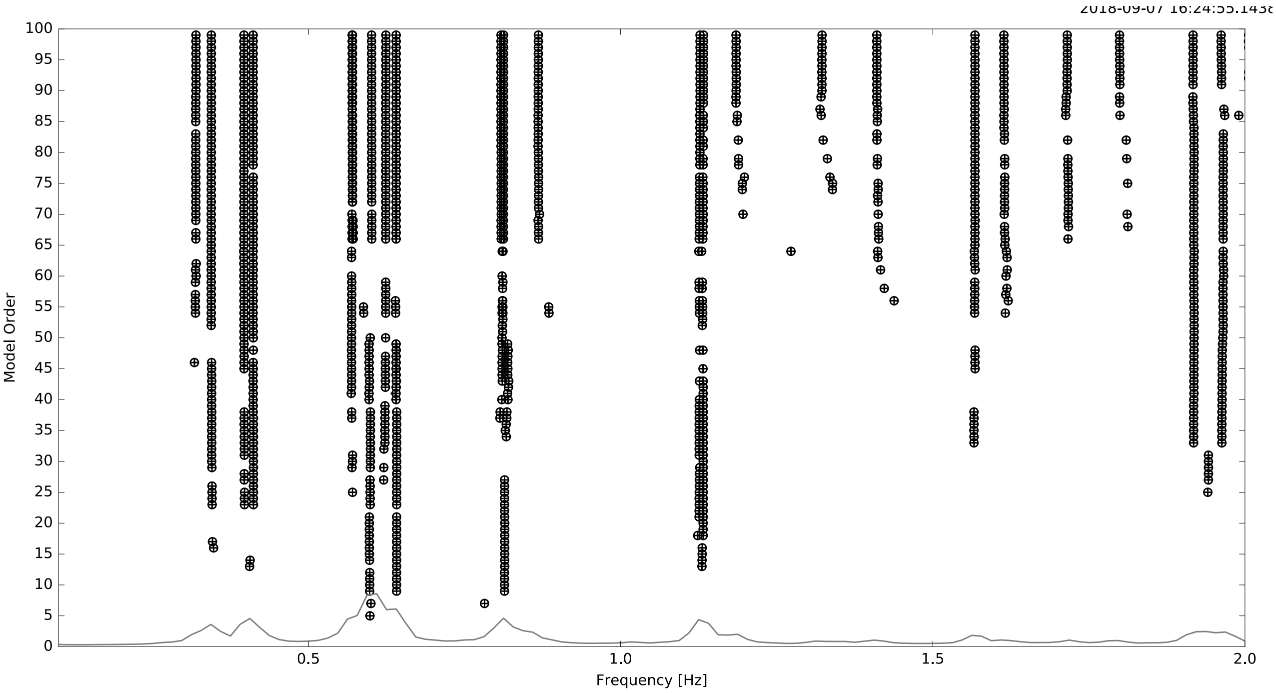

Figure 6.21: Guyed mast: stabilisation diagram

Table 6.9: Guyed mast: point estimates of the identified modal parameters

No.	natural frequencies	modal damping ratios	mode shapes			
			xz-plane	*yz*-plane	*xy*-plane	isometry
1	0.320 Hz	1.20 %	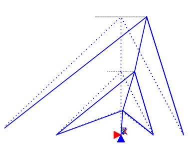	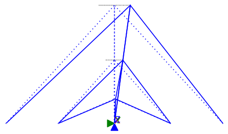	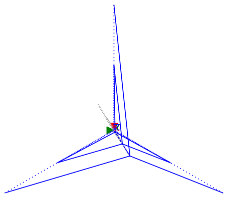	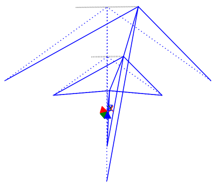
2	0.344 Hz	1.42 %	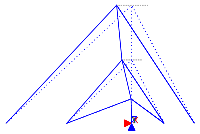	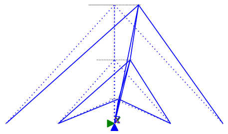	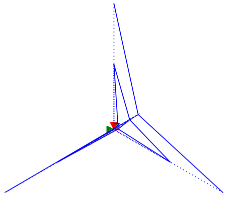	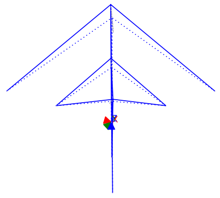
3	0.397 Hz	0.68 %	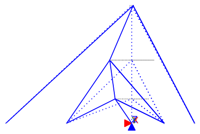	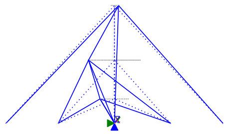	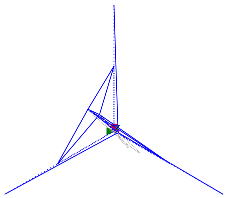	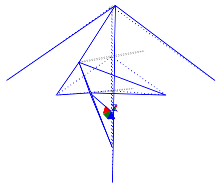
4	0.412 Hz	1.55 %	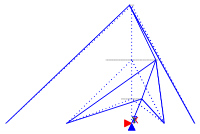	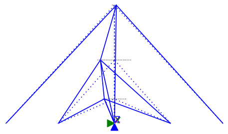	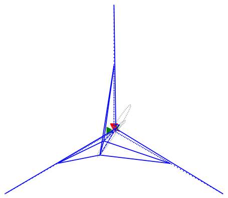	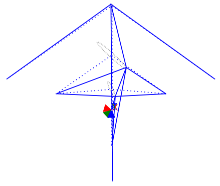

Guyed mast: point estimates of the identified modal parameters (cont.)

No.	natural frequencies	modal damping ratios	mode shapes			
			xz-plane	yz-plane	xy-plane	isometry
5	0.571 Hz	1.20 %	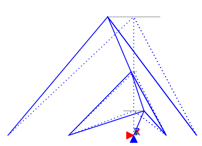	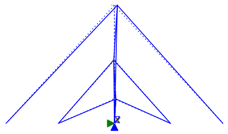	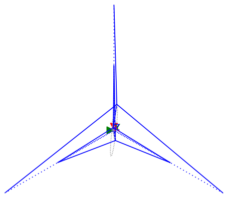	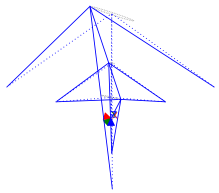
6	0.601 Hz	0.35 %	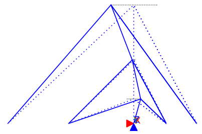	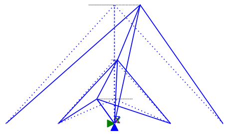	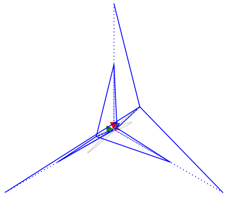	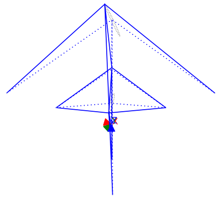
7	0.640 Hz	0.47 %	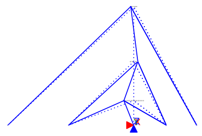	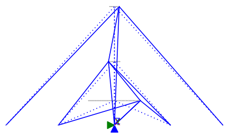	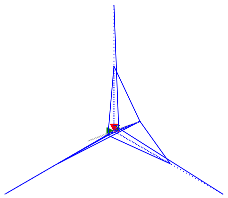	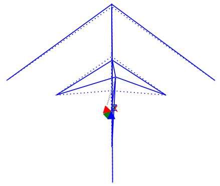
8	0.809 Hz	1.95 %	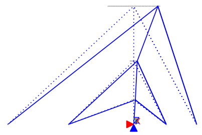	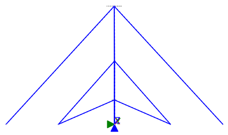	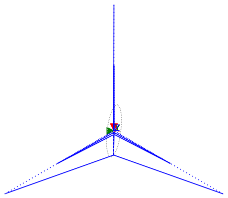	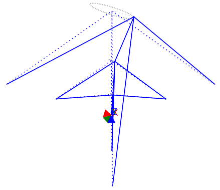

Guyed mast: point estimates of the identified modal parameters (cont.)

No.	natural frequencies	modal damping ratios	mode shapes			
			xz-plane	yz-plane	xy-plane	isometry
9	0.812 Hz	0.77 %	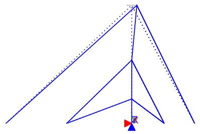	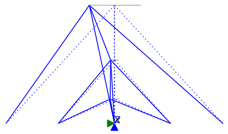	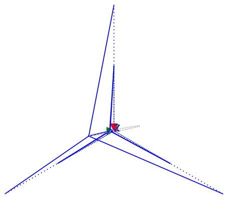	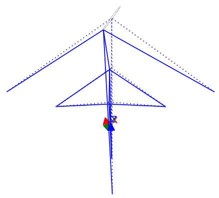
10	1.126 Hz	0.39 %	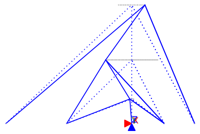	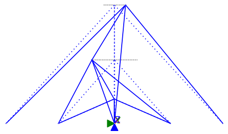	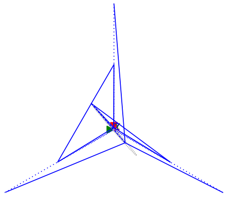	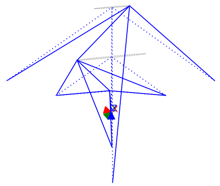
11	1.132 Hz	0.67 %	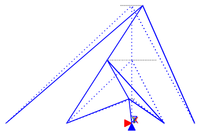	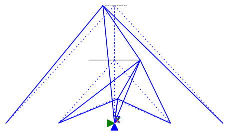	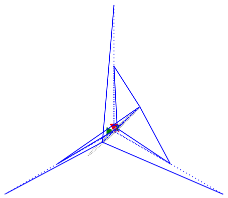	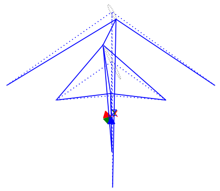
12	1.568 Hz	0.31 %	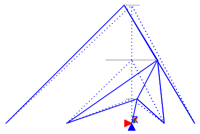	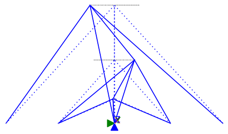	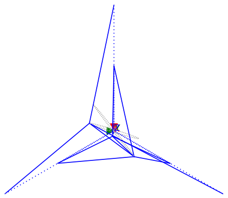	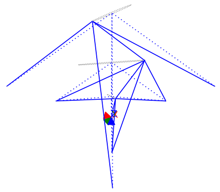

Due to the limited spacial resolution of the identified mode shapes the correct assignment of the resepctive modes from the static figures is not straightforward. However, one feature that is important with respect to the modal behaviour of the mast are its symmetry properties. Similar as for the antenna mast considered in section 6.1, one should also expect for the guyed mast that several bending modes occur pairwise with close natural frequencies and mode shapes in perpendicular vibration planes. As the z-axis of the coordinate system used for the visualisation of the identified mode shapes was defined to be parallel to the longitudinal axis of the mast, the projection of the mode shapes into the xy-plane given in table 6.9 provides information about the directions of vibration of the respective modes.

Taking into account that the natural frequencies of two pairwise occuring modes should be similar, the following observations can be made in table 6.9:

1. Modes 1 and 2, 3 and 4, 8 and 9 as well as 10 and 11 are likely to be paired bending modes of the mast. The identified mode shapes have pairwise a very similar appearance and perpendicular vibration planes, respectively.
2. The mode shapes of modes 5 and 6 are also very similar, however their vibration planes are not orthogonal to each other. Therefore it is likely that these two modes are not primarily characterised by mast vibrations but probably rather by cable vibrations.
3. For mode 7 no counterpart with a similar mode shape could be identified in the frequency range documented here. Accordingly, this mode is probably not a bending mode of the mast.
4. Modes 10 and 12 appear to be almost identical, they have also more or less a common vibration plane. However, the corresponding natural frequencies deviate from each other by about 40 %. Therefore one can conclude, that these modes should actually have distinct mode shapes that require a higher spatial resolution to be represented correctly.

These observations can be validated considering the modal assurance criterion (MAC). Figure 6.22 gives an overview about the MAC values related to the identified mode shapes. This graphical representation of the MAC matrix allows the formulation of several conclusions related to the observations above:

- The mode pairs designated in observation 1 have obviously respective orthogonal mode shapes.
- The eigenvectors of the identified modes 5 and 6 are obviously not orthogonal to each other as indicated by the red frame in figure 6.22. This confirms the second formulated observation.
- The MAC values show also no similarities between the 7th mode shape and those of all other identified modes. The 7th column and row of the MAC matrix are filled with very small values apart from the diagonal element.
- In the fourth observation a high degree of similarity between the identified modes 10 and 12 has been ascertained. The corresponding $MAC_{10,12} = 0.87$ supports this finding as well.

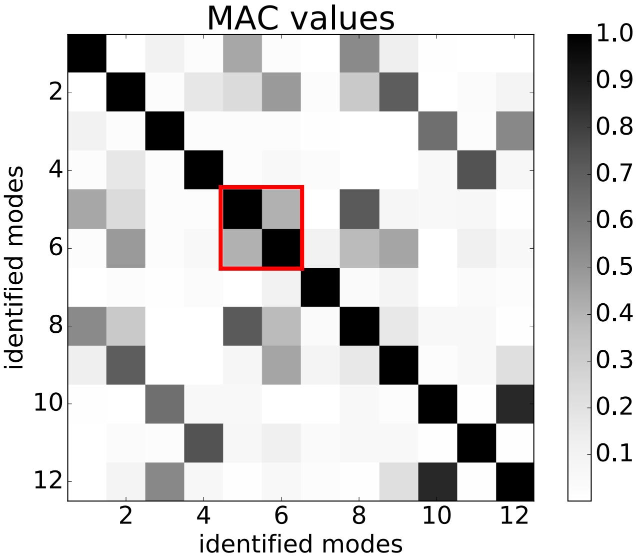

Figure 6.22: Guyed mast: MAC matrix for the identified modes

There are many off-diagonal values in the MAC matrix that are clearly greater than zero which means that the corresponding eigenvectors do not form orthogonal pairs. This should not surprise as the six degrees-of-freedom captured during the tests are too few to describe the relatively complex mode shapes of the mast, especially those of higher order, with a sufficient degree of completeness.

The example of the guyed mast shows that structures consisting of numerous elements with very distinct structural properties often show several modes that mainly pertain to only parts of the structure rather than to the complete system. Depending on the specific structure, a comparison with a numerical model can support the correct assignment of identified mode shapes. However, in some situations, as in the case of the presented example, this approach has also limitations. The approach presented in this section relies as well on preliminary knowledge that depends on individual properties of the respective system. It involves to a certain extent engineering judgement and experience. A formalisation of this strategy and automation of this method will require further development.

Chapter 7

Discussion and Outlook

7.1 Discussion and Conclusions

Operational modal analysis (OMA) is not only an established discipline of research within the field of structural dynamics. Due to the development of respective software tools it is nowadays also often applied in engineering practice. However, for the successful and correct application, solid knowledge of the theoretical background, the different methods are based on, is advisable. Therefore, some relevant theory from the fields of numerical modelling in structural mechanics and signal analysis were revised in chapter 2. These theoretical fundamentals serve an enhanced understanding of the algorithms of operational modal analysis presented in chapter 3.

There exist several parametric and non-parametric algorithms related to either time or frequency domain. However, it is very difficult to recommend a single OMA method as *the best* approach. In the context with one specific application, one method may have advantages compared to others. In another case study with different requirements another algorithm may be preferable.

In section 6.1 different methods were applied to the same experimental data set. Even though small deviations could be observed in the results, a conclusion such as a general superiority of one method cannot be formulated.

There are numerous applications of OMA and in many individual situations different methods may provide satisfactory results. Nevertheless, it should be always of advantage to compare the performance of different algorithms with each other for the sake of an enhanced assessability of the level of confidence into the identification results or a respective uncertainty.

Several sources for uncertainties in identified modal parameters are known. They do not only depend on the chosen method. Beside the quality of the experimental data, that is related to many factors, also the choice of algorithmic parameters can have a significant influence on the outcome of an operational modal analysis. This aspect has been illustrated by means of a practical example in section 6.2. Even though the question of *algorithmic uncertainties* in OMA is generally known among experts in the field, it has hardly been addressed in research so far.

Another type of uncertainty is the topic of spacial resolution. If certain restraints limit the instrumentation of a structure in certain parts, mode shapes with complex deformation patterns can hardly be clearly identified. Therefore, practical conditions that can occur especially in case of in-situ tests may result in great challenges with respect to the correct assignment of identified incomplete mode shapes to respective solutions obtained by means of a numerical model. One example for how additional knowledge can be used in a very specific situation has been described in section 6.3. This study shows that the interpretation of the results of an OMA may require engineering experience and judgement that can hardly be replaced by an automated algorithm.

Nevertheless, many steps in operational modal analysis have already been automated as shown in chapter 5. Though these developments can facilitate the analysis of experimental data acquired during any ambient vibration test, the major applications of automation in OMA will be the long-term monitoring of structures. There enormous amounts of data have to be processed and analysed. Without automation this task cannot be managed.

Even though the actual algorithms can be considered as the core of operational modal analysis, their successful application relies to a great extent on appropriate tools to support the postprocessing of the identification results. This does not only include a visualisation of identified mode shapes and measures that help the analyst in the assessment of the quality of the identification. From postprocessing also important information for further use of identified modal parameters can be derived. For example, quantified measures of uncertainty are needed as an input into a stochastic model updating that uses modal parameters in the objective function.

The latter remark points to further use of identified modal parameters. As modal analysis can be seen as a *bridge* between numerical modelling of a structure and the physical system, perspective research and developments should concern this role and how the outcome of a modal analysis can improve this bridging function.

7.2 Outlook to further research and developments

Identified modal parameters may scatter due to several reasons. As has been shown in the examples described in chapter 6, identified modal damping ratios have usually a higher coefficient of variation than the corresponding natural frequencies. By varying respective algorithmic parameters and with great experience it is in most cases possible to reduce the uncertainties. However, this trial-and-error process is time-demanding and if the final result is indeed the one with minimal uncertainty still remains an open question.

The sources of uncertainty in operational modal analysis are manifold. On the one hand, the quality of the results depends on the characteristics of the experimental data such as the frequency bandwidth, the signal-to-noise ratio, the sampling rate and the duration of the test. Further, the fundamental assumptions for an OMA, in particular stationarity of the excitation and time-invariance of the considered structure may be not perfectly satisfied. On the other hand, the quality of identified modal parameters is also related to data processing and parameters to be defined in context with the applied identification algorithm. One example for the variation of identification results depending on the choice of algorithmic parameters has been described in section 6.2.

Even if some factors such as an ambient excitation or the physical properties of the structure can hardly be changed, one can still assume that the uncertainties in identified modal parameters can be minimised by an appropriate choice of values for all other influence variables [35]. Uncertainties with respect to the characteristics of the used sensors and data acquisition, summarised as measurement uncertainties, may be estimated, for example, following the recommendations in [74]. However, due to the non-repoducibility of an ambient excitation and possible time-variant behaviour of the considered structure, there are also limitations in the application of the approach to ambient vibration tests conducted for an OMA.

Apart from few recommendations for the choice of some algortihmic parameters in literature, there exists no general guideline addressing this question. One reason is, that the performance of a certain method depends not only on the chosen set of algorithmic parameters but also on the specifics of a respective case study. Nevertheless, several conclusions concerning uncertainties in identified modal parameters in relation to the settings for some parametric OMA methods were drawn and can be found in literature, for example in [113] and [115]. Based on these findings, research on more general relations between influencing quantities and uncertainties in identified modal parameters is recommended.

Also sophisticated software packages still require an interactive user input for the parameter settings. Several analysis steps can be already automated. However, a general procedure that systematically considers all influences on the quality of identified modal parameters from the characteristics of the measured signals via the choice of algorithmic parameters to the postprocessing is still missing. The objective of such a procedure should be the minimisation of uncertainty in the identified modal parameters. As mentioned earlier, the results of a modal analysis is often used as input information for further investigations by means of numerical models. Typical examples are life-cycle analyses or the prediction of the structural response under modified loading conditions. In these situations a reduction of uncertainty in the numerical model that was calibrated on identified modal parameters is of significant importance.

Despite the fact, that operational modal analysis has already become a widely used technology in recent years, there still remain open problems. These questions are in particular linked to the qualified and automated application of operational modal analysis to practical engineering problems, not only in civil engineering but perhaps especially there due to current increasing digitalisation in construction, structural design and maintenance on the one hand and the very individual specifics of each civil structure.

It has to be expected that, for example, automated operational modal analysis will become a frequently used module in monitoring systems that are part of structural management and maintenance systems. In this context, de-centralised data processing is an evolving discipline for which also respective algorithmic solutions for OMA have to be developed. Accordingly, operational modal analysis can be considered as a special field within structural dynamics with a high potential for perspective developments.

Bibliography

[1] Abonyi, J., and Feil, B. *Cluster Analysis for Data Mining and System Identification.* Birkhäuser, 2007.

[2] Allemang, R. J. The modal assurance criterion – twenty years of use and abuse. *Sound and Vibration 37*, 8 (August 2003), 14–21.

[3] Allemang, R. J., and Brown, D. L. A correlation coefficient for modal vector analysis. In *Proc. of the 1st International Modal Analysis Conference (IMAC)* (Orlando, FL, USA, 1982), pp. 110–116.

[4] Andersen, P. *Identification oc civil engineering structures using vector ARMA models.* PhD thesis, Aalborg University, Department of Building Technology and Structural Engineering, Aalborg, Denmark, 1997.

[5] Andersen, P., and Brincker, R. Estimation of modal parameters and their uncertainties. In *Proc. of the 17th International Modal Analysis Conference (IMAC)* (Kissimmee, FL, USA, 1999), pp. 323–329.

[6] Andersen, P., Brincker, R., Ventura, C., and Cantieni, R. Automated modal parameter estimation for operational modal analysis of large systems. In *Proc. of the 2nd International Operational Modal Analysis Conference (IOMAC)* (Copenhagen, Denmark, 2007).

[7] Andersen, P., Brincker, R., Ventura, C., and Cantieni, R. Modal estimation of civil structures subject to ambient and harmonic excitation. In *Proc. of the 26th International Modal Analysis Conference (IMAC)* (Orlando, FL, USA, 2008).

[8] Asmussen, J. C. *Modal analysis based on the random decrement technique – application to civil engineering structures.* PhD thesis, Aalborg University, Department of Building Technology and Structural Engineering, Aalborg, Denmark, 1997.

[9] Asmussen, J. C., and Brincker, R. Estimation of frequency response functions by random decrement. In *Proc. of the 14th International Modal Analysis Conference (IMAC)* (Dearborn, MI, USA, 1996), pp. 246–252.

[10] Asmussen, J. C., and Brincker, R. Statistical theory of the vector random decrement technique. *Journal of Sound and Vibration 226*, 2 (1999), 329–344.

[11] Asmussen, J. C., Ibrahim, S. R., and Brincker, R. Random decrement and regression analysis of traffic responses of bridges. In *Proc. of the 14th International Modal Analysis Conference (IMAC)* (Dearborn, MI, USA, 1996), pp. 453–458.

[12] Asmussen, J. C., Ibrahim, S. R., and Brincker, R. Application of vector triggering random decrement. In *Proc. of the 15th International Modal Analysis Conference (IMAC)* (Orlando, FL, USA, 1997), pp. 1165–1171.

[13] Asmussen, J. C., Ibrahim, S. R., and Brincker, R. Random decrement: Identification of structures subjected to ambient excitation. In *Proc. of the 16th International Modal Analysis Conference (IMAC)* (Santa Barbara, CA, USA, 1998), pp. 914–921.

[14] Backhaus, K., Erichson, B., Plinke, W., and Weiber, R. *Multivariate Analysemethoden – Eine anwendungsorientierte Einführung*, 13th ed. Springer, 2011.

[15] Bakir, P. G. Automation of the stabilization diagrams for subspace based system identification. *Expert Systems with Applications 38* (2011), 14390–14397.

[16] Barnett, S. *Polynomials and linear systems.* Marcel Dekker, New York, NY, USA, 1983.

[17] Bendat, J. S., and Piersol, A. G. *Random data: Analysis and measurement procedures*, 4th ed. John Wiley & Sons, Hoboken, NJ, USA, 2010.

[18] Brewer, J. W. Kronecker Products and Matrix Calculus in System Theory. *IEEE Transactions on Dircuits and Systems CAS-25*, 9 (1978), 772 – 781.

[19] Bricker, R., and Zhang, L. Frequency domain decomposition revisited. In *Proc. of the 3rd International Operational Modal Analysis Conference (IOMAC)* (Portonovo, Italy, 2009).

[20] Brincker, R., and Andersen, P. ARMA models in modal space. In *Proc. of the 17th International Modal Analysis Conference (IMAC)* (Kissimmee, FL, USA, 1999), pp. 330–334.

[21] Brincker, R., Andersen, P., and Jacobsen, N.-J. Automated frequency domain decomposition for operational modal analysis. In *Proc. of the 25th International Modal Analysis Conference (IMAC)* (Orlando, FL, USA, 2007).

[22] Brincker, R., Andersen, P., and Zhang, L. Modal identification from ambient responses using frequency domain decomposition. In *Proc. of the 18th International Modal Analysis Conference (IMAC)* (San Anonio, TX, USA, 2000), pp. 625–630.

[23] Brincker, R., Andersen, P., and Zhang, L. Damping estimation by frequency domain decomposition. In *Proc. of the 19th International Modal Analysis Conference (IMAC)* (Kissimmee, FL, USA, 2001), pp. 324–330.

[24] Brincker, R., and Asmussen, J. C. Random decrement based FRF estimation. In *Proc. of the 15th International Modal Analysis Conference (IMAC)* (Orlando, FL, USA, 1997), pp. 1571–1576.

[25] Brincker, R., Kirkegaard, P. H., and Rytter, A. Identification of system parameters by the random decrement technique. In *Proc. of the Florence Modal Analysis Conference* (Florence, Italy, September 1991), Fintito di Stampare presso il Centro Duplicazione Offset, pp. 465–472.

[26] Brincker, R., Krenk, S., and Jensen, J. L. Estimation of correlation functions by the random decrement technique. In *Fracture and Dynamics* (Aalborg, Denmark, November 1990), vol. R9041, 28, Aalborg University, Dept. of Building Technology and Structural Engineering.

[27] Brincker, R., and Ventura, C. *Introduction to operational modal analysis.* John Wiley & Sons Ltd, Chichester, West Sussex, UK, 2015.

[28] Brown, D., Allemang, R., Zimmerman, R., and Mergeay, M. Parameter estimation techniques for modal analysis. *SAE Technical Paper 790221* (1979).

[29] Cantieni, R., Bajrić, A., and Brincker, R. Damping characteristics of a footbridge - mysteries and truths. In *Proc. of the 34th International Modal Analysis Conference (IMAC)* (Orlando, FL, USA, 2016).

[30] Cantieni, R., Brehm, M., Zabel, V., Rauert, T., and Hoffmeister, B. Ambient Testing and Model Updating of a Filler Beeam Bridge for High-Speed Trains. In *Proc. of the 7th European Conf. on Structural Dynamics – EURODYN 2008* (Southampton, 7th to 6th July 2008).

[31] Cara, F. J., Jesús, J., Alarcón, E., Reynders, E., and De Roeck, G. Modal contribution and state space order selection in operational modal analysis. *Mechanical Systems and Signal Processing 38* (2013), 276–298.

[32] Carden, E. P., and Brownjohn, J. M. W. Fuzzy clustering of stability diagrams for vibration-based structural health monitoring. *Computer-Aided Civil and Infrastructure Engineering 23* (2008), 360–372.

[33] Cauberghe, B. *Applied frequency-domain system identification in the field of experimental and operational modal analysis.* PhD thesis, Vrije Universiteit Brussel, Faculteit Toegepaste Wetenschappen, Brussels, Belgium, 2004.

[34] Chopra, A. K. *Dynamics of structures*, 5th edition ed. Prentice-hall International Series. Pearson, London, New York, 2017.

[35] Ciloglu, K., Zhou, Y., Moon, F., and Aktan, A. E. Impacts of epistemic uncertainty in operational modal analysis. *Journal of Engineering Mechanics 138*, 9 (2012), 1059–1070.

[36] Clough, R. W., and Penzien, J. *Dynamics of structures*, 2nd edition, reprint ed. McGraw-Hill, New York, 2004.

[37] Cole, H. A. On-the-line analysis of random vibrations. In *Proc. of the 9th Structures, Structural Dynamics and Materials Conference* (Palm Springs, CA, USA, April 1968), AIAA / ASME Paper No. 68-288.

[38] Cole, H. A. *Failure detection of a space shuttle wing flutter model by random decrement.* NASA Technical Memorandum: NASA TM X-62,041. NASA, 1971.

[39] De Troyer, T., Guillaume, P., Pintelon, R., and Vanlanduit, S. Fast calculation of confidence intervals on parameter estimates of least-squares frequency-domain estimators. *Mechanical Systems and Signal Processing 23* (2009), 261–273.

[40] Deraemaeker, A., Reynders, E., De Roeck, G., and Kullaa, J. Vibration-based structural health monitoring using output-only measurements under changing environment. *Mechanical Systems and Signal Processing 22* (2008), 34–56.

[41] Desforges, M. J., Cooper, J. E., and Wright, J. R. Mode tracking during flutter testing using the modal assurance criterion. *Proceedings of the Institution of Mechanical Engineers, Part G: Journal of Aerospace Engineering 210*, 1 (January 1996), 27–37.

[42] Döhler, M. *Subspace-based system identication and fault detection: Algorithms for large systems and application to structural vibration analysis.* PhD thesis, Université Rennes 1, Rennes, France, 2011.

[43] Döhler, M., Andersen, P., and Mevel, L. Data merging for multi-setup operational modal analysis with data-driven SSI. In *Proc. of the 28th International Modal Analysis Conference (IMAC)* (Jacksonville, FL, USA, 2010).

[44] Döhler, M., Lam, X.-B., and Mevel, L. Uncertainty quantification for modal parameters from stochastic subspace identification on multi-setup measurements. *Mechanical Systems and Signal Processing 36* (2013), 562–581.

[45] Döhler, M., and Mevel, L. Modular subspace-based system identification from multi-setup measurements. *IEEE Transactions on Automatic Control 57*, 11 (November 2012), 2951–2956.

[46] Döhler, M., and Mevel, L. Efficient multi-order uncertainty computation for stochastic subspace identification. *Mechanical Systems and Signal Processing 38* (2013), 346–366.

[47] Döhler, M., Reynders, E., Magalhães, F., Mevel, L., De Roeck, G., and Cunha, A. Pre- and post-identification merging for multi-setup OMA with covariance-driven SSI. In *Proc. of the 28th International Modal Analysis Conference (IMAC)* (Jacksonville, FL, USA, 2010).

[48] Everitt, B. S., Landau, S., Leese, M., and Stahl, D. *Cluster Analysis*, 5th ed. John Wiley & Sons, 2011.

[49] Ewins, D. *Modal testing: Theory, practice and application*, 2nd ed. Research Studies Press, Baldock, Hertfordshire, England, 2000.

[50] Felber, A. J. *Development of a hybrid bridge evaluation system.* PhD thesis, University of British Columbia, Department of Civil Engineering, Vancouver, Canada, 1993.

[51] Fladung, W. A., and Brown, D. L. Multiple reference impact testing. In *Proc. of the 11th International Modal Analysis Conference (IMAC)* (Kissimmee, FL, USA, 1993).

[52] Fransen, S., Rixen, D., Henriksen, T., and Bonnet, M. On the operational modal analysis of solid rocket motors. In *Proc. of the 28th International Modal Analysis Conference (IMAC)* (Jacksonville, FL, USA, 2010).

[53] Füllekrug, U. Computation of real normal modes from complex eigenvectors. In *Proc. of the 13th International Congress on Sound and Vibration* (Vienna, Austria, 2006).

[54] Füllekrug, U. Computation of real normal modes from complex eigenvectors. *Mechanical Systems and Signal Processing 22* (2008), 57–65.

[55] Gera, A. E. The relationship between the Z-transform and the discrete-time Fourier transform. *IEEE Transactions on Automatic Control 44*, 2 (February 1999), 370–371.

[56] Goethals, I. *Subspace identification for linear, Hammerstein and Hammerstein-Wiener systems.* PhD thesis, Katholieke Universiteit Leuven, Departement Elektrotechniek, Leuven, Belgium, 2005.

[57] Goethals, I., and De Moor, B. Model reduction and energy analysis as a tool to detect spurious modes. In *Proc. of ISMA2002 International Conference on Noise and Vibration Engineering* (Leuven, Belgium, 2002), pp. 1307–1314.

[58] Granger, C. W. J., and Hatanaka, M. *Spectral analysis of economic time series.* Princeton University Press, Princeton, NJ, USA, 1964.

[59] Grove, A. C. *An introduction to the Laplace transform and the z transform.* Prentice Hall International, Hemel Heampstead, Hertfordshire, UK, 1991.

[60] Guillaume, P., De Troyer, T., Devriendt, C., and De Sitter, G. Omax – Operational Modal Analysis in presence of eXogenous inputs. In *Proc. of the 25th International Modal Analysis Conference (IMAC)* (Orlando, FL, USA, 2007).

[61] Guillaume, P., Schoukens, J., and Pintelon, R. Sensitivity of roots to errors in the coefficient of polynomials obtained by frequency-domain estimation methods. *IEEE Transactions on Instrumentation and Measurement 38*, 6 (December 1989), 1050–1056.

[62] Guillaume, P., Verboven, P., and Vanlanduit, S. Frequency-domain maximum likelihood identification of modal parameters with confidence intervals. In *Proc. of ISMA 23 International Conference on Noise and Vibration Engineering* (Leuven, Belgium, 1998).

[63] Guillaume, P., Verboven, P., Vanlanduit, S., Van der Auweraer, H., and Peeters, B. A poly-reference implementation of the least-squares complex frequency-domain estimator. In *Proc. of the 21st International Modal Analysis Conference (IMAC)* (Kissimmee, FL, USA, 2003).

[64] Gustafson, D., and Kessel, W. Fuzzy clustering with a fuzzy covariance matrix. In *Proc. of the IEEE Conference on Decision and Control* (San Diego, USA, 1979), pp. 761–766.

[65] Häckell, M. W., and Rolfes, R. Monitoring a 5 MW offshore wind energy converter – Condition parameters and triangulation based extraction of modal parameters. *Mechanical Systems and Signal Processing 40* (2013), 322–343.

[66] Hair, J. F., Black, W. C., Babin, B. J., Anderson, R. E., and Tatham, R. L. *Multivariate Data Analysis*, sixth ed. Pearson Prentice Hall, 2006.

[67] Heylen, W., Lammens, S., and Sas, P. *Modal analysis theory and testing.* Katholieke Universiteit Leuven, Department of Mechanical Engineering, Leuven, Belgium, 1999.

[68] Ibrahim, S. R., Asmussen, J. C., and Brincker, R. Vector triggering random decrement technique for higher identification accuracy. In *Proc. of the 15th International Modal Analysis Conference (IMAC)* (Orlando, FL, USA, 1997), pp. 502–509.

[69] Ibrahim, S. R., Brincker, R., and Asmussen, J. C. Modal parameter identification from responses of general unknown random inputs. In *Proc. of the 14th International Modal Analysis Conference (IMAC)* (Dearborn, MI, USA, 1996), pp. 446–452.

[70] Ibrahim, S. R., and Mikulcik, E. C. A method for the direct identification of vibration parameters from the free response. *The Shock and Vibration Bulletin 47* (September 1977), 183–198.

[71] Ibrahim, S. R., and Sestieri, A. Existence and normalization of complex modes in post experimental use in modal analysis. In *Proc. of the 13th International Modal Analysis Conference (IMAC)* (Nashville, TN, USA, 1995), pp. 483–489.

[72] Imregun, M., and Ewins, D. J. Realisation of complex mode shapes. In *Proc. of the 11th International Modal Analysis Conference (IMAC)* (Kissimmee, FL, USA, 1993), pp. 1303–1309.

[73] Imregun, M., and Ewins, D. J. Complex modes – origins and limits. In *Proc. of the 13th International Modal Analysis Conference (IMAC)* (Nashville, TN, USA, 1995), pp. 496–506.

[74] International Organization for Standards (ISO). Guide to the expression of uncertainty in measurement, 2008.

[75] Jacobsen, N.-J. Separating structural modes and harmonic components in operational modal analysis. In *Proc. of the 24th International Modal Analysis Conference (IMAC)* (St. Louis, MO, USA, 2006).

[76] Jacobsen, N.-J., Andersen, P., and Brincker, R. Using enhanced frequency domain decomposition as a robust technique to harmonic excitation in operational modal analysis. In *Proc. of ISMA 2006 International Conference on Noise and Vibration Engineering* (Leuven, Belgium, 2006), pp. 3129–3140.

[77] Jacobsen, N.-J., Andersen, P., and Brincker, R. Eliminating the influence of harmonic components in operational modal analysis. In *Proc. of the 25th International Modal Analysis Conference (IMAC)* (Orlando, FL, USA, 2007).

[78] Jacobsen, N.-J., Andersen, P., and Brincker, R. Applications of frequency domain curve-fitting in the EFDD technique. In *Proc. of the 26th International Modal Analysis Conference (IMAC)* (Orlando, FL, USA, 2008).

[79] James, G. H., Carne, T. G., and Lauffer, J. P. The natural excitation technique (NExT) for modal parameter extraction from operating wind turbines. Sandia Report SAND92–1666, Sandia National Laboratories, Alburquerque, NM, USA, February 1993.

[80] James, G. H., Carne, T. G., and Lauffer, J. P. The natural excitation technique (NExT) for modal parameter extraction from operating structures. *Modal Analysis: the International Journal of Analytical and Experimental Modal Analysis 10*, 4 (1995), 260–277.

[81] James, G. H., Carne, T. G., Lauffer, J. P., and Nord, A. R. Modal testing using natural excitation. In *Proc. of the 10th International Modal Analysis Conference (IMAC)* (San Diego, CA, USA, February 1992).

[82] Jenkins, G. M., and Watts, D. G. *Spectral analysis and its applications.* Holden-Day, San Francisco, CA, USA, 1968.

[83] Juang, J.-N. *Applied system identification.* Prentice-Hall, Englewood Cliffs, NJ, USA, 1994.

[84] Kaufman, L., and Rousseeuw, P. *FindiAnalysis in Data: An introduction to Cluster Analysis.* John Wiley & Sons, 1990.

[85] Kausel, E. *Advanced Structural Dynamics.* Cambridge University Press, Cambridge, U.K., New York, 2017.

[86] Krämer, C., de Smet, C. A. M., and Peeters, B. Comparison of ambient and forced vibration testing of civil engineering structures. In *Proc. of the 17th International Modal Analysis Conference (IMAC)* (Kissimmee, FL, USA, 1999), pp. 1030–1034.

[87] Ku, C. J., Cermak, J. E., and Chou, L.-S. Random decrement based method for modal parameter identification of a dynamic system using acceleration responses. *Journal of Wind Engineering and Industrial Aerodynamics 95* (2007), 389–410.

[88] Lanslots, J., Rodiers, B., and Peeters, B. Automated pole-selection: Proof-of concept & validation. In *Proc. of the International Conference on Noise and Vibration Engineering - ISMA 2004* (Leuven, Belgium, September 2004).

[89] Lau, J., Lanslots, J., Peeters, B., and Van der Auweraer, H. Automatic modal analysis: reality or myth? In *Proc. of the International Modal Analysis Conference - IMAC 25* (Orlando, FL, USA, February 2007).

[90] Ljung, L. *System identification: theory for the user.* Prentice-Hall, Englewood Cliffs, NJ, USA, 1987.

[91] Magalhães, F. *Operational modal analysis for testing and monitoring of bridges and special structures.* PhD thesis, Universidade do Porto, Faculdade de Engenharia, Porto, Portugal, 2011.

[92] Magalhães, F., Cunha, A., and Caetano, E. Online automatic identification of the modal parameters of a long span arch bridge. *Mechanical Systems and Signal Processing 23* (2009), 316–329.

[93] Malekjafarian, A., Bricker, R., Ashory, M. R., and Khatibi, M. M. Identification of closely spaced modes using Ibrahim time domain method. In *Proc. of the 4th International Operational Modal Analysis Conference (IOMAC)* (Istanbul, Turkey, 2011).

[94] Marwitz, S., and Zabel, V. An experimental evaluation of two potential improvements for 3d laser vibrometer based operational modal analysis. *Experimental Mechanics 57*, 7 (2017).

[95] Mevel, L., Basseville, M., Benveniste, A., and Goursat, M. Merging sensor data from multiple measurement st-ups for non-stationary subspace-based modal analysis. *Journal of Sound and Vibration 249*, 4 (2002), 719–741.

[96] Mevel, L., Benveniste, A., Basseville, M., and Goursat, M. Blind subspace-based eigenstructure identification under nonstationary excitation using moving sensors. *IEEE Transactions on Signal Processing 50*, 1 (January 2002), 41–48.

[97] Mittag, H.-J. *Statistik: Eine Einführung mit interaktiven Elementen*, 3rd ed. Springer-Lehrbuch. Springer Berlin Heidelberg, Berlin, Heidelberg, 2014.

[98] Mohanty, P. *Operational modal analysis in the presence of harmonic excitations.* PhD thesis, Technische Universiteit Delft, Delft, The Netherlands, 2005.

[99] Mohanty, P., and Rixen, D. J. Operational modal analysis in the presence of harmonic excitation. *Journal of Sound and Vibration 270* (2004), 93–109.

[100] Niedbal, N. Analytical determination of real normal modes from measured complex responses. In *Proc. of the 25th Structures, Structural Dynamics and Materials Conference* (Palm Springs, CA, USA, 1984), pp. 292–295.

[101] Oppenheim, A. V., and Schafer, R. W. *Discrete-time signal processing.* Prentice-Hall, Englewood Cliffs, NJ, USA, 1989.

[102] Oppenheim, A. V., Willsky, A. S., and Nawab, S. H. *Signals & systems*, 2nd ed. Prentice Hall, Upper Saddle River, NJ, USA, 1997.

[103] Pappa, R. S., Elliott, K. B., and Schenk, A. *A consistent-mode indicator for the eigensystem realization algorithm.* NASA Technical Memorandum 107607. NASA, 1992.

[104] Parloo, E. *Application of frequency-domain system identification techniques in the field of operational modal analysis.* PhD thesis, Vrije Universiteit Brussel, Faculteit Toegepaste Wetenschappen, Brussels, Belgium, 2003.

[105] Parloo, E., Guillaume, P., and Cauberghe, B. Maximim likelihood identification of non-stationary operational data. *Journal of Sound and Vibration 268* (2003), 971–991.

[106] Peeters, B. *System identification and damage detection in civil engineering.* PhD thesis, Katholieke Universiteit Leuven, Departement Burgerlijke Bouwkunde, Leuven, Belgium, 2000.

[107] Peeters, B., and De Roeck, G. Reference-based stochastic subspace identification for output-only modal analysis. *Mechanical Systems and Signal Processing 13*, 6 (1999), 855–878.

[108] Peeters, B., and Van der Auweraer, H. PolyMAX: a revolution in operational modal analysis. In *Proc. of the 1st International Operational Modal Analysis Conference (IOMAC)* (Copenhagen, April 2005).

[109] Peeters, B., Van der Auweraer, H., Guillaume, P., and Leuridan, J. The PolyMAX frequency-domain method: a new standard for modal parameter estimation? *Shock and Vibration 11* (2004), 395–409.

[110] Peeters, B., Vanhollebeke, F., and Van der Auweraer, H. Operational PolyMAX for estimating the dynamic properties of a stadium structure during a football game. In *Proc. of the 23rd International Modal Analysis Conference (IMAC)* (Orlando, FL, USA, 2005).

[111] Petersen, C. *Dynamik der Baukonstruktionen.* Viehweg, Wiesbaden, 2000.

[112] Pintelon, R., Guillaume, P., and J., S. Uncertainty calculation in (operational) modal analysis. *Mechanical Systems and Signal Processing 21* (2007), 2359–2373.

[113] Pridham, B. A. andWilson, J. C. A study of damping errors in correlation-driven stochastic realizations using short data sets. *Probabilistic Engineering Mechanics 18*, 1 (2003), 61–77.

[114] Prony, R. Essai expérimental et analytique Sur le lois de la Dilatabilité des fluides élastiques et sur celles de la Force expansive de la vepeur de l'eau et de la vapeur de l'alkool, á différentes températures. *Journal de L'École Polytechnique 1* (1795), 24–76.

[115] Rainieri, C., and Fabbrocino, G. Influence of model order and number of block rows on accuracy and precision of modal parameter estimates in stochastic subspace identification. *International Journal of Lifecycle Performance Engineering 1*, 4 (2014), 317–334.

[116] Rainieri, C., and Fabbrocino, G. *Operational modal analysis of civil engineering structures.* Springer, New York, NY, USA, 2014.

[117] Rainieri, C., Fabbrocino, G., and Cosenza, E. Some remarks on experimental estimation of damping for seismic design of civil constructions. *Shock and Vibration 17* (2010), 383–395.

[118] Randall, R. B. *Frequency analysis*, 3rd ed. Brüel & Kjær, Nærum, Denmark, 1987.

[119] Regalia, P. A., and Mitra, S. K. Kronecker Products, Unitary Matrices and Signal Processing Applications. *SIAM Review 31*, 4 (Dec. 1989), 586–613.

[120] Reynders, E. *System identification and modal analysis in structural mechanics.* PhD thesis, Katholieke Universiteit Leuven, Departement Burgerlijke Bouwkunde, Leuven, Belgium, 2009.

[121] Reynders, E., and De Roeck, G. Reference-based combined deterministic-stochastic subspace identification for experimental and operational modal analysis. *Mechanical Systems and Signal Processing 22* (2008), 617–637.

[122] Reynders, E., Houbrechts, J., and De Roeck, G. Fully automated (operational) modal analysis. *Mechanical Systems and Signal Processing 29* (2012), 228–250.

[123] Reynders, E., Pintelon, R., and De Roeck, G. Uncertainty bounds on modal parameters obtained from stochastic subspace identification. *Mechanical Systems and Signal Processing 22* (2008), 948–969.

[124] Ribeiro, D., Calçada, R., Delgado, R., Brehm, M., and Zabel, V. Finite element model updating of a bowstring-arch railway bridge based on experimental modal parameters. *Engineering Structures 40* (2012), 413–435.

[125] Rodrigues, J., and Brincker, R. Application of random decrement technique in operational modal analysis. In *Proc. of the 1st International Operational Modal Analysis Conference (IOMAC)* (Copenhagen, April 2005).

[126] Rodrigues, J., Brincker, R., and Andersen, P. Improvement of frequency domain output-only modal identification from the application of the random decrement technique. In *Proc. of the 22nd International Modal Analysis Conference (IMAC)* (Dearborn, MI, USA, 2004).

[127] Scionti, M., and Lanslots, J. P. Stabilisation diagrams: Pole identification using fuzzy clustering techniques. *Advances in Engineering Software 36* (2005), 768–779.

[128] Seo, B., and Chen, C. T. The relationship between the Laplace transform and the Fourier transform. *IEEE Transactions on Automatic Control AC-31*, 8 (August 1986), 751.

[129] Seo, B., and Chen, C. T. The relationship between the z-transform and the Fourier transform. *IEEE Transactions on Automatic Control 37*, 10 (October 1989), 1626–1627.

[130] Shih, C. Y., Tsuei, Y. G., Allemang, R. J., and Brown, D. L. Complex mode indication function and its applications to spatial domain parameter estimation. *Mechanical Systems and Signal Processing 2*, 4 (October 1988), 367–377.

[131] Siringoringo, D. M., and Fujino, Y. Experimental study of laser Doppler vibrometer and ambient vibration for vibration-based damage detection. *Engineering Structures 28* (2006), 1803–1815.

[132] Söderström, T. Test of pole-zero cancellation in estimated models. *Automatica 11* (1975), 537–541.

[133] Vacher, P., Jacquier, B., and Bucharles, A. Extensions of the MAC criterion to complex modes. In *Proc. of ISMA 2010 International Conference on Noise and Vibration Engineering* (Leuven, Belgium, 2010), pp. 2713–2725.

[134] Van Overschee, P., and De Moor, B. Subspace algorithms for the stochastic identification problem. In *Proc. of the 30th Conference on Decision and Control* (Brighton, England, December 1991).

[135] Van Overschee, P., and De Moor, B. Subspace algorithms for the stochastic identification problem. *Automatica 29*, 3 (1993), 649–660.

[136] Van Overschee, P., and De Moor, B. Choice of state-space basis in combined deterministic-stochastic subspace identification. *Automatica 31*, 12 (1995), 1877–1883.

[137] Van Overschee, P., and De Moor, B. A unifying theorem for three subspace system identification algorithms. *Automatica 31*, 12 (1995), 1853–1864.

[138] Van Overschee, P., and De Moor, B. *Subspace identification for linear systems – Theory, implementation, applications.* Kluwer Academic Publishers, Dordrecht, The Netherlands, 1996.

[139] Vandiver, J. K., Dunwoody, A. B., Campbell, R. B., and Cook, M. F. A mathematical basis for the random decrement signature analysis technique. *Journal of Mechanical Design 104* (April 1982), 307–313.

[140] Vanlanduit, S., Verboven, P., Guillaume, P., and Schoukens, J. An automatic frequency domain modal parameter estimation algorithm. *Journal of Sound and Vibration 265* (2003), 647–661.

[141] Verboven, P. *Frequency-domain system identification for modal analysis.* PhD thesis, Vrije Universiteit Brussel, Faculteit Toegepaste Wetenschappen, Brussels, Belgium, 2002.

[142] Verboven, P., Guillaume, P., Cauberghe, B., Parloo, E., and Vanlanduit, S. Stabilization charts and uncertainty bounds for frequency-domain linear least squares estimators. In *Proc. of the 21st International Modal Analysis Conference (IMAC)* (Kissimmee, FL, USA, 2003).

[143] Verboven, P., Parloo, E., Guillaume, P., and Van Overmeire, M. Autonomous structural health monitoring – part i: Modal parameter estimation and tracking. *Mechanical Systems and Signal Processing 16*, 4 (2002), 637–657.

[144] Vu-Manh, H., Abe, M., Fujino, Y., and Kaito, K. The eigensystem realization algorithm for ambient vibration measurement using laser Doppler vibrometers. In *Proc. of the American Control Conference* (Arlington, VA, USA, 2001), pp. 435–440.

[145] Welch, P. D. The use of fast Fourier transform for the estimation of power spectra: a method based on time averaging over short, modified periodograms. *IEEE Transactions on Audio and Electroacoustics AU-15*, 2 (June 1967), 70–73.

[146] Wiener, N. *Extrapolation, interpolation, and smoothing of stationary time series.* The M.I.T. Press, Cambridge, MA, USA, 1949.

[147] Zabel, V., and Brehm, M. Das dynamische Verhalten von Eisenbahnbrücken mit kurzer Spannweite – numerische und experimentelle Untersuchungen. *Bauingenieur 83* (März 2008), S9–S14.

[148] Zabel, V., Brehm, M., and Nikulla, S. The influence of temperature varying material parameters on the dynamic behaviour of short span railway bridges. In *Proc. of the International Conference on Noise and Vibration Engineering - ISMA* (Leuven, Belgium, September 2010).

[149] Zabel, V., and Gössinger, J. Modal analysis and numerical models of a typical railway bridge. In *Proc. of the International Modal Analysis Conference IMAC-XXXII* (Orlando, Florida USA, February 2014).

[150] Zhang, G., Ma, J., Chen, Z., and Wang, R. Automated eigensystem realisation algorithm for operational modal analysis. *Journal of Sound and Vibration 333* (2014), 3550–3563.

[151] Zhang, L., Brincker, R., and Andersen, P. A unified approach for two-stage time domain modal identification. In *Proc. of the International Conference on Structural Dynamics Modelling: Test, Analysis and Validation* (Madeira Islands, Portugal, 2002).

[152] Zhang, L., Wang, T., and Tamura, Y. A frequency-spatial domain decomposition (FSDD) technique for operational modal analysis. In *Proc. of the 23rd International Modal Analysis Conference (IMAC)* (Orlando, FL, USA, 2005).

[153] Zhang, Y., Wu, L. J., and Song, H. W. Triggering expectation and residual excitation of distributed random decrement technique. *Journal of Sound and Vibration 340* (2015), 368–382.

Appendix A

Modal parameters identified for a model beam

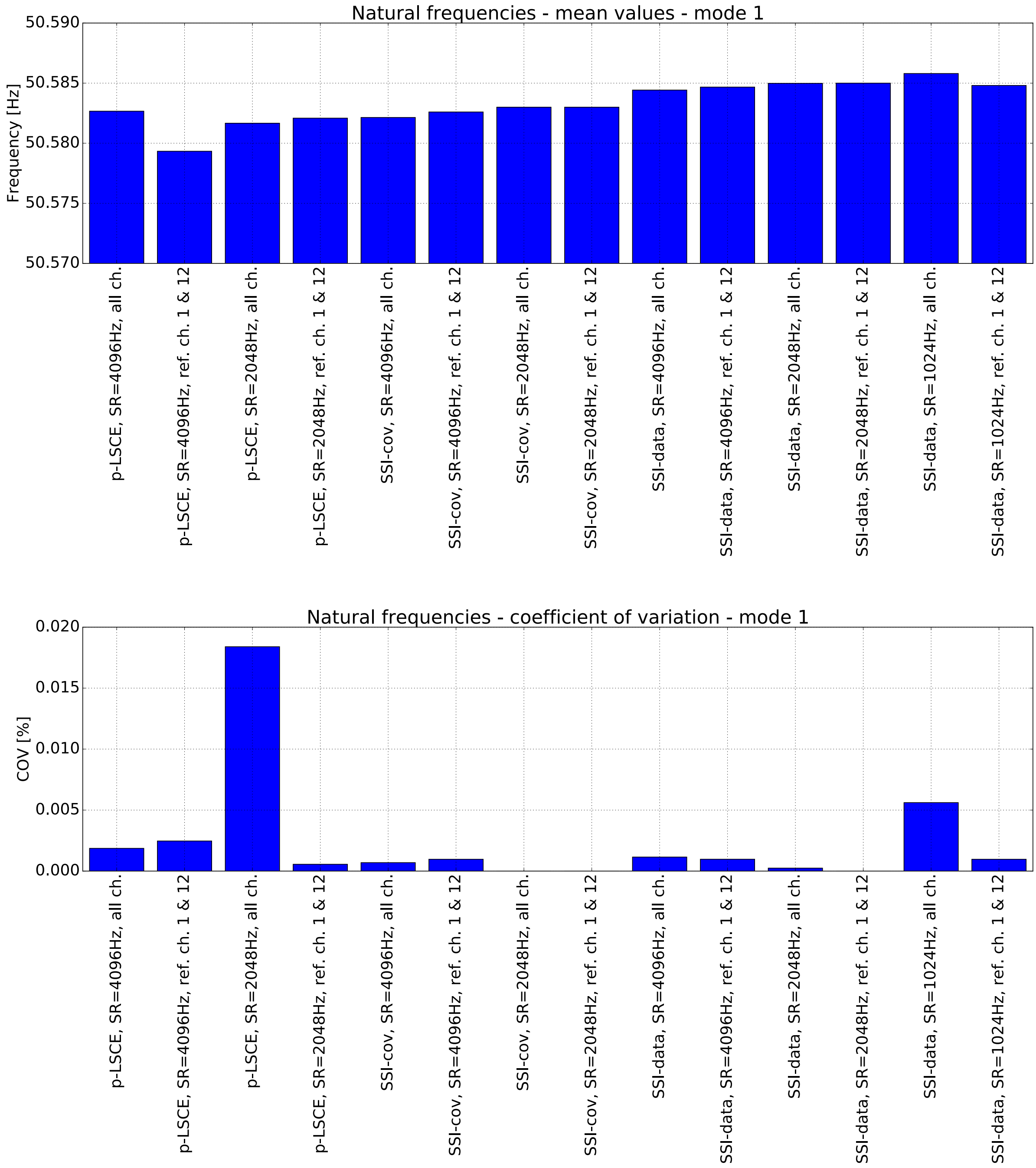

Figure A.1: Mean values and COV of the natural frequencies identified for mode 1 by means of different OMA methods using various parameters

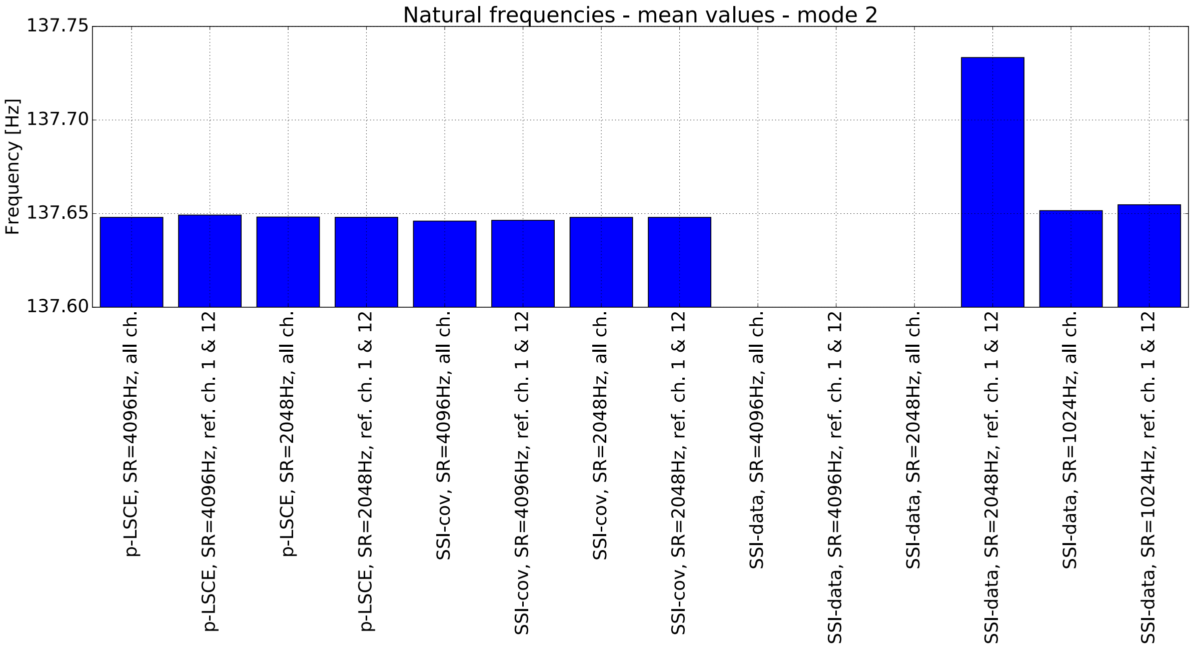

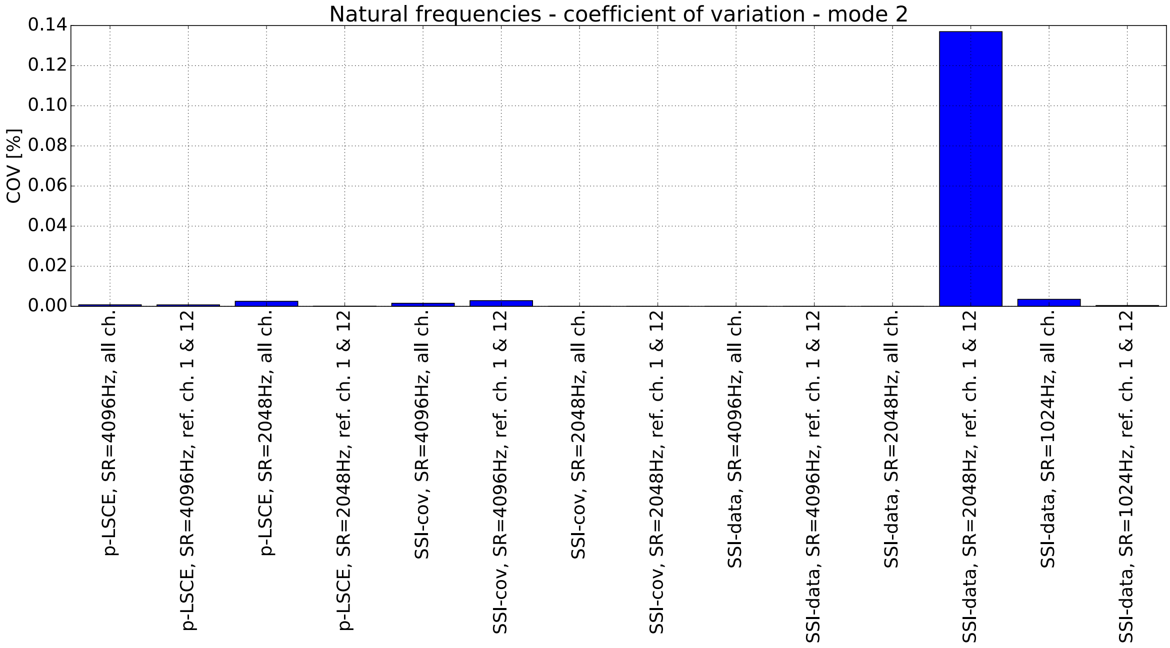

Figure A.2: Mean values and COV of the natural frequencies identified for mode 2 by means of different OMA methods using various parameters

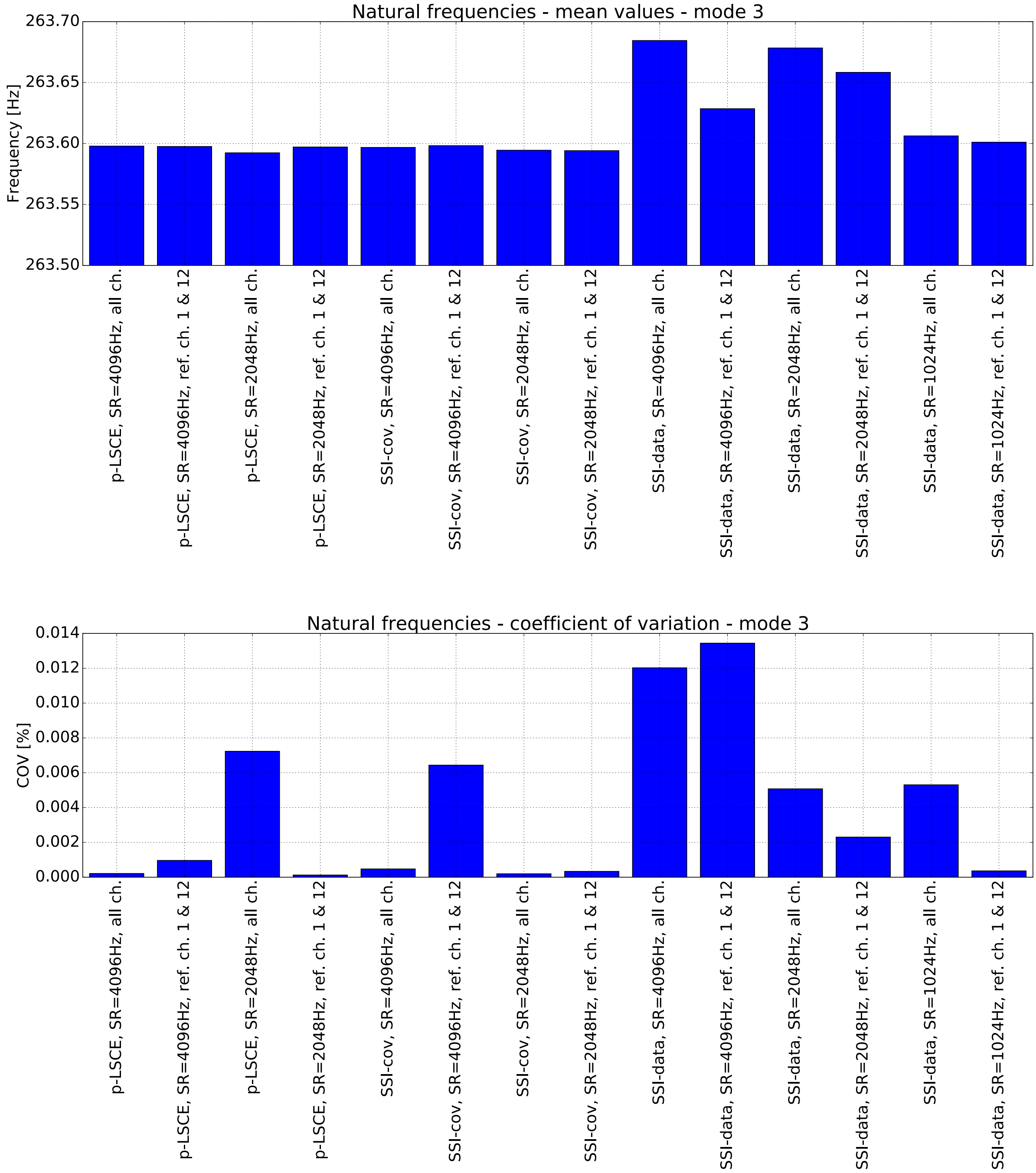

Figure A.3: Mean values and COV of the natural frequencies identified for mode 3 by means of different OMA methods using various parameters

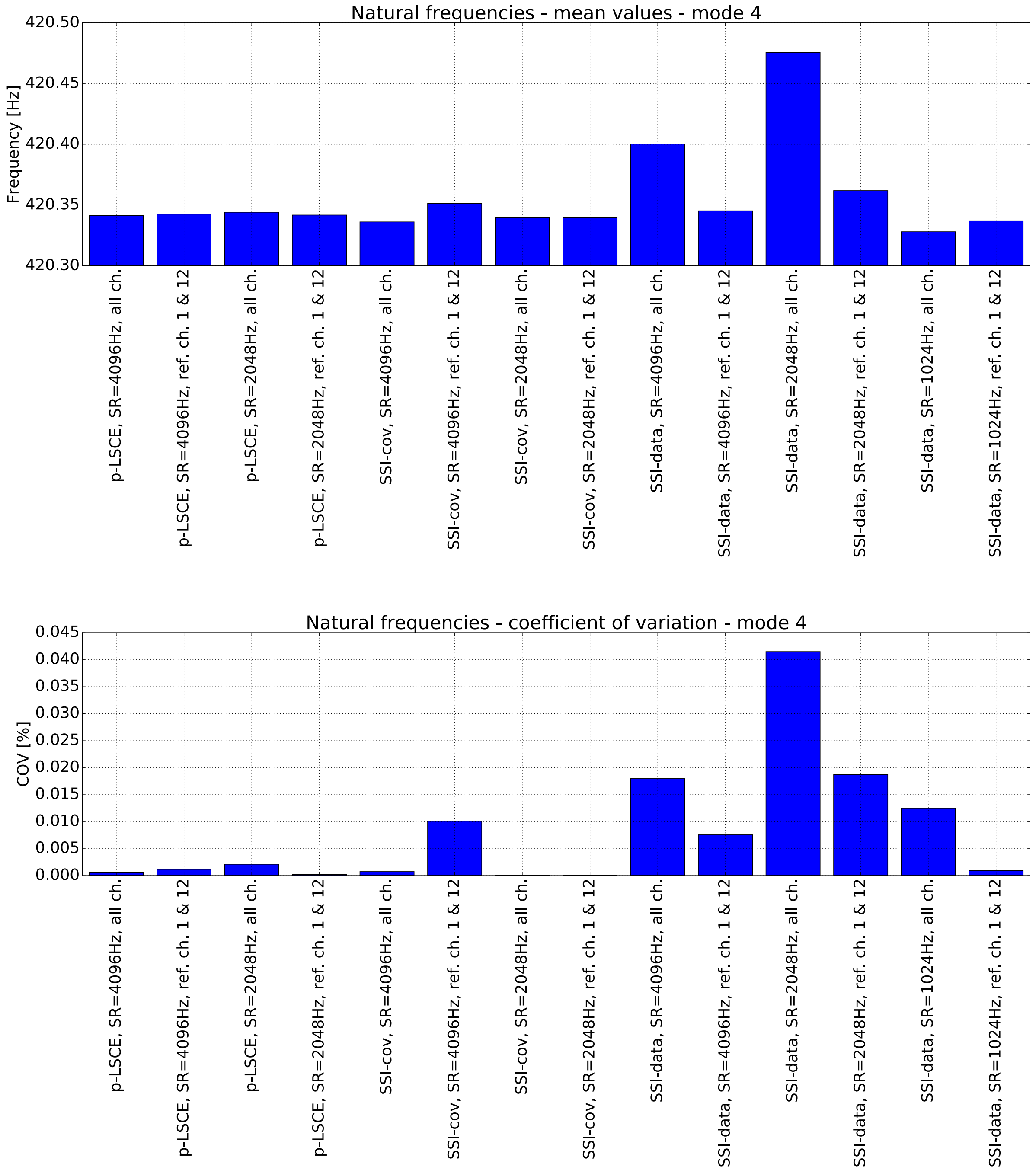

Figure A.4: Mean values and COV of the natural frequencies identified for mode 4 by means of different OMA methods using various parameters

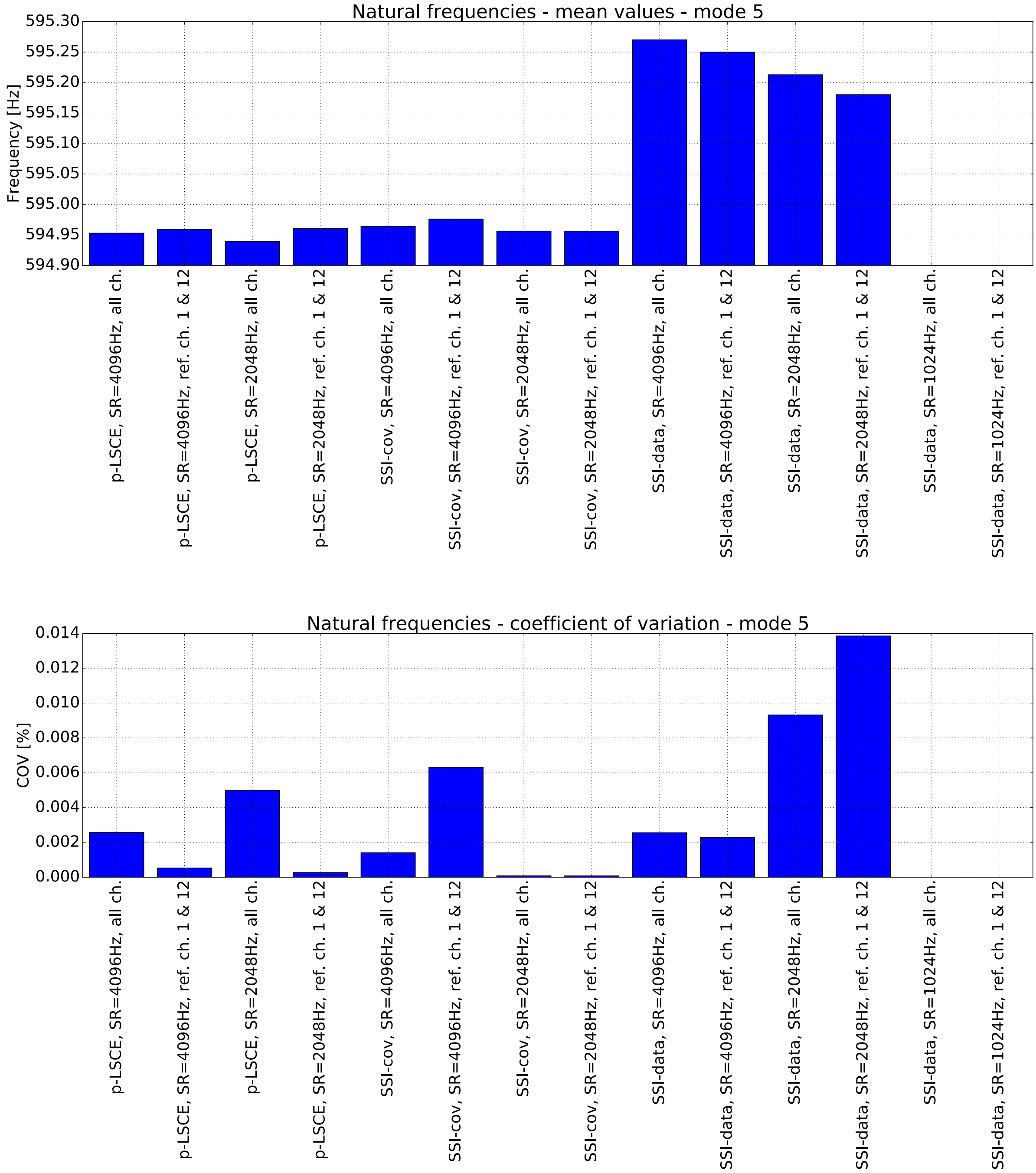

Figure A.5: Mean values and COV of the natural frequencies identified for mode 5 by means of different OMA methods using various parameters

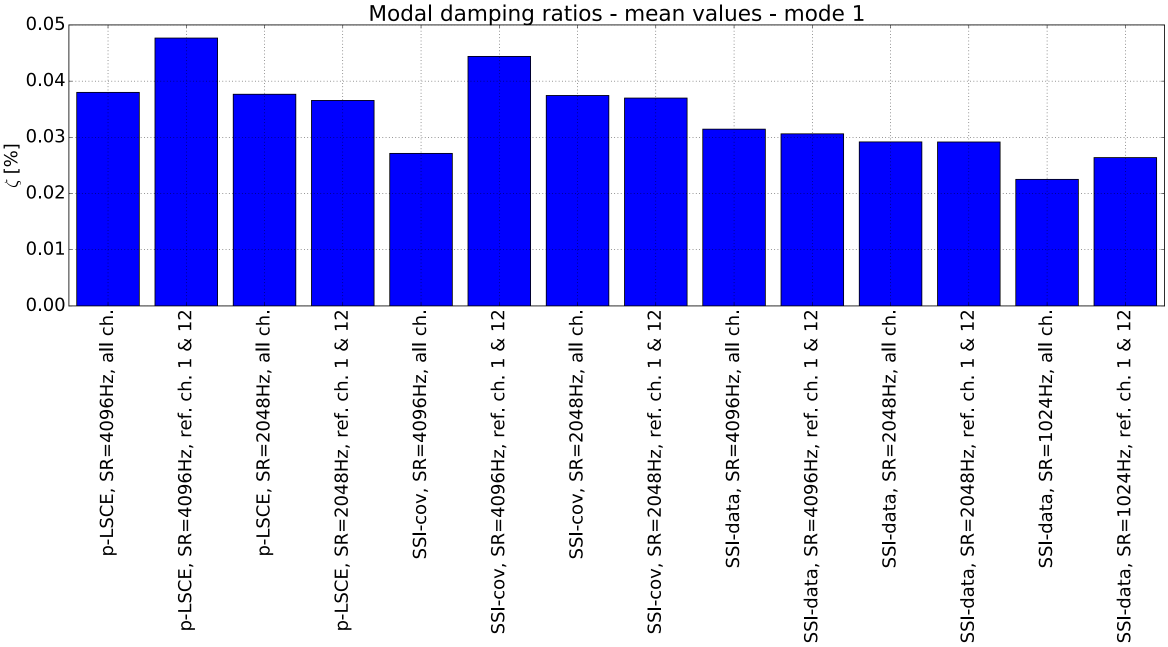

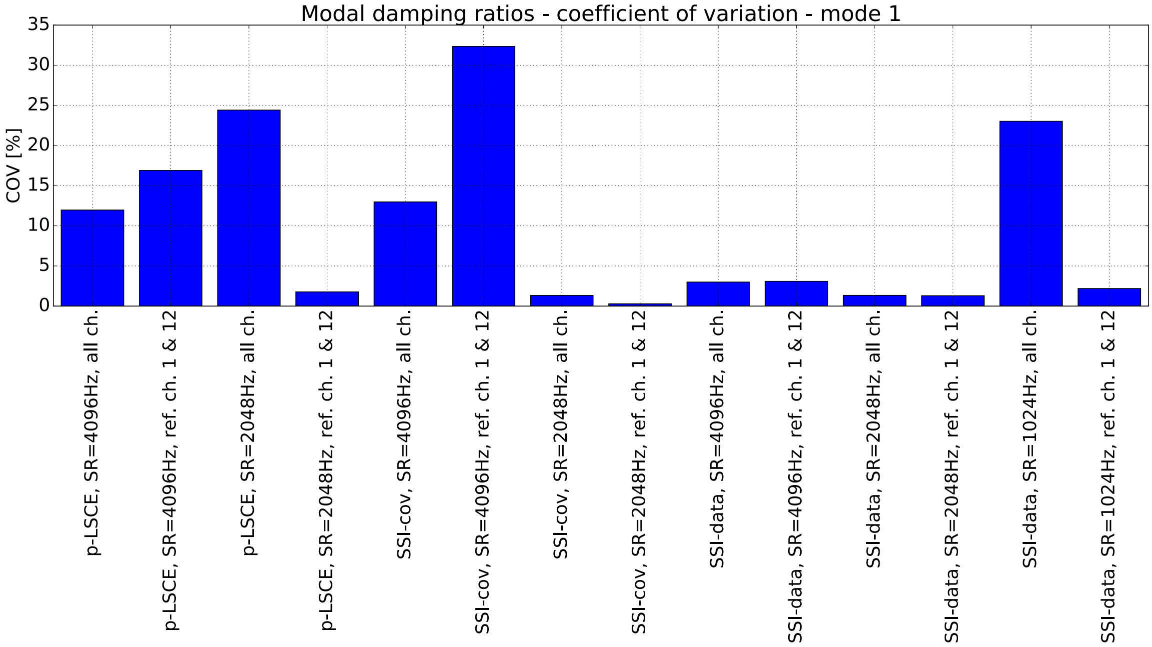

Figure A.6: Mean values and COV of the modal damping ratios identified for mode 1 by means of different OMA methods using various parameters

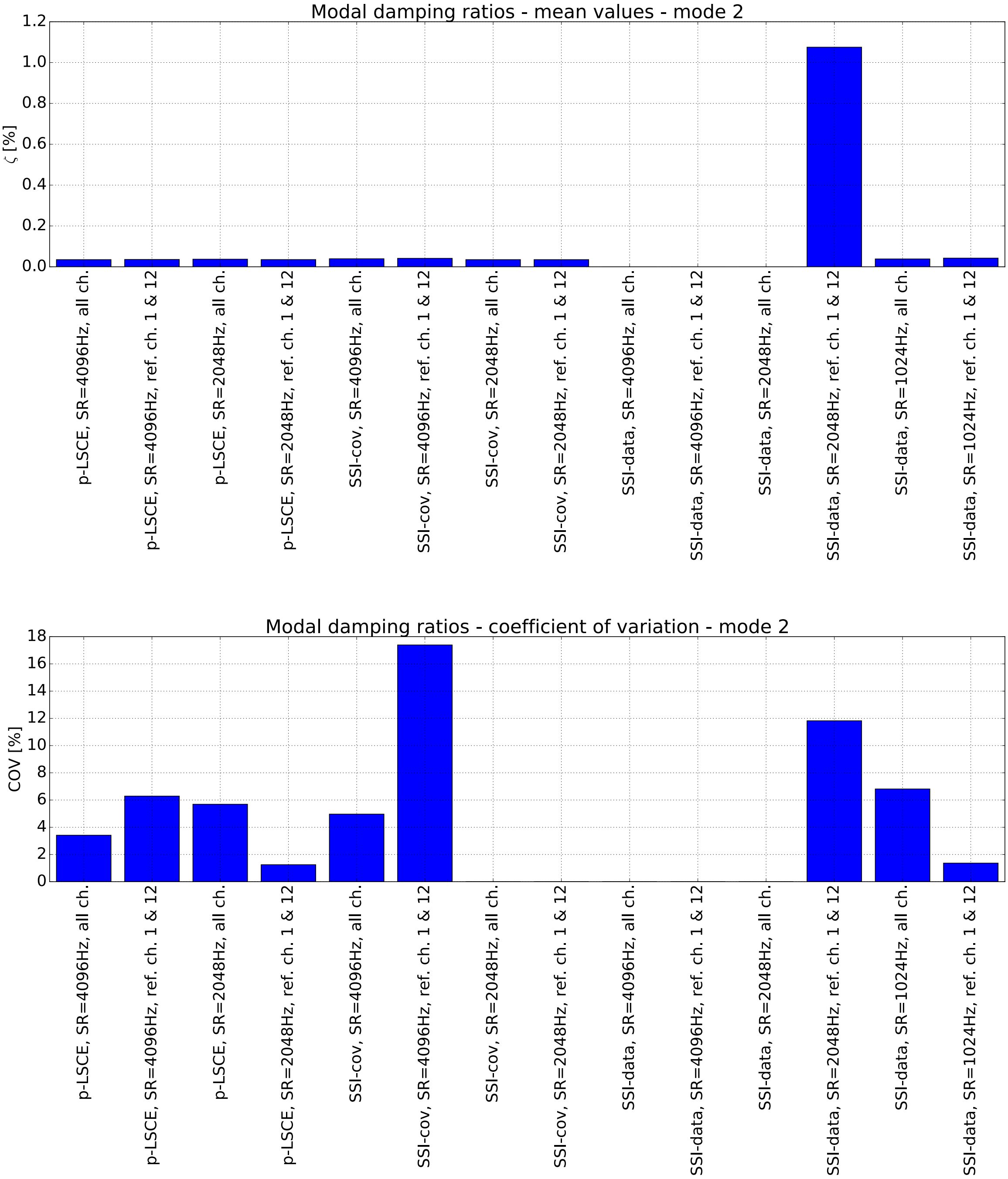

Figure A.7: Mean values and COV of the modal damping ratios identified for mode 2 by means of different OMA methods using various parameters

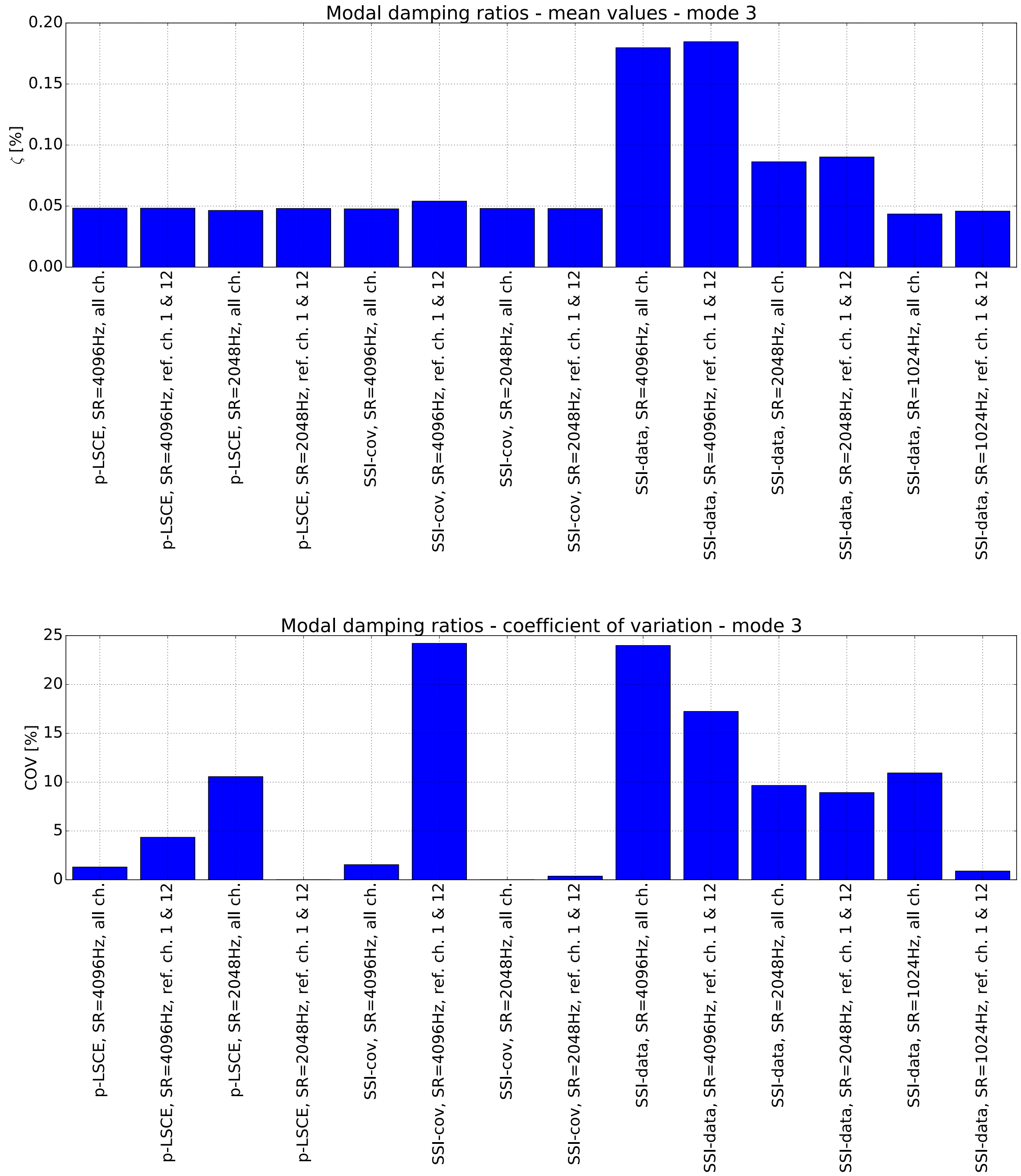

Figure A.8: Mean values and COV of the modal damping ratios identified for mode 3 by means of different OMA methods using various parameters

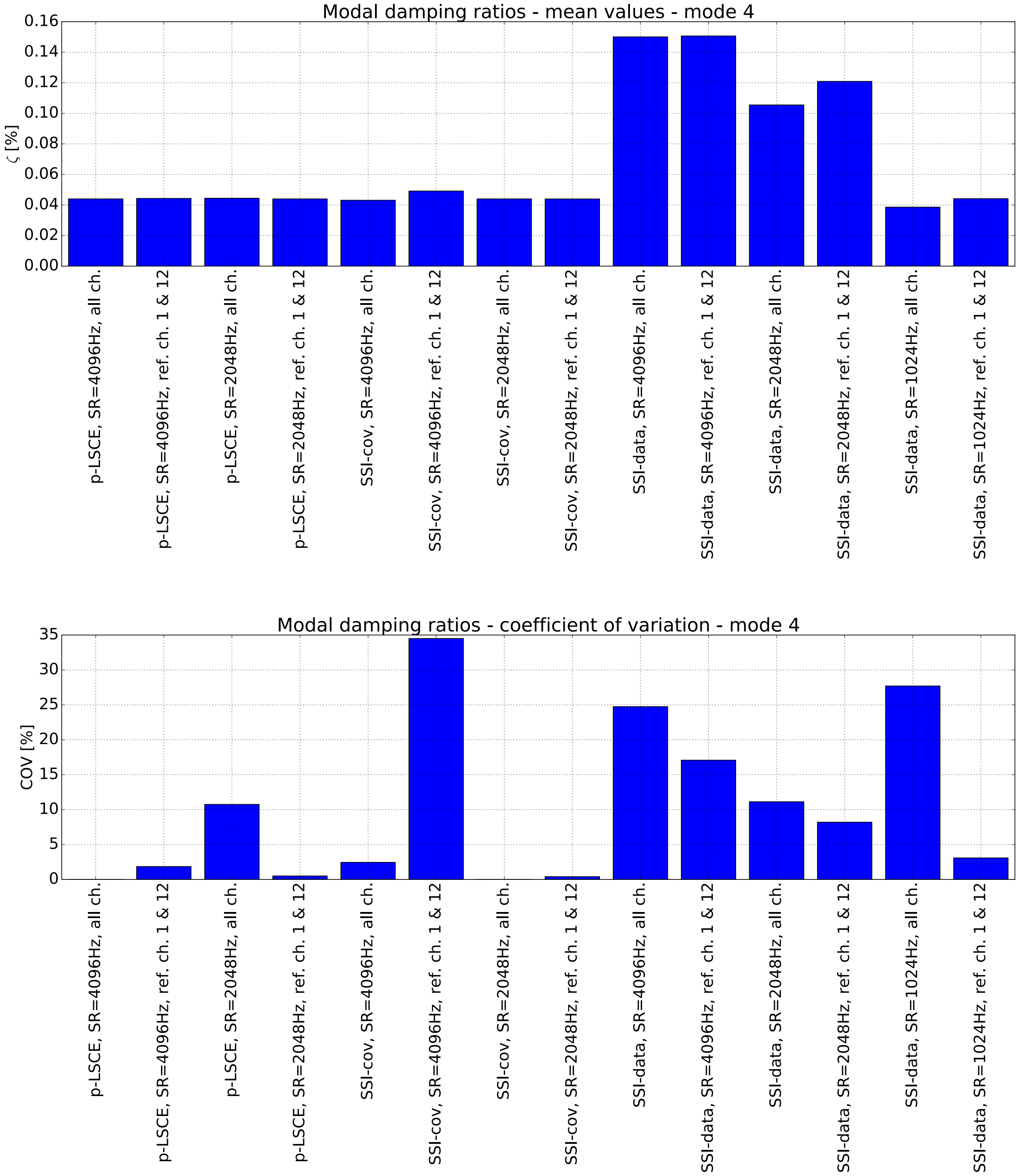

Figure A.9: Mean values and COV of the modal damping ratios identified for mode 4 by means of different OMA methods using various parameters

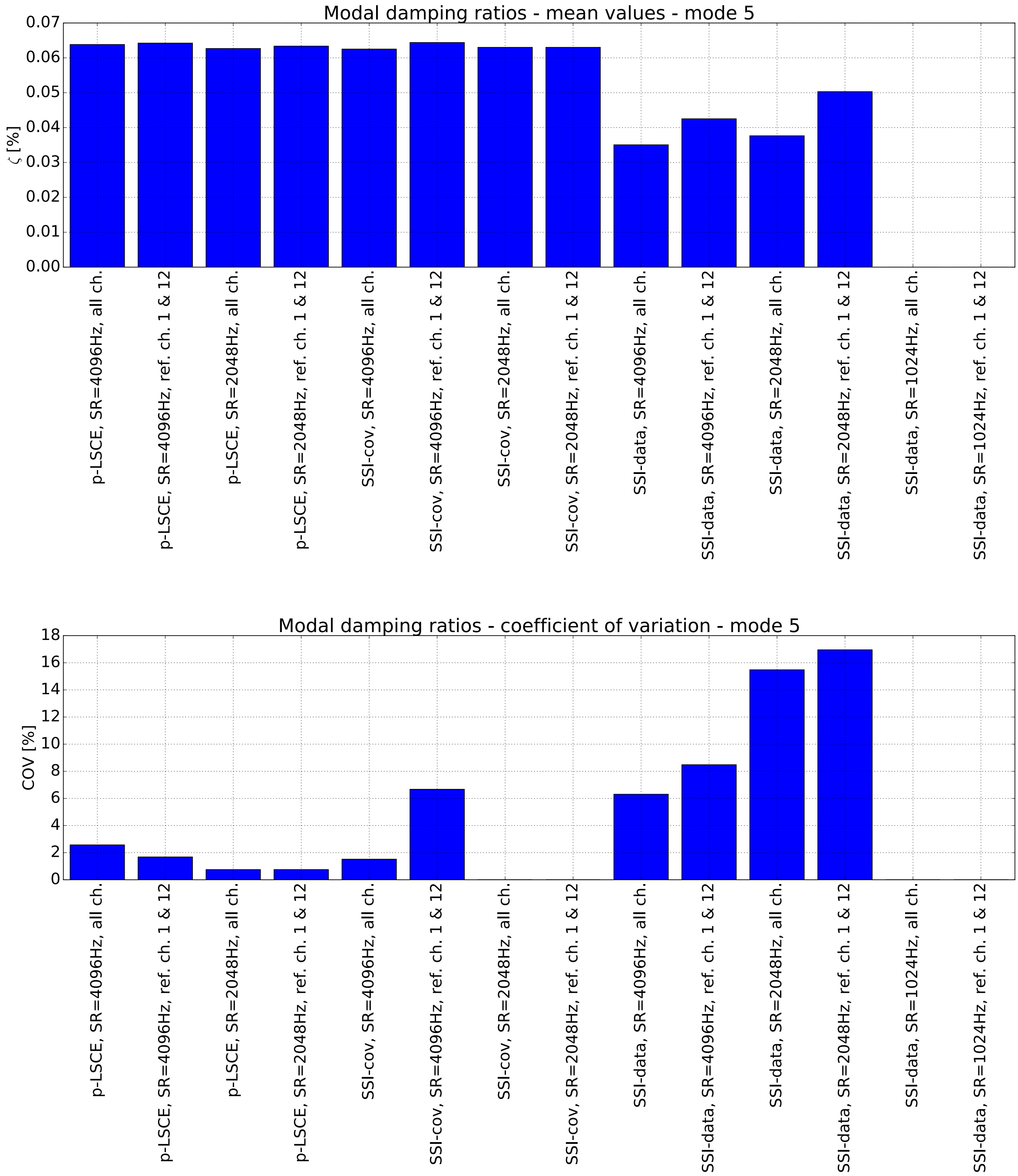

Figure A.10: Mean values and COV of the modal damping ratios identified for mode 5 by means of different OMA methods using various parameters